Thèse présentée pour obtenir le grade de

DOCTEUR DE L'ÉCOLE POLYTECHNIQUE

par

Matteo GUZZO

Dynamical correlation in solids:
a perspective in photoelectron spectroscopy

Soutenue le 8 Octobre 2012 devant le jury composé de :

Silke	BIERMANN	Président
Claudia	DRAXL	Rapporteur
Friedhelm	BECHSTEDT	Rapporteur
Steven G.	LOUIE	Examinateur
Giancarlo	PANACCIONE	Examinateur
Patrick	RINKE	Examinateur
Francesco	SOTTILE	Directeur
Lucia	REINING	Directrice

Contents

Abstract

My thesis fits into the domain of theoretical spectroscopy. This term describes a set of theoretical approaches that go hand-in-hand with several experimental techniques such as optical absorption and reflectivity, inelastic X-ray scattering (IXS), electron energy-loss spectroscopy (EELS) and photoelectron (or photoemission) spectroscopy. This set of *ab-initio* theories is used to simulate, study, predict and understand what is and will be seen in experiment. These spectroscopies are all connected to the dielectric function $\varepsilon(\omega)$ of an electronic system which is, in fact, a fundamental quantity in many modern electronic structure theories. In particular I focused my research on photoemission spectroscopy, where the dielectric function enters as the screening of the hole due to the system. During my thesis I have worked on the development of new theoretical approaches, the aim of my project being to go beyond state-of-the-art methods used in electronic structure calculations. These methods stem mainly from two larger theoretical frameworks: Time-Dependent Density-Functional Theory (TDDFT) and Green's function theory — also known as Many-Body Perturbation Theory (MBPT). I carried on the theoretical development in parallel with numerical simulations on real materials and with experimental measurements, performed to verify the reliability of theory. Thus, the thesis is organized in three main parts.

Theoretical part   In the first part of my thesis the theoretical development focused on the *GW* approximation. This is a method derived from MBPT and it is the current state of the art for the first-principle description of the photoemission process and the calculation of photoemission band gaps. The method is based on the one-particle Green's function or propagator G and the dynamical screening of the system $W = \varepsilon^{-1}v$. Here v is the bare Coulomb interaction. In *GW* the screening is calculated within the Random-Phase Approximation (RPA). The product of G and W gives a many-body dynamical exchange-correlation potential called the *self-energy* $\Sigma = iGW$. The self-energy is usually treated as a perturbation with respect to an effective non-interacting system. I have explored a number of ways to overcome the limits of this approach using partially self-consistent calculations. While getting an improvement over the simpler version, the use of self-consistency has its own limits that make apparent the need to find new methods beyond the *GW* approximation.

The first attempt to go beyond *GW* has been to look for better approximations for Σ and W or, technically speaking, to look for *vertex corrections*. This

is a complicated task, which has been carried out in a simplified way. This simplified way uses TDDFT to reduce the number of degrees of freedom and reformulate the problem as an optimized calculation of the inverse dielectric function ε^{-1}. I have tried different possible approximations for vertices derived from TDDFT. I have studied how different approximations affect the self-energy by calculating the value of the band-gap. This is a path already explored in literature that has given limited improvement with respect to *GW* and limited physical insight in the case of some real materials, but in fact literature lacked an actual extensive study. In particular, the case of *d*-electron systems seemed interesting since *GW* suffers a strong *self-screening* problem in this kind of systems and it appears that a correct vertex correction could fix this particular pathology (see [P. Romaniello, S. Guyot, and L. Reining, J. Chem. Phys., 131, 154111 (2009)]). I extended the study of this simpler type of vertex correction by comparing several approximations and analysing possible pathologies. I explored different possible ways of applying vertex corrections and their influence on the self energy and on the band gap. It turns out that vertex corrections derived from TDDFT can have relatively little effect with respect to a standard *GW* self energy, mainly because of cancellations between effects in the screening *W* and the self energy Σ.

A second way to go beyond *GW* involves the study of spectral properties like satellites, which in *GW* are often poorly described. The new approach I have developed relies on an exponential expression for the one-particle Green's function that, with an optimal inclusion of the neutral excitations of the system via *W*, couples them to the primary photo-induced excitations. The analytical derivation yields a final expression for the one-particle Green's function $\mathcal{G}$ that reads

$$\mathcal{G}(t_1 t_2) = \mathcal{G}^H(\tau) e^{-i \int_{t_1}^{t_2} dt' \int_{t'}^{t_2} dt'' \mathcal{W}(t' t'')}, \tag{1}$$

where $\tau = t_1 - t_2$, $\mathcal{W}$ is a diagonal matrix element of the screened interaction and $\mathcal{G}^H$ is the Hartree Green's function. This solution is obtained directly from the exact equation of motion of the fully interacting Green's function by applying a series of approximations. The final expression for $\mathcal{G}$ is obtained solving exactly the approximate equation of motion, as shown in [Matteo Guzzo *et al.*, Phys. Rev. Lett. 107, 166401 (2011)]. The equations leading to this approximation are based on the PhD work by G. Lani and published in [Lani, G., Romaniello, P., & Reining, L., New Journal of Physics, 2012, 14, 013056]. A similar expression for the Green's function, commonly known as the *Cumulant Expansion*, was derived making an ansatz on the exponential form of $\mathcal{G}$ [F. Aryasetiawan, L. Hedin, and K. Karlsson, Phys. Rev. Lett. 77, 2268 (1996)] or as the solution of a model Hamiltonian where electrons are coupled to bosons [D.C. Langreth, Phys. Rev. B 1, 471 (1970)]. This approach gives a far better description of the coupling between quasiparticle (QP) and neutral excitations than nowadays state-of-the-art methods (e.g. *GW*) and is able to describe satellite peaks of photoemission spectra in the prototype case of Silicon with excellent agreement with experiment. In fact this approximation is able to describe multiple excitations of plasmons that give rise to a series of satellites, greatly improving with respect to *GW* (See Figure 1, taken from [Matteo Guzzo *et al.*, Phys. Rev. Lett. 107, 166401 (2011)]). In particular, my approach gets rid of a

spurious peak that in *GW* gives a wrong satellite shape; this peak is known as a *plasmaron*, after [L. Hedin, B.I. Lundqvist and S. Lundqvist, Solid State Comm. 5, pp. 237–239, 1967 and L. Hedin, Solid State Comm. 5, pp. 451–454, 1967]. This excellent result could also be achieved by the additional inclusion of several effects which are inherent to the experiment — i.e. not removable from the experimental data — such as matrix elements and secondary electron background. An important aspect of the work has been the collaboration with theoreticians and experimentalists from other groups: the inclusion of extrinsic losses effect is the result of a collaboration with Prof. John Rehr and Dr. Josh J. Kas from the University of Washington at Seattle WA, USA; the new experimental data on bulk silicon were provided by Dr. Fausto Sirotti and Dr. Mathieu G. Silly of the TEMPO beamline at the Soleil synchrotron facility in France. Additional results of this collaboration are to appear on the European Physical Journal B topical issue on "Challenges and solutions in *GW* calculations", focusing on the photon energy dependence of the photoemission spectra.
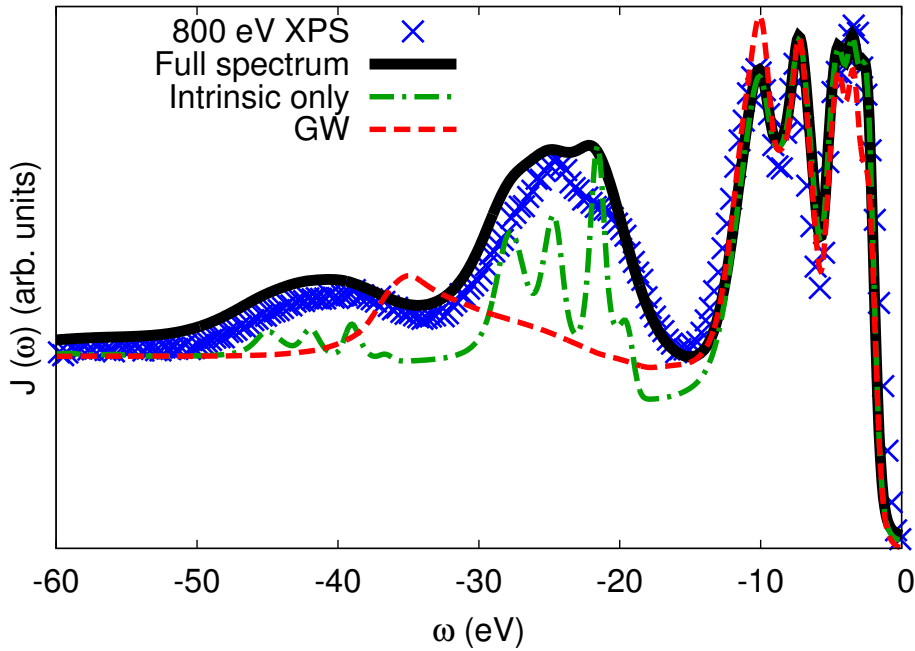
Figure 1: Experimental XPS spectrum of Si at 800 eV photon energy (blue crosses), compared to the theoretical intrinsic $A(\omega)$ calculated from G_0W_0 (red dashed), and from Eq. (1) (green dot-dashed). On top of the latter the black solid line also includes extrinsic and interference effects. All spectra contain photo-absorption cross sections, a calculated secondary electron background and 0.4 eV Gaussian broadening to account for finite k-point sampling and experimental resolution. The Fermi energy is set to 0 eV. From [Matteo Guzzo *et al.*, Phys. Rev. Lett. 107, 166401 (2011)]).

Computational part   Part of my thesis work was also to evaluate the effectiveness of the theoretical development by numerical calculation on real systems

and comparison with existing methods. The calculations were mainly carried out with two software packages, i.e. *dp* and *abinit*. Both codes are written in the *Fortran90* programming language. Implementations and modifications in the software were needed to perform the calculations. One type of calculation gives photoemission addition and removal energies (QP energies) calculating the self-energy Σ. The most computationally demanding calculations produce the *spectral function* $A(\omega) = \mathrm{Im}G(\omega)$, which is a quantity that gives a much more complete description of the photoemission spectrum than just the band structure. I calculated QP energies for a simple semiconductor like Si and for a transition metal oxide like NiO to eventually calculate band-gaps and densities of states and evaluate the effects of vertex corrections. Silicon was again a good test case for the calculation of the spectral function. I also calculated $A(\omega)$ for others semiconductors such as graphite and for the peculiar case of graphene. I studied the effect of self consistency on the QP energies and on the spectral function of these materials. Partial self consistency can be achieved in different manners: via iteration on the QP energies in G only or in both G and W or including also the QP wavefunctions, which is the heaviest task of the three. Depending on the system a different degree of self consistency can be needed. While the iteration over QP energies only in G is preferred in most cases — usually it is enough in all sp semiconductors — for more complex systems (like NiO) it becomes apparent that the Kohn-Sham LDA wavefunctions used as a starting point are too poor and need to be recalculated. This often goes hand-in-hand with d-electron systems. The *GW* spectral function is the starting point for the calculation of the exponential approximation of G in Eq. (1). Since this part of the development was completely analytical (i.e. it did not need any numerical technique to solve the equations), it was sufficient to build a post-processing tool using the *Python* scripting language.

Experimental part   Another important part of my thesis involved measuring photoemission spectra of real materials. This has been crucial to obtain data that could provide a solid reference for theory. In fact, the necessary data to perform an exhaustive comparison between theory and experiment were not available in literature and probably never measured. I submitted a proposal at the Soleil synchrotron facility that was accepted and I could benefit from a week-long shift in July 2011, during which I had the opportunity to perform experimental measurements on graphite. These measurements helped to test and verify the theory I have developed (paper in preparation). Graphite was a good test for theory and a less trivial case than silicon, since the appearance of intrinsic satellites in this system was questioned in literature. Our measurements allowed to confirm that intrinsic satellites in graphite are indeed present and that our theoretical description can handle anisotropic systems of this kind. A second proposal was accepted at the last 2011 call and, consequently, another week of measurements was performed in February 2012. During this beamtime our team measured graphene, another allotrope of carbon. The comparison with graphite will shed some light on the peculiarities of this two-dimensional system. The aim is to highlight similarities and differences of the two systems and to have another test for my theoretical method. In

fact graphene can be seen as an extreme case of graphite, where the inter-plane distance has gone to infinity. The data are undergoing analysis, but the critical points will be the interaction between graphene and its substrate (SiC) and the ability to separate the two contributions.

1 | Introduction

An electronic system, as one can deduce from the Schrödinger equation, is described by a multi-dimensional differential equation. This equation is solvable analitically for a number of particles $N \leq 2$, but any higher number of electrons requires some approximated approach to obtain the solution to the problem. This is what is called the N- or many-body problem. The many-electron problem can be reformulated in terms of Green's functions; however, one still ends up with a set of coupled equations with virtually no solution for an actual electronic system. The concept of correlation is closely connected to the mathematical intricacy of the problem: one may think of removing all interactions between particles from the Hamiltonian: in this case the problem becomes separable and a solution can be calculated, analytically or numerically. In this case one speaks of an independent-particle system, where correlation is neglected. A winning strategy in solid-state physics has been to use pseudo-independent-particle (also called single-particle or *mean-field*) Hamiltonians embedding an effective local potential, to include the effect of the interaction between electrons without increasing the complexity of the equations.

Correlation in solids is, in practice, a quite different matter than correlation in atoms and molecules. The most apparent difference between these two worlds is, generally speaking, the magnitude of the correlation energy. In fact in finite system the correlation energy is a fraction of the exchange energy and hence requires, for a number of cases, little adjustments with respect to the non-interacting (Hartree-Fock) description. This is an easy way to understand why the Hartree-Fock theory, where correlation is totally absent, is able to give a decent description of atoms and molecules, while the description of solids is in general quite poor.

In this manuscript I will focus on correlation effects in solids, notably in the field of photoelectron spectroscopy. To illustrate the practical challenge the physicist faces, I show the valence-band photoemission spectrum of bulk silicon in Figure 1.1 as an example. This is a measurement of photoelectrons close to the Fermi energy (set here at $0\,\text{eV}$) and integrated over the full Brillouin zone. The experimental spectrum is here compared with the density of states of the Kohn-Sham system, that is possibly the most popular among single-particle methods used by physicists. The picture shows how the single-particle density of states matches decently with a limited part of the spectrum, even though the relative weights of the peaks are wrong. This is the part of the spectrum which corresponds to the valence bands of silicon. The problem here is that there are
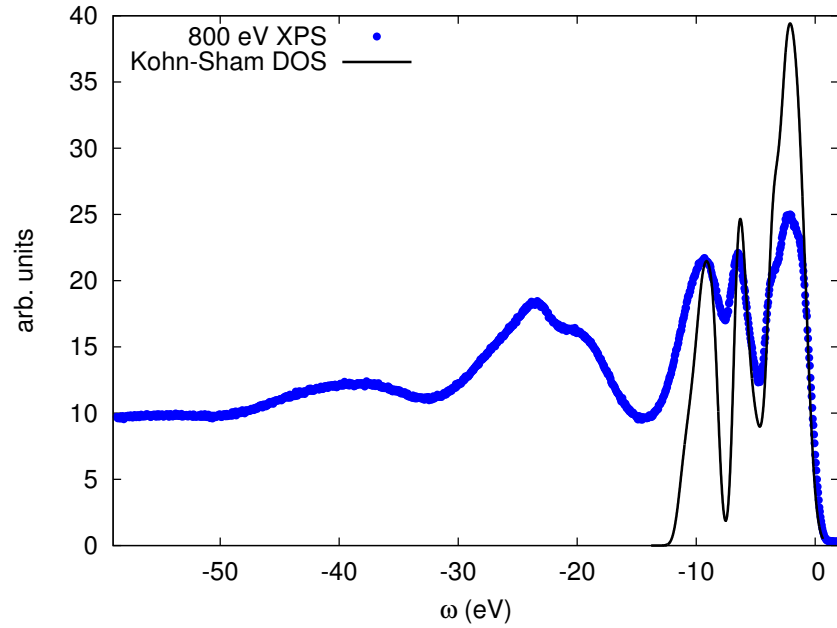
Figure 1.1: Valence-band photoemission spectrum of bulk silicon, measured at the TEMPO beamline [1–3] using 800 eV photons. The Fermi energy is at 0 eV. The spectrum is the result of an integration over the Brillouin zone. The experimental curve shows multiple structures over a range of 60 eV: the first group of peaks on the right, between 0 and -15 eV, can be identified as corresponding to the single-particle band structure of silicon; two other structures — centered at -23 and -40 eV, respectively — can be identified in the experimental curve below -15 eV. The spectrum is compared with a density of states (DOS) calculated using the eigenvalues of the Kohn-Sham system. While this single-particle approach can give a decent qualitative description of the spectrum down to −12 eV, it does not predict any structure below that energy. A gaussian broadening of 0.4 has been added to the theoretical curve to take into account finite k-point sampling and experimental resolution.

a number of structures in the spectrum that are not found in the theory. These are called *satellites* and are a pure signature of correlation. For core-level photoemission spectra, satellites are a known phenomenon and have been studied in several solid-state systems. In valence-band spectra though, they are still poorly discussed. This is because the valence states are often more "messy" than core-level states, which are quite isolated and more easily tractable. This implies additional complexity in experiment and in theory as well. In experiment, valence-band satellites are less obvious to detect than core-level ones as in the same energy range spurious peaks from surface defects and contaminants can arise (Oxygen above all). They therefore require very clean samples. Moreover, as they are supposedly due to excitations coming from all the valence electrons, this produces a noisier spectrum and less sharp features. In theory, one has to deal with the interactions of the numerous valence electrons that are a challenge *per se*. One then would also like to model the collective behavior of electrons beyond the single-particle picture. This is not an easy task.
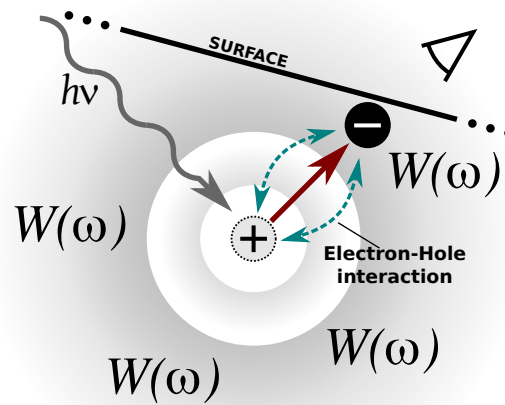
Figure 1.2: Sketch of the photoemission process. A photon of energy $h\nu$ creates a hole (+) ejecting an electron (−) out of the system. The system reacts to the creation of the hole screening the positive charge. $W(\omega)$ is the dynamical screened Coulomb interaction, containing excitations such as excitons and plasmons. Beside that, the outgoing electron is itself interacting with the hole and it is also screened by the system via $W(\omega)$. Furthermore, the photoelectron has to travel to the vacuum through the surface before getting to the detector. The number of additional processes (beyond the propagation of the hole) described here shows the intricacies inherent to the photo-excitation process.

To elucidate the complexity of the problem, I have sketched in Figure 1.2 a scheme of the photemission process. It starts with a photon, penetrating in the bulk. This photon has a probability of giving its energy to the system,

that will react expelling an electron that carries most of the original energy of the photon. This is the basic principle of the photoelectric effect. Now, the photoelectron leaves a depletion positive charge (+) called a *hole*. The creation of the hole is equivalent to a perturbation to the system, that reacts dynamically to the new excited state. This is represented by the dynamic screening $W(\omega)$, that contains all possible excitations of the system, notably creation of electron-hole pairs or collective excitations as plasmons. The hole can interact with the outgoing photoelectron, increasing the complexity of the problem.[1] On the other hand, the photoelectron is also interacting with the system through $W(\omega)$ before it gets out through the surface. The surface itself has an influence on the propagation of the hole and of the electron. All these factors can modify the kinetic energy of the electron that is detected.

While many theoretical approaches focus on the propagation of the hole as the main process that affects the photoemission spectrum, other methods consider the system as a whole, including all elements listed above in the treatment. This is certainly more correct than the former, but it has several shortcomings because of its complexity. I will discuss in this manuscript the theoretical description of the photemission process and the legitimacy of several possible approximations. I will show how all these effects have to be considered when one wants to describe the photoemission spectrum in its entirety, including both quasiparticles and satellites. For this purpose, a discussion of the experimental techniques involved is included.

A quantity that describes properly the propagation of the hole is the single-particle Green's function G. This object contains a fair amount of information, also beyond what is related to the photoemission spectrum, and its equation of motion is an exact reformulation of Schrödinger equation, restricted to one-particle properties. One popular way to calculate G is by means of an effective non-local energy-dependent potential Σ, the *self-energy*, that is in principle able to include all many-body effects. This is a major increase in complexity with respect to single-particle approaches, where potentials are usually static and local.[2] In this framework, *quasiparticles* are the remnants of single-particle excitations, damped and shifted by many-body effects. Then satellites also arise as additional excitations contained in the Green's function and due to pure collective excitations. For quasiparticles the GW approximation for the self-energy has proven to be a success, but the results for satellites have been contradictory, to say the least. I will discuss here whether it is possible to assess precisely the

---

[1]This view of the photoemission process that focuses on the hole as the main actor of the process is absolutely arbitrary. Within this picture, the hole is effectively interacting with a "cloud" of electron-hole pairs through $W(\omega)$. This originates from the fact that, although having a (coupled) quantum system, one has to separate the problem to be able to find a solution. In general terms however, one can think that, once the photoelectron is removed, the main actors are one hole and an electron-hole pair. Once this is known, the description of this three-body system can be achieved using different techniques, that lead to different approximations. While i.e. GW correlates the electron-hole pair and propagates the hole as just depicted, one can correlate the two holes and propagate the electron, obtaining what is called the *particle-particle T-matrix* [4]. A more sophisticated approach is the so-called *three-body scattering*, that takes full account of the quantum nature of all particles [5].

[2]A notable exception is Hartree-Fock where a non-local — yet static — potential describes non-interacting fermions.

description of satellites given by *GW* or not. In parallel, I will explore several ways to improve the description of photoemission spectra and compare them with *GW*. This will be achieved following either the route of so-called *vertex corrections* to the self-energy or a direct way to a better formulation for the single-particle Green's function *G*. The theoretical development will be followed by experimental measurements. The close comparison with experimental spectra and the evaluation of all the components of the photoemission process will be key to a final comprehensive discussion and understanding about satellites in photoemission spectra.

2 | Electron spectroscopies

A spectroscopy experiment in general involves (i) the use of a probe to perturb the system under study and (ii) the measurement of an output signal that carries the information about the interaction between the probe and the sample. In spectroscopy one eventually collects the data changing one of the parameters of the experimental setup. A *spectrum* is the graph resulting from the collected data. As an example, a beam of white light refracted through a glass prism projects the *visible light spectrum* which shows how white light is composed by photons of different wavelengths that one can see as different colors.

Probe and output signal can consist, in practical terms, of any kind of particles, but I will refer here mainly to photons and electrons. There are several types of spectroscopy, but one can distinguish two main families: neutral and charged excitation spectroscopies. Neutral excitations are connected with electron-hole excitations or electron-density fluctuations. The quantity describing these excitations is the macroscopic dielectric function ε_M. Plasmon excitations, which are of great interest in the scope of this manuscript, are due to density fluctuations. Plasmon excitations can be measured by means of electron energy-loss spectroscopy (EELS) or inelastic X-ray scattering (IXS). In fact the two techniques yield proportional spectra. In EELS, an electron is sent through the sample and measured at the exit, thus measuring its losses. EELS is given by the imaginary part of the inverse dielectric function or

$$\text{EELS} = -\,\text{Im}\left[\varepsilon_M^{-1}\right]. \tag{2.1}$$

Charged excitations are connected to a sudden change in the number of particles of the system, caused by an additional particle in the system or by an ejected particle. The quantity describing these excitations is the one-particle Green's function G. The one-particle spectral function is the imaginary part of the Green's function. Under suitable assumptions, one can measure the spectral function by means of photoemission spectroscopy and obtain information on charged excitations in the system. In photoemission spectroscopy one sends a photon beam on the system under study, exciting electrons that are ejected from the system. The spectral function can be written using Fermi's golden rule as [6]

$$A(\omega) \propto \sum_m \delta(\omega - E_m^{N\pm1} + E_i^N). \tag{2.2}$$

Here E_i^N is the energy of the initial N-particle state and $E_m^{N\pm1}$ are the energies of the final $N \pm 1$-particle states, depending whether an electron is added or

removed, respectively. Charged excitation can produce additional neutral excitations in the system, that influence the resulting photoemission spectra. This connection between charged and neutral excitations will be clarified in the following chapters.

2.1   Electron energy-loss spectroscopy

This thesis will focus mainly on photoelectron spectroscopy, but there is a close link between that and electron energy-loss spectroscopy. Therefore I will briefly introduce this technique here. Electron energy-loss spectroscopy or EELS is a powerful experimental technique that uses electrons as a probe to study the properties of materials. This is done usually with a tunneling electron microscope (TEM). In a TEM a beam of high-energy electrons (several
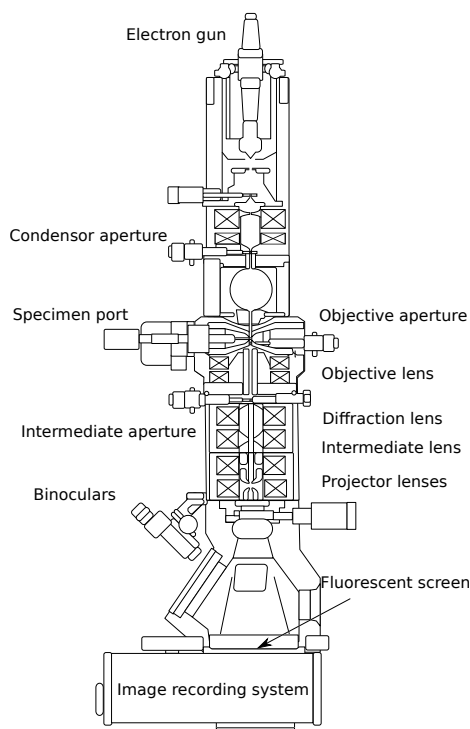
Figure 2.1: Scheme representing a generic transmission electron microscope. Most of the vertical space of the apparatus is taken by the system of electro-magnetic lenses used to focus the inpinging and escaping electron beams. The system is kept under ultra high vacuum ($< 10^{-9}$ Pa). Image taken from the Wikimedia Commons [7].

hundreds keV of kinetic energy) illuminates the sample and electrons are scattered all around after interacting with it. The electrons transmitted behind the sample are then collected and analyzed quite like the way photons would be treated in an absorption experiment. In fact TEMs are equipped with electro-

magnetic lenses which are used to focus the electron beam in the microscope. Measuring kinetic energy and momentum of the transmitted electrons one is able to study structural as well as electronic properties of materials with a high resolution. In particular EELS gives access to the neutral excitations of the system from both core and valence losses. The same kind of excitations can also be probed in inelastic X-ray scattering measurements (IXS), where high-energy photons take the place of electrons.

2.1.1 Connection with photoemission

The EELS and IXS spectra are directly proportional to the imaginary part of the macroscopic inverse dielectric function $\varepsilon_{\mathrm{M}}^{-1}(\mathbf{q}, \omega)$. This quantity is fundamental also for the physics of photoelectron spectroscopy where its microscopic version ε^{-1} enters in the dynamical screening $W = \varepsilon^{-1} v$, v being the Coulomb potential. In photoelectron spectroscopy the screening of the hole produces renormalization and lifetimes of excitations, and non-trivial spectral features like satellites. Hence a correct description of the screening is of utmost importance for a correct description of photoemission. Notably, approximations derived making use of Green's function theory and explicitly including $\varepsilon^{-1}(\mathbf{q}, \omega)$ — as e.g. the *GW* approximation for the self-energy — exploit this link in a direct way. The link between EELS and PES and the importance of combining the two approaches have been highlighted by e.g. Kohiki and others [8]. In this manuscript I will show how one can improve the description of photoemission spectra by improving the approximations used for the calculation of $\varepsilon^{-1}(\mathbf{q}, \omega)$. For a deeper insight on electron energy-loss spectroscopy and ab-initio calculations see [9, 10].

2.2 Photoelectron spectroscopy

X-ray photoelectron or *photoemission spectroscopy* (PES or XPS) is a term that refers to all types of experimental techniques based on the photoelectric effect [11, 12].[1] The general description of this effect is that when a photon of (sufficiently high) energy collides on a sample, an electron can absorb that photon and leave the sample. This is called a *photoelectron*. A sketch of the photoemission process is shown in Figure 1.2. Photoemission spectroscopy is nowadays an established tool for the analysis of the electronic structure of solids and molecules [15]. Its increasing capability in energy-resolution and flexibility has made more urgent, in the last twenty years, the need for advanced theoretical approaches able to cope with the huge range of systems being measured and with the high precision needed to match the experiment [6]. The great improvement of the experimental capabilities have been possible mainly because of third-generation synchrotron radiation facilities [16], such as SOLEIL [17], and the developement of the Scienta electron spectrometers [18, 19]. The former has made possible to obtain higher photon fluxes and the latter is responsible for increasing angular and energy resolution. Photoelectron spectroscopy

---

[1]While the acronym PES is general, XPS is preferred when speaking of photon energies above 100 eV. There can also be ultra-violet PES (UVPES) and angle-resolved PES (ARPES).
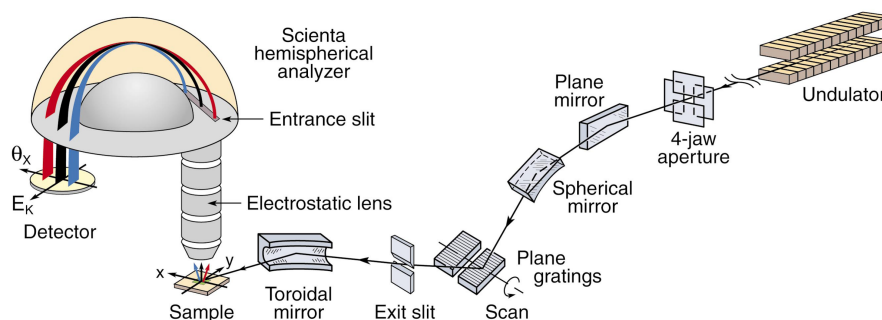
Figure 2.2: Sketch of a generic beamline for photoelectron spectroscopy equipped with a plane grating monochromator and a Scienta electron spectrometer. The ondulator magnet produces a beam of photons from the electron beam in the synchrotron. The photons are then focused on the sample using a set of mirrors and monocromators. The photoelectrons escaping from the sample are then collected and focused by a system of electro-magnetic lenses into the Scienta analyzer to the detector. From [6].

is an extremely accurate technique for chemical analysis. In fact in a PES experiment it is possible to obtain the concentration of different elements in a solid with accuracies of less than a part per million and it is possible to obtain information on the chemical environment (bonding) surrounding an atom. A good example of this feature is given in Figure 2.3. Each peak of the spectrum identifies an electronic state of the substrate, included any substance present on the surface. It is the case for this piece of iron that has evidently not been cleaned. This example shows the great chemical sensitivity of PES and demonstrates how important is to have clean samples if one is to measure bulk properties. In fact one can say that in photoemission one is always surface sensitive. In order to measure bulk properties, the only thing that one can do is trying to minimize the contribution of the surface to the final spectrum, by varying the experimental parameters, such as the photon energy or the sample orientation. For the same reason PES is always performed in chambers under ultra-high vacuum. Most of the information reported in this section can be found in [6, 16, 20], that give a broad and extensive overview of photoemission spectroscopy, its applications and evolution over the past thirty years.

2.2.1   A bit of theory

An independent-particle description is a good start for the understanding of the photoemission process. In this framework one assumes that the incoming photon gives all its energy $2\pi\nu$ to an electron in the bulk, that is then ejected out of the sample with a certain kinetic energy. The maximum kinetic energy E_{kin} of the electron outside the sample will be $2\pi\nu - \Phi$, with Φ the work function of the material. Using this basic principle, photoemission spectroscopy allows one to access the properties of electrons in the bulk. Using an electron analyzer
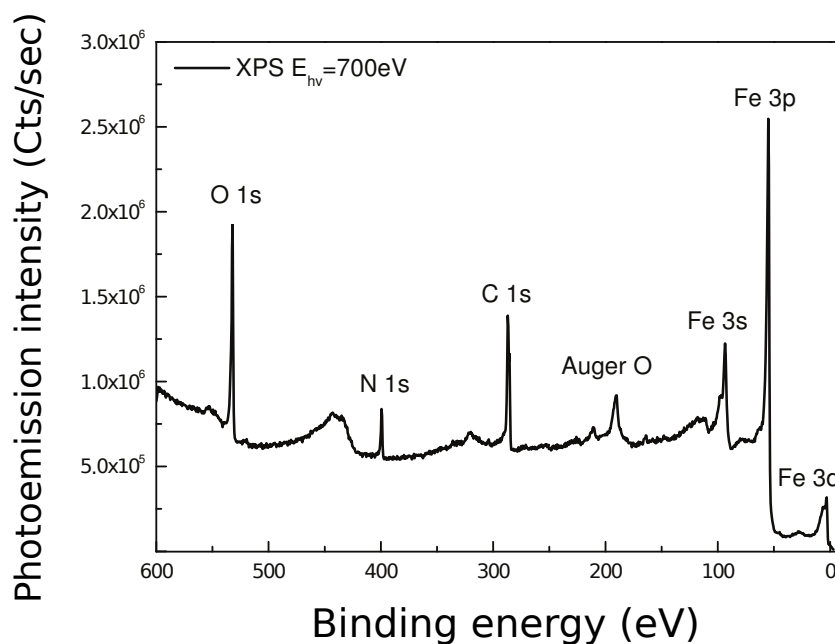
Figure 2.3: Photoemission spectrum of a piece of iron (Fe). The spectrum has been taken at a photon energy $h\nu = 700$ eV. In this large overview there are a lot of peaks showing up in the spectrum. The bulk electronic levels of iron can be spotted in the first 100 eV below the Fermi energy (fixed at 0 eV). The $3d$ (valence), $3s$ and $3p$ (semi-core) shells are all clearly visible. The sample has been exposed to air, hence there are contaminants on the surface that are very easily detected in XPS: the core-level $1s$ peaks of oxygen (O), nitrogen (N) and carbon (C) all show up in the spectrum, as well as their Auger peaks. Such data could be used to calculate with a high precision the concentration of these contaminants on the surface. This is a clear example of the high sensitivity of XPS for chemical analysis. It shows as well the importance of having clean surfaces in order to avoid spurious structures in the spectra. From [13].
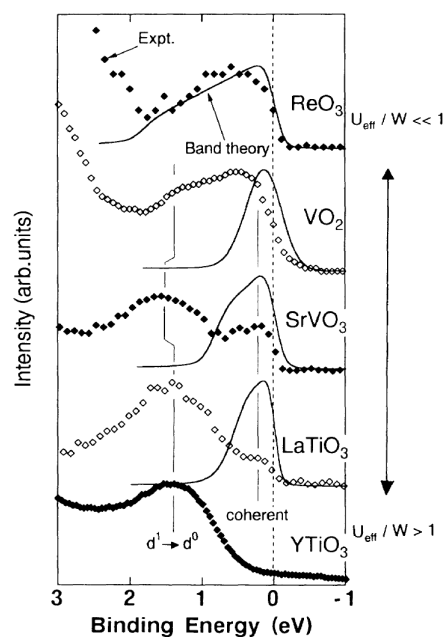
Figure 2.4: Photoemission spectra (dots) of metallic compounds with a d^1 config-uration. From top to bottom the value of U/W increases and correlation effects become more important. Here (and only here) W is the bandwidth and is not to be confused with the dynamical screening discussed in this manuscript. The quasipar-ticle peak — marked as *coherent* — next to the Fermi energy (0 eV) gets weaker and disappears while the satellite structure at -1.5 eV becomes more and more pro-nounced. The data are compared to independent-particle calculations. The image is taken from [14].

one can then collect the photoelectrons and measure their kinetic energy. Keeping in mind that this is strictly possible only in a independent-particle description of the problem, one can define a binding energy E_B and a crystal momentum $\mathbf{k}$ for an electron in the solid. Using energy- and momentum-conservation laws, one can connect, respectively, the binding energy to the kinetic energy and the crystal momentum to the polar emission angle θ of the photoelectron, that can be selected changing the orientation of the analyzer with respect to the surface:

$$E_{\text{kin}} = 2\pi\nu - \Phi - E_B \tag{2.3}$$

$$\mathbf{k}_{||} = \sqrt{2E_{\text{kin}}} \cdot \sin\theta. \tag{2.4}$$

Here $\mathbf{k}_{||}$ is the parallel-to-the-surface component of the crystal momentum $\mathbf{k}$. Information on the perpendicular component of $\mathbf{k}$ is in general non-trivial to obtain at $\theta \neq 0$ (i.e. not at normal emission) because of the breaking of translational symmetry along the surface normal. When an angle-resolved measurement is performed, one speaks of angle-resolved photoelectron spectroscopy or ARPES.

2.2.2 The spectral function and the sudden approximation

A theoretical quantity that is appropriate to compare to XPS experiments is the one-particle spectral function $A(\omega)$. The simplest version of this quantity can be written, in the single-particle case, as

$$A(\omega) = \sum_j \delta(\omega - \epsilon_j). \tag{2.5}$$

Here one assumes to have a system of independent-particle states, as e.g. in Hartree-Fock. In this case the excitations of the system are delta peaks centered at the excitation energies of the system. They therefore have an infinite lifetime. In an interacting system, the spectral function can be written in terms of many-body states using the one-particle Green's function. The current of photoelectrons $J(\omega)$ can be written using Fermi's golden rule as

$$J(\omega) \propto \sum_m \left| M_{m,i} \right|^2 \delta(\omega - E_m^{N\pm1} + E_i^N), \tag{2.6}$$

with $A_m(\omega) = \delta(\omega - E_m^{N\pm1} + E_i^N)$ is the spectral function written using many-body states total energies. Here E_i^N is the energy of the initial N-particle state and $E_m^{N\pm1}$ are the energies of the final $N\pm1$-particle states, depending whether an electron is added or removed, respectively. The matrix elements $M_{m,i}$ contain additional effects due to the energy and polarization of the photon and to the overlap of many-body $N\pm1$ states with the initial state. The main features of the interacting spectral function $A(\omega)$ are quasiparticle peaks with finite lifetime. The interacting spectral function usually shows additional structures that are called *satellites* (See Figure 2.5). These cannot be described by single-particle approaches. In *sp* semiconductors these satellites are mainly due to the excitation of plasmons (both surface and bulk). However the nature of
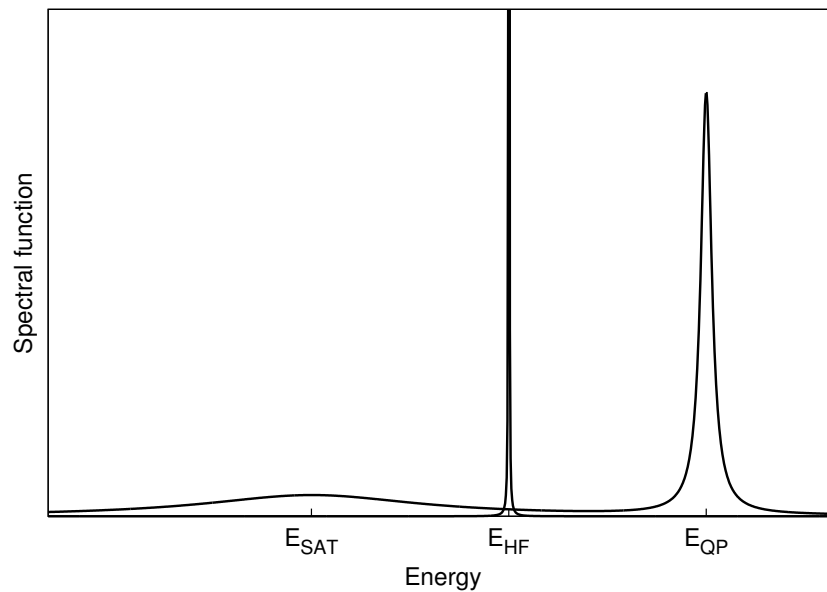
Figure 2.5: General picture of the one-particle spectral function for the independent-particle case (Hartree-Fock) and the interacting case The non-interacting Hartree-Fock (HF) spectral function is a delta peak centered on the HF energy E_{HF}. Its infinitesimal width yields an infinite lifetime. The quasiparticle (QP) spectral function has a very different shape. The main structure is the QP peak, centered on the QP energy E_{QP}, which is shifted with respect to E_{HF}. This peak has a lorentzian shape with a finite width, hence finite lifetime. There is an additional structure at E_{SAT} that is called a *satellite*. This structure comes from collective excitations (e.g. plasmons) that can be accessed using a many-body formalism. The quasiparticle spectral function maintains its center of mass at the non-interacting energy E_{HF}. This is a property guaranteed by the first-moment sum rule (3.48).

satellites in many systems is still heavily debated and begs for a clear explanation. Satellites in photoemission spectroscopy have been extensively studied for core-level spectra [21–23], while for valence-band spectroscopy there has been much less effort [24–26]. Still, valence-band satellites have been measured in a number of systems and are at the center of the debate around some highly interesting systems like e.g. transition metal oxides [14]. Valence-band satellites have been interpreted as a signature of strong correlation effects in terms of the Hubbard model, where the electrons interact by an "ultra-local" Coulomb term called U. The spectral function of this model exhibits, in general, a QP peak at the Fermi level and satellite peaks at lower energies, called *Hubbard band*. For increasing values of U, the QP peak disappears and only the Hubbard band is left (See Figure 2.4). One then speaks of a *strongly-correlated* system. While initially dismissed as an effect of the energy-loss of the photoelectron, satellites have proved to be able to give information about excitations of the system that can be triggered by the creation of the hole.

When making comparisons between theory and experiment, it is worth noting that there is not a complete coincidence between the spectral function $A(\omega)$ and the PES spectrum. This is because $A(\omega)$ only describes the propagation of the hole created by the incoming photon, while completely neglecting the losses of the photoelectron before it leaves the system and possible interactions between photoelectron and hole. The use of $A(\omega)$, within these limits, to describe PES is known as the *sudden approximation*.

2.2.3 The three-step model

While the sudden approximation simplifies the description of PES, there is a number of factors that suggest that this assumption is never actually true. In fact it turns out that the average effective losses of the photoelectrons are roughly the same at all photon energies. There are two competing quantities that contribute to maintain extrinsic losses non-negligible:

1. the mean free path of the electron as a function of its kinetic energy (for high enough photon energy, the inelastic scattering electron cross section decreases as the photon energy, and hence the kinetic energy of photoelectrons, increases); and

2. the maximum depth of a hole for which the corresponding photoelectron is fast enough to reach the surface and be detected (for high enough energy, the value of the mean free-path of electrons increases as their kinetic energy increases).

Once this is established, one must know that the effect of extrinsic losses on the QP part of the spectrum is often only an overall renormalization of the peaks, that transfers some spectral weight from the quasiparticle to the satellite part. This explains the success of the sudden approximation for the description of QP band structures. However, an appropriate calculation and interpretation of satellite structures in photoemission spectra requires one to go beyond the sudden approximation. A more complete, yet simplistic way of modeling the photoemission process is to divide it in three independent sequential steps:

1. Optical excitation of the electron in the bulk.

2. Travel of the excited electron to the surface.

3. Escape of the photoelectron into vacuum.

This is known as the *three-step* model, as first proposed by Berglund and Spicer [27]. The total photoemission intensity is then given by the product of the probabilities of the three different processes. The first step is described by the one-particle spectral function $A(\omega)$. Losses included in $A(\omega)$ are called *intrinsic* and A is therefore called the intrinsic spectral function. Step two is described by the electron energy-loss spectrum of the system and, along with step three, is considered part of the *extrinsic* losses. At this point, to get the total intensity, it would be sufficient to convolute $A(\omega)$ with the energy-loss spectrum; this is called the *sudden limit*. However, this condition is met only at very high photon energies that are rarely accessed in usual PES conditions. There is, in fact, quantum-mechanical interference between intrinsic and extrinsic losses, which is due to the interaction between the outgoing photoelectron and the hole it has left behind. The changes occurring in the photoemission spectrum following this kind of process, are referred to as *interference effects*. To describe this kind of processes one should in principle make use of a two-particle propagator [28], but it is possible to treat this effect in an approximate way retaining at the same time a good amount of physical insight [21]. At low photon energies interference effects are supposed to dominate and the three-step model is no longer valid; this is called the *adiabatic limit*. The sudden approximation and the three-step model may look oversimplistic, but their application allows one an easy treatment of the separate steps and an intuitive understanding of the otherwise very complex photoemission process. A more rigorous approach to photoemission describes the process as a whole in a single calculation. This is a more complex approach that includes bulk, surface and vacuum in the Hamiltonian of the system; it is called the *one-step* model (see e.g. [29]). The simpler three-step model and the sudden approximation are however more widely used, as they have proved that they can be very successful in describing photoelectron spectroscopy. I will report in this manuscript a technique that can effectively include interference effects in the framework of the three-step-model and help to give quantitative information on satellites in photoemission spectra [21].

3 | Theoretical Background

In this chapter I will review the theoretical basis essential to the accomplishment of my thesis. I will first describe how the ground-state problem is treated. The theoretical tool of choice for ground-state properties is density-functional theory (DFT). Then I will concentrate on excited-state properties. Time-dependent density-functional theory (TDDFT) and Green's function theory are the tools that I have used to treat neutral and charged excitations, respectively. At the end of this chapter I will discuss the connection between theory and experimental spectra.

3.1 The many-body problem in solid-state physics

The general many-body problem of quantum mechanics has found in solid-state physics one of its most successful fields of application. All information about the quantum state of a system is contained in its *wavefunction* Ψ. The stationary Schrödinger equation for a many-electron system can be written as[1]

$$H\Psi = E\Psi. \tag{3.1}$$

This is an eigenvalue problem where the unknown are E and Ψ. The Hamiltonian operator H is

$$H = \sum_i^N h_i + \frac{1}{2}\sum_{i\neq j}^N v_{ij}. \tag{3.2}$$

Here h_i are single-particle Hamiltonians, containing the kinetic energies and the external local potential. In this formulation, the ions are fixed (according to the Born-Oppenheimer approximation [30]) and implicitly included in the external potential. N is the number of particles in the system. The interesting term in Equation (3.2) is the two-particle Coulomb interaction term v_{ij} which reads:

$$v_{ij} = \frac{1}{|\mathbf{r}_i - \mathbf{r}_j|}, \tag{3.3}$$

where $\mathbf{r}_j$ is the position of the j-th particle. This term includes in the Hamiltonian the electron-electron interaction and makes virtually impossible to solve the Schrödinger equation for a real system (where $N \sim 10^{23}$, i.e. Avogadro's

---

[1] Throughout the text, the use of atomic units is understood, i.e. $\hbar = m = e^2 = 1$. Also, relativistic effects are neglected.

number).[2] Beside that, the wavefunction of the system Ψ depends on the position and spin of the N particles in the system, i.e. $\Psi = \Psi(\mathbf{x}_1, \ldots, \mathbf{x}_N)$. Just to store this information in a digital memory, one would need more than several thousands of billions of TB of space. This is to say that in practice, to approach the many-body problem, one is obliged to make use of some approximations and/or to find different ways than the straightforward solution of the Schrödinger equation. In the following discussion spin is neglected, if not otherwise stated.

3.1.1 Independent particles: the Hartree approximation

The easiest way to make the many-body problem tractable is to ignore completely the electron-electron interaction, choosing what is called an *independent particle* approximation. In this case the potential $V_{\text{ext}}(\mathbf{r})$ acting on the electrons is only due to the static charge of the ions. This kind of approximation is obviously quite gross. However it turns out that several properties of solids can be decently described by such model once V_{ext} is replaced by some clever guess V_{eff}. This substitution adds to the external potential a correction V_{el} that takes into account the effect of the surrounding electrons on the independent electron i considered, so that $V_{\text{eff}} = V_{\text{el}} + V_{\text{ext}}$. The effective potential could (or not) be function of the single-particle wavefunctions $\phi_i(\mathbf{r})$. A general form of the Schrödinger equation for an independent-particle Hamiltonian would then be the following:

$$H^{\text{ind}}\phi_i(\mathbf{r}) = \left[-\frac{\nabla^2}{2} + V_{\text{eff}}(\mathbf{r}) \right]\phi_i(\mathbf{r}) = \varepsilon_i\phi_i(\mathbf{r}). \qquad (3.4)$$

The above is a set of equations, one for each particle in the system. The eigenvalues ε_i are called *independent-particle energies*. When this kind of Hamiltonian is used to describe a many-electron system one refers to it as a *mean-field* or *single-particle* approach. One possible choice for V_{el} takes into account the potential due to the static electron charge density $\rho(\mathbf{r})$:

$$V_{\text{H}}(\mathbf{r}) = \int d\mathbf{r}' \frac{\rho(\mathbf{r}')}{|\mathbf{r} - \mathbf{r}'|}. \qquad (3.5)$$

This approximation is called the Hartree approximation and V_{H} is the Hartree potential. The density $\rho(\mathbf{r})$ is here defined as

$$\rho(\mathbf{r}) = \sum_i^N |\phi_i(\mathbf{r})|^2. \qquad (3.6)$$

In this case the interaction between the electrons is taken into account by the Hartree term which makes a sort of average over the electrostatic potential of the electrons. A straightforward issue of this approximation is that the Hartree potential acting on the j-th electron is due to the total density calculated using also the electron itself. This is called the *self-interaction* problem. A clear

---

[2]The only case where an analytic solution can be calculated is with $N \leq 2$, e.g. the hydrogen atom or a two-electron system with a classical external potential. Numerical solutions can be obtained with quantum montecarlo techniques for systems with a limited number of particles.

advantage of this kind of single-particle approaches is that the computational cost needed to solve this set of equations is very limited (and feasible) with respect to other approaches (say Hartree-Fock) where the potential is more complicated (e.g. non-local or energy-dependent).

3.1.2   The Hartree-Fock approximation

Another way of simplifying the electronic problem can be to approximate Ψ instead of H. In the Hartree-Fock approximation electrons are considered as non-interacting fermions. Direct consequence of this fact is that the many-body wavefunction Ψ is, in this case, an antisymmetrized product (Slater determinant) of eigenfunctions ϕ_i of a single-particle Hamiltonian:

$$\Psi(\mathbf{r}_1,\ldots,\mathbf{r}_N) = (N!)^{-1/2}\det\{\phi_i(\mathbf{r}_j)\}. \tag{3.7}$$

Assuming that the single-particle eigenfunctions ϕ_i form an orthonormal basis, i.e.

$$\int d\mathbf{r}\, \phi_i^*(\mathbf{r})\phi_j(\mathbf{r}) = \delta_{ij}, \tag{3.8}$$

one can minimize the total energy (using the full Hamiltonian)

$$E = \langle\Psi|H|\Psi\rangle, \tag{3.9}$$

obtaining the *Hartree-Fock* (HF) equations:

$$\int d\mathbf{r}' \left[(h_i + V_H)\delta(\mathbf{r} - \mathbf{r}') + V_x(\mathbf{r},\mathbf{r}')\right]\phi_i(\mathbf{r}') = \varepsilon_i\phi_i(\mathbf{r}), \tag{3.10}$$

where the exchange potential V_x is

$$V_x(\mathbf{r},\mathbf{r}') = -\sum_j^N \phi_j(\mathbf{r})\phi_j^*(\mathbf{r}')\frac{1}{|\mathbf{r} - \mathbf{r}'|}. \tag{3.11}$$

These equations markedly differ from (3.4) in that they contain a non-local operator V_x which includes a sum over the one-particle states in the system. The exchange potential V_x is also called the *Fock operator*. The quantity

$$\rho(\mathbf{r},\mathbf{r}') = \sum_j^N \phi_j(\mathbf{r})\phi_j^*(\mathbf{r}') \tag{3.12}$$

is the *density matrix*. An important consequence of the Hartree-Fock approximation is that the exchange potential corrects the self-interaction problem of the Hartree approximation. In fact when in the sum in (3.11) one has that $j = i$ — the eigenfunction index in (3.10) — the exchange term cancels exactly the Hartree potential.

Koopmans' theorem, exchange and correlation

Koopmans proved that the eigenvalues ε_i of the Hartree-Fock equations (3.10) can be interpreted as energies for addition and removal of electrons in the system [31], i.e. as differences of total energies. This is true provided that, once a

particle has been added/removed, the other particles in the system do not undergo any change. Another way of saying this would be that in Hartree-Fock the screening is neglected, i.e. there is no reaction to a sudden change in the system.

Historically, Hartree-Fock was the first approximation giving a reasonable description of ionization potentials and electronic affinities. The Hartree-Fock approximation is also crucial in solid-state physics as it defines *correlation* as opposed to exchange. In Hartree-Fock exchange is exactly taken into account by construction because the wavefunction Ψ is built to respect the Pauli principle. On the other hand electrons are non-interacting and in this sense there is no correlation. The formal definition of correlation is exactly this: correlation is whatever goes beyond the HF approximation, including additional terms accounting for electron-electron interaction.

3.2   Ground state

The ground state is defined as an equilibrium state of a system described by a stationary Hamiltonian, with the lowest possible total energy. The total energy of an electronic system is defined by (3.9). In this sense, Hartree-Fock appropriately describes the ground-state as it minimizes the total energy of the system for a particular class of wavefunctions. However HF has turned out to be quite bad for total energies of solids. The most successful ground-state theory in the last 40 years is without any doubt density-functional theory.

3.2.1   Density-functional theory

Density-functional theory (DFT) is a ground-state theory in which the emphasis is on the charge density as the relevant physical quantity [32]. DFT has proved to be highly successful in describing structural and electronic properties of a vast class of materials, ranging from atoms and molecules to simple crystals to complex extended systems (including glasses and liquids). Furthermore DFT is computationally simpler than wavefunction-based methods like Hartree-Fock or MP2 and MP3 (very popular techniques among quantum chemists, but with applicability mostly limited to finite systems) [33]. DFT is computationally cheap because its standard application implies the diagonalization of an independent-particle-type Hamiltonian where the potential is local and density-dependent. For these reasons DFT has become a common tool in first-principles calculations aimed at describing — or even predicting — properties of molecular and condensed-matter systems. DFT is based on the Hohenberg-Kohn theorem [32]. This theorem states that (i) there is a one-to-one mapping between a ground-state observable of an electronic system (e.g. the total energy) and the total electronic density via a universal functional and (ii) the ground-state density minimizes the total energy. If one knew the exact functional of the density, one would be able to calculate every observable for a given density. Thus there would be no need to calculate the many-body wavefunction, which is much more complicated to compute than the density and carries much more information, of which only a small part is actually needed

to calculate the ground-state observables. The energy density functional is so defined:

$$E[\rho] = \langle \Psi[\rho] | H | \Psi[\rho] \rangle, \tag{3.13}$$

where $\Psi[\rho_0]$ is the ground-state Ψ_0 in a given external potential. H is the Hamiltonian of the system (3.2). The total energy can be expressed as a functional of the density:

$$E[\rho] = \int d\mathbf{r}\, \rho(\mathbf{r}) V_{\text{ext}}(\mathbf{r}) + F[\rho] \tag{3.14}$$

and it is minimal with respect to ρ with minimum ρ_0 (the ground-state electron density):

$$E_0 = E[\rho_0] < E[\rho], \quad \rho(\mathbf{r}) \neq \rho_0(\mathbf{r}). \tag{3.15}$$

$F[\rho]$ is a universal functional of the density as it does not depend on the external potential. Density-functional theory is then an exact reformulation of the many-electron problem that relies on the ground-state total energy and density as fundamental quantities. An important remark is that the Hohenberg-Kohn theorem gives a solid theoretical justification to the theory, but it does not provide any practical tool that could allow an actual application of the theory. In fact everything relies on the unknown universal functional of the density $F[\rho]$, which one needs to know to solve the problem.

3.2.2 The Kohn-Sham system

A practical application of DFT is possible thanks to the so-called Kohn-Sham scheme [34]. Kohn and Sham stated that it is possible to define a non-interacting electronic system with an effective potential that has exactly the same density as the interacting one. This system is usually referred to as the Kohn-Sham system. The density is thus defined as:

$$\rho(\mathbf{r}) = \sum_{i=1}^{N} |\phi_i(\mathbf{r})|^2 \tag{3.16}$$

where $\phi_i(\mathbf{r})$ are the single-particle wavefunctions and are called the Kohn-Sham orbitals. To obtain the density one has then to solve the non-interacting equations. The Kohn-Sham equations are the following:

$$\left[-\frac{\nabla^2}{2} + V_{\text{KS}}(\mathbf{r}) - \epsilon_i \right] \phi_i(\mathbf{r}) = 0, \tag{3.17}$$

where ϵ_i are Lagrange multipliers. The effective potential (called the Kohn-Sham potential) is composed by three different parts:

$$V_{\text{KS}}(\mathbf{r}) = V_{\text{ext}}(\mathbf{r}) + \int d\mathbf{r}'\, \frac{\rho(\mathbf{r}')}{|\mathbf{r} - \mathbf{r}'|} + V_{\text{xc}}(\mathbf{r}), \tag{3.18}$$

where one can recognize the Hartree potential as the second term on the right-hand side. The exchange-correlation potential $V_{\text{xc}}(\mathbf{r})$ contains all the remaining interactions and it is defined as

$$V_{\text{xc}}(\mathbf{r}) = \left. \frac{\delta E_{\text{xc}}}{\delta \rho} \right|_{\rho = \rho(\mathbf{r})}, \tag{3.19}$$

where E_{xc} is the exchange-correlation energy functional. This functional is linked to the Hohenberg-Kohn energy functional in (3.14) via the following formula:

$$E[\rho] = T'[\rho] + \int d\mathbf{r}\, V_{\text{ext}}(\mathbf{r})\rho(\mathbf{r}) + \frac{1}{2}\int d\mathbf{r}d\mathbf{r}' \frac{\rho(\mathbf{r})\rho(\mathbf{r}')}{|\mathbf{r} - \mathbf{r}'|} + E_{\text{xc}}[\rho], \qquad (3.20)$$

where $T'[\rho]$ is the total kinetic energy of the Kohn-Sham system (i.e. sum of the single-particle kinetic energies). The second and third term are the external field interaction energy and the electrostatic classical energy (Hartree) respectively. The Kohn-Sham formulation has the advantage to have removed the kinetic energy and Hartree contribution from the density functional in the Hohenberg-Kohn original formula (3.14), having left the unknown part of the problem in the smaller E_{xc}. At this point all the effects due to complicated many-body interactions are still hidden in the exchange-correlation functional. The exact dependence of E_{xc} on ρ is a functional dependence, i.e. in general the energy per particle in a point does not only depend on the value of the density in that point, but in fact it depends on the value of the density in all points (i.e. it is *non-local*). Moreover, the exact functional form of E_{xc} is not known and there is no prescription on how to obtain it. The eventual difficulty of the Kohn-Sham approach still remains to find a sensible approximation for the density functional. This has been (and continues to be) an extremely active field of research and the number of different approximations proposed throughout the years is countless. The first and still one of the most popular approximations proposed is called the local density approximation.

The local density approximation

The local density approximation (LDA) consists in neglecting the non-local dependence of the functional on the density $\rho(\mathbf{r})$ re-defining the exchange-correlation functional E_{xc} as the following:

$$E_{\text{xc}}^{\text{LDA}} = \int d\mathbf{r}\, \epsilon_{\text{xc}}^{\rho}(\mathbf{r})\rho(\mathbf{r}), \qquad (3.21)$$

where $\epsilon_{\text{xc}}^{\rho}$ is the exchange-correlation energy per electron of a homogeneous electron gas with density $\rho(\mathbf{r})$. The LDA removes a big problem with a very simple assumption, making the calculation cheaper at the same time. In fact the energy has in principle a functional dependence on the total density ρ, for all values of $\mathbf{r}$. Now to calculate the energy one needs to know the energy density $\epsilon_{\text{xc}}^{\rho}(\mathbf{r})$ only in a given point and not over the whole space. The Kohn-Sham equations are solved self-consistently, minimizing the total energy of the system, and the form of the Kohn-Sham potential, which is local in space and depends on the density only in that single point, allows one to reach the minimum in a much quicker way than e.g. the Hartree-Fock equations. In the latter case the calculation of the exchange operator, which is non-local, is the major computational drawback, while the effective Kohn-Sham potential is local. The other major advantage of DFT-LDA over say HF is that it gives the possibility to calculate total energies including both exchange and correlation. In that, the LDA has proven to give better total energies than HF, notably for solids.

3.3 Excited States

An electronic system jumps into an excited state following a variation of the external potential. This is what happens in spectroscopy, where an external field (the probe) is used to perturb the system and measure its response. That is why the description of excited states is crucial to a theoretical description of spectroscopies. One can draw two main types of excited states looking at the variation in number of particles:

Neutral excitations In this case the number of particles does not change, and one usually refers to an excited N-particle state as $|N,s\rangle$ as opposed to the ground state $|N\rangle$. The key quantity here is the polarizability χ which determines the variation of the density as a response to an external perturbation.

Charged excitations This kind of excitations involve changing number of particles. One refers to the excited state as $|N \pm 1,s\rangle$, if a particle has been added or removed, respectively. The so-called one-particle propagator G is the key quantity for this kind of excitation. G is the one-particle Green's function of the system and describes the probability amplitude for the propagation of an electron/hole.

3.3.1 Time-dependent density-functional theory

Time-dependent density-functional theory (TDDFT) can be simply seen as the time-dependent extension of DFT. In fact in TDDFT there is an equivalent of the Hohenberg-Kohn theorem of DFT which is called the Runge-Gross theorem. Runge and Gross have proved that, given an initial state, there is a one-to-one mapping between the time-dependent external potential $V_{ext}(\mathbf{r},t)$ and the time-dependent density $\rho(\mathbf{r},t)$ [35]. This is true up to a purely time-dependent function. The exact time-dependent density can be reproduced by a non-interacting system, which is a generalized version of the Kohn-Sham system:

$$\left[-\frac{\nabla^2}{2} + V_{KS}(\mathbf{r},t) \right] \phi_i(\mathbf{r},t) = i\frac{\partial}{\partial t}\phi_i(\mathbf{r},t) \tag{3.22}$$

and one can calculate the exact time-dependent density using the single-particle wavefunctions:

$$\rho(\mathbf{r},t) = \sum_{i=1}^{N} |\phi_i(\mathbf{r},t)|^2. \tag{3.23}$$

As in the static case, all the complicated effects lie inside the effective Kohn-Sham potential $V_{KS}(\mathbf{r},t)$ which reads:

$$V_{KS}(\mathbf{r},t) = V_{ext}(\mathbf{r},t) + V_{H}(\mathbf{r},t) + V_{xc}(\mathbf{r},t), \tag{3.24}$$

where V_{ext} includes the external time-dependent perturbation and $V_{H}(\mathbf{r},t)$ is the usual Hartree potential but for a time-dependent density. The time-dependent exchange-correlation functional V_{xc} is defined as

$$V_{xc}(\mathbf{r},t) = \left. \frac{\delta A_{xc}[\rho]}{\delta \rho} \right|_{\rho=\rho(\mathbf{r},t)}, \tag{3.25}$$

where A_{xc} is the exchange-correlation action and it is a functional of the time-dependent density. A_{xc} is defined through the action functional of the Kohn-Sham system A_{KS}:

$$V_{\mathrm{KS}}(\mathbf{r}, t) = \left. \frac{\delta A_{\mathrm{KS}}[\rho]}{\delta \rho} \right|_{\rho = \rho(\mathbf{r}, t)} \tag{3.26}$$

and the exact action of the system $A[\rho]$ as follows:

$$A[\rho] = A_{\mathrm{KS}}[\rho] - \frac{1}{2} \int_C \mathrm{d}\tau \, \bar{t}(\tau) \int \mathrm{d}\mathbf{r}\mathrm{d}\mathbf{r}' \frac{\rho(\mathbf{r}, \tau)\rho(\mathbf{r}', \tau)}{|\mathbf{r} - \mathbf{r}'|} - A_{\mathrm{xc}}[\rho], \tag{3.27}$$

where the second term is related to the Hartree potential and involves an integration on the Keldish contour. The physical time $\bar{t}$ is parametrized by the parameter τ — called *pseudotime* — that runs over a contour C in the complex plane [36, 37].[3] The exact action is stationary with respect to the exact density, i.e.

$$\left. \frac{\delta A[\rho]}{\delta \rho} \right|_{\rho = \rho(\mathbf{r}, t)} = V_{\mathrm{ext}}(\mathbf{r}, t) \tag{3.28}$$

and thus establishes the connection between density and external potential.

Adiabatic local density approximation

The practical challenge of TDDFT is to find a suitable approximation for the exchange-correlation functional $V_{\mathrm{xc}}(\mathbf{r}, t)$. Following the parallel with static DFT, the simplest approximation proposed is the adiabatic local density approximation (ALDA) [36]:

$$V_{\mathrm{xc}}^{\mathrm{ALDA}}(\mathbf{r}, t) = V_{\mathrm{xc}}^{\mathrm{LDA}}\big(\rho(\mathbf{r}, t)\big), \tag{3.29}$$

i.e. the value of V_{xc} at each space-time point $(\mathbf{r}, t)$ is given by the value of the LDA exchange-correlation potential in the same point and at the same time and it is not anymore a functional of the density, in that it does not depend on the density in all positions in space and all times in history.

3.3.2   Linear response in TDDFT

If the variation of the external potential is small, one can make use of linear-response theory. The focus here is on the variation of the density with respect to the external potential. If the potential is weak, one can expand and linearize the density variation $\delta\rho$ in terms of the external potential V_{ext}:

$$\delta\rho(\mathbf{r}, t) = \int \mathrm{d}\mathbf{r}'\mathrm{d}t' \, \chi(\mathbf{r}, t, \mathbf{r}', t') \delta V_{\mathrm{ext}}(\mathbf{r}', t'). \tag{3.30}$$

$\chi(\mathbf{r}, t, \mathbf{r}', t')$ is the linear density-response function (polarizability), defined as

$$\chi(\mathbf{r}, t, \mathbf{r}', t') = \left. \frac{\delta\rho(\mathbf{r}, t)}{\delta V_{\mathrm{ext}}(\mathbf{r}', t')} \right|_{V_{\mathrm{ext}}(\mathbf{r}', t') = V_{\mathrm{ext}}(\mathbf{r}', t_0)}, \tag{3.31}$$

---

[3]This is done in order to respect the causality condition (See [37]).

where $V_{\text{ext}}(\mathbf{r}_2, t_0)$ is the static external potential, i.e. before the perturbation starts to vary after t_0. This χ is a *retarded* response function, as it respects the causality condition: $\chi(\mathbf{r}, \mathbf{r}', t - t') = 0$ for $t < t'$. The calculation of the density-response function χ is key for the study of neutral excitations. It is also crucial in Green's function theory, as it enters in the screened Coulomb interaction W.[4] The density variation is also linked to the variation of the Kohn-Sham potential via the Kohn-Sham polarizability χ^{KS}:

$$\delta\rho(\mathbf{r}, t) = \int d\mathbf{r}' dt' \, \chi^{\text{KS}}(\mathbf{r}, t, \mathbf{r}', t') \delta V_{\text{KS}}(\mathbf{r}', t'), \tag{3.32}$$

χ^{KS} being defined as

$$\chi^{\text{KS}}(\mathbf{r}, t, \mathbf{r}', t') = \frac{\delta\rho(\mathbf{r}, t)}{\delta V_{\text{KS}}(\mathbf{r}', t')}\bigg|_{V_{\text{KS}}(\mathbf{r}', t') = V_{\text{KS}}(\mathbf{r}', t_0)}. \tag{3.33}$$

One can calculate $\delta V_{\text{KS}}/\delta V_{\text{ext}}$ using (3.24) and Schwinger chain rule for functional derivatives:

$$\frac{\delta V_{\text{KS}}(\mathbf{r}, t)}{\delta V_{\text{ext}}(\mathbf{r}', t')} = \delta(\mathbf{r}, t, \mathbf{r}', t') + \frac{\delta V_{\text{H}}(\mathbf{r}, t)}{\delta V_{\text{ext}}(\mathbf{r}', t')} + \frac{\delta V_{\text{xc}}(\mathbf{r}, t)}{\delta V_{\text{ext}}(\mathbf{r}', t')}, \tag{3.34}$$

obtaining the Dyson equation in linear-response TDDFT for the polarizability:

$$\chi(\mathbf{r}, t, \mathbf{r}', t') = \chi^{\text{KS}}(\mathbf{r}, t, \mathbf{r}', t') + \int d\mathbf{r}'' dt'' d\mathbf{r}''' dt''' \, \chi^{\text{KS}}(\mathbf{r}, t, \mathbf{r}'', t'')$$
$$\times \left[v(\mathbf{r}'' - \mathbf{r}''')\delta(t'' - t''') + f_{\text{xc}}(\mathbf{r}'', t'', \mathbf{r}''', t''') \right] \chi(\mathbf{r}''', t''', \mathbf{r}', t'). \tag{3.35}$$

Here f_{xc} is the exchange-correlation kernel, defined as

$$f_{\text{xc}}(\mathbf{r}, t, \mathbf{r}', t') = \frac{\delta V_{\text{xc}}(\mathbf{r}, t)}{\delta\rho(\mathbf{r}', t')}. \tag{3.36}$$

The ALDA for the exchange-correlation kernel (also know as time-dependent LDA or TDLDA) reads:

$$f_{\text{xc}}^{\text{ALDA}}(\mathbf{r}, \mathbf{r}', t, t') = \delta(\mathbf{r} - \mathbf{r}')\delta(t - t')\frac{dV_{\text{xc}}^{\text{LDA}}}{d\rho}\bigg|_{\rho = \rho(\mathbf{r}, t)}. \tag{3.37}$$

The ALDA simplifies remarkably the structure of the kernel. In this approximation all non-locality (space and time) is neglected, as V_{xc} depends only on the local value of $\rho(\mathbf{r}, t)$, in an equivalent way to the static case of LDA in KS-DFT. The ALDA brings also a computational advantage in that it halves the number of integrals that have to be calculated in (3.35).

---

[4]There is an important distinction between response functions in TDDFT and in Green's function theory: the former follow the causality condition and are then called *retarded*; the latter obey a time-symmetry condition, as they are meant to describe particles and anti-particles (i.e. electrons and holes), and are called *time-ordered*. This distinction does not change the general definition of the objects, which is equivalent in the two frameworks; however, is very important when these quantities have to be integrated in the complex plane.

3.3.3   Green's Function Theory

Green's functions are used in all fields of physics and there defined in different ways.[5] The many-body one-particle Green's function is here defined as the propagator of a hole (electron) from space-time point 2 to space-time point 1 (from 1 to 2). G is time-ordered and defined at zero temperature:[6]

$$iG(1,2) = \langle N|\mathcal{T}\left[\hat{\psi}(1)\hat{\psi}^\dagger(2)\right]|N\rangle = \begin{cases} \langle N|\hat{\psi}(1)\hat{\psi}^\dagger(2)|N\rangle & t_1 > t_2 \\ \\ -\langle N|\hat{\psi}(2)^\dagger\hat{\psi}(1)|N\rangle & t_1 < t_2 \end{cases} \tag{3.38}$$

where $\hat{\psi}^\dagger(1)$ and $\hat{\psi}(1)$ are the second-quantization field operators in the Heisenberg representation, for creation and annihilation, respectively. $\mathcal{T}$ is Wick's time-ordering operator. $|N\rangle$ stands for $\Psi(\mathbf{r}_1, \sigma_1, \dots, \mathbf{r}_N, \sigma_N, t)$, the ground-state N-particle many-body wavefunction. The one-particle Green's function carries all the information about one-particle properties of the system. One can therefore use it to calculate the expectation value of any single-particle operator of a given system, e.g.:

- the ground-state density;

- the ground-state total energy;[7]

- the single-particle excitation spectrum (i.e. the photoemission spectrum).

As an example, one can write the ground-state density as:

$$\rho(1) = -iG(1, 1^+) \tag{3.39}$$

i.e. the ground-state density is in fact the Green's function's diagonal in space and time. Extra care must be taken when taking time limits: 1^+ stands here for $\lim_{\eta \to 0} \mathbf{r}_1, t_1 + \eta$ with $\eta > 0 \wedge \eta \ni \mathbb{R}$. This simple equality is the link between DFT and Green's function theory.

3.3.4   Lehmann representation and the spectral function

After one has properly defined G, the problem is how to extract information from it. First, one has to introduce $N+1$ and $N-1$ many-body eigenstates. Using the closure relations of the $|N \pm 1, i\rangle$ in Fock space, inserting them between the field operators in (3.38) and writing $\tau = t_1 - t_2$ one can derive

$$G(\mathbf{r}_1, \mathbf{r}_2, \tau) = -i \sum_i f_i(\mathbf{r}_1) f_i^*(\mathbf{r}_2) \left[\theta(\tau)\theta(\epsilon_i - \mu) - \theta(-\tau)\theta(\mu - \epsilon_i)\right] e^{-i\epsilon_i \tau}. \tag{3.40}$$

The Heaviside step functions remind the reader that μ is the upper bound for hole states (removal energies) and the lower bound for electron (addition energies). This is the Lehmann representation of one-particle Green's function [44].

---

[5]To have a complete overview on Green's functions theory, see [38–42].

[6]$(1, 2, \dots)$ is a shorthand notation for time, space and spin variables $(\mathbf{r}_1, t_1, \xi_1; \mathbf{r}_2, t_2, \xi_2; \dots)$.

[7]The total energy is not a single-particle operator, but it has been shown that it can be calculated once G is known (See e.g. [43]).

Lehmann amplitudes $f_i(\mathbf{r})$ are defined in Fock space as:

$$f_i(\mathbf{r}) = \begin{cases} \langle N|\psi(\mathbf{r})|N+1,i\rangle, & \epsilon_i = E_{N+1,i} - E_N \quad \text{for} \quad \epsilon_i > \mu \\ \langle N-1,i|\psi(\mathbf{r})|N\rangle, & \epsilon_i = E_N - E_{N-1,i} \quad \text{for} \quad \epsilon_i < \mu \end{cases} \tag{3.41}$$

where ϵ_i are the one-particle excitation energies, defined here as differences of total energies of an excited $|N \pm 1, i\rangle$ state and the ground state $|N\rangle$. One can transform this equation in Fourier space, using (B.4) for the step function and obtain

$$G(\mathbf{r}_1, \mathbf{r}_2, \omega) = \sum_i \frac{f_i(\mathbf{r}_1)f_i^*(\mathbf{r}_2)}{\omega - \epsilon_i - i\eta\,\mathrm{sgn}(\mu - \epsilon_i)} \tag{3.42}$$

where the term $i\eta\,\mathrm{sgn}(\epsilon_i - \mu)$ (with $\eta \to 0$ real and positive) is introduced to allow convergence of integrals in the Fourier transform. The form (3.42) of the Green's function highlights its connection with excitation energies and experiment. In fact $G(\mathbf{r}_1, \mathbf{r}_2, \omega)$ is the sum over the i possible configurations of an $N+1$ state ($N-1$ in case of holes) and its poles, which are the excitation energies, are weighted by Lehmann's amplitudes. The ϵ_i are electron addition and removal energies, i.e. the energies that are measured in direct and inverse photoemission experiments. This shows how the Green's function is the appropriate tool to calculate the photoemission spectrum of a system.

A key quantity in Green's function theory and essential for the connection with experiment is the *spectral weight function* $A(\mathbf{r}_1, \mathbf{r}_2, \omega)$. It is also called spectral density function or simply spectral function (when it is unambiguous). The spectral function A is defined as

$$A(\mathbf{r}_1, \mathbf{r}_2, \omega) = \sum_i f_i(\mathbf{r}_1)f_i^*(\mathbf{r}_2)\delta(\omega - \epsilon_i) \tag{3.43}$$

The spectral function is real-valued and it is closely related to the imaginary part of G. This reduces to (2.5) in the case of a system of independent particles, once one has integrated over space to obtain the total spectral function. Knowing that $\lim_{\eta \to 0^+} \frac{1}{x+i\eta} = \mathcal{P}\frac{1}{x} - i\pi\delta(x)$ and applying it to (3.42) one can derive

$$\mathrm{Im}G(\mathbf{r}_1, \mathbf{r}_2, \omega) = \pi\,\mathrm{sgn}(\mu - \epsilon_i)\sum_i f_i(\mathbf{r}_1)f_i^*(\mathbf{r}_2)\delta(\omega - \epsilon_i). \tag{3.44}$$

One can then write a positive-definite expression for A that connects A and G:

$$A(\mathbf{r}_1, \mathbf{r}_2, \omega) = \frac{1}{\pi}\left|\mathrm{Im}G(\mathbf{r}_1, \mathbf{r}_2, \omega)\right| \tag{3.45}$$

A is a real and positive function of ω, which is a numerical advantage with respect to a complex function. It carries the same amount of information as the Green's function, since real and imaginary part of G are connected via Kramers-Kronig relations [45]. The spectral function follows *sum rules*, that can be derived from (3.43):

$$\int_{-\infty}^{+\infty} d\omega\, A(\mathbf{r}_1, \mathbf{r}_2, \omega) = \delta(\mathbf{r}_1 - \mathbf{r}_2), \tag{3.46a}$$

$$\int_{-\infty}^{\mu} d\omega\, A(\mathbf{r}_1, \mathbf{r}_1, \omega) = \rho(\mathbf{r}_1), \tag{3.46b}$$

where $\rho(\mathbf{r}_1)$ is the ground-state density. Both A and G are in practice used as matrices in space with the use of some suitable orthonormal set of single-particle states ϕ_j. One then obtains for G and A

$$
\begin{aligned}
G_{ij}(\omega) &= \int d\mathbf{r}d\mathbf{r}'\, \phi_i^*(\mathbf{r})G(\mathbf{r},\mathbf{r}',\omega)\phi_j(\mathbf{r}'), \\
A_{ij}(\omega) &= \int d\mathbf{r}d\mathbf{r}'\, \phi_i^*(\mathbf{r})A(\mathbf{r},\mathbf{r}',\omega)\phi_j(\mathbf{r}')
\end{aligned}
\tag{3.47}
$$

and all the properties and relations between the two remain unchanged. Now $A_{ii}(\omega)$ is what is calculated when one wants to compare it with ARPES spectra. To calculate the total spectral function one has instead to calculate the trace of $A_{ij}(\omega)$. Another important sum rule for A, provided that it can be diagonalized over some orthonormal basis, is

$$
\int_{-\infty}^{+\infty} d\omega\, \omega A_{ii}(\omega) = \epsilon_{ii}^{\mathrm{HF}},
\tag{3.48}
$$

which puts the center of mass of the spectral function of a given state i at the Hartree-Fock energy $\epsilon_{ii}^{\mathrm{HF}}$ [46]. At this point one only needs a method to calculate the Green's function. This will be the subject of the next part.

3.3.5 Equation of motion for G and the self-energy

The properties of the one-particle Green's function and of the spectral function are now defined. Still, to calculate G one needs to know the many-body states $|N\rangle$ and use one of the definitions in the previous paragraph. This does not make much sense though, as having $|N\rangle$ means having already solved the many-body problem. One needs an alternative approach. The field operators $\hat{\psi}(1)$ used to define G in (3.38) satisfy an equation of motion that one can use to derive a hierarchy of equations of motion for the Green's function. The one-particle Green's function will depend on the two-particle one:

$$
\left[i\frac{\partial}{\partial t_1} - h(\mathbf{r}_1)\right]G(1,2) + i\int d3\, v(1,3)G_2(1,3^+;2,3^{++}) = \delta(1,2),
\tag{3.49}
$$

the two-particle one on the three-particle one, and so on. $h(\mathbf{r}_1)$ is the independent particle hamiltonian, which contains the external potential and $v(1,3) = \delta(t_1 - t_3)/|\mathbf{r}_1 - \mathbf{r}_3|$ is the Coulomb interaction. This set of N-particle Green's function equations retains the complexity of the initial many-body problem. The above is called the equation of motion for the one-particle Green's function. The two-particle Green's function is defined as

$$
i^2 G_2(1,2;1',2') = \langle N|\mathcal{T}\left[\hat{\psi}(1)\hat{\psi}(2)\hat{\psi}^\dagger(2')\hat{\psi}^\dagger(1')\right]|N\rangle
\tag{3.50}
$$

and it is clearly a more complicated quantity than the one-particle G, as it depends on 4 space-time points. Equation (3.49) shows that the propagation of a particle in a solid is mediated by the Coulomb interaction, which is a two-particle interaction. One can think of the hole/electron as a field that polarizes the system, creating electron-hole pairs. This is a simple explanation of

why the two-particle Green's function, which describes the propagation of two particles, appears in the formula. Now, the fundamental idea of many-body perturbation theory is that if one is mainly interested in one-particle properties, the only quantity needed is the one-particle Green's function. Therefore it would seem legit to try and write higher-order Green's functions in an approximate way. As an example, it would be ideal to find good approximations to rewrite the two-particle Green's function in terms of one-particle ones. In the following I will show how it is possible to reformulate the two-particle Green's function in terms of the one-particle G and of an operator Σ (which operates on the one-particle Green's function) called *self-energy* that accounts for all many-body effects. Σ^{xc} is defined by the following relation:

$$i \int d3\, v(1,3) G_2(1,3^+;2,3^{++}) = i \int d3\, v(1,3) G(3,3^+) G(1,2) +$$

$$- \int d3\, \Sigma^{\text{xc}}(1,3) G(3,2), \quad (3.51)$$

where the first term on the right-hand side is the Hartree term, as the electronic density $\rho(\mathbf{r}_3)$ is equal to $-iG(3,3^+)$. The Hartree term can be either included in Σ or treated separately, depending on the case. The self-energy Σ is defined by $\Sigma = V_{\text{H}} + \Sigma^{\text{xc}}$.

The Dyson equation

The expression (3.51) for G_2 can be put in (3.49) to obtain the *Dyson equation* for the one-particle G:

$$\left[i \frac{\partial}{\partial t_1} - h_{\text{H}}(\mathbf{r}_1) \right] G(1,2) - \int d3\, \Sigma^{\text{xc}}(1,3) G(3,2) = \delta(1,2), \quad (3.52)$$

where the Hartree term is now included in $h_{\text{H}}(\mathbf{r}_1)$. The purpose of many-body perturbation theory is then to find suitable approximations for the operator Σ to reformulate it as a functional of one-particle Green's function only. It is possible to define a non-interacting Green's function of a non-interacting particle in the common way used in many fields of physics, as the functional inverse of the non-interacting Hamiltonian:

$$\left[i \frac{\partial}{\partial t_1} - h(\mathbf{r}_1) \right] G_0(1,2) = \delta(1,2), \quad (3.53)$$

where h is the single-particle Hamiltonian *without* the Hartree potential. This shows that we can write the non-interacting Hamiltonian in the Dyson equation (3.52) as G_0^{-1}, multiplying everything by G^{-1}, and re-write

$$G_0^{-1}(1,3) - G^{-1}(1,2) = \Sigma(1,2). \quad (3.54)$$

The definition of G_0 can be used to work out (3.52) and obtain the Dyson equation for G (indices and integrals are here dropped for simplicity):

$$G = G_0 + G_0 \Sigma G. \quad (3.55)$$

These formulas show how Σ carries all information about many-body interactions and connects the interacting system with the non-interacting one. The problem of finding the exact Green's function has been mapped into the problem of finding the self-energy. The self-energy remains here an unknown operator, but, once it is determined, one is able to calculate the one-particle Green's function. In this sense, the self-energy plays here the same role played by the Kohn-Sham potential in KS-DFT. It is an unknown exchange-correlation potential containing all the complicated physics of the system. In the next subsection I will describe Hedin's approach to this problem. This approach introduces a prescription to calculate Σ and gives some physical insight on the problem.

The quasiparticle equation

It would be convenient to have an effective Schrödinger equation from which one can calculate eigenvalues and eigenfunctions for the many-body system. The quasiparticle equation serves exactly this purpose. The Fourier transform of the Dyson equation (3.52) gives

$$[\omega - h_{\mathrm{H}}(\mathbf{r}_1)]\, G(\mathbf{r}_1, \mathbf{r}_2, \omega) - \int d\mathbf{r}_3\, \Sigma^{\mathrm{xc}}(\mathbf{r}_1, \mathbf{r}_3, \omega) G(\mathbf{r}_3, \mathbf{r}_2, \omega) = \delta(\mathbf{r}_1 - \mathbf{r}_2). \quad (3.56)$$

To overcome the complexity of the equation due to the energy dependence of both G and Σ, it is necessary to analytically continue G in the complex plane. One then assumes that the dominant contribution to G comes in the proximity of some complex energies E_i. At the same time one assumes that Σ is slowly-varying in the same neighborhood. This is the *quasiparticle approximation*. Writing G on a set of single-particle wavefunctions and then taking ω at the dominant energies E_i gives

$$\int d\mathbf{r}_3\, [h_{\mathrm{H}}(\mathbf{r}_3)\delta(\mathbf{r}_1 - \mathbf{r}_3) + \Sigma^{\mathrm{xc}}(\mathbf{r}_1, \mathbf{r}_3, E_i)]\, \phi_i(\mathbf{r}_3) = E_i \phi_i(\mathbf{r}_1), \quad (3.57)$$

This is called the quasiparticle equation. In this equation the self-energy acts as a complex, non-local and energy-dependent potential which includes all many-body interactions of the system. The wavefunctions ϕ are called quasiparticle wavefunctions. The E_i are called *quasiparticle excitation energies*. The real part of E_i represents the photoemission excitation energies of the system. The imaginary part is proportional to the inverse of the lifetime of the excitation.

3.3.6   Spectral function from a self-energy

The quantity one usually compares with photoemission experiments is the spectral function, that can be calculated using the imaginary part of the one-particle Green's function (3.43) [24, 25, 39, 47–51]. In Hedin's framework one focuses on the self-energy as the key quantity of the problem, but once the self-energy is known one can use it to calculate the one-particle G using the Dyson equation:

$$G^{-1} = G_0^{-1} - V_{\mathrm{H}} - \Sigma^{\mathrm{xc}}, \quad (3.58)$$

where I have explicitly written the Hartree potential V_{H} — contained before in Σ — and ditched space indices for clarity. Now G, G_0 and Σ are not in general

diagonal on the same basis set. However, in practical applications one assumes these three operators to be diagonal on a common basis and writes

$$G = \frac{1}{\omega - \epsilon_H - \Sigma^{xc}},\tag{3.59}$$

so that the calculation of the imaginary part of G is straightforward and

$$A(\omega) = \frac{1}{\pi} \frac{|\text{Im}\Sigma^{xc}(\omega)|}{[\omega - \epsilon_H - \text{Re}\Sigma^{xc}(\omega)]^2 + [\text{Im}\Sigma^{xc}(\omega)]^2}.\tag{3.60}$$

This expression for the spectral function makes it possible to give a straightforward analysis of its structure and relate it to the case of independent particles. In the independent-particle case (say Hartree) the self-energy is purely real. Therefore the spectral function is a sum of delta functions centered on the energies ϵ_H. This is the case for any static self-energy. When the self-energy is energy-dependent and we talk about quasiparticle energies, the spectral function has the more complex general structure reported above. In this case the spectral function exhibits peaks at the zeros of $\omega - \epsilon_H - \text{Re}\Sigma(\omega)$ with a width which is equal to $|\text{Im}\Sigma(\omega)|$ in the neighboring area. These are in general called quasiparticle peaks and are interpreted as a renormalized version of the independent-particle peaks. *A* can have additional structures, beside quasiparticle peaks. These structures are called *satellites* and form the *incoherent* part of the spectrum, as opposed to the *coherent* part, formed by the quasiparticle peaks. Satellites can arise when the real part of sigma is slowly-varying and comparable to the imaginary part, that must have a local maximum to produce a visible structure in the self-energy.

3.3.7 Energy shift in the G_0W_0 spectral function

When one calculates the self-energy starting from a non-interacting Green's function, the relative shift of the bands can be small with respect to the absolute energy shift, that can be quite significant. This results in a shift ΔE of the Fermi energy that, if not taken into account, can affect the shape of the spectral function. This problem comes from the non-self-consistent nature of the eigenvalues used to construct the Green's function and is automatically solved if self-consistency in G is imposed. According to Hedin [25], one should add a correction term ΔE, imposing self-consistency at the Fermi level, i.e.

$$\varepsilon_{\text{top-valence}} + \Delta E = E_{\text{top-valence}}^{QP}\tag{3.61}$$

and shift all energies by this value. After a change of variables, the spectral function can then be written as

$$A_i(\omega) = \frac{1}{\pi} \frac{\left|\text{Im}\Sigma_i^{xc}(\omega)\right|}{\left[\omega - \varepsilon_i + \Delta E - \text{Re}\Sigma_i^{xc}(\omega)\right]^2 + \left[\text{Im}\Sigma_i^{xc}(\omega)\right]^2}.\tag{3.62}$$

The effect of the correction is of course proportional to the shift. One can take the example of bulk silicon (See Figure 3.1). Here the shift is of the order of 0.1 eV and the effect on the total spectral function is very small. The visible

trend is that the QP peaks are enhanced and there is a slight reduction of the satellite weight. The greatest effect appears to be close to the fermi energy. This example is of course not representative of a general case. The effect of the
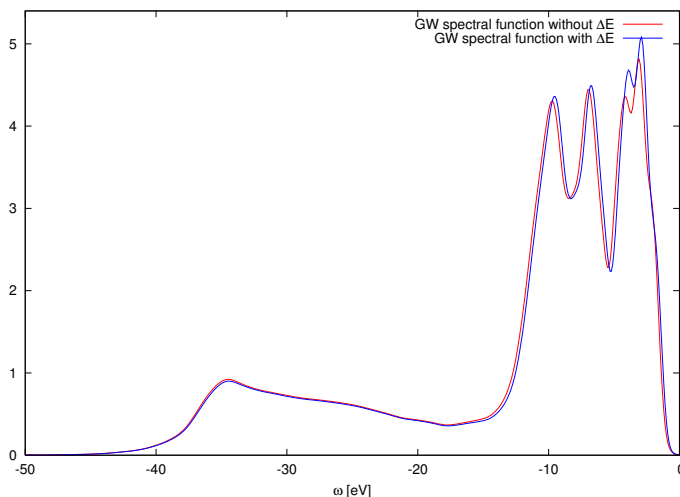
Figure 3.1: GW spectral function for bulk silicon with (solid red) and without (solid blue) the ΔE correction. The Fermi energy is at 0 eV. Both curves include a gaussian broadening with $\sigma = 0.4$ eV.

correction will strongly depend on the magnitude of the shift and on the shape of the self-energy. An example of this is VO_2, where the energy shift is crucial to correct the position of satellites close to the Fermi energy [52].

3.4   Hedin's equations and *GW*

At this point the problem of calculating G has been transferred to the problem of calculating Σ, a complex energy-dependent non-local potential. Yet, there is no prescription on what the self-energy should be (apart from a function of the utterly complicated G_2) or how to find reliable approximations. Hedin's approach aims exactly at giving an easier tool than the bare Dyson equation to find approximations for the self-energy, with a particular accent on the dynamical screening W that leads to the *GW* approximation.

Schwinger [53] proved that, in the presence of a small perturbing potential φ, it is possible to formally eliminate the dependence on G_2 using functional derivatives. Thanks to Schwinger's technique, it can be shown that:

$$\frac{\delta G(1,2)}{\delta \varphi(3)} = G(1,2)G(3,3^+) - G_2(1,3,2,3^+). \tag{3.63}$$

With this equation it is possible to write the two-particle Green's function in terms of one-particle ones. The external perturbation φ is put to 0 at the end

of the derivation. One can use this relation to substitute G_2 in the equation of motion of the one-particle Green's function (3.49) to obtain

$$\left[i\frac{\partial}{\partial t_1} - h_{\mathrm{H}}(\mathbf{r}_1)\right] G(1,2) - i\int \mathrm{d}3\, v(1^+,3)\frac{\delta G(1,2)}{\delta\varphi(3)}\bigg|_{\varphi=0} = \delta(1,2). \tag{3.64}$$

Now one has to calculate G solving (3.64) to obtain the solution of the one-particle problem. This would imply the solution of a multi-dimensional functional differential equation for G, a problem that is nearly as difficult as the many-body problem (See Section 3.6), since one has to know the explicit dependence of G with respect to φ. As an alternative, one can try to iterate the equation for G making in practice an expansion in the Coulomb potential v using perturbation theory. This kind of approach has been tried and the series is known to diverge after a few orders.

The problem can be reformulated in terms of a self-energy, finding two equivalent expressions[8] for Σ:

$$\Sigma(1,2) = -i\int \mathrm{d}345\, G(1,4)\frac{\delta G^{-1}(4,2)}{\delta\varphi(3)}v(1^+,3) \tag{3.65a}$$

$$= i\int \mathrm{d}345\, G^{-1}(4,2)\frac{\delta G(1,4)}{\delta\varphi(3)}v(1^+,3). \tag{3.65b}$$

These two can also serve as an alternative definition of the self-energy, once the Schwinger relation is known. On the path to obtain Σ and G, Hedin [38, 39] introduces at first the local classical potential $V(1)$:

$$V(1) = \varphi(1) - i\int \mathrm{d}2\, v(1,2)G(2,2^+), \tag{3.66}$$

which is the sum of the external perturbation φ and the Hartree potential $V_H(1) = -i\int \mathrm{d}2\, v(1,2)G(2,2^+)$. Using the functional derivative's chain rule by Schwinger[9] one can reformulate equation (3.65a) as

$$\Sigma(1,2) = -i\int \mathrm{d}345\, G(1,4)\frac{\delta G^{-1}(4,2)}{\delta V(5)}\frac{\delta V(5)}{\delta\varphi(3)}v(1,3^+). \tag{3.67}$$

One then introduces the time-ordered inverse dielectric function:

$$\varepsilon^{-1}(1,2) = \frac{\delta V(1)}{\delta\varphi(2)}, \tag{3.68}$$

and the irreducible vertex function:

$$\tilde{\Gamma}(1,2;3) = -\frac{\delta G^{-1}(1,2)}{\delta V(3)}; \tag{3.69}$$

the term "irreducible" means that the functional derivative is performed with respect to the classical total potential V and not only with respect to the external potential φ. For each irreducible quantity, is possible to define a reducible

---

[8]For two generic functionals $G(1,2)$ and $\varphi(1)$, $\frac{\delta G(1,2)}{\delta\varphi(3)} = -\int \mathrm{d}45\, G(1,4)\frac{\delta G^{-1}(4,5)}{\delta\varphi(3)}G(5,2)$

[9]For three generic functionals A,B and C with $A = A[B[C]]$, $\frac{\delta A[B[C]](1)}{\delta C(2)} = \int \mathrm{d}3\, \frac{\delta A[B](1)}{\delta B(3)}\frac{\delta B[C](3)}{\delta C(2)}$

function differentiating with respect to φ. The dynamical screened Coulomb interaction, a fundamental quantity in Hedin's framework, is then introduced:

$$W(1,2) = \int d3\, v(1,3)\varepsilon^{-1}(3,2). \tag{3.70}$$

Now one can rewrite the self-energy as

$$\Sigma(1,2) = i \int d34 G(1,4)W(3,1^+)\tilde{\Gamma}(4,2;3). \tag{3.71}$$

One still has to provide some tractable expressions for $\tilde{\Gamma}$ and ε^{-1}. Using the Dyson equation $G^{-1} = G_0^{-1} - V - \Sigma$, equation (3.68) is worked out with some functional analysis to give

$$\tilde{\Gamma}(1,2;3) = \delta(1,2)\delta(1,3) + \int d4567 \frac{\delta\Sigma(1,2)}{\delta G(4,5)} G(4,6)G(7,5)\tilde{\Gamma}(6,7;3). \tag{3.72}$$

For ε^{-1} one can use the definition of V in (3.66) and write:

$$\varepsilon^{-1}(1,2) = \delta(1,2) + \int d3 v(1,3)\chi(3,2), \tag{3.73}$$

where

$$\chi(1,2) = -i\frac{\delta G(1,1^+)}{\delta\varphi(2)} \tag{3.74}$$

is the time-ordered reducible polarizability of the system. One can introduce the irreducible polarizability as

$$\tilde{\chi}(1,2) = -i\frac{\delta G(1,1^+)}{\delta V(2)} \tag{3.75}$$

which is related to χ by

$$\chi(1,2) = \tilde{\chi}(1,2) + \int d34 \, \tilde{\chi}(1,3)v(3,4)\chi(4,2). \tag{3.76}$$

Finally, $\tilde{\chi}(1,2)$ can be written as a function of G and Σ:

$$\tilde{\chi}(1,2) = -i \int d34 \, G(1,3)G(4,1)\tilde{\Gamma}(3,4;2). \tag{3.77}$$

One can finally write Hedin's set of five equations in five unknown quantities [38, 39]:

$$G(1,2) = G_0(1,2) + \int d34 \, G_0(1,3)\Sigma(3,4)G(4,2) \tag{3.78a}$$

$$\tilde{\Gamma}(1,2;3) = \delta(1,2)\delta(1,3) + \int d4567 \frac{\delta\Sigma(1,2)}{\delta G(4,5)} G(4,6)G(7,5)\tilde{\Gamma}(6,7;3) \tag{3.78b}$$

$$\tilde{\chi}(1,2) = -i \int d34 \, G(2,3)G(4,2)\tilde{\Gamma}(3,4;1) \tag{3.78c}$$

$$W(1,2) = v(1,2) + \int d34 \, v(1,3)\tilde{\chi}(3,4)W(4,2) \tag{3.78d}$$

$$\Sigma(1,2) = i \int d34 \, G(1,4)W(3,1^+)\tilde{\Gamma}(4,2;3) \tag{3.78e}$$

where W is written as a function of $\tilde{\chi}$ to avoid introducing the intermediate quantities ε^{-1} and χ. In his original paper [38], Hedin mentioned that these equations can be viewed as a starting point for an iterative solution of the many-body problem, but he stressed that they would be interesting if only very few iterations were actually needed (because of the increasing difficulty of the calculation). For a practical use of Hedin's equations, the calculation starts with some hypothesis on Σ and G; then $\tilde{\Gamma}$ and $\tilde{\chi}$ are evaluated. At this point W and then Σ can be calculated. Now one knows an improved Green's function G and can start again the same procedure, with the new Σ and G. This procedure can be represented by the pentagon in figure 3.2, where each corner represents an unknown variable and each edge one of the five Hedin's equations. The exact solution can be in principle obtained upon completion of several cycles of the pentagon, once convergence is reached. This is an in principle
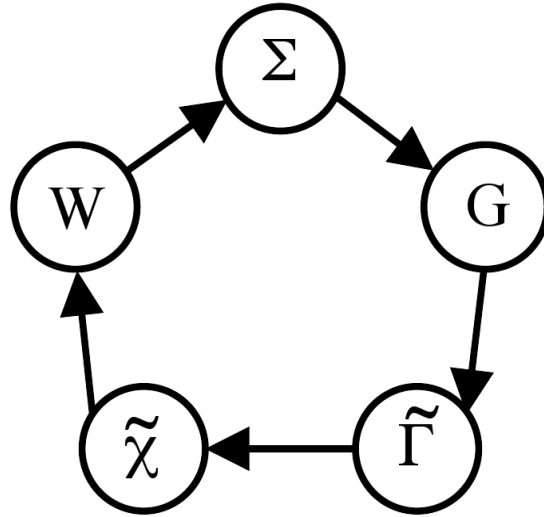
Figure 3.2: Hedin's pentagon, representing the calculation cycle of Σ. Every corner represents a quantity and one of the five equations. The *GW* approximation is represented by a single cycle of the pentagon where one starts with $\Sigma = 0$.

exact procedure and will be in practice unfeasible because of the complexity of the quantities involved. The difference with the previous reformulations of the many-body problem is that now one has a framework where physical quantities — namely W — are recognizable. This point is important in that it can help finding approximation for the self-energy. The most successful example of this is probably the *GW* approximation. Hedin proposed also the COHSEX approximation (a static version of *GW*), that contains physical insight and yet it is static, hence computationally cheaper.

3.4.1 The *GW* approximation

One of the advantages of Hedin's equations is that they use the screened interaction W instead of the Coulomb interaction v. Using W instead of v as basic interaction is motivated by the hope that the perturbation theory will converge faster with respect to powers of W, than with respect to the powers of v. Having this hope in mind, Hedin proposed to retain only first-order contributions in W. This principle yields the so-called *GW* approximation that consists in initiating the iterative scheme with $\Sigma = 0$ in the vertex equation:

$$\tilde{\Gamma}(1,2;3) = \delta(1,2)\delta(1,3). \tag{3.79}$$

The resulting self-energy becomes then

$$\Sigma(1,2) = iG(1,2)W(2,1^+). \tag{3.80}$$

This form for the self-energy gives the name to the approximation. The corresponding irreducible polarizability reads

$$\tilde{\chi}(1,2) = -iG(1,2)G(2,1) \tag{3.81}$$

which is the definition of the independent-particle (or RPA) polarizability.

One-shot GW

The standard approach that is used to calculate photoemission excitation energies within the *GW* approximation starts with a close comparison of the quasiparticle equation (3.57) and the Kohn-Sham equation (3.17). The exchange-correlation potential and the self-energy act both as a potential in a pseudo-Schrödinger equation, with Σ being much more complicated than V_{xc}^{KS}. If one assumes that the Kohn-Sham orbitals are a decent approximation of quasiparticles — which in principle they are not — it is reasonable to consider $\Sigma - V_{xc}^{KS}$ as a first-order perturbation to the Kohn-Sham Hamiltonian. This *a priori* meaningless comparison — the Kohn-Sham orbitals are fictitious wavefunctions constructed to give the exact total density and the eigenvalues ϵ_i^{KS} are Lagrange multipliers — has proven to be reasonable for a large class of materials, especially *sp* semiconductors [54]. *GW* energies are hence most often calculated as first-order corrections to the Kohn-Sham energies, for a quasiparticle state i, as

$$\epsilon_i^{GW} = \epsilon_i^{KS} + Z\langle\phi_i|\Sigma(\epsilon_i^{KS}) - V_{xc}^{KS}|\phi_i\rangle, \tag{3.82}$$

where Σ has been linearized in the vicinity of ϵ_i^{KS}, so that the problem of its dependence on ϵ_i^{GW} is solved. The Z factor comes from the linearization:

$$Z = \frac{1}{1 - \frac{\partial\Sigma}{\partial\epsilon}\Big|_{\epsilon_i^{KS}}}. \tag{3.83}$$

The self-energy is constructed with Kohn-Sham LDA wavefunctions and energies via the Green's function G and the RPA screening W. This procedure is known as *one-shot GW*, G_0W_0 or *perturbative GW*, and has proven to be very

successful in predicting photoemission gaps of various compounds. The perturbative approach is valid as long as the electronic structure of the starting point is considered reasonable. This is known not to be the case for LDA in several systems, most notably in transition metal oxides. In these systems the KS orbitals have shown to give a very different electronic structure with respect to quasiparticles. Several methods have been developed to improve the description of the electronic structure in difficult cases like these and there is still a lot of activity in the field. The typical solution is to use an improved V_{xc}^{KS} to correct this problem, but there are also simple approximations of the self-energy that can be used instead [55, 56]. The lasting issue of perturbative *GW* is that it relies on the quality of the starting point. The only way to remove this dependence is to adopt a partial or full self-consistent scheme for the calculation of the self-energy.

3.4.2 Hartree-Fock self-energy

Using the quasiparticle equation and selected approximations for the self energy, one can trace a path from the simpler to the more complex approximations and understand better the concept of correlation. While the Hartree approximation can be retrieved putting $\Sigma = 0$, the Hartree-Fock approximation can be recovered writing the self-energy as

$$
\begin{aligned}
\Sigma_x(1,2) &= i\,v(1^+,2)G(1,2) \\
&= -v(\mathbf{r}_1,\mathbf{r}_2)\rho(\mathbf{r}_1,\mathbf{r}_2) = -\sum_{occ}\phi_i(\mathbf{r}_1)\phi_i^*(\mathbf{r}_2)v(\mathbf{r}_1,\mathbf{r}_2).
\end{aligned}
\tag{3.84}
$$

$\Sigma_x(1,2)$ is the Fock exchange operator, or Hartree-Fock self-energy. $\rho(\mathbf{r}_1,\mathbf{r}_2)$ is the density matrix. The Fock operator can be derived from *GW* self-energy, assuming that $\varepsilon^{-1} = 1$. The direct consequence is that the dynamical screened Coulomb interaction *W* is replaced by the bare static Coulomb interaction *v*. The physical meaning is that within this approximation the system is not allowed to relax after the addition or removal of an electron, as it is stated by Koopmans' theorem [31]. This procedure is the proof that Fock exchange is contained in *GW* — as it can be retrieved simplifying the *GW* self-energy — and thus correlation effects are included in *GW*. The concept of correlation is linked here to the response of the many-electron system after a perturbation (e.g. a change in number of particles). In general it is always possible to separate the self-energy in an exchange part Σ_x and a correlation part Σ_c just by defining $\Sigma_c = \Sigma - \Sigma_x$. In the case of *GW* this yields to a Σ_c that reads

$$
\Sigma_c = iGW_p
\tag{3.85}
$$

where one has written the screening *W* as $W = v + W_p$, where $W_p = v\tilde{\chi}v$ is the polarization part of the screening.

3.4.3 COHSEX self-energy

The COHSEX approximation for the self-energy, first proposed by Hedin as an affordable approximation of *GW* [38], produces an hermitian self-energy

which is static and requires only a sum over the occupied states. This makes the COHSEX approximation much more affordable than *GW*, where the self-energy is dynamical. The COHSEX self-energy is the sum of two terms. The first term is

$$\Sigma^{\text{SEX}}(\mathbf{r}_1, \mathbf{r}_2) = -\sum_i \theta(\mu - \epsilon_i) \phi_i(\mathbf{r}_1) \phi_i^*(\mathbf{r}_2) W(\mathbf{r}_1, \mathbf{r}_2, \omega = 0) \qquad (3.86)$$

which is called the *screened exchange* part (SEX). This formula is almost identical to equation (3.84), except that here the static screened Coulomb interaction has taken the place of the bare Coulomb interaction v. This term takes into account correctly the fermionic nature of electrons, including exchange. At the same time it includes the fact of being in a polarizable medium and it damps the exchange interaction. The sum over occupied states ensures a limited computational effort, whereas in the *GW* self-energy one has to sum over all the empty states as well. The calculation of W requires to calculate ε^{-1} at $\omega = 0$, which is less effort than in *GW*. The second term of the COHSEX self-energy is

$$\Sigma^{\text{COH}}(\mathbf{r}_1, \mathbf{r}_2) = \frac{1}{2} \delta(\mathbf{r}_1 - \mathbf{r}_2) W_p(\mathbf{r}_1, \mathbf{r}_2, \omega = 0), \qquad (3.87)$$

where $W_p = W - v$ is again the polarization part of W. This second term is called the *Coulomb-hole* (COH) contribution to the self-energy. It is static and local in space. This latter term represents the energy shift due to the istantaneous polarization of the system induced by an added hole or electron, represented by a classical point charge. Then $\Sigma^{\text{COHSEX}} = \Sigma^{\text{SEX}} + \Sigma^{\text{COH}}$. The COHSEX approximation for the self-energy gives an immediate physical insight. One can easily understand what effects are included in the self-energy (exchange and polarization) and what are missing (dynamical correlation, e.g. satellites). Furthermore COHSEX has a distinct computational advantage over *GW*. This approximation is known to be a reliable approach for self-consistent calculations, purpose of which is to calculate new wavefunctions [55, 57, 58]. In fact the *GW* self-energy is in general non-hermitian. Using COHSEX one can diagonalize the self-energy and solve the quasiparticle equation (3.57). The dynamical effects neglected in Σ^{COHSEX} are normally included in the calculation by a last perturbative *GW* step on top of the converged COHSEX band structure.

3.4.4 Plasmon-pole model

The calculation of the self-energy in *GW* involves a convolution of *G* and *W* in the frequency domain (dropping space indices):

$$\Sigma(\omega) = \frac{i}{2\pi} \int \mathrm{d}\omega' \, e^{i\omega'\eta} G(\omega + \omega') W(\omega'). \qquad (3.88)$$

This part of the calculation is very time-consuming. To calculate W, the matrix $\varepsilon^{-1}_{\mathbf{G}\mathbf{G}'}(\mathbf{q}, \omega)$ must be calculated for different values of $\mathbf{q}$ in the Brillouin zone, for all values of ω.[10] When one is interested only in the value of the integral

---

[10] The inverse dielectric function is defined here in reciprocal space on the $\mathbf{G}$ vectors of the plane wave basis and in frequency space.

it is acceptable to approximate the integrand to a simple form. It has been proposed to model the dependence on ω of the matrix $\varepsilon^{-1}_{\mathbf{GG'}}(\mathbf{q}, \omega)$ by a single plasmon-pole model [48, 49, 59–62]:

$$\varepsilon^{-1}_{\mathbf{GG'}}(\mathbf{q}, \omega) = \delta_{\mathbf{GG'}} + \frac{\Omega^2_{\mathbf{GG'}}(\mathbf{q})}{\omega^2 - (\tilde{\omega}(\mathbf{q}) - i\eta)^2} \tag{3.89}$$

where $\Omega^2_{\mathbf{GG'}}(\mathbf{q})$ and $\tilde{\omega}(\mathbf{q})$ are the two parameters of the model. The inverse dielectric function is here approximated as a single-peak structure. This model allows one to evaluate ε^{-1} everywhere in the complex plane, once the two parameters are set. To fit the parameters two constraints are needed. As an example, the ABINIT *GW* code [63] chooses two frequencies where the RPA ε^{-1} is computed: $\omega = 0$ and $\omega = i\omega_p$. It is convenient to take an imaginary value for the second frequency because ε^{-1} is always well-behaved on the imaginary axis. The frequency ω_p is usually the classical plasmon frequency which is calculated using the average value of the electronic density. However, as long as the model is close to the actual function, any value of ω_p is in principle correct as it just acts as a fitting parameter. Using a plasmon-pole model reduces the effort for the calculation of $\varepsilon^{-1}(\omega)$ as only two frequencies are required. Moreover the use of such model permits an analytic calculation of the integral in (3.88) which also increases computational speed.

3.5 Self-energy beyond *GW*: vertex corrections

Approximations that include more effects than *GW* are said to include *vertex corrections*. The vertex Γ is a three-point quantity defined in Hedin's framework. The exact expression for the irreducible vertex (3.78b), one of of Hedin equations, is repeated here for clarity:

$$\tilde{\Gamma}(1,2;3) = \delta(1,2)\delta(1,3) + \int d4567 \frac{\delta\Sigma(1,2)}{\delta G(4,5)} G(4,6)G(7,5)\tilde{\Gamma}(6,7;3). \tag{3.90}$$

The vertex enters both in the screening (3.78d) and in the self-energy (3.78e). To obtain the *GW* approximation the vertex function is taken as $\delta(4,2)\delta(4,3)$. This is equivalent to taking $\Sigma^0 = 0$ at the beginning of a single cycle of Hedin's equations. In this case one says that vertex corrections are neglected. This may seem like a quite drastic approximation, but it has proven to behave very well in practical applications for the calculation of band gaps [54, 64]. The original reason for neglecting the vertex was very practical: the vertex function is a three-point quantity that has to be integrated with G and W to calculate the self-energy. This becomes easily quite demanding in a numerical computation. Approximating the vertex to a product of two delta functions simplifies the double integral (which is in fact a multi-dimensional integral over space, time and spin) in the exact self-energy (3.78e) to a simple product of G and W. The quest for effective and yet affordable vertex corrections is a path already walked in literature [28, 65–67] and discussed in early applications of the *GW* approximation on real materials [59, 68, 69], but the actual usefulness of such endeavor is still under debate and a systematic way of finding effective vertex

corrections with application to real systems is yet to be discovered. Possible vertex corrections derived from the connection between Green's function theory and TDDFT are discussed in References [57, 58].

3.5.1   A two-point vertex

Assuming to have an appropriate orthonormal basis, one would be tempted to write

$$\tilde{\Gamma}(1,2;3) = \sum_{ijkl} \phi_j(\mathbf{x}_1)\phi_l^*(\mathbf{x}_3)\Gamma_{iljk}(t_1 - t_3, t_2 - t_3)\phi_i(\mathbf{x}_3)\phi_k^*(\mathbf{x}_2)$$

$$= \sum_{ik} \Gamma_{ik}(\bar{1},\bar{2})\phi_i(\mathbf{x}_3)\phi_k^*(\mathbf{x}_2)$$

$$\simeq \sum_{k} \Gamma_k(\bar{1},\bar{2})\phi_k(\mathbf{x}_3)\phi_k^*(\mathbf{x}_2)$$

$$\simeq \Gamma(\bar{1},\bar{2})\sum_{k} \phi_k(\mathbf{x}_3)\phi_k^*(\mathbf{x}_2), \quad (3.91)$$

which exploits time homogeneity, making the vertex dependent on two time differences, i.e. effectively dependent on two time variables and three space variables. This somewhat shows that one can think of the vertex as if it was composed by a different two-point Γ_k for each state k in the system.[11] If now one assumes that this state dependence of $\Gamma_k(1,2)$ is weak — i.e. the vertex is about the same for all states in the system — it seems fair to extract it from the summation and approximate the three-point vertex to a simpler two-point one [66], formally

$$\tilde{\Gamma}(1,2;3) = \Gamma(1,2)\delta(\mathbf{x}_2 - \mathbf{x}_3). \quad (3.92)$$

Formally, once the vertex is approximated to a two-point object, the self-energy can be written as

$$\Sigma(1,2) = iG(1,2)W(3,1)\Gamma(2,3) = iG(1,2)\tilde{W}(1,2), \quad (3.93)$$

with $\tilde{W} = W\Gamma$. In practice, one then calculates $\tilde{W}$ and $\Sigma = G\tilde{W}$ in an equivalent way to W and $\Sigma = GW$, with the new $\tilde{W}$ that has to be specified. A good example of this kind of approach to vertex corrections can be derived from TDDFT.

3.5.2   Vertex corrections from TDDFT

A cheap way to derive vertex corrections for the self-energy is to use a connection to TDDFT via the inverse dielectric function $\varepsilon^{-1}(\mathbf{q}, \omega)$. This procedure was suggested by Hybertsen and Louie [59] and studied by Del Sole *et al.* [65] in the case of the ALDA approximation. One can think of GW as a single cycle of Hedin's equations started with $\Sigma^0 = 0$. It can be shown that, using a different *ansatz* for Σ^0, one can derive a modified self-energy whithout worsening

---

[11] As I show above, the exact vertex is actually more complicated than this: the basis transformation would imply additional off-diagonal jk elements to enter in the game. The matrix element Γ_{jk} is here approximated as $\Gamma_{jk} = \Gamma_k \delta_{jk}$.

the computational complexity with respect to *GW*. In [65] the authors start the calculation approximating Σ with the LDA exchange-correlation potential $V_{xc}^{LDA}(\mathbf{r})$. However, this procedure is valid for any local and static approximation of V_{xc}. The starting self-energy then becomes

$$\Sigma^0(1,2) = \delta(1,2)V_{xc}(1). \tag{3.94}$$

This starting point produces, in the first iteration of Hedin's equations, a self-energy of the form $\Sigma = iG\tilde{W}$, where $\tilde{W}$ is an effective dynamical screened Coulomb interaction of the form

$$\tilde{W} = \left[1 - (v + f_{xc})\chi^0\right]^{-1} v \tag{3.95}$$

where χ^0 is the independent-particle polarizability and $f_{xc} = \delta V_{xc}/\delta\rho$ [70]. The difference between W and $\tilde{W}$ is that the in the latter case the screening is described by the so-called test-electron dielectric function. $\tilde{W}$ also includes a TDDFT polarizability χ^{TDDFT} that goes beyond the RPA polarizability χ. To be more precise, one can define $\tilde{W}$ as the test-electron screening using the time-ordered test-electron inverse dielectric function ε_{TE}^{-1} and re-write (3.95) as

$$W^{TE} = \varepsilon_{TE}^{-1}v = \left\{1 + (v + f_{xc})\left[1 - \chi^0(v + f_{xc})\right]^{-1}\chi^0\right\}v \tag{3.96}$$

While the RPA inverse dielectric function used in *GW* describes the classical screening between two classical charges, in this case ε_{TE}^{-1} describes the effect of an additional charge on the potential felt by an electron. The essential difference is that in W, the induced charge generates only a Coulomb potential, while in W^{TE} the induced charge also generates an exchange-correlation potential. To be precise, this type of screening is due to a *test-charge–test-electron* (TE) dielectric function. Using this expression for $\tilde{W}$, the polarizability χ, recognisable in the right-hand side of (3.96), is modified in that it includes Kohn-Sham electron-hole interaction through the TDDFT kernel f_{xc}:

$$\chi^{TDDFT} = \chi^0 + \chi^0(v + f_{xc})\chi^{TDDFT}. \tag{3.97}$$

This goes beyond the RPA polarizability that is used in *GW*. Quantum mechanical effects are in this way included in the screening and in the self-energy. The true W defined in Hedin's equations is of the *test-charge–test-particle* (TP) type, i.e. it describes the screening of a cloud of classical charges felt by a classical particle. One can choose to opt for such kind of screening while retaining the improved polarizability and define

$$W^{TP} = \varepsilon_{TP}^{-1}v = \left(1 + v\chi^{TDDFT}\right)v \tag{3.98}$$

where ε_{TP}^{-1} is the time-ordered inverse dielectric function already defined in Hedin's equations. Within this framework one is able to control vertex corrections in the screening and in the self-energy in a well-defined way. Both GW^{TP} and GW^{TE} go back to RPA putting $f_{xc} = 0$. The vertex in the screening is also

called *internal* while the vertex in the self-energy is called *external*. The approach has the advantage to go beyond the *GW* approximation while retaining the same computational cost. [12]

3.6   The Kadanoff-Baym equation

Instead of defining a self-energy, one can use Schwinger's technique to write a differential equation for the one-particle Green's function that depends only on the external perturbation. In this case G_0 is defined as the inverse of the non-interacting hamiltonian, i.e. including only the external static potential, and the Hartree potential is explicitly treated. Using (3.64) and this definition of G_0, it is possible to write a generalized form of the equation, connecting G and G_0:

$$
G(1,2)[\varphi] = G_0(1,2) + \int d3\, G_0(1,3) V_H(3)[\varphi] G(3,2)[\varphi]
$$
$$
+ \int d3\, G_0(1,3)\varphi(3) G(3,2)[\varphi] \tag{3.99}
$$
$$
+ \int d34\, G_0(1,3) v(3^+,4) \frac{\delta G(3,2)[\varphi]}{\delta \varphi(4)},
$$

where the Hartree potential is $V_H(1) = -i \int d2\, v(1,2) G(2,2^+)$. This equation was first derived by Baym and Kadanoff [71, 72]. It is a set of coupled non-linear functional differential equations. The non-linearity comes from the Hartree term, that contains itself a Green's function. Using the self-energy as a first-order perturbation with respect to a suitable starting point one can obtain a solution for G. The interest of using a self-energy instead of this is to avoid the complexity of such equation, which is exact but virtually unsolvable.

3.6.1   Linearized equation of motion for G

Recently G. Lani *et al.* [73, 74] have studied the Kadanoff-Baym equation and tried to solve it directly without the use of a self-energy. One of the paths they explored to find a solution involves the linearization of the Hartree potential. The Hartree potential depends on the external perturbation through the density. Assuming that the perturbation φ is small, one can Taylor-expand the density around $\varphi = 0$ and write

$$
V_H(1)[\varphi] = - i \int d2\, v(1,2) G(2,2^+)[\varphi]\big|_{\varphi=0} +
$$
$$
- i \int d23\, v(1,2) \frac{\delta G(2,2^+)[\varphi]}{\delta \varphi(3)}\bigg|_{\varphi=0} \varphi(3) + o(\varphi^2). \tag{3.100}
$$

One can then truncate at first order and define a G_H^0 so that

$$
G_H^0(1,2) = G_0(1,2) + \int d2\, G_0(1,3) V_H^0(3) G_H^0(3,2) \tag{3.101}
$$

---

[12]This statement holds provided that the computational effort required to calculate f_{xc} (which depends on the chosen approximation) is negligible with respect to the one required by χ. This does not hold for any TDDFT exchange-correlation kernel.

where $V_H^0(3) = -i \int d2\, v(3,2) G(2,2^+)[\varphi]\big|_{\varphi=0}$ is the ground-state Hartree potential. Here the time-ordered inverse dielectric function is

$$\varepsilon^{-1}(1,2) = \delta(1,2) - i \int d2\, v(1,2) \frac{\delta G(2,2^+)[\varphi]}{\delta \varphi(3)}\bigg|_{\varphi=0}. \qquad (3.102)$$

At this point one introduces a *screened* perturbing potential $\bar{\varphi}$:

$$\bar{\varphi}(1) = \int d2\, \varepsilon^{-1}(1,2)\varphi(2). \qquad (3.103)$$

One is then able to rewrite (3.99) as

$$G(1,2)[\varphi] = G_H^0(1,2) + \int d3\, G_H^0(1,3)\bar{\varphi}(3) G(3,2)[\bar{\varphi}]$$
$$+ \int d34\, G_H^0(1,3) W(3^+,4) \frac{\delta G(3,2)[\bar{\varphi}]}{\delta\bar{\varphi}(4)}, \qquad (3.104)$$

where W is the screened Coulomb interaction at $\varphi = 0$. One has that $W = \varepsilon^{-1} v$ with ε^{-1} as defined above. Hedin's *GW* approximation (See following sections) can be retrieved in a straightforward way with the substitution

$$\frac{\delta G(3,2)[\bar{\varphi}]}{\delta\bar{\varphi}(4)} = G(3,2)G(2,4). \qquad (3.105)$$

3.7 The quasi-boson model

D.C. Langreth [75], taking up the work of Nozières and De Dominicis [76], studied a model Hamiltonian where deep core electrons were coupled to boson excitations. This Hamiltonian was earlier used by B.I. Lundqvist to study the *GW* approximation [77] and it reads

$$H = \epsilon_c c^\dagger c + c c^\dagger \sum_q g_q (a_q + a_q^\dagger) + \sum_q \omega_q a_q^\dagger a_q \qquad (3.106)$$

where $c^\dagger$ is the second-quantization creation operator and c is the annihilation operator for a core electron of energy ϵ_c and $a^\dagger$ and a are the creation and annihilation operators for a plasmon of energy ω_q. g_q is the coupling constant. Plasmon dispersion can be included using a model dispersion for ω_q. Langreth, generalizing the result by Nozières and De Dominicis, gave the exact solution of the electron-boson Hamiltonian. The resulting spectral function of the model has an exponential form and yields a spectrum containing a quasi-particle peak and a series of satellites, all represented by differently normalized delta peaks (See Figure 3.3), decaying as a Poissonian distribution. This model has proved its validity for the photoemission spectrum of core electrons. This result is also a major improvement with respect to *GW* (See Figure 3.3), where the incoherent part of the spectrum is just one broad peak centered around $\epsilon - 2\omega_p$. This structure has been accounted for as an average of the exact solution, consequence of the approximate self-energy and was initially called a
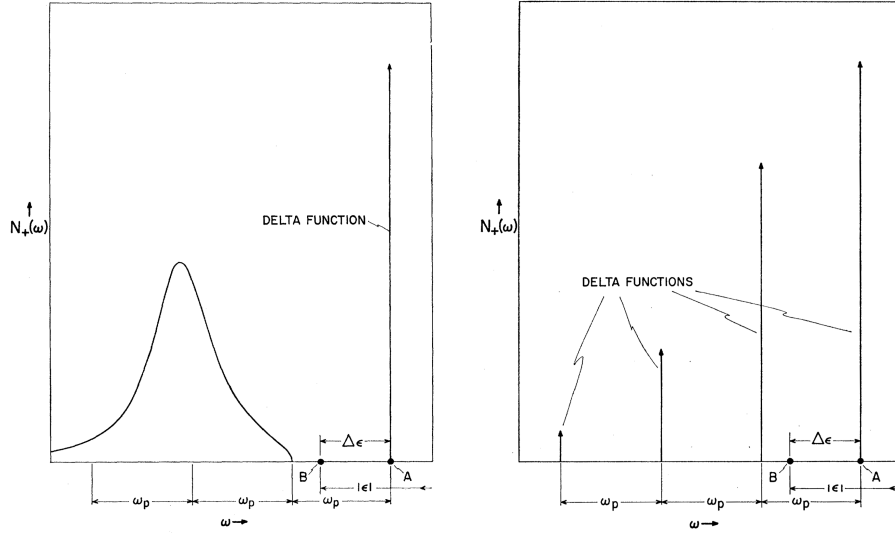
Figure 3.3: (Left panel) GW core-hole spectral function (here labeled with $N^+(\omega)$) vs (Right panel) exact solution, both obtained using (3.106). Here ω_p is the plasmon frequency and $\Delta\epsilon$ the quasiparticle shift from the non-interacting energy in B to the quasiparticle energy in A. Plasmon dispersion is neglected in the right panel. From [75].

plasmaron [77, 78].[13] The correct description of core-level satellites by this polaronic Hamiltonian was later acknowledged and summarized by several authors [22, 24, 79]. Hedin has proposed to use the same expression for G also in the valence-electron case and proved it adequate in certain regimes [80]. Eventually, summarizing all the previous work, he showed that one could employ a more general Hamiltonian, applicable both to core and valence electrons [25]:

$$H = \sum_k \epsilon_k c_k^\dagger c_k + \sum_s \omega_s a_s^\dagger a_s + \sum_{skk'} V_{kk'}^s (a_s + a_s^\dagger) c_k c_{k'}^\dagger. \tag{3.107}$$

This generalized version of the original electron-boson Hamiltonian is also known under the name of *quasi-boson* model. Here the fermions are allowed to have a momentum dispersion (k,k') and the energy of the boson is ω_s. The coupling constants are the so-called *fluctuation potentials* that contain the effects of polarization. If recoil (i.e. k dispersion) is neglected, the model is reduced to Langreth's. The exact core-hole Green's function reads then

$$G_c(\omega) = -i \int_{-\infty}^0 \mathrm{d}t\, e^{i(\omega - \epsilon_c - \Delta E)t} \exp\left\{ \sum_q \frac{g_q^2}{\omega_q^2} e^{i\omega_q t} - 1 \right\} \tag{3.108}$$

---

[13]More on that in Chapter 6.

Defining $Z = \exp\{-\sum_q g_q^2/\omega_q^2\}$ and $E_c = \epsilon_c + \Delta E$ one can proceed Taylor expanding (3.108) and obtaining

$$G_c(\omega) = Z\left\{\frac{1}{\omega - E_c} + \sum_q \frac{g_q^2}{\omega_q^2}\frac{1}{\omega - E_c + \omega_q} \sum_q \frac{g_q^4}{\omega_q^4}\frac{1}{\omega - E_c + 2\omega_q} + \cdots\right\}.$$
(3.109)

This Green's function yields in the spectral function an infinite sum of delta functions. The first peak is at the quasiparticle energy E_c and it is followed by a Poisson-decaying series of satellite terms, which are centered at multiples of ω_q, as one can see in Figure 3.3.

The solution of the quasi-boson model is not the only way to obtain the exponential expression for G. Notably, this expression for G has become commonly known as the *cumulant expansion*, after several authors had derived it inspired by an idea originally used in statistics [50, 81]. Another alternative derivation was proposed by Almbladh and Hedin [24] who manipulated the Dyson equation for G to obtain the same result.

The cumulant expansion

The cumulant formalism is part of the domain of statistics and it is an equivalent alternative to the moments formulation. This formalism can be expressed in the form of a cumulant-generating function that can be expanded as an infinite summation, where the cumulants are the coefficients of the terms of this summation [82]. Drawing a parallel with statistics, some authors found an alternative derivation for the exponential expression of the one-particle G [50, 81]. Starting from an ansatz for G of the form

$$G_k(t) = i\theta(-t)e^{-i\epsilon_k t + C(k,t)},$$
(3.110)

with $G_k^0(t) = i\theta(-t)e^{-i\epsilon_k t}$, the authors take the value for the cumulant $C(k,t)$ from the first order of the expansion of G in Σ, the self-energy being expanded to first order in W (i.e. using a G_0W_0 self-energy). The expansion of the exponential in G yields then an infinite series of diagrams in powers of W. It is done in the following way: one can Taylor expand the exponential in terms of C as $G = G^0(1 + C + 1/2C^2 + \ldots)$; then one expands the Dyson equation, $G = G^0 + G^0\Sigma G^0 + G^0\Sigma G^0\Sigma G^0 + \ldots$. To first order in the correction to G^0, comparison suggests $C = \Sigma G^0$. The resulting expression for G is equivalent to the solution of the polaron model, containing the same exact diagrams. At the same time, it takes advantage of the *GW* quasiparticle energies and does not require any external parameter. While it can be considered a convenient derivation with built-in *GW* corrections, this approach to the exponential expression of G is not as intuitive as the polaron model and — even though it might be considered more *ab-initio* — lacks physical motivation. I will show in Chapter 5 how one can derive an equivalent expression for the Green's function using an approximate equation of motion and retaining physical insight.

3.8   Theory of the Photoemission Process

In this chapter I have put much attention on the one-particle Green's function and its spectral function $A(\omega)$ as the fundamental ingredients to obtain the photoemission spectrum of solid-state systems. However, the spectral function alone is not, in general, immediately comparable with experimental spectra, as I already discussed in Chapter 2. The photoemission intensity $J(\omega)$ that is measured in experiment is connected to $A(\omega)$, but a number of additional effects — that can modulate what is contained in the spectral function — have to be taken into account to perform a correct comparison of theory and experiment. I will give here a concise review with the fundamental points. For a more complete overview of the theory of photoelectron spectroscopy, please refer to [6, 24, 25]. Here the removal of an electron is considered — i.e. the case of direct photoemission — but the treatment is equivalent for inverse photoemission. To develop a formal description of the photoemission process, one has to calculate the transition probability w_{fi} for an optical excitation between the N-electron ground state $\|N\rangle$ and one of the possible final states $|N, f\rangle$, where the photoelectron has left the system, but it is still considered as part of the many-body system. This can be written using Fermi's golden rule:

$$w = 2\pi \big|\langle N, f|H_{\text{int}}|N\rangle\big|^2 \delta(E_f^N - E^N - 2\pi\nu) \qquad (3.111)$$

where $E^N = E^{N-1} - E_B^{\mathbf{k}}$ and $E_f^N = E_f^{N-1} + E_{kin}$ are the initial- and final-state energies of the N-particle system ($E_B^{\mathbf{k}}$ is the binding energy of the photoelectron with kinetic energy E_{kin} and momentum $\mathbf{k}$). The interaction with the photon is treated as a classical perturbation given by

$$H_{\text{int}} = -\frac{1}{2}(\mathbf{A} \cdot \mathbf{p} + \mathbf{p} \cdot \mathbf{A}) \simeq -\mathbf{A} \cdot \mathbf{p}, \qquad (3.112)$$

where $\mathbf{p}$ is the electronic momentum operator and $\mathbf{A}$ is the electromagnetic vector potential. Within the sudden approximation, one can think that the electron travels outside the system to the detector without any interaction with the system. In this case one can write the many-body wavefunction as an antisymmetrized product of a single-particle wavefunction and an $N - 1$-particle many-body wavefunction. For the initial state one has to use single-particle creation operators to include the fact that the electron does not leave the rest of the system in an eigenstate of the $N - 1$-particle Hamiltonian. Taken the above into account, the transition probability $w^{\mathbf{k}}(\mathbf{A})$ for a final state where the photoelectron has a momentum $\mathbf{k}$ is then

$$w^{\mathbf{k}}(\mathbf{A}) = 2\pi |M_i^{\mathbf{k}}(\mathbf{A})|^2 \sum_m |c_{m,i}|^2 \delta(E_{kin} + E_m^{N-1} - E^N - 2\pi\nu) \qquad (3.113)$$

where $M_i^{\mathbf{k}} = \langle \phi_f^{\mathbf{k}}|H_{\text{int}}|\phi_i^{\mathbf{k}}\rangle$ is the one-electron dipole matrix element. It contains cross-section effects and selection rules defining the parity of the final state. $\phi_f^{\mathbf{k}}$ and $\phi_i^{\mathbf{k}}$ are single-particle wavefunctions for the initial and the final state. The coefficients $|c_{m,i}|^2$ are the probability that the removal of an electron from state i will leave the $N - 1$-particle system in the excited eigenstate m [6]. In the case

where the $N-1$-particle system is exactly described by an eigenstate, there will be only one c left and it will be equal to unity. The peaks in the spectral function — provided that $M_i \neq 0$ — will be then delta functions centered at the Hartree-Fock energies of the system. In general these states are not eigenstates and produce many delta peaks in the spectrum that will cause (i) broadening of the main peak and (ii) arising of satellite peaks according to the number of m excited states.

In this same formula one can retrieve the one-particle excitation energies $\epsilon_m = E^N - E_m^{N-1}$ defined earlier with the Lehmann representation for the one-particle Green's function. After a substitution using $\omega = E_{kin} - 2\pi\nu$, one can rewrite the photoemission intensity using the spectral function as

$$J_{\mathbf{k}}(\omega, \mathbf{A}) \propto \sum_j |M_j^{\mathbf{k}}(\mathbf{A})|^2 A(\omega - \epsilon_j) \qquad (3.114)$$

where the dependence on light polarization and cross sections is contained in the coefficients M_j. These coefficients have an important role when it comes to comparison between theory and experiment as the can make the signal disappear under certain conditions, even though the spectral function is not 0. One can use the commutator relations of the momentum and position opera-

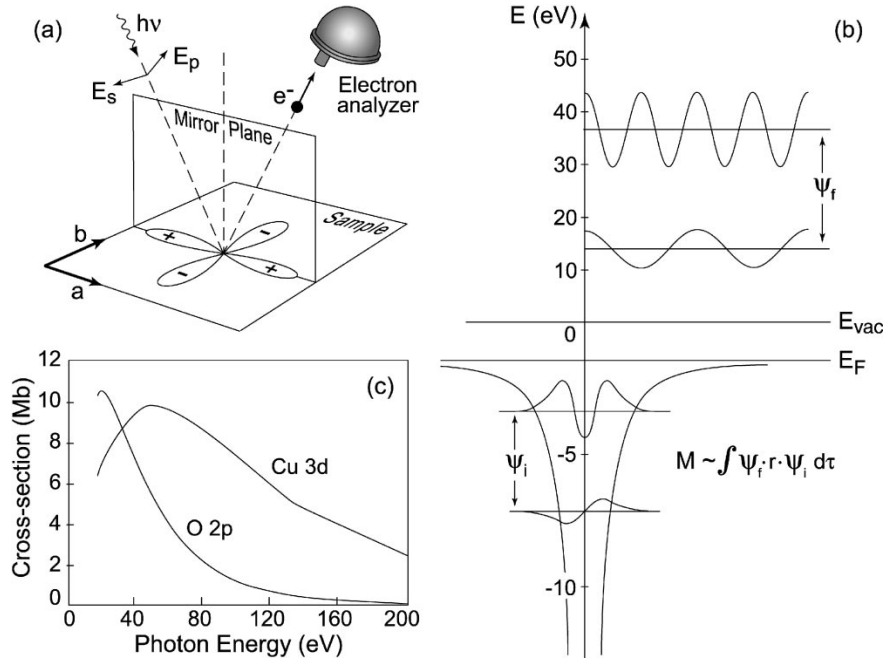Figure 3.4: (a) Sketch of a photoemission experiment. The figure shows how polarization and wavefunction parity are connected with the experimental setup. In this example a d-type orbital of even parity is sketched. (b) Schematic example of an optical transition between atomic orbitals with different momenta. (c) Example of photo-ionization cross sections for Cu $3d$ and O $2p$ atomic orbitals [83]. Image taken from [6].

tors to show that $|M_j^{\mathbf{k}}|^2 \propto |\langle \phi_f^{\mathbf{k}} | \hat{\varepsilon} \cdot \mathbf{x} | \phi_i^{\mathbf{k}} \rangle|^2$, where $\hat{\varepsilon}$ is a versor in the direction of the vector potential $\mathbf{A}$. This formula sets a selection rule for the symmetry of the states that can be detected. If the integrand is an odd function with respect to parity, the integral will be zero and no signal will be detected. Thus the integrand must have an even parity in order to detect a photocurrent. The symmetry of the integrand is the result of the combination of three terms: the final state, the polarization vector and the initial state. Given that the final state is fixed by the geometry of the experimental setup (See Figure 3.4), the remaining term $\hat{\varepsilon} \cdot \mathbf{x} | \phi_i^{\mathbf{k}} \rangle$ has to have the same parity in order to obtain a total even parity. In a practical example one usually has a vertical (i.e. parallel to the normal to the surface) plane that contains both the incoming photon beam and the outgoing photoelectrons and the detector (See Figure 3.4). In this case the final state has to have the parity of the experiment, which is even with respect to the mirror vertical plane. This means that the total symmetry of the other two terms must be even as well. Now it gets interesting because if one is able to change the direction of the polarization vector — hence its parity — this selects automatically the parity of the initial state with respect to the mirror plane. One calls P polarization the one with even parity and S polarization the one with odd parity. The coefficient $M_j^{\mathbf{k}}$ contains also the photoabsorption cross sections (See Figure 3.4) that determine a dependence of the spectrum on the photon energy in a not trivial way. In fact this dependence is strictly related to the symmetry of the initial state and to the atomic species. Tables of calculated values have been published for most of the atomic species [83, 84]. It becomes now clear that there are effects (e.g. parity effects) that are not removable from the experiment and that have to be accounted for when comparing with theory. I will show in Chapter 6 and 7 how the inclusion of some of these effects can improve the quality of the spectra and allow one to make a better comparison with experiment, understanding what is actually the contribution from the spectral function and what is due to secondary effects such as those described in this section.

4 | Exploring vertex corrections from TDDFT

The point of this chapter is to show how it is possible to use time-dependent density-functional theory to derive approximations for vertex corrections. Therefore, the aim here is to go beyond the *GW* approximation to calculate an improved the self-energy, for QP energies and for the spectral function through the Dyson equation. These approximations are limited in that the vertex functions that can be derived within this framework are two-point quantities. In the general case, the vertex function as defined in Hedin's equations is a three-point object. On the other hand, the fact that with this procedure the vertex is contracted to a two-point object is obviously a computational advantage as it is an easier quantity to deal with. In fact in many cases these vertex corrections do not add any substantial computational weight to the calculation of the self-energy with respect to *GW*. A way to connect TDDFT kernels and three point vertex corrections was proposed e.g. by A. Marini and R. Del Sole [66], but that in general implies a larger computational effort.

The dependence on the momentum q of the kernel in TDDFT has been shown to be important. Notably, a kernel for $q = 0$ was derived from Green's function theory and proved to be successful for the absorption spectra of semiconductors [85, 86]. There are systems (e.g. NiO) that display interesting features in spectra at finite q. I will show how exact conditions in the homogeneous electron gas can be used to derive a q-dependent approximation for the exchange-correlation kernel and, subsequently, vertex corrections. I will explore finite-q approximations and show how they compare to other approximations such as the ALDA.

4.1 Exact relations for the TDDFT kernel in the electron gas

The simplest of the approximations for DFT comes from the homogeneous electron gas (HEG) with a very simple constrain: the local density. This is the LDA and it has shown to perform well for a large class of materials. The TDDFT equivalent, the ALDA, does not seem to perform as well as its "little brother". There is quite a number of exact asymptotic conditions for the TDDFT kernel in the HEG. One would like to see if using some of them it is pos-

sible to derive useful approximations, following the example of the LDA. In the homogeneous electron gas some exact relations for the exchange-correlation kernel f_{xc} must hold. In particular one has the following relations [87]:

1. the compressibility sum rule,

$$\lim_{q \to 0} f_{xc}(q, \omega = 0) = \frac{d^2 \rho \epsilon_{xc}(\rho)}{d\rho^2} \qquad (4.1)$$

   where $\epsilon_{xc}(\rho)$ denotes the exchange-correlation energy per particle at a given density ρ;

2. the third frequency moment sum rule:

$$\lim_{q \to 0} f_{xc}(q, \omega = \infty) = -\frac{4}{5} \rho^{2/3} \frac{d\epsilon_{xc}(\rho)/\rho^{2/3}}{d\rho} + 6\rho^{1/3} \frac{d\epsilon_{xc}(\rho)/\rho^{1/3}}{d\rho}; \quad (4.2)$$

3. the static short-wavelength ($q \to \infty$) behaviour:[1]

$$\lim_{q \to \infty} f_{xc}(q, \omega = 0) \propto c - (b/q^2) \left[1 - g(0)\right] \qquad (4.3)$$

   and frequency-dependent short-wavelength ($q \to \infty$) behavior:

$$\lim_{q \to \infty} f_{xc}(q, \omega \neq 0) = -\frac{8\pi}{3} \frac{1}{q^2} \left[1 - g(0)\right], \qquad (4.4)$$

   where g(0) is the pair-correlation function evaluated at zero distance;[2]

4. the following relations are satisfied in the high-frequency limit by the real and imaginary parts of f_{xc} for $q < \infty$:

$$\lim_{\omega \to \infty} \mathrm{Re} f_{xc}(q, \omega) = f_{xc}(0, \infty) + \frac{c}{\omega^{3/2}} \qquad (4.5)$$

$$\lim_{\omega \to \infty} \mathrm{Im} f_{xc}(q, \omega) = -\frac{c}{\omega^{3/2}} \qquad (4.6)$$

   with $c = 23\pi/15$ in the high-density limit evaluation of the irreducible polarizaton propagator $\tilde{\chi}$.

4.1.1   Static response and local field factor of the electron gas

Moroni *et al.* proposed a method to compute f_{xc} at zero temperature for the electron gas from the static density-density linear response function using Monte Carlo (MC) methods [88]. In their paper, f_{xc} is written as

$$f_{xc}(q) = -v(q)G(q), \qquad (4.7)$$

---

[1] The correct values of the constants b and c can be found in Moroni *et al.* [88]. In fact the values originally used by Gross and Kohn are not correct [89].

[2] The term $[1 - g(0)]$ can be taken equal to 1 for $r_s > 1$, which is a representative range for most semiconductors [90].

where $v(q) = 4\pi/q^2$ is the Coulomb interaction and $G(q)$ is the *local field factor*. They focus on the calculation of G. As $q \to 0$, to dominant order,

$$G(q) = A(q/k_F)^2 \tag{4.8}$$

with

$$A(r_s) = \frac{1}{4} + \frac{-d\mu_c/dn_0}{4\pi e^2/q_F^2} \tag{4.9}$$

where $k_F = (3\pi^2\rho)^{1/3}$ is the Fermi wave vector and μ_c the correlation contribution to the chemical potential in the HEG. The density ρ with respect to the Wigner-Seitz radius r_s in the HEG is $\rho = 1/(4\pi r_s^3 a_B^3/3)$, where a_B is Bohr's radius. Following Moroni *et al.*, for $q \to \infty$,

$$G(q) = C(q/k_F)^2 + B \tag{4.10}$$

This expression is equivalent to eq. (4.3) for f_{xc}. C is related to the fractional change of kinetic energy, δ_2: $C(r_s) = (\pi/2e^2k_F)[-d(r_s\varepsilon_c)/dr_s]$ with ε_c the correlation energy per particle. $B(r_s)$ is calculated fitting DMC (diffusion Monte Carlo) calculation for different values of r_s, thanks also to the known result $B(0) = 1/3$. The extended behaviour is then fitted by the following polynomial expression:

$$B(r_s) = \frac{1 + a_1 x + a_2 x^3}{3 + b_1 x + b_2 x^3} \tag{4.11}$$

where $x = \sqrt{r_s}$ and $a_1 = 2.15$, $a_2 = 0.435$, $b_1 = 1.57$, $b_2 = 0.409$.

4.1.2 Analytic expression for the exchange-correlation kernel

Corradini *et al.* presented an expression of the local-field factor $G(q)$ based on the MC calculations by Moroni *et al.* [91]. This result is obtained fitting the MC results with an analytical expression. This expression is also Fourier-transformable, which is an advantage in numerical applications on real systems. The formula is based on Lorentzian and Gaussian functions and it reads

$$G(q) = CQ^2 + \frac{BQ^2}{g + Q^2} + \alpha Q^4 e^{-\beta Q^2} \tag{4.12}$$

where $Q = q/k_F$ and $g = B/(A - C)$ and A, B and C are the same as in (4.9) and (4.10). They report the best results are obtained by taking

$$\alpha = \frac{1.5}{r_s^{1/4}} \frac{A}{Bg}, \tag{4.13}$$

$$\beta = \frac{1.2}{Bg}. \tag{4.14}$$

They obtain the expression of the exchange-correlation kernel f_{xc} in real space with its Fourier transform

$$f_{xc}(q) = \int d^3 r e^{-iq \cdot r} f_{xc}(r) = -v(q)G(q) \tag{4.15}$$

that, applied to (4.12) yields

$$f_{xc}(r) = -\frac{4\pi e^2 C}{k_F^2}\delta^3(r) + \frac{\alpha k_F}{4\pi^2\beta}\left(\frac{\pi}{\beta}\right)^{3/2}\left[\frac{k_F^2 r^2}{2\beta} - 3\right]e^{-k_F^2 r^2/4\beta} - B\frac{e^{-\sqrt{g}k_F r}}{r}.$$
(4.16)

This expression for the exchange-correlation kernel has been tested against several others by Cazzaniga *et al.* yielding good performances with respect to say ALDA [92]. The kernels were compared evaluating the dynamic structure factor $S(\mathbf{q}, \omega)$, directly proportional to the imaginary part of the inverse dielectric function ε^{-1}, at finite values of the momentum $\mathbf{q}$.

4.2 Asymptotic behavior of some kernels

I will here discuss the asymptotic behavior of a few selected approximations for f_{xc} and compare it to the exact limits in the homogeneous electron gas. Notably, the ALDA shows a systematic breakdown for $q \to \infty$. I will discuss the effects of different approximations on the calculation of the dielectric function $\varepsilon(\omega)$ and its inverse $\varepsilon^{-1}(\omega)$ in both the Test-particle (TP) and Test-electron (TE) cases.

4.2.1 The ALDA kernel

The ALDA kernel shows to be pathologic at several levels. If one looks at the TE dielectric function this reads

$$\varepsilon^{\mathrm{TE}} = 1 - (v + f_{xc}^{\mathrm{ALDA}})\chi^0.$$
(4.17)

Here in the $v + f_{xc}$ term $v = 4\pi/q^2$, while $f_{xc} = c(\rho)$ where c is a constant determined by the local density, since in ALDA f_{xc} is not dependent on ω nor q. Notably, f_{xc} has opposite sign with respect to v. For $q \to 0$ the contribution of f_{xc}^{ALDA} becomes negligible. Instead the trend for $q \to \infty$ is quite different: v approaches 0; the ALDA kernel is constant and negative. Thus there is some value of q for which $v \simeq f_{xc}$. At this point the term $v + f_{xc}$ will change sign and produce a negative spectrum for $\mathrm{Im}(\varepsilon)$. This effect will affect also calculations of the polarizability χ including local fields, only in a less predictable way because of the matrix inversions involved. It is a completely unphysical effect. Figure 4.1 shows very clearly how the ALDA kernel produces this effect beyond a certain value of q and the $v + f_{xc}$ term becomes negative. This effect is an unphysical artifact due to the local approximation of the kernel.

The exact behaviour for f_{xc} in the homogeneous electron gas is given by eq. (4.4). This equation shows how the term $v + f_{xc}$ does not change sign in the case of huge momentum transfer. In fact in the exact case $v + f_{xc}$ behaves like $4/3\pi/q^2$ as q approaches infinity, as $f_{xc} \to -8/3\pi/q^2$ in that limit. Thus the kernel goes smoothly to 0. In the ALDA case as, $q \to \infty$, one has instead $v + f_{xc}^{ALDA} \to f_{xc}^{ALDA}$, which does not depend on q and thus produces the anomaly. This problem has been reported by several authors, e.g. [93, 94].
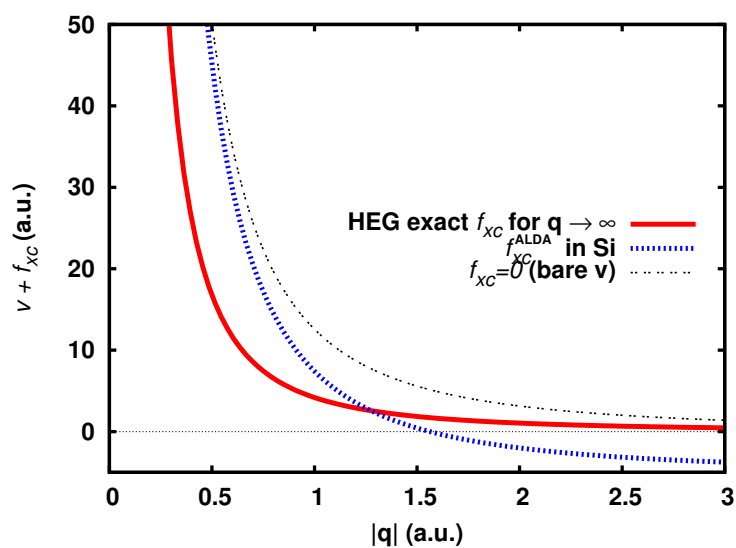
Figure 4.1: Trend of $v + f_{xc}$ for $q \to \infty$. The adiabatic local density approximation (ALDA) in bulk silicon and a kernel following the exact large-q behavior in the homogeneous electron gas (HEG) from (4.4) are compared. At $|q| \sim 1.5$ atomic units the pathologic ALDA kernel causes sign inversion in the $v + f_{xc}$ term, which leads to unphysical negative spectra.

4.2.2 The Corradini kernel

The Corradini kernel can be written as

$$f_{xc}^{Corr} = \frac{4\pi}{k_F^2} \left(C + \frac{B}{g + Q^2} + \alpha Q^2 e^{-\beta Q^2} \right) \tag{4.18}$$

and one can show that, as q approaches infinity, this kernel will go asymptotically as $f_{xc}^{Corr} \to (4\pi/k_F)C$, which does not depend on q. In fact the value of C is

$$C(r_s) = \frac{\pi}{2k_F} \left[-\frac{d(r_s\varepsilon_c)}{dr_s} \right] \tag{4.19}$$

with ε_c the correlation energy per particle in the electron gas. As already pointed out, there is no dependency on q. Hence, this kernel should suffer from the same pathology as the ALDA one. This kernel is derived from the static limit in the HEG and it is therefore static, as the ALDA kernel. The performance of the Corradini kernel has been tested by Cazzaniga *et al.* yielding good results at small non-zero momenta [92] for the calculation of the dynamic structure factor.

4.2.3 The Hubbard kernel

The Hubbard kernel was originally proposed by Hubbard as an approximation for the local field factor $G(q)$ to go beyond the RPA [95]. It can be considered the first attempt of vertex correction or kernel, even though at that time TDDFT was yet to be thought. The corresponding kernel reads

$$f_{xc}^H = -\frac{4\pi}{q^2 + k_F^2}. \tag{4.20}$$

Now, for $q \to 0$ this kernel approaches a constant, i.e. $f_{xc} \to -4\pi/k_F^2$. The asymptotic behavior for $q \to \infty$ instead, is $f_{xc}^H \to 0$. It is clear then that the Hubbard kernel is a well-behaved kernel, in the sense that it does not suffer from a pathology similar as the ALDA or the Corradini kernel. Nevertheless, it does not follow the exact theoretical limit for $q \to \infty$ in the electron gas. The Hubbard kernel was also tested for the calculation of the dynamic structure factor by Cazzaniga *et al.* [92]. It produced good results even though limited to small finite valuse of q.

Tunability of the Hubbard kernel

It is worth noting that $k_F = (3\pi^2\rho)^{1/3}$, where ρ is the average density of the system or the exact density in the homogeneous electron gas. Writing f_{xc} explicitly one has

$$f_{xc}^H = -\frac{4\pi}{q^2 + (3\pi^2\rho)^{2/3}}. \tag{4.21}$$

Interestingly, the Hubbard kernel can be tuned using k_F or ρ as a parameter. It is understood that in general one is considering a TE screening. To analyse the

effect of this tuning one has to observe the $v + f_{xc}$ term that one can write as (keeping k_F to have a more compact notation)

$$v + f_{xc}^H = \frac{4\pi}{q^4/k_F^2 + q^2} \tag{4.22}$$

Now, as a function of ρ, this term has the following asymptotic limits:

- as ρ reaches zero, $f_{xc} \to -v$, i.e. the kernel tends to compensate exactly the Coulomb term. It follows that

$$\varepsilon^{TE} = 1 + (v + f_{xc})\chi = \varepsilon^{-1} = 1. \tag{4.23}$$

  This means that if one were to use the tuned Hubbard kernel in this limit as a vertex correction to calculate the self-energy, the resulting Σ would be equal to the Fock operator. In other words, this limit eliminates the screening.

- For ρ going to infinity one can see that $f_{xc} \to 0$. As a consequence, the polarizability becomes

$$\chi = [1 - \chi^0 v]\chi^0 = \chi^{RPA} \tag{4.24}$$

  and the dielectric function can be written as

$$\varepsilon^{TE} = 1 + v\chi = \varepsilon^{RPA}, \tag{4.25}$$

  i.e. the RPA inverse dielectric function is recovered. This is the dielectric function that is used to calculate the self-energy within the *GW* approximation, which is a high-density approximation [96].

4.3 Results for the exact large-q kernel on Si

In this part I show the performance of a kernel built to match the exact f_{xc} in the HEG for the limit of large values of q, as reported in (4.4). I will refer to this kernel as "HEG-bigq" kernel. Following the exact condition in (4.4), such kernel reads

$$f_{xc} = -\frac{8}{3}\frac{\pi}{q^2} \approx -8.38\frac{1}{q^2} \tag{4.26}$$

The correct dependence on q will assure no anomalies for increasing q as in the case of the ALDA. It can be interesting to see its performance at small values of q. For this purpose it is useful to compare it with the long-range contribution (LRC) kernel [36, 85, 86, 97]. This kernel reads $f_{xc} = -\alpha/q^2$ and it is meant to describe excitonic effects in optical absorption as it was derived to describe the correct behavior of the exchange-correlation kernel at $q \to 0$. In fact typical values of α for semiconductors are of the order of 0.2. At this point, considering the difference of the coefficients in the two cases, one can expect the large-q kernel not to behave well for small values of q. Moreover, the LRC kernel have shown to need a prior calculation of quasiparticle energies to be effective [86].

4.3.1   Macroscopic dielectric function at finite q

In this part I show how the exact HEG-bigq kernel performs on bulk silicon for the calculation of the dielectric function ε_M. This approximation is compared with several others, in the test-particle and in the test-electron cases. Namely I compare it with the ALDA kernel, the Hubbard kernel and the RPA. The spectra are calculated over a range of 25 eV for increasing finite momenta with $q_x = q_y = q_z$. As expected, there are no negative spectra for the HEG-bigq kernel, while the ALDA exhibits its pathology at $q = (1.75, 1.75, 1.75)$ (See Figure 4.5). Also the Hubbard kernel behaves well at large q.

At $q = (0.25, 0.25, 0.25)$ and $q = (0.5, 0.5, 0.5)$ the TP-Hubbard kernel over-screens considerably with respect to RPA and to the rest of the lot. In Figure 4.2 and 4.3 one can see that $\varepsilon_1(\omega = 0)$ is larger than for the other approximations while ε_2 has a larger onset. TP-ALDA is the only slightly different case from the others, screening a little more than the rest.

At $q = (0.75, 0.75, 0.75)$ (See Figure 4.4) the TP-big-q kernel is the one to stand out as it over-screens considerably with respect to RPA and to the rest of the lot. The TP-Hubbard is weaker than th HEG kernel, but $\varepsilon_1(0)$ has the second greatest value and ε_2 has still a larger onset with respect to the other approximations, that give all a very similar result. Also, the TE dielectric function tend to under-screen with respect to RPA.

At $q = (1.75, 1.75, 1.75)$ the TP dielectric functions are quite on a par and slightly over-screen with respect to RPA. As one can see in Figure 4.5, TE-Hubbard and TE-big-q visibly under-screen with respect to RPA ant TP cases. TE-ALDA is at this point giving an unphysical result, produced by the sign inversion in the $v + f_{xc}$ term: while ε_1 gives values smaller than 1, ε_2 has negative values.

The largest calculated value for q is $q = (3.5, 3.5, 3.5)$ and the results are reported in Figure 4.6. For this comparatively large value of q one can see that there is almost no signal, as χ^0 is approaching 0. In fact $\varepsilon_1 = 1$ for almost all approximations and values of ω and ε_2 is very small. While the TP dielectric functions are substantially identical to RPA, one can spot some differencies for the TE cases: TE-Hubbard and TE-big-q visibly under-screen with respect to RPA ant TP cases; instead TE-ALDA is in complete breakdown and gives smaller-than-one values for ε_1 and all-negative values for ε_2, that in fact does not appear in the graph.

This analysis shows some trends of a set of exchange-correlation kernels, but a definite answer on which are an actual improvement with respect to e.g. ALDA can only come from the application of these approximations as vertex corrections to the self-energy.

Figure 4.2: Real (Eps1) and imaginary (Eps2) parts of the dielectric function $\varepsilon(q, \omega)$ at $q = (0.25, 0.25, 0.25)$ for a number of different approximations for f_{xc}. The dielectric function is shown for the test-particle and the test-electron case. The TP-Hubbard kernel stands out here as it over-screens considerably with respect to RPA and to the rest of the lot.
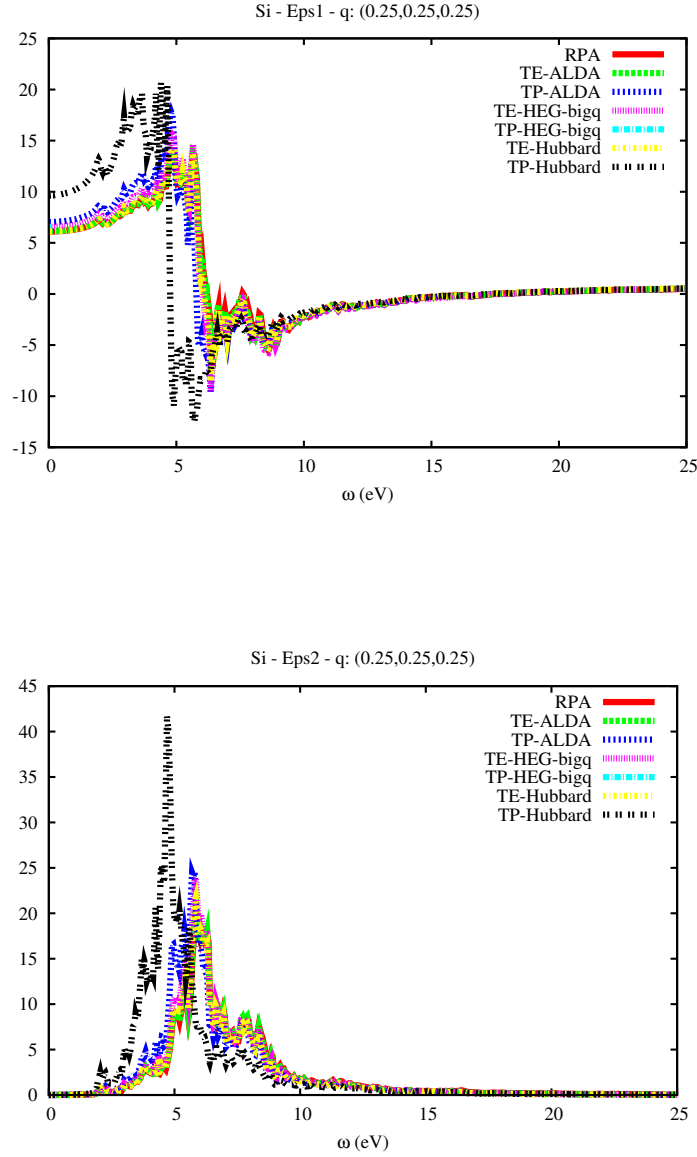
Figure 4.3: Real (Eps1) and imaginary (Eps2) parts of the dielectric function $\varepsilon(q,\omega)$ at $q = (0.5, 0.5, 0.5)$ for a number of different approximations for f_{xc}. The dielectric function is shown for the TP and the TE case. Again, the TP-Hubbard kernel stands out here as it over-screens considerably with respect to RPA and to the rest of the lot.

Si - Eps1 - q: (0.75,0.75,0.75)
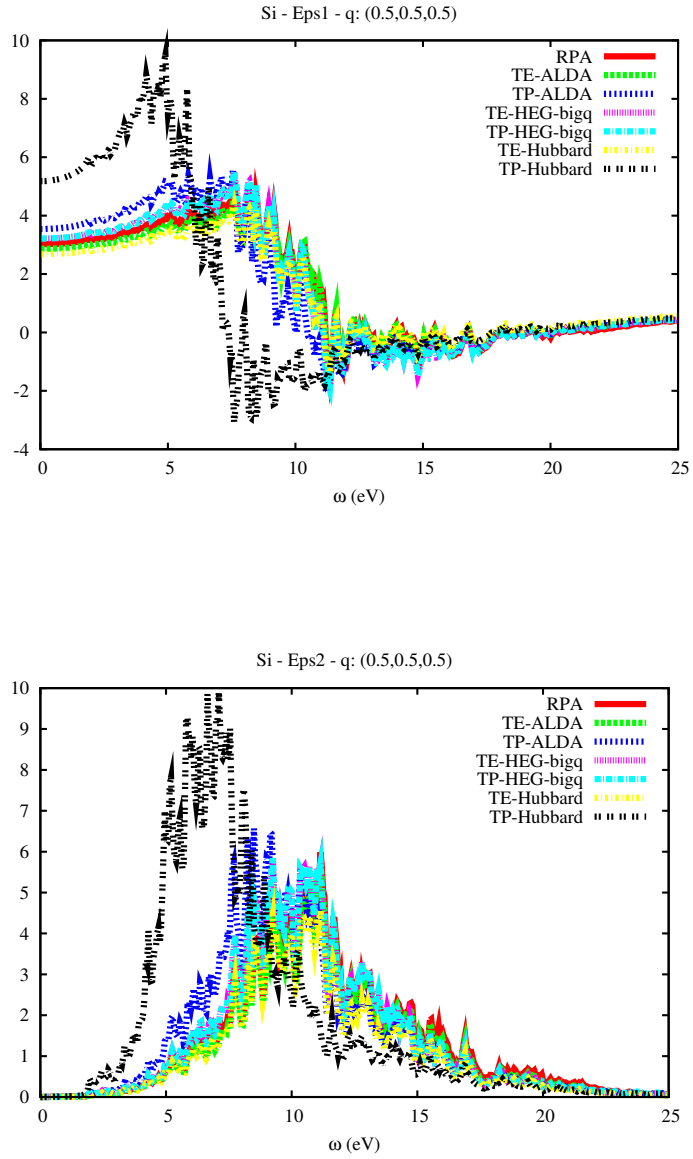

Si - Eps2 - q: (0.75,0.75,0.75)

Figure 4.4: Real (Eps1) and imaginary (Eps2) parts of the dielectric function $\varepsilon(q,\omega)$ at $q = (0.75, 0.75, 0.75)$ for a number of different approximations for f_{xc}. The dielectric function is shown for the TP and TE case. The TP-big-q kernel is the one to stand out here as it over-screens considerably with respect to RPA and to the rest of the lot. The TP-Hubbard is weaker than th HEG kernel, but $\varepsilon_1(0)$ has the second greatest value and ε_2 has still a larger onset with respect to the other approximations, that give all a very similar result. Visibly the TE dielectric function tend to under-screen with respect to RPA.
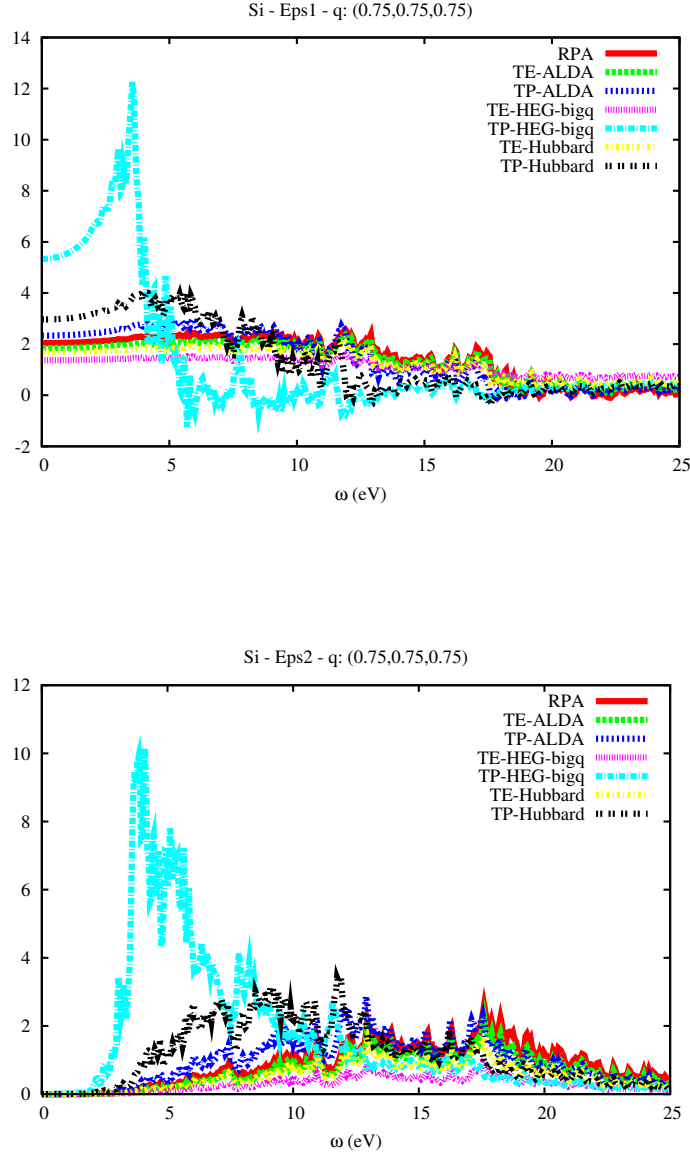
Figure 4.5: Real (Eps1) and imaginary (Eps2) parts of the TP and TE dielectric function $\varepsilon(q,\omega)$ at $q = (1.75, 1.75, 1.75)$ for a number of different approximations for f_{xc}. Here the TP dielectric functions are quite on a par and slightly over-screen with respect to RPA. TE-Hubbard and TE-big-q visibly under-screen with respect to RPA ant TP cases. TE-ALDA is at this point giving an unphysical result, produced by the sign inversion in the $v + f_{xc}$ term: while ε_1 gives values smaller than 1, ε_2 has negative values and almost disappears from the graph.
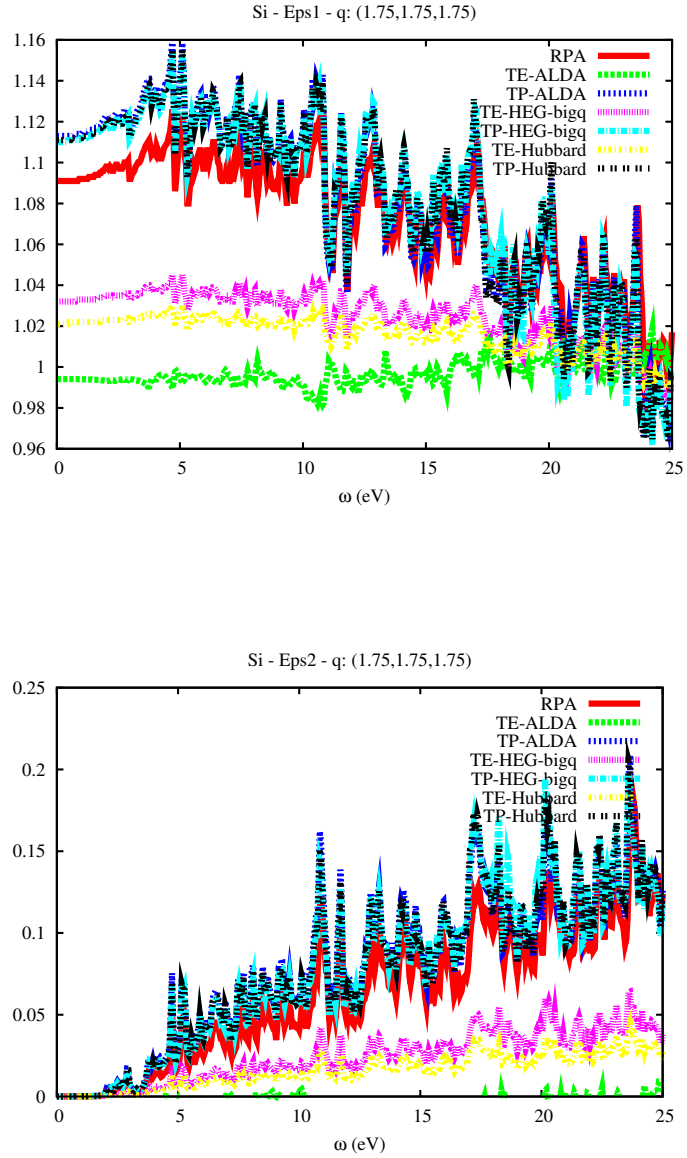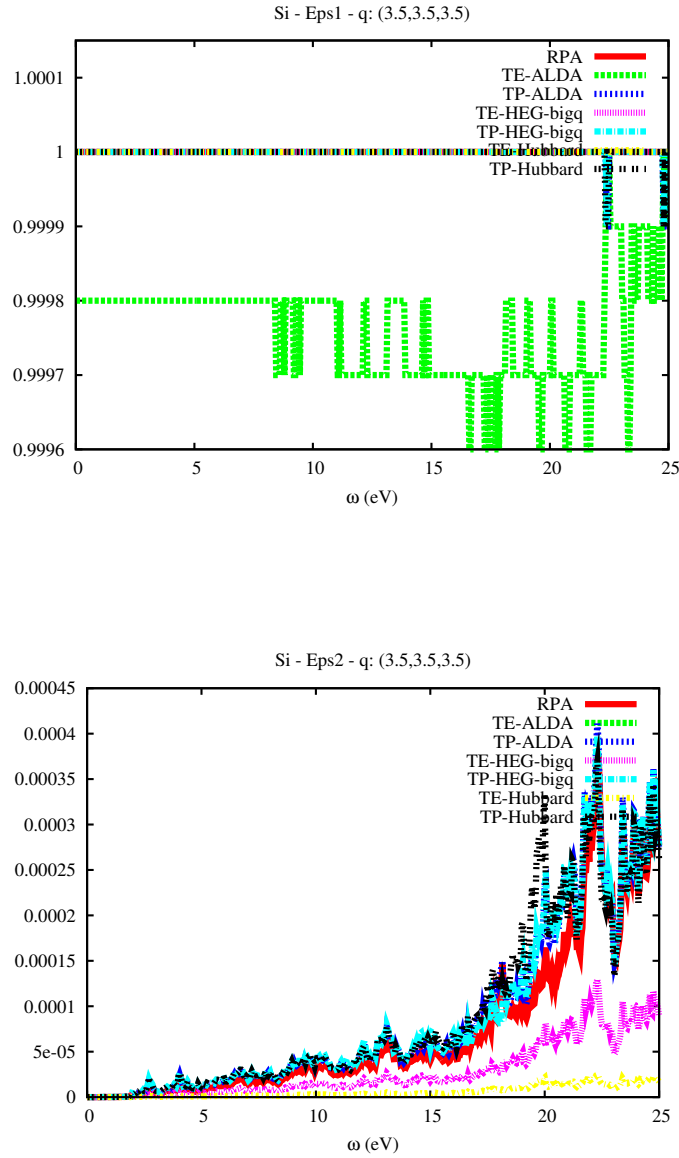
Figure 4.6: Real (Eps1) and imaginary (Eps2) parts of the TP ad TE dielectric function $\varepsilon(q, \omega)$ at $q = (3.5, 3.5, 3.5)$ for a number of different approximations for f_{xc}. For this high value of q one can see that χ^0 is approaching 0. In fact $\varepsilon_1 = 1$ for almost all approximations and values of ω and ε_2 is very small. While the TP dielectric functions are substantially identical to RPA, one can spot some differencies for the TE cases: TE-Hubbard and TE-big-q visibly under-screen with respect to RPA ant TP cases; instead TE-ALDA is in complete breakdown and gives smaller-than-one values for ε_1 and all-negative values for ε_2, that does not appear in the graph.

4.3.2 Inverse dielectric function at finite q

In this part I show how the exact large-q kernel performs on bulk silicon for the calculation of the imaginary part of the inverse dielectric function $\text{Im}\left[\varepsilon_M^{-1}\right]$. This approximation is compared with ALDA, in the test-particle and in the test-electron cases, and RPA. As expected, there are no negative spectra for the exact kernel, while the ALDA exibits its pathology above $q == (1.75, 1.75, 1.75)$. The spectra are calculated using

$$\text{EELS} = -\text{Im}\left[\varepsilon_M^{-1}\right] = \frac{1}{\pi}\frac{\varepsilon_2}{\varepsilon_1^2 + \varepsilon_2^2}. \tag{4.27}$$

The inverse dielectric function is a fundamental quantity in GW, as it enters in the screening $W = v\varepsilon^{-1}$.

At $q = (0.25, 0.25, 0.25)$ and $q = (0.5, 0.5, 0.5)$ the spectra do not differ substantially from RPA (See Figure 4.7 and 4.8). TE-big-q is the only slightly different case from the others, showing a slightly sharper peak at $q = (0.25, 0.25, 0.25)$. All the spectra have a slight offset to smaller energies with respect to RPA at $q = (0.5, 0.5, 0.5)$.

At $q = (0.75, 0.75, 0.75)$ the TP-big-q case shows a prominent onset with respect to RPA and ALDA while the TE-big-q one has quite low intensity with respect to RPA and ALDA (See Figure 4.9). One can show with a little algebra (See appendix A) that in the large-q limit one has

$$\varepsilon_{TE}^{-1} = \frac{1}{3}\varepsilon_{TP}^{-1}. \tag{4.28}$$

This relation is confirmed by the spectra calculated with the HEG-bigq kernel.

At $q = (1.75, 1.75, 1.75)$ (See Figure 4.10), both ALDA and big-q TP dielectric functions are quite similar to RPA, with a slightly higher intensity. TE-big-q visibly under-screens with respect to RPA. TE-ALDA gives at this point an unphysical result, producing a spectrum that almost disappears from the graph, as the plots of the dielectric function have already shown.

The largest calculated value of q is $q = (3.5, 3.5, 3.5)$ (See Figure 4.11). For this value of q the intensity is very low. TE-ALDA is in complete breakdown and gives negative values; it has therefore disappeared from the graph. While the TP dielectric functions are substantially identical to RPA, one can spot some differences for the TE cases: TE-big-q visibly under-screens with respect to RPA ant TP cases. This can be ascribed to the TE spectrum systematically being one third of the TP one and to the TP spectrum approaching the RPA result as $q \to \infty$.

In general, RPA is know to give a decent description of the inverse dielectric function. The results presented here for the dielectric function are not a *per se* indication of the good behavior of certain approximations in the perspective of vertex corrections. The way ε^{-1} enters in the self-energy is far from obvious and only analyzing how vertex corrections influence the quality of the self-energy one is allowed to draw conclusions.

Figure 4.7: Imaginary part of the inverse dielectric function for Si (EELS). $\varepsilon^{-1}(q,\omega)$ at $q = (0.25, 0.25, 0.25)$ for a number of different approximations for f_{xc}. The dielectric function is shown for the Test-Particle and the Test-Electron case. The spectra do not differ substantially from RPA. TE-big-q is the only slightly different case from the others, showing a slightly sharper peak.

Figure 4.8: Imaginary part of the inverse dielectric function for Si (EELS). $\varepsilon^{-1}(q,\omega)$ at $q = (0.5, 0.5, 0.5)$ for a number of different approximations for f_{xc}. The dielectric function is shown for the Test-Particle and the Test-Electron case. Here all the spectra have a slight offset to smaller energies with respect to RPA.
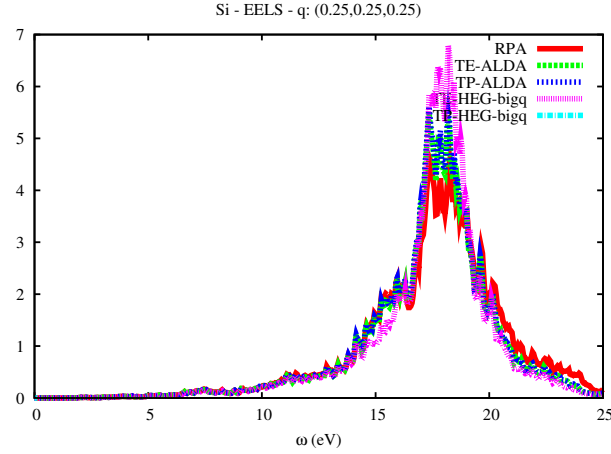
Figure 4.9: Imaginary part of the inverse dielectric function for Si (EELS). $\varepsilon^{-1}(q,\omega)$ at $q = (0.75, 0.75, 0.75)$ for a number of different approximations for f_{xc}. The dielectric function is shown for the Test-Particle and the Test-Electron case. The TP-big-q case shows a prominent onset with respect to RPA and ALDA while the TE-big-q one has quite low intensity with respect to RPA and ALDA.
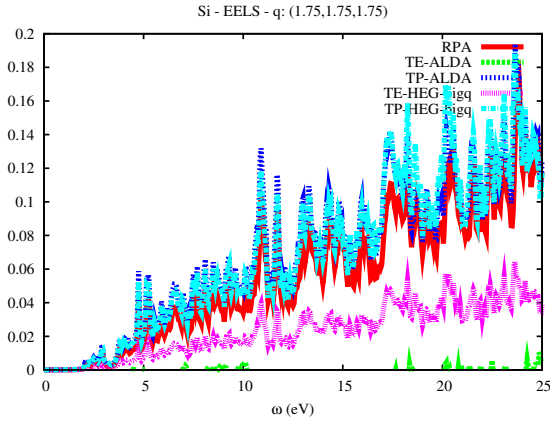
Figure 4.10: Imaginary part of the inverse dielectric function for Si (EELS). $\varepsilon^{-1}(q,\omega)$ at $q = (1.75, 1.75, 1.75)$ for a number of different approximations for f_{xc}. The dielectric function is shown for the Test-Particle and the Test-Electron case. Here both ALDA and big-q TP dielectric functions are quite similar to RPA, with a slightly higher intensity. TE-big-q visibly under-screens with respect to RPA. TE-ALDA gives at this point an unphysical result, producing a spectrum that almost disappears from the graph, as the plots of the dielectric function have already shown.
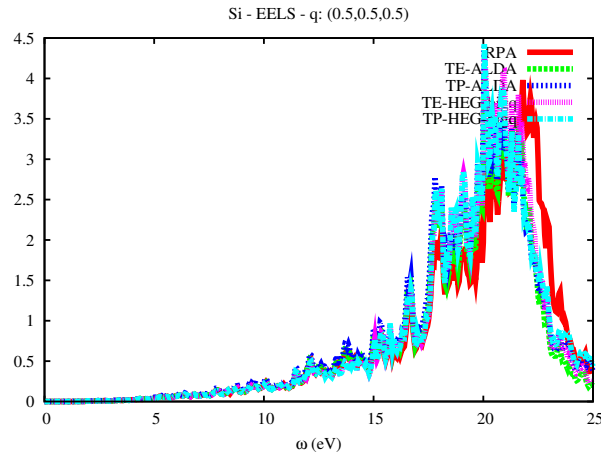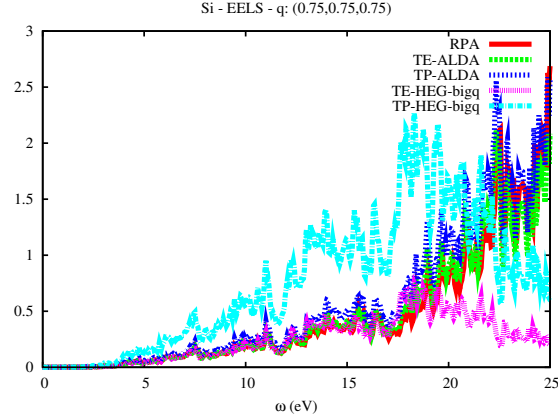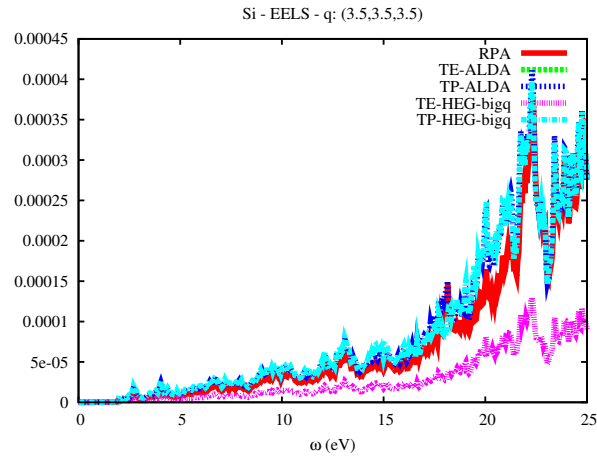
Figure 4.11: Imaginary part of the inverse dielectric function for Si (EELS). $\varepsilon^{-1}(q,\omega)$ at $q = (3.5, 3.5, 3.5)$ for a number of different approximations for f_{xc}. The dielectric function is shown for the Test-Particle and the Test-Electron case. For this high value of q the intensity is very low. TE-ALDA is in complete breakdown and gives negative values; it has therefore disappeared from the graph. While the TP dielectric functions are substantially identical to RPA, one can spot some differencies for the TE cases: TE-big-q visibly under-screens with respect to RPA ant TP cases.

4.4   Quasiparticle energies

In this part I apply vertex corrections derived from TDDFT using the approximations studied in the previous section. I will focus on the way vertex corrections affect band-gaps and quasiparticle energies with respect to the reference case of *GW*. Quasiparticle energies E_i are calculated using

$$E_i = \epsilon_i^{LDA} + Z\langle\phi_i|\Sigma(\epsilon_i^{LDA}) - V_{xc}|\phi_i\rangle \tag{4.29}$$

where Σ can contain an RPA W, a test-particle or a test-electron one, depending what kind of correction one is applying. The test-electron dielectric function is $\varepsilon^{TE} = 1 - (v + f_{xc})\chi^0$. Quasiparticle energies and energy-gap values are reported for the case of RPA W, test-particle W or test-electron W.

ALDA   Several authors have already calculated quasiparticle energies using vertex corrections from ALDA in silicon [59, 65]. While the two publications basically agree on the values of the band-gap, there is some discrepancy in the values of the quasiparticle energies. This issue has been recently discussed and clarified by *et al.* [98]: the type of plasmon-pole model used in [59] can give correct band-gaps, but there is a convergence problem on the quasiparticle energies in that the number of empty states needed to converge is extremely high. There are also issues with *d*-electrons systems [98]. On the other hand, the Godby-Needs plasmon-pole model [60] used by Del Sole *et al.* and also used for the presented calculations is not affected by such problems. In fact I retrieve in my calculations the values found by Del Sole *et al.* [65]. A full-integration (no plasmon pole) calculation of quasiparticle energies with vertex corrections can be found in [51]. For ALDA, the value of the band-gap is about the same in GW and GW^{TE} (See Figure 4.12). In the TP case there is a slight difference and the band-gap is smaller. On the other hand there is almost a rigid shift between GW and GW^{TE}.

Exact large-q kernel (in HEG)   The kernel derived from the exact condition in the HEG is here compared to GW (See Figure 4.13). While the trend of the TE calculation is similar to the TE-ALDA one, the value of the band-gap shift in GW^{TE} is larger by ~ 0.1 eV. The TP case is quite similar to the TE case and the gap becomes even larger. This is very different from the TP-ALDA corrections and it is related to the small-q behavior of the TDDFT kernel.

Hubbard kernel   The Hubbard kernel is here compared to GW (See Figure 4.14). The trend of the TE calculation is similar to the TE-ALDA one: the band-gap shift is slightly larger. The TP case is quite different from ALDA and from the HEG kernel, in that both valence and conduction have a negative quasiparticle correction. This is very different from the TP-ALDA corrections and it is related to the small-q behavior of the TDDFT kernel.

The results for the different approximations (ALDA, Hubbard and big-q) are summarized in Figure 4.15. The TE band-gap shifts are not very different from the GW reference, with the big-q kernel giving a larger final gap. The most
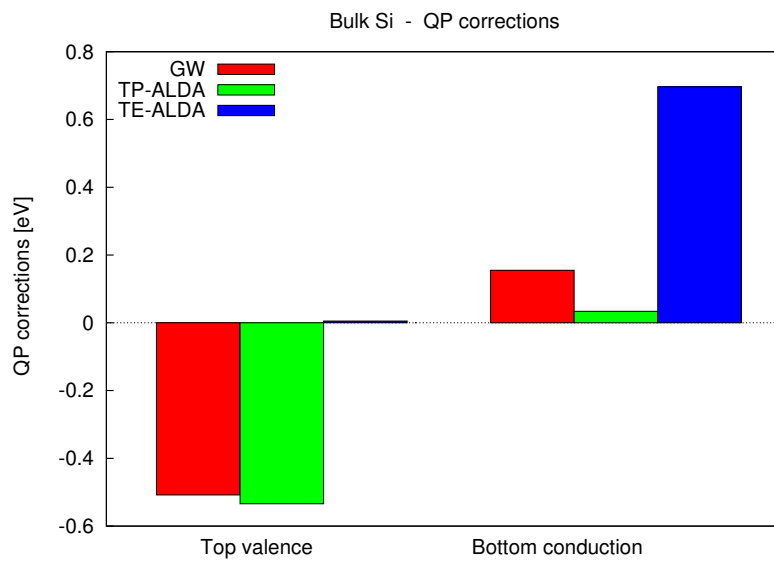
Figure 4.12: Quasiparticle correction at the Γ point $(0.0; 0.0; 0.0)$ in bulk Si for top-valence and bottom-conduction bands within the GW approximation and adding the ALDA-derived vertex in both the polarization and the self-energy (TE) or in the polarization only (TP). The value of the band-gap shift is about the same in GW and GW^{TE}. In the TP case there is a slight difference and the band-gap is smaller. On the other hand there is almost a rigid shift between GW and GW^{TE}.
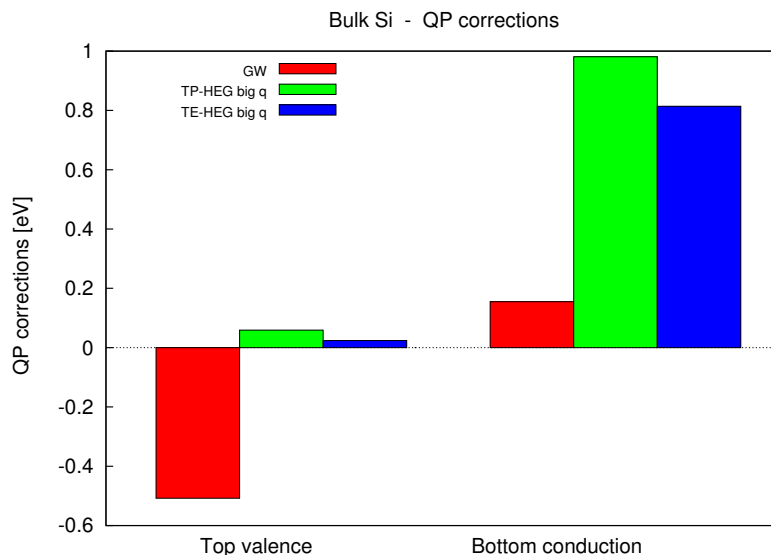
Figure 4.13: Quasiparticle correction at the Γ point $(0.0; 0.0; 0.0)$ in bulk Si for top valence and bottom conduction. GW and large-q HEG vertex are compared. While the trend of the TE calculation is similar to the TE-ALDA one, the value of the band-gap shift in GW^{TE} is larger by ~ 0.1 eV. The TP case is quite similar to the TE case and the gap becomes even larger.

noticeable changes are for the TP calculations: while ALDA gives a slightly smaller band-gap, the Hubbard kernel yields a correction a half the size of *GW*; the big-q kernel gives instead a larger gap than *GW*.

One can consider that the behavior of the Hubbard kernel is correct, as I have shown above that it is free from the pathologies that affect the ALDA. On the other hand the kernel derived from the large-q condition in the HEG is not very reliable if used for all ranges of q. If one thinks of it as an LRC kernel with a too-large value of α, it is sensible to say that one can expect unphysical results at $q \to 0$. This has been shown also by F. Sottile [70]. Once this is clear, one can consider that the main effect of using a test-particle screening in the self-energy is to increase the screening and reduce the self-energy correction to the Kohn-Sham energy gap with respect to *GW*. This is equivalent to applying the vertex correction only to the polarizability. The results for the test-electron screening show, in all cases, that the difference with the *GW* reference is compensated, whether the TP case had a stronger or weaker correction. This would suggest that applying vertex corrections to both the self-energy and the polarizability brings to a result that is not far from that of the *GW* self-energy. This sort of cancellation effects would be at the origin of the good performances of the *GW* approximation. However, it is not clear whether a more complex approximation for the vertex (three- or four-point) would yield different outcomes.

Morris *et al.* have studied the effect of vertex corrections derived from the ALDA TDDFT kernel on atoms and on the homogeneous electron gas. Their
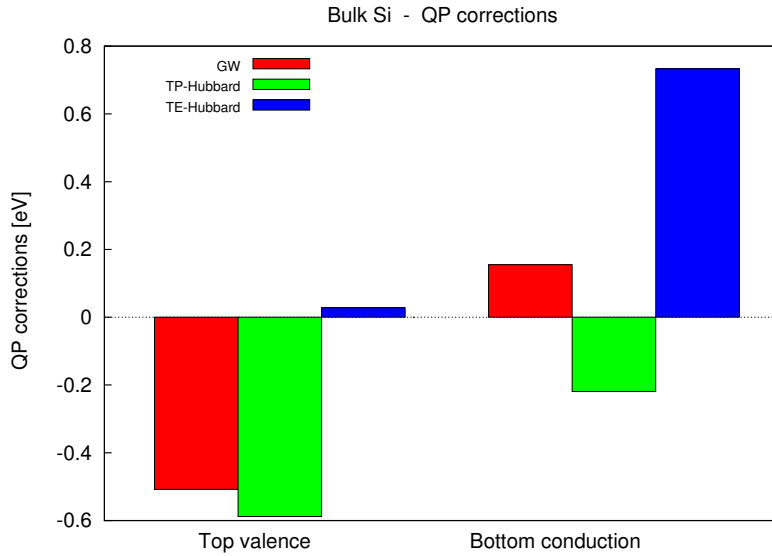
Figure 4.14: Quasiparticle correction at the Γ point $(0.0; 0.0; 0.0)$ in bulk Si for top valence and bottom conduction. GW and Hubbard are compared. The trend of the TE calculation is similar to the TE-ALDA one: the band-gap shift is slightly larger. The TP case is quite different from ALDA and from the large-q HEG kernel, in that both valence and conduction have a negative quasiparticle correction.

conclusions are similar to mine in that they find that appreciable improvements appear only using a GW^{TP} self-energy. However, comparison between a solid and finite systems is always difficult, as they are very different systems. In fact, the authors do not look at band gaps, but only at absolute values of quasiparticle energies. Notably, what they find for the first ionization potential is comparable to the the results presented here for the top-valence band of silicon and they agree fairly well.
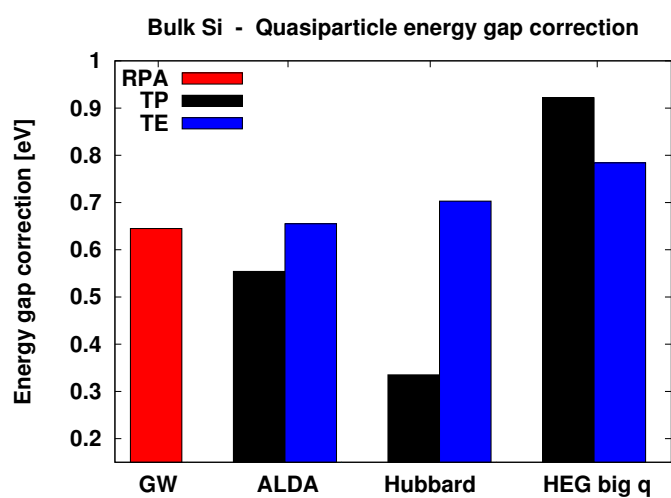
Figure 4.15: Gap correction at the Γ point $(0.0; 0.0; 0.0)$ in bulk Si for several approximations. The results for the different approximations (ALDA, Hubbard and big-q) are here summarized. The TE band-gap shifts are not very different from the GW reference, with the big-q kernel giving a larger final gap. The most noticeable changes are for the TP calculations: while ALDA gives a slightly smaller band-gap, the Hubbard kernel yields a correction a half the size of GW; the big-q kernel gives instead a larger gap than GW.

4.4.1   Static screening at finite q

One can try to obtain more insight on the approximations used and on their effects on the self-energy, focusing on their q-dependence and using the static limit of ε^{-1}. In fact one can show that

$$E_{gap} \propto 1/\varepsilon_\infty, \qquad (4.30)$$

where $\varepsilon_\infty = \lim_{\omega \to 0} \varepsilon(\omega)$.[3] Now one has to remember that the self-energy contains a sum over all possible q vectors. If one plots $1/\varepsilon_\infty$ for a range of q vectors, different kernels will give different line shapes. One can compare in Figure 4.16 the ALDA values of $1/\varepsilon_\infty$ with the RPA values. It is immediately clear that TP values are always smaller than RPA, while TE values are always larger. Moreover, for small values of q, the TE curve is much closer to RPA than the TP curve. This is exactly what is found for the band-gap correction in the previous section. Small-q values have a larger weight in the self-energy integral and this plot is a confirmation of this characteristic feature of the self-energy in silicon. The anomalous point caused by the ALDA pathology is at this point non-influent on the value of the band-gap. In Figure 4.17, where RPA and Hubbard are compared, the general picture is similar, but somewhat more pronounced. There is no anomalous point, of course. Instead, for the same range of small $|q|$, TP values of $1/\varepsilon_\infty$ are more different than RPA with respect to TP-ALDA. As a consequence, the expected (and verified) behavior of band-gap corrections is to have a smaller correction using a TP screening. At this point the study of the large-q limit is clearly not going to bring revolutionizing results in this system: the self-energy of silicon is apparently sensitive to small values of q and by consequence a correction to the large-q limit is not going to change much at the quasiparticle level. This is probably the reason why the clear pathology of the ALDA kernel for large values of q has never been a problem for the calculation of vertex corrections: although — using an ALDA vertex correction — anomalous points enter in the self-energy, their weight is too small to make a difference.

Still, vertex corrections could possibly make a difference for spectral properties such as quasiparticle lifetimes and satellites. To analyse this kind of features one has to calculate the one-particle spectral function as discussed in Chapter 3.

---

[3]The dependence of quasiparticle energies and band gaps on ε_∞ with application on hybrid DFT functionals has been discussed e.g. in a paper by Marques *et al.* [99].
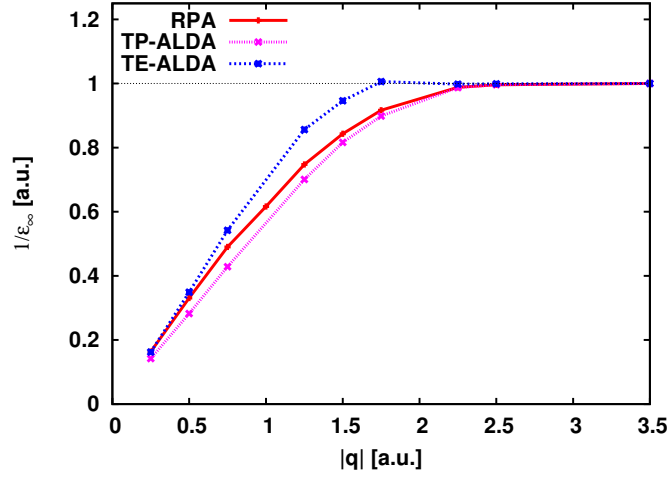
Figure 4.16: Static limit of ε^{-1} with respect to the momentum transfer q. RPA is compared to TE-ALDA and TP-ALDA. TP values are always smaller than RPA, while TE values are always larger. This causes a larger opening of the band gap for TE and a lesser opening for TP than with an RPA screening. One can remark here the anomalous behavior of TE-ALDA at q=1.75 a.u.
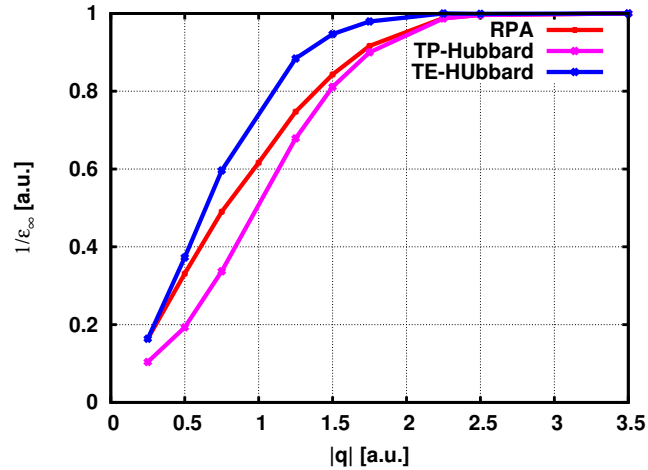

Figure 4.17: Static limit of ε^{-1} with respect to the momentum transfer q. RPA is compared to TE-Hubbard and TP-Hubbard. TP values are always smaller than RPA, while TE values are always larger. This causes a larger opening of the band gap for TE and a lesser opening for TP than with an RPA screening.

4.5 Spectral properties

To study spectral features such as quasiparticle lifetimes and satellites one has to calculate the one-particle spectral function for a single quasiparticle state, as reported in (3.60):

$$A(\omega) = \frac{1}{\pi} \frac{|\operatorname{Im}\Sigma(\omega)|}{[\omega - \epsilon_{\mathrm{H}} - \operatorname{Re}\Sigma(\omega)]^2 + \operatorname{Im}\Sigma(\omega)^2}. \qquad (4.31)$$

The total spectral function is then obtained summing over all the states of the system. To obtain the spectral function is thus necessary to obtain the full energy dependence of the self-energy. This is more cumbersome than obtaining QP energies with a plasmon-pole model, as it is extensively described in [57]. I report in Figure 4.18 the spectral function of silicon for the bottom valence, as a representative example. This is also where the changes are most apparent among the states in the BZ, as in e.g. the top-valence states the differences are even less pronounced. Sharp peaks in the spectral function rise from zeros in $\omega - \epsilon_{\mathrm{H}} - \operatorname{Re}\Sigma(\omega)$: the peak at -12.5 eV is the quasiparticle peak and the other peak at 24 eV below is a satellite. The most apparent changes with respect to RPA are: (i) in the test-particle spectral function there is a transfer of weight from the quasiparticle to the satellite, which is enhanced due to a higher intensity and slight blue shift of $\operatorname{Im}\Sigma$; (ii) in the test-electron spectral function the quasiparticle peak is almost identical to RPA, while there is a slight blue shift of the satellite peak due to a change in the real part of the self-energy. The changes with respect to the *GW* spectral function (RPA) are very slight. The effects of these vertex correction are negligible in the total spectral function obtained integrating over the full Brillouin zone. The theoretical implication of the *GW* satellites in silicon are much broader than this and will be extensively discussed in Chapter 6.

While the results of this chapter suggest that two-point vertices are too limited to improve spectral properties, there might be space left for improvement in the calculation of QP energies. The link between QP corrections and q dependence of the dielectric function has been clarified. Nevertheless my results confirm that the use of two-point vertex corrections both in the self-energy and in the polarizability is subject to mutual cancellations that limit the effects on the value of the quasiparticle band gap. This also suggests that the *GW* approximation is solid and has been successful also thanks to this kind of error cancellation between polarization and self-energy effects.

Vertex corrections could in principle help to solve the so-called *self-screening* problem in *GW*. This problem arises because in *GW* the screening to which a hole is subjected is the same as the one that screens an electron; this is not correct, as the former is screened by an $|N-1,s\rangle$ state, while the latter is screened by $|N,s\rangle$. In this sense the hole is "self-screened" also by the photoelectron. A cheap solution to the self-screening problem of *GW* using two-point vertex corrections has been proposed by Romaniello *et al.* [67]. A poor-man solution to the self-screening problem would be to put both vertices for occupied states and use only the internal one (i.e. in the polarizability) for the empty states. One would then use a test-electron screening in the self-energy of oc-
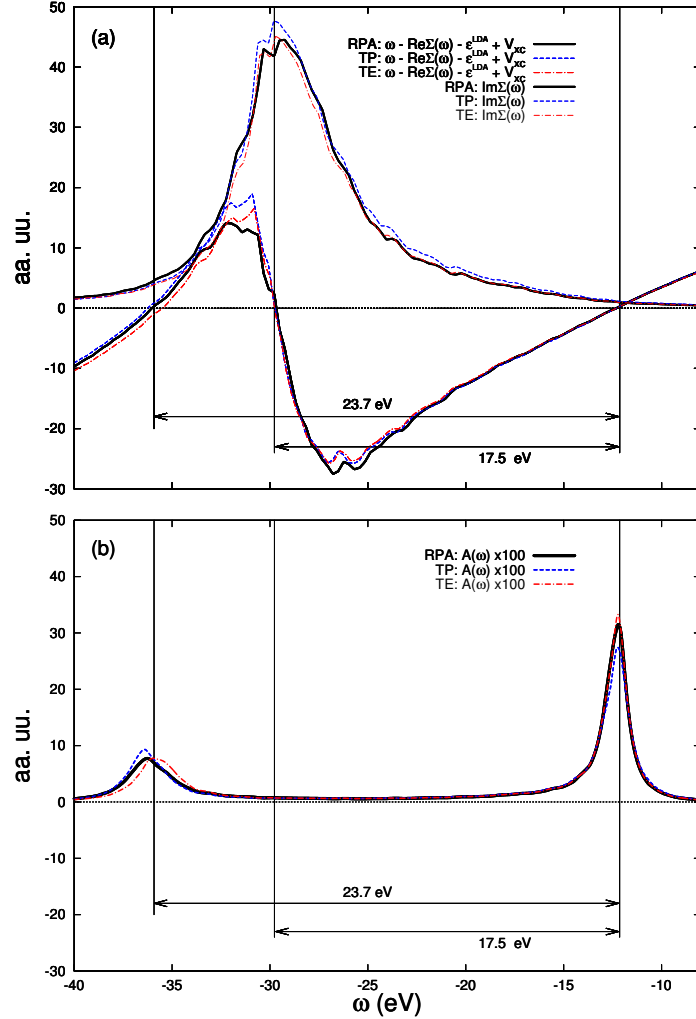
Figure 4.18:   (a) Real and imaginary part of the self-energy of the bottom-conduction band of bulk silicon for GW^{RPA}, GW^{TP} and GW^{TE} with the ALDA kernel. (b) Intrinsic spectral function $A_j(\omega)$ of the bottom-conduction band of bulk silicon calculated as in (3.60) using the GW^{RPA}, GW^{TP} and GW^{TE} self-energies. Sharp peaks in the spectral function rise from zeros in $\omega - \epsilon_{\mathrm{H}} - \mathrm{Re}\Sigma(\omega)$: the peak at -12.5 eV is the quasiparticle peak and the other peak at 24 eV below is a satellite. The most apparent changes with respect to RPA are: in TP there is a transfer of weight from the QP to the satellite, which is enhanced due to a higher intensity and slight blue shift of $\mathrm{Im}\Sigma$; in TE the QP peak is almost identical to RPA, while there is a slight blue shift of the satellite peak due to a change in $\mathrm{Re}\Sigma$. The changes with respect to the GW spectral function (RPA) are very slight and negligible in the total spectral function obtained integrating over the full BZ. See Chapter 6 for a deeper discussion of the spectral function of silicon.

cupied states and a test-particle screening in the self-energy of empty states. The effectiveness of this approach has yet to be investigated and it is an interesting outlook. I calculated preliminary results on NiO that suggest that this kind of vertex corrections could give an improvement with respect to a *GW* self-energy, notably in systems such as this, where electrons are localised and there is a more "atomic-like" physics, as it has been suggested by Romaniello *et al.* [67]. In the particular case of NiO these effects are interwoven with self-consistency effects, that make the analysis more difficult. For now, this kind of vertex corrections appear to affect just the quasiparticle energies, as it is the case in silicon.

Vertex corrections are just one way of improving the calculation of the spectral function beyond the *GW* approximation. In the Chapter 5 I will show how it is possible to derive new approximations for the one-particle Green's function that can improve the properties of the spectral function $A(\omega)$, on the path of what already done by G. Lani *et al.* [73, 74]. In Chapter 6 and 7 I will explore the performance of an alternative approximation for the one-particle Green's function that is able to improve the description of satellites. I will also show how it is important to take into account additional effects inherent to the experiment in order to obtain a correct comparison between theory and experiment.

5 | Dynamical effects beyond *GW* in Green's function theory

In this chapter I will show how one can use an approximate equation of motion for the single-particle Green's function to derive an exact solution that goes beyond *GW*, including dynamical effects, and retains a fair amount of physical insight. This result derives from the general idea of restricting the configuration space of the problem in order to simplify and solve it. The linearized equation of motion for *G* showed in 3.6.1 is the product of exactly this idea. I will show that one can solve the linearized equation obtaining an exponential expression for *G* that is practically identical to the Green's function solution of an electron-boson model Hamiltonian.[1] This model has been re-named by Lars Hedin, in his last generalized revision, the *quasi-boson* model [25]. The advantage over the latter of the derivation presented in this chapter is that this is the result of systematic approximations on fundamental equations, that can be retraced and, in principle, relaxed at will.

In the first part of the chapter I will show how one can derive an exponential representation for *G* through approximations on the equation of motion that lead to an exact solution. I will then show how this can be improved and connected to *GW* in order to use the latter as an improved quasiparticle starting point on top of which one adds dynamical effects. The Green's function obtained with this approach includes dynamical effects and can be in principle used to derive vertex corrections; in the second part of the chapter I will show how one can use the exponential form of the Green's function to calculate vertex corrections and how the use of the exponential representation of *G* can suggest alternative routes for the calculation of the vertex and of the self-energy.

---

[1] This model was initially used to study core electrons coupled to plasmons [75–77, 79] and was later generalized for valence electrons [25, 50, 80] and for the coupling with phonons [81].

5.1   The linearized equation

The derivation starts from (3.104), the linearized equation of motion for G (integrals are for now omitted):

$$G(12) = G_{\mathrm{H}}^0(12) + G_{\mathrm{H}}^0(13)\bar{\varphi}(3)G(32) + iG_{\mathrm{H}}^0(13)W(34)\frac{\delta G(32)}{\delta\bar{\varphi}(4)} \tag{5.1}$$

where $\bar{\varphi}$ is the screened external perturbation to the system. W is the screened Coulomb interaction. The main interest is the coupling between a single state (electron or hole) to a plasmon. Using the shorthand notation $t_{12} = t_1 - t_2$. and introducing an auxiliary Green's function G^{φ} defined via a Dyson equation $G^{\varphi} = G_H^0 + G_H^0\bar{\varphi}G^{\varphi}$ one can translate the linearized equation of motion in the following set of equations defined on a discrete basis:[2]

$$G_{ij}^{\varphi}(t_{12}) = G_i^H(t_{12})\delta_{ij} + \int dt_3\, G_i^H(t_{13})\sum_k \bar{\varphi}_{ik}(t_3)G_{kj}^{\varphi}(t_{32}) \tag{5.2}$$

$$G_{ij}(t_{12}) = G_{ij}^{\varphi}(t_{12}) + \int dt_3 dt_4 \sum_{klmn} G_{ik}^{\varphi}(t_{13})W_{klmn}(t_{34})\frac{\delta G_{nj}(t_{32})}{\delta\bar{\varphi}_{lm}(t_4)}, \tag{5.3}$$

where the equations have been written on a basis where G^H is diagonal,

$$W_{ijkl}(t_{34}) = \int dr dr'\, \phi_i^*(r)\phi_j^*(r')W(r,r',t_3,t_4)\phi_k(r')\phi_l(r) \tag{5.4}$$

is a matrix element of the screened Coulomb interaction W and

$$\bar{\varphi}_{ik}(t_3) = \int dr \phi_i^*(r)\bar{\varphi}(r,t_3)\phi_k(r) \tag{5.5}$$

is a matrix element of the screened external perturbation $\bar{\varphi}$. G^H is the linearized Hartree Green's function (in the limit $\bar{\varphi} \to 0$) and G is the full interacting Green's function.

5.2   Diagonal equation

I here introduce a very drastic assumption: G and G^{H} are both diagonal on the same basis (G^{φ} follows). This is a rough hypothesis but in the following I will show that it can be refined improving the non-interacting starting point. I also put $\bar{\varphi}_{ij} \to \varphi_{ij}$ to speed up the notation. The equation at this point can be rewritten as

$$G_l(t_1 t_2) = G_l^{\mathrm{H}}(t_1 t_2) + G_l^{\mathrm{H}}(t_1 t_3)\varphi_{ll}(t_3)G_l(t_3 t_2)$$
$$+ iG_l^{\mathrm{H}}(t_1 t_3)\sum_{ij} W_{ijll}(t_3 t_4)\frac{\delta G_l(t_3 t_2)}{\delta\varphi_{ij}(t_4)}. \tag{5.6}$$

---

[2] This double set of equations can be written in a completely equivalent way as a single integro-differential equation, without introducing G^{φ}. This representation is here preferred because it is clearer. It is worth noting that for $\varphi \to 0$ one has $G^{\varphi} \to G^H$.

It is possible to simplify further the equation. When one starts to iterate the equation it becomes clear that G_l will only depend on diagonal terms φ_{ll} of the external perturbation. Moreover the l component of G will only depend on φ_{ll}. As a consequence, the derivative $\delta G_l / \delta \varphi_{ij}$ will be 0 for any $i \neq j \neq l$. Thus only diagonal terms are retained throughout the equation, which becomes a set of scalar equations, one for each single state l. The index can therefore be dropped and one can rewrite the *diagonal equation* in a compact form as

$$G(t_1 t_2) = G^{\mathrm{H}}(t_1 t_2) + G^{\mathrm{H}}(t_1 t_3)\varphi(t_3)G(t_3 t_2) + iG^{\mathrm{H}}(t_1 t_3)W(t_3 t_4)\frac{\delta G(t_3 t_2)}{\delta \varphi(t_4)},$$
(5.7)

where one implicitly integrates over all repeated time indices. This version of the equation neglects mixing between states. The interaction of the particle with the system is effectively contained in $W(t_3 t_4)$. The scalar equation can be written as a set of two equations using the auxiliary Green's function G^φ as

$$G^\varphi(t_{12}) = G^H(t_{12}) + \int dt_3\, G^H(t_{13})\varphi(t_3)G^\varphi(t_{32});$$
(5.8)

$$G(t_{12}) = G^\varphi(t_{12}) + \int dt_3 dt_4\, G^\varphi(t_{13})W(t_{34})\frac{\delta G(t_{32})}{\delta \bar{\varphi}(t_4)}.$$
(5.9)

As it will be clear in the following, this form of the equations is convenient for the calculation of the solution.

5.2.1 Solution for an occupied state

In this particular case one assumes that the level considered in the equation is occupied, but a completely equivalent procedure can be done for the case of an empty state. One can write down the following expressions for the Green's functions, with an explicit time ordering:

$$\mathcal{G}_{\mathrm{H}}(t_1 t_2) = i\theta(t_2 - t_1)e^{-i\varepsilon(t_1 - t_2)}$$
(5.10a)

$$\mathcal{G}_\varphi(t_1 t_2) = i\theta(t_2 - t_1)\tilde{y}_\varphi(t_1 t_2)$$
(5.10b)

$$\mathcal{G}(t_1 t_2) = i\theta(t_2 - t_1)\tilde{y}(t_1 t_2)$$
(5.10c)

where ε is the Hartree energy of the state one is considering. Using these definitions in (5.8), defining

$$\tilde{y}_\varphi(t_1 t_2)e^{i\varepsilon(t_1 - t_2)} = y_\varphi(t_1 t_2)$$
(5.11)

$$\tilde{y}(t_1 t_2)e^{i\varepsilon(t_1 - t_2)} = y(t_1 t_2)$$
(5.12)

and with explicit integration over t_3, one can write

$$y_\varphi(t_1 t_2) = 1 + i\int_{t_1}^{t_2} dt_3 \varphi(t_3)y_\varphi(t_3 t_2).$$
(5.13)

The solution of this equation is

$$y_\varphi(t_1 t_2) = \exp\left\{i\int_{t_1}^{t_2} dt' \varphi(t')\right\}$$
(5.14)

as one can verify with a substitution in the original equation. Now, the functional $y_\varphi(t_1 t_2)$ has two interesting properties, as one can verify using (5.14). The first property is

$$\frac{\delta y_\varphi(t_3 t_2)}{\delta \varphi(t_4)} = i\theta(t_2 - t_4)\theta(t_4 - t_3)y_\varphi(t_3 t_2). \tag{5.15}$$

and second property is

$$y_\varphi(t_1 t_3)y_\varphi(t_3 t_2) = e^{i \int_{t_1}^{t_3} dt' \varphi(t') + i \int_{t_3}^{t_2} dt' \varphi(t')} = y_\varphi(t_1 t_2). \tag{5.16}$$

Consider now (5.9) and substitute (5.10a), (5.10b) and (5.10c) in it. One gets

$$y(t_1 t_2) = y_\varphi(t_1 t_2) + i^2 y_\varphi(t_1 t_3)\mathcal{W}(t_3 t_4)\frac{\delta y(t_3 t_2)}{\delta \varphi(t_4)}, \tag{5.17}$$

where $t_1 < t_3 < t_2$. Now if one iterates (5.17) one can use the properties listed above to demonstrate that the solution will have the form

$$y(t_1 t_2) = y_\varphi(t_1 t_2) \cdot \mathcal{F}(t_1 t_2) \tag{5.18}$$

where $\mathcal{F}$ is some functional that does not depend on φ. From (5.17), the functional $\mathcal{F}$ is solution of the following equation:

$$\mathcal{F}(t_1 t_2) = 1 + i^3 \int_{t_1}^{t_2} dt_3 \int_{t_3}^{t_2} dt_4 \, \mathcal{W}(t_3 t_4)\mathcal{F}(t_3 t_2). \tag{5.19}$$

The solution of this equation is

$$\mathcal{F}(t_1 t_2) = \exp\left\{-i \int_{t_1}^{t_2} dt' \int_{t'}^{t_2} dt'' \, \mathcal{W}(t't'')\right\} \tag{5.20}$$

as it can be verified by a substitution in the original equation. At this point the solution for y is straightforward and reads

$$y(t_1 t_2) = \exp\left\{i \int_{t_1}^{t_2} dt' \varphi(t') - i \int_{t_1}^{t_2} dt' \int_{t'}^{t_2} dt'' \mathcal{W}(t't'')\right\}. \tag{5.21}$$

This implies that the solution for the full Green's function $\mathcal{G}$ — according to the definition in (5.10c) — now reads

$$\mathcal{G}(t_1 t_2) = i\theta(t_2 - t_1)e^{-i\varepsilon(t_1 - t_2)}e^{-i \int_{t_1}^{t_2} dt' \int_{t'}^{t_2} dt'' \mathcal{W}(t't'')}e^{i \int_{t_1}^{t_2} dt' \varphi(t')}. \tag{5.22}$$

This is an exact solution to the scalar equation that has an explicit functional dependence on W and φ. The two approximations that were made with respect to the full equation of motion for G to reach this point are:

- the linearization of the Hartree potential: this yields the linearized equation of motion in (5.1);

- the diagonal approximation for G: one assumes that the full G and the Hartree G^H are diagonal on the same basis. This approximation yields the separation of the set of matrix equations into a set of decoupled scalar equation, with one equation for each state of the system.

Notably, the diagonal approximation appears here quite crude: in the presence of φ only, the exact Green's functions are already not diagonal and this is enhanced further by the addition of electron-electron interaction.

A very important feature of this solution is that it depends explicitely on φ. This is crucial if one is interested in the calculation of vertex corrections. In fact the vertex is defined as $\Gamma = \delta G^{-1}/\delta\varphi$. If one has the explicit dependence of G on φ it is in principle possible to calculate directly this quantity. I will show further in the manuscript how one can try and calculate vertex corrections using the properties of this solution for G. At this point one can put the external field φ to 0 and write, in a compact way, the solution to the diagonal equation:

$$\mathcal{G}(t_1 t_2) = \mathcal{G}^H(t_1 t_2) e^{-i \int_{t_1}^{t_2} dt' \int_{t'}^{t_2} dt'' \mathcal{W}(t't'')}. \tag{5.23}$$

Looking at this equation it becomes clear that any exchange and correlation effect beyond Hartree (e.g. quasiparticle corrections, satellites) must be contained in the exponent containing W. As an example, the Hartree-Fock solution can be obtained by putting

$$W(t't'') = v\delta(t' - t''). \tag{5.24}$$

One obtains then for G:

$$\mathcal{G}(t_1 t_2) = i\theta(t_2 - t_1) e^{-i(\varepsilon - v)(t_1 - t_2)} \tag{5.25}$$

where $\varepsilon - v$ is the Hartree-Fock energy.

The linearized equation contains the GW approximation, so its exact solution is expected to describe effects beyond that. However it remains to be seen what are the effects of the diagonal approximation. In the following I will analyze the structure of G and of the spectral function A for a model W and then show how the results can be generalized for an arbitrary screened interaction.

5.2.2 Comparison with the electron-boson solution

One can realize how striking the result for G is when it is compared to what has been previously obtained for the polaron model shown in Section 3.7. It is possible to rewrite the expression for G, making use of Fourier tranforms, as

$$\mathcal{G}(\tau) = \mathcal{G}^H(\tau) \exp\left\{ \frac{i}{2\pi} \int d\omega\, W(\omega) \left[\frac{e^{i\omega\tau} - i\omega\tau - 1}{\omega^2} \right] \right\}, \tag{5.26}$$

where $\tau = t_1 - t_2$ and

$$W(\omega) = \int d\tau\, e^{i\omega\tau} W(\tau) \tag{5.27}$$

is the Fourier transform of W. This has the same form as the exact solution for the Green's function of the electron-boson model studied by many authors, e.g. [25, 75]. This expression for G is useful in that one can already recognize three terms — getting hints from the work on the model — that will give, through W, quasiparticle correction, renormalization and satellite contribution. In the following this will become clearer. One can take a plasmon-pole model for W of the form:

$$\mathcal{W}(t_1 - t_2) = -i\lambda \left[e^{-i\omega_p(t_1 - t_2)} \theta(t_1 - t_2) + e^{i\omega_p(t_1 - t_2)} \theta(t_2 - t_1) \right]. \tag{5.28}$$

Here λ is the intensity of the plasmon and ω_p is the plasmon frequency. This model represents a screening with a sharp peak in the imaginary part centered at ω_p, as it is the case in simple semiconductors. Substituting this in the expression for $\mathcal{G}$ one obtains

$$\mathcal{G}(\tau) = \mathcal{G}_H(\tau) \exp\left\{ \frac{\lambda}{\omega_p^2} \left[e^{i\omega_p\tau} - i\omega_p\tau - 1 \right] \right\} \tag{5.29}$$

where $\mathcal{G}_H(\tau) = i\theta(-\tau)\exp(-i\varepsilon\tau)$ is the Hartree (non-interacting) Green's function for the hole. This is identical to the one-particle Green's function calculated by Langreth for a core level [75]. The Green's function can be written as

$$\mathcal{G}(\tau) = i\theta(-\tau) \exp\left\{ -\frac{\lambda}{\omega_p^2} \right\} \exp\left\{ -iE^{QP}\tau \right\} \exp\left\{ \frac{\lambda}{\omega_p^2} e^{i\omega_p\tau} \right\} \tag{5.30}$$

where $E^{QP} = \varepsilon + \frac{\lambda}{\omega_p}$ is the quasiparticle energy. After the expansion of the last term on the right-hand side of the equation, one can calculate $A(\omega) = \frac{1}{\pi}|\operatorname{Im}G(\omega)|$ and obtain

$$A(\omega) = \frac{1}{\pi} e^{-\frac{\lambda}{\omega_p^2}} \left[\delta(\omega - E^{QP}) + \frac{\lambda}{\omega_p^2}\delta(\omega - E^{QP} + \omega_p) \right.$$

$$+ \frac{1}{2}\left(\frac{\lambda}{\omega_p^2}\right)^2 \delta(\omega - E^{QP} + 2\omega_p)$$

$$\left. + \frac{1}{6}\left(\frac{\lambda}{\omega_p^2}\right)^3 \delta(\omega - E^{QP} + 3\omega_p) + \dots \right]. \tag{5.31}$$

The spectral function displays a main quasiparticle delta-peak at the quasiparticle energy E^{QP}. This is followed by an infinite series of satellite delta-peaks that decays following a Poisson distribution. At order n, the satellite peak is located at $\omega - E^{QP} + n\omega_p$ and its strength is $(\lambda/\omega_p^2)^n$. The whole spectrum is renormalized by a factor $Z = \exp\{-\lambda/\omega_p^2\}$. Again, this result for the spectral function is identical to the one found by Langreth using the polaron model for a core level [75]. This result can be generalized taking into account plasmon dispersion adding a model dispersion in ω_p. In practice, this means that the diagonal approximation for the linearized equation is exactly equivalent to the electron-boson Hamiltonian for core levels when a plasmon-pole model is applied and it is generally equivalent to the quasi-boson model by Hedin. The advantage here is that in principle one could use the solution for G and calculate it using a numerical integration for W. Moreover, the direct link to the fundamental differential equations stresses which are the underlying approximations, and how one might try to go beyond.

5.2.3   Starting from non-interacting quasiparticles

To consolidate the assumption that the non-interacting Green's function and the interacting $\mathcal{G}$ are diagonal on the same basis, one would like to use a different starting point than Hartree's $\mathcal{G}^H$. One of the best that one can think of

is certainly $\mathcal{G}^{GW}$, but for a matter of generality one can think to have a generic self-energy Σ^{QP} that gives a good quasiparticle description of the system. One can define then the following set of equations

$$G^{QP} = G^H + G^H \Sigma^{QP} G^{QP} \tag{5.32}$$

$$G = G^{QP} + G^{QP} \check{\Sigma} G \tag{5.33}$$

where $\check{\Sigma} = \Sigma - \Sigma^{QP}$. Assuming the GW approximation as the best available for QP energies, one can use $\Sigma^{QP} = \Sigma^{GW}(E)$, with E the quasiparticle GW energy. The task of Σ^{QP} is then to correct the Hartree energies to quasiparticle energies and obtain G^{QP}. If one approximates the Green's functions to be diagonal as in the present problem it is possible to write the equation as

$$G(t_1 t_2) = G^{QP}(\tau) e^{i\Delta^{QP}\tau} e^{-i \int_{t_1}^{t_2} dt' \int_{t'}^{t_2} dt'' W(t't'')}, \tag{5.34}$$

where

$$G^{QP}(\tau) = i\theta(-\tau) e^{-iE\tau} \tag{5.35}$$

is the quasiparticle Green's function, containing the complex quasiparticle energy $E = \epsilon + i\gamma$ and

$$\Delta^{QP} = \Sigma^{GW}(E) = -\frac{i}{2\pi} \int d\omega \frac{W(\omega)}{\omega} \tag{5.36}$$

is the GW self-energy calculated at the QP energy E using for G^{QP} and W the current approximations used to derive the diagonal equation (5.7). One can use Fourier transform to rewrite (5.34) as

$$\mathcal{G}(\tau) = \mathcal{G}^{QP}(\tau) \exp\left\{ \frac{i}{2\pi} \int d\omega \, W(\omega) \left[\frac{e^{i\omega\tau} - 1}{\omega^2} \right] \right\}. \tag{5.37}$$

The key difference between this equation and (5.26) is in a missing $i\omega\tau$ term in the nominator at the exponent and in the fact that here one has the QP Green's function instead of the Hartree one. This difference is easily explained in that the missing term is exactly what produces the QP shift to give the correct QP energy. This result was found also in the model treatment by Hedin and by Langreth [25, 75]. Using the plasmon-pole model (5.28) already applied in the previous section, one can obtain more insight and calculate the Green's function in this particular case. One obtains the same expression as (5.30) *but* with a fundamental difference: the real-valued E^{QP} is replaced by the *complex* quasiparticle GW energy E. One can then calculate the spectral function that reads

$$A(\omega) = \frac{\gamma}{\pi} e^{-\frac{\lambda}{\omega_p^2}} \left[\frac{1}{(\omega - \epsilon)^2 + \gamma^2} + \frac{\lambda}{\omega_p^2} \frac{1}{(\omega - \epsilon + \omega_p)^2 + \gamma^2} \right.$$

$$+ \frac{1}{2} \left(\frac{\lambda}{\omega_p^2} \right)^2 \frac{1}{(\omega - \epsilon + 2\omega_p)^2 + \gamma^2}$$

$$\left. + \frac{1}{6} \left(\frac{\lambda}{\omega_p^2} \right)^3 \frac{1}{(\omega - \epsilon + 3\omega_p)^2 + \gamma^2} + \ldots \right]. \tag{5.38}$$

This version of the spectral function is similar to (5.31), but it has key difference in that the QP peak is at the *GW* quasiparticle energy *and* it has a finite lifetime, which is the quasiparticle lifetime calculated in *GW*. In this sense this spectral function reproduces exactly the QP part of the *GW* self-energy and it adds the ability to reproduce plasmon satellites at all orders. This in contrast to the *GW* approximations, that is able to reproduce just one satellite in its standard application. This is in practice the same result that is found in the so-called *ab-initio* cumulant expansion, that relies on an *ad-hoc* diagrammatic expansion that uses the *GW* self-energy as an input [50]. This formulation can be connected even better to *GW*: using the plasmon-pole model and the current diagonal approximation in the *GW* self-energy, one can write some relations for the parameters of the plasmon-pole model as functions of Σ:

$$\mathrm{Im}\Sigma(\omega) = \pi\lambda\,\delta(\omega - \epsilon + \omega_p) \tag{5.39}$$

and, integrating both sides,

$$\lambda = \frac{1}{\pi} \int d\omega\,\mathrm{Im}\Sigma(\omega) \tag{5.40}$$

which is very reasonable in the sense that notoriously the imaginary part of *W* is proportional to the imaginary part of the self-energy [54]. Interestingly, if one evaluates the real part of Σ at the QP energy ϵ the result is

$$\mathrm{Re}\Sigma(\epsilon) = \frac{\lambda}{\omega_p} \tag{5.41}$$

which is what is found as the QP shift when one starts from the Hartree Green's function. This demonstrates how the effect of the *GW* self-energy is included in the Green's function calculated in (5.23).

At this point, one has a prescription to calculate the spectral function starting from a *GW* calculation. The real part of the self-energy will then give the value for the QP energy ϵ and the imaginary part of Σ will be used to fit the parameters of the plasmon-pole model. In the next chapter I will study how this approach can improve the study of the photoemission spectrum of bulk silicon, which can be considered as a paradigmatic case. In this particular case the exponential expression for *G* will be crucial to obtain a correct description of the incoherent spectrum, where the *GW* approximation is problematic.

5.2.4   Solution for a generalized *W*

A very interesting extension of the result in 5.38 can be applied in an easy way using a generalized model for the screening *W*. This improvement has some interesting consequences on the form of the spectral function. One assumes that *W* is a sum of N_p poles $\tilde{\omega}_j$ with strength λ_j:

$$\mathcal{W}(\tau) = \sum_j^{N_p} \lambda_j \left[e^{i\tilde{\omega}_j\tau}\theta(-\tau) + e^{-i\tilde{\omega}_j\tau}\theta(\tau) \right], \tag{5.42}$$

which is an exact representation for $N_p \to \infty$. This model for *W* is quite general and was e.g. used to model the inverse dielectric function by J.J. Kas *et al.* [100].

Following the same steps as those shown in the previous sections, one can calculate the spectral function $A(\omega) = \frac{1}{\pi}|\text{Im}G(\omega)|$. After defining

$$a_j = \frac{\lambda_j}{\tilde{\omega}_j^2} \tag{5.43}$$

one obtains, using (5.37) as shown before,

$$A(\omega) = \frac{\gamma}{\pi} e^{-\sum_j^{N_p} a_j} \left[\frac{1}{(\omega - \epsilon)^2 + \gamma^2} + \sum_j^{N_p} a_j \frac{1}{(\omega - \epsilon + \tilde{\omega}_j)^2 + \gamma^2} + \right.$$

$$+ \frac{1}{2} \sum_{jk}^{N_p} a_j a_k \frac{1}{(\omega - \epsilon + \tilde{\omega}_j + \tilde{\omega}_k)^2 + \gamma^2} +$$

$$+ \frac{1}{6} \sum_{jkl}^{N_p} a_j a_k a_l \frac{1}{(\omega - \epsilon + \tilde{\omega}_j + \tilde{\omega}_k + \tilde{\omega}_l)^2 + \gamma^2} +$$

$$\left. + \frac{1}{24} \sum_{jklm}^{N_p} a_j a_k a_l a_m \frac{1}{(\omega - \epsilon + \tilde{\omega}_j + \tilde{\omega}_k + \tilde{\omega}_l + \tilde{\omega}_m)^2 + \gamma^2} + \dots \right] . \tag{5.44}$$

In this expression for the spectral function, W is included in full detail, provided that the given multipole representation is correctly fitted. This means that this general formulation includes also lifetime of plasmons and plasmon dispersion, along with the full frequency dependence of W. The parameters entering the spectral function can be calculated from the results of a *GW* calculation with a prescription equivalent to the one of the previous section. This expression has interesting consequences for systems where W can have strong poles at very different energies. This is the case in anisotropic systems like graphite or graphene, or in systems where surface effects are important. As an example, one can think of such W as characterized by two main plasmon frequencies ω_1 and ω_2. If one was to use the plasmon-pole model for this system — in the single-pole version presented in the last section — one would have to choose either one of the two values, or an average, say $\bar{\omega}$, between ω_1 and ω_2. Either way, the resulting spectral function would have, as expected, a single series of satellite peaks, decaying as a Poisson distribution and centered at $\bar{\omega}$. Instead, using both frequencies in a two-pole model, one will have, according to (5.44):

1. a decaying series of satellites centered at multiples of ω_1 with an intensity proportional to a_1;

2. a decaying series of satellites centered at multiples of ω_2 with an intensity proportional to a_2;

3. a new series of satellites centered at other frequencies, results of the sum of multiples of ω_1 and ω_2, with the smallest being $\omega_1 + \omega_2$; the intensity of this first peak will be proportional to $a_1 a_2$. One can assume, without loss of generality, that $\omega_1 < \omega_2$. In this case the peak will be clearly visible and centered between $2\omega_1$ and $2\omega_2$ and will be more intense than

the smaller second-order peak of the two. In fact, assuming the general case where $a_1 < a_2$, it is straightforward that $a_1^2 < a_1 a_2 < a_2^2$. Higher orders become less trivial to track, but they will in general form additional structures centered at $n\omega_1 + m\omega_2$ and intensity $na_1 ma_2$.

This simple example illustrates how the generalization of the plasmon-pole model can bring interesting features in the spectral function. As a general conclusion, helped by this simple two-frequency model, one can expect that including the full frequency dependence of *W* in the spectral function will cause the incoherent part of the spectrum to broad considerably. At the same time, this allows the model to describe the effect of complex features that can arise in *W* and are not described by a single plasmon-pole model. An effective example of how complex features in *W* can affect the photoemission spectrum is described in Chapter 7. The example of bulk graphite will test the exponential expression for *G* in this generalized formulation, proving its validity and great ability in giving an interpretation of experimental spectra.

5.3 Vertex corrections

The following section will try to answer the fundamental question: *Is it possible to use the exponential expression for G to derive an expression for the vertex?* The first part of this chapter has been dedicated to the derivation of an *exact* solution to an *approximate* differential equation for the single-particle Green's function *G*. The *GW* self-energy is, on the other hand, an approximation of an *exact* expression that can in principle be used to calculate the full *G*. Having access to the full one-particle Green's function is in principle equivalent to having access to the exact self-energy, in fact the Dyson equation reads

$$G = G_0 + G_0 \Sigma G \tag{5.45}$$

and the non-interacting G^0 is known. Usually what would be done is to use an approximate self-energy to calculate *G* through the inversion of the Dyson equation as $G^{-1} = G_0^{-1} - \Sigma$. In the case of the exponential expression for *G*, the situation is the opposite. In fact one has obtained a solution for *G* without recurring to the Dyson equation and to the self-energy. This means that if *G* is already known, one is in principle able to use the Dyson equation to calculate the equivalent self-energy that would give that *G* starting from G_0. This is notably interesting here for two reasons: (i) I have shown that the exponential *G* includes the *GW* approximation and would then yield to a self-energy more advanced than Σ^{GW}; (ii) a vertex correction in the form of a self-energy can be easily implemented in any software package that already includes the calculation of the *GW* self-energy, needing a little effort with respect to a ground-up implementation.

On the other hand, having an analytic expression for the full interacting Green's function opens the way to another possibility: one can use the definition of the vertex

$$\Gamma(1,2;3) = -\frac{\delta G^{-1}(1,2)}{\delta\varphi(3)} \tag{5.46}$$

and try to calculate directly the functional derivative. In this case it is ideal because the exponential G has an explicit dependence on φ.
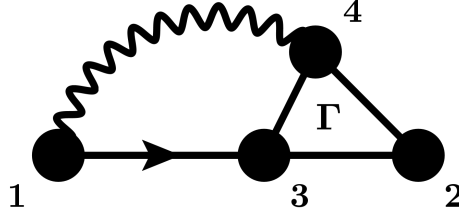

Figure 5.1: Feynman diagram of the exact self-energy. The solid line with an arrow is a Green's function, the wiggly line is W and the triangle is the vertex Γ. The self-energy reads $\Sigma(1,2) = G(1,3)W(1,4)\Gamma(3,2,4)$, as reported in (3.78e).

In the next part I will try to use the knowledge obtained in the previous part of this chapter, i.e. the exact solution for the diagonal equation of motion and the use of the diagonal approximation. Hence I will in the following neglect the spatial dependence of all the quantities involved. This is an idea that was developed in the framework of the thesis work of G. Lani and has proved to be valuable when it comes to: (i) understand the dynamical structure of the equation in a simplified framework and (ii) find exact solutions for the simplified equations that can later be expanded to the larger and more complicated problem. Therefore in the following I will:

- analyze the structure of the self-energy using a plasmon-pole model for W and a non-interacting Green's function — *mimicking* what done earlier in the chapter — and compare the result with the self-energy calculated using the solution of the diagonal equation, to gain some insight on the structure of the vertex and try to get an explicit solution;

- tackle directly the vertex in its definition as a functional derivative of the Green's function and use the acquired knowledge from the approach to the diagonal equation to look for an analytic solution to the problem.

5.3.1 The mimical way

In this section I will derive an expression for the exact self-energy and one for the self-energy derived using the solution of the diagonal equation for G. The comparison of the two will single out the vertex function and possibly an explicit analytic solution for it.

The exact self-energy

I will here neglect diagonal terms and thus retain only the time dependence of all quantities. The definition of Σ by Hedin, repeated here for clarity from (3.78e), is

$$\Sigma(1,2) = iG(1,3)W(1^+,4)\Gamma(3,2;4). \tag{5.47}$$

Neglecting the space dependence (i.e. assuming all the objects diagonal) and making use of Fourier transform one can rewrite the equation for $\Sigma(\omega)$ as

$$\Sigma(\omega) = \frac{i}{2\pi} \int d\omega' G(\omega') W(\omega - \omega') \Gamma(\omega', \omega - \omega') \tag{5.48}$$

If one substitutes here G and W with a non-interacting G^{QP} and a single plasmon-pole W one gets

$$\Sigma(\omega) = \frac{\lambda}{2\pi} \int d\omega' \frac{\Gamma(\omega', \omega - \omega')}{\omega' - E} \left(\frac{1}{\omega - \omega' - \omega_p + i\eta} - \frac{1}{\omega - \omega' + \omega_p - i\eta} \right). \tag{5.49}$$

which is already a quite complicated expression. To simplify the structure and create a connection to GW, it is a very good idea to write

$$\Gamma(\omega, \omega') = 1 + \Delta\Gamma(\omega, \omega') \tag{5.50}$$

Which is the way the vertex is written also in Hedin's equations in (3.78). Now, in the case of

$$\Delta\Gamma(\omega, \omega') = 0, \tag{5.51}$$

which means that the vertex is now a delta function in time and one has restored the GW approximation, Σ becomes

$$\Sigma^{GW}(\omega) = \frac{\lambda}{\omega - E + \omega_p} \tag{5.52}$$

which is clearly a self-energy coming from a single plasmon-pole model, as one can see comparing with (5.39). This is a simplified version of the result for the self-energy Σ^{GW} found by L. Hedin in [25]. If one includes here the rest of the vertex, restoring $\Gamma = 1 + \Delta\Gamma$, the self-energy reads

$$\begin{aligned}
\Sigma(\omega) &= \frac{\lambda}{\omega - E + \omega_p} \\
&+ \frac{\lambda}{2\pi} \int d\omega' \frac{\Delta\Gamma(\omega', \omega - \omega')}{\omega' - E} \left(\frac{1}{\omega - \omega' - \omega_p + i\eta} - \frac{1}{\omega - \omega' + \omega_p - i\eta} \right),
\end{aligned} \tag{5.53}$$

where the first terms on the right-hand side of the equation is the GW part of the self-energy, while the second term contains all the effects beyond GW, which are described by the unknown quantity $\Delta\Gamma$. It is helpful to define this quantity $X(\omega)$:

$$X(\omega) = \frac{\lambda}{2\pi} \int d\omega' \frac{\Delta\Gamma(\omega', \omega - \omega')}{\omega' - E} \left(\frac{1}{\omega - \omega' - \omega_p + i\eta} - \frac{1}{\omega - \omega' + \omega_p - i\eta} \right), \tag{5.54}$$

which, again, contains all vertex corrections and is put to 0 to recover the GW approximation.

Self-energy from the exponential solution

At this point one would like to have a frequency-dependent expression of Σ derived from the solution of the diagonal equation to compare with the one above and obtain an expression for $\Delta\Gamma$ and the whole vertex. To calculate the self-energy one can write the Dyson equation (3.52) as

$$\Sigma = G_0^{-1} - G^{-1}. \tag{5.55}$$

Using this expression the self-energy can be calculated using the exact G and then compared to the exact expression above. Now G^0 is

$$G_0^{-1}(\omega) = \omega - E, \tag{5.56}$$

with E the quasiparticle energy. Now the full G^{-1} from the diagonal equation is, with $a = -\lambda/\omega_p^2$:

$$G^{-1}(\omega) = \left[e^{-a} \sum_{n=0}^{\infty} \frac{a^n}{n!} \frac{1}{\omega - E + n\omega_p} \right]^{-1}, \tag{5.57}$$

i.e. it is the inversion of an infinite summation of terms. The full G generates the following self-energy:

$$\Sigma(\omega) = \omega - E - \left[e^{-a} \sum_{n=0}^{\infty} \frac{a^n}{n!} \frac{1}{\omega - E + n\omega_p} \right]^{-1}. \tag{5.58}$$

This is the self-energy that would give exactly the same spectral function as the exponential representation of G, containing QP corrections and satellite peaks at all orders. At this point one can equalize the two self-energies (5.53) and (5.58) and obtain

$$\Sigma(\omega) = \frac{\lambda}{\omega - E + \omega_p} + X(\omega) = \omega - E - \left[\sum_{m=0}^{\infty} \frac{(-a)^m}{m!} \sum_{n=0}^{\infty} \frac{a^n}{n!} \frac{1}{\omega - E + n\omega_p} \right]^{-1}. \tag{5.59}$$

One can then single out $X(\omega)$, using (5.52) as Σ^{GW} and evaluate the expression containing all vertex corrections:

$$X(\omega) = \omega - E - \Sigma^{GW} - \left[\sum_{m=0}^{\infty} \frac{(-a)^m}{m!} \sum_{n=0}^{\infty} \frac{a^n}{n!} \frac{1}{\omega - E + n\omega_p} \right]^{-1}. \tag{5.60}$$

This term is in principle equivalent to the exact self-energy or, more precisely, contains all vertex corrections beyond GW. In symbols:

$$X = \Sigma - \Sigma^{GW}. \tag{5.61}$$

In fact one can find in the expression for X, respectively:

- the G_0^{-1} term, i.e. $\omega - E$;

- minus the GW self-energy $(-\Sigma^{GW})$; this term is there to avoid a "double counting" of the GW self-energy;

- the actual G^{-1} coming from the exponential solution; this expression contains all self-energy effects, i.e. quasiparticle corrections and satellites; it consists of the inversion of an infinite sum of terms.

The derivation in this section shows how the actual calculation of vertex corrections using this self-energy would imply a complicated calculation as the inversion of an infinite sum of terms. This is not a practical path. However, it is very instructive: it shows how complex the dynamical dependence of the self-energy can be, even for a simple case as this, where a plasmon-pole model is used for W and a non-interacting G is used. Moreover, the space dependence of all quantities has been completely neglected. This validates the kind of approach used to obtain the exponential expression for G with the direct solution of a differential equation that is shown in the first part of this chapter. In fact, if the space dependence of the quantities involved had been retained, the equivalent expression for X would have been much more complicated. The diagonal approach leads to a simpler expression that can help to understand the problem. Of course in an actual calculation for a real system one would not be allowed to apply it. Apparently then, trying to reverse-engineer the self-energy starting from a known full Green's function G can be a dead end, if done as shown above. The problem lies in the inversion of the full G, which gives a cumbersome term here and would be unfeasible if done numerically. Avoiding to use the self-energy might be an advantage in this case.

To summarize, the outcome of this section is that trying to calculate vertex corrections inverting a known G is not the way to go. In the next part I will show an alternative way to the vertex: I will use directly the definition of the vertex function to calculate it using the functional derivative of the Green's function. I will also propose a way to circumvent the problem of the inversion of G that will still hinder the calculation of the vertex Γ.

5.3.2   Direct calculation of the vertex

The vertex is an explicit functional of the interacting Green's function G for any value of φ. Therefore, once the explicit dependence of G on φ is known, one is able to calculate Γ using the definition. The vertex Γ is defined as

$$
\begin{aligned}
\Gamma(1,2;3) &= -\frac{\delta G^{-1}(1,2)}{\delta\varphi(3)} \\
&= \int d4d5 G^{-1}(1,4)\frac{\delta G(4,5)}{\delta\varphi(3)}G^{-1}(5,2)
\end{aligned}
\tag{5.62}
$$

where φ is the external perturbation potential. The second equivalence can be proved using the functional derivative of $G^{-1}G$ (the identity) with respect to φ, using Schwinger's chain rule technique [53]. In the following I will make clear why the latter formula for the vertex is more convenient than the former. From a very practical point of view, one would prefer not to calculate the functional derivative of the inverse, since the calculation of G^{-1} can already be a problem, as seen in the previous section. However, if one has an explicit expression for G depending on φ, the calculation of $\delta G/\delta\varphi$ is straightforward. The problem

of the calculation of G^{-1} can be worked out using algebra and approximations, as I will show in the following.

I will retain only the time dependence of the vertex and G, as done with all quantities in the previous section. One can define a useful quantity $\mathcal{D}$ as

$$\mathcal{D}(t_4 - t_3, t_5 - t_3) = \frac{\delta G(t_4, t_5)}{\delta \varphi(t_3)}. \tag{5.63}$$

The vertex can then be written, in frequency space, as

$$\Gamma(\omega, \omega') = G^{-1}(\omega'')\mathcal{D}(\omega, -\omega')G^{-1}(-\omega'). \tag{5.64}$$

It is possible to recover the *GW* approximation at this point, by imposing

$$\mathcal{D}(\omega, -\omega') = G(\omega'')G(-\omega'), \tag{5.65}$$

which implies $\Gamma(\omega, \omega') = 1$. To understand how this quantity can be convenient, one can analyze the structure of the self-energy. Using $\mathcal{D}$ instead of Γ one can write the exact self-energy as

$$\Sigma(\omega) = \frac{i}{2\pi} \int d\omega' e^{-i(\omega - \omega')\eta} W(\omega - \omega')\mathcal{D}(\omega', \omega)G^{-1}(\omega), \tag{5.66}$$

with $\eta \to 0$. One can write an expression for the full G using this self-energy. One can work out the self-energy using the Dyson equation and a little algebra

$$\begin{aligned}
\Sigma(\omega) &= G_0^{-1}(\omega) - G^{-1}(\omega) \\
&= G_0^{-1}(\omega)\left[G(\omega) - G_0(\omega)\right]G^{-1}(\omega)
\end{aligned} \tag{5.67}$$

and combining the two expressions obtain

$$G(\omega) = G_0(\omega)\left[1 + \frac{1}{2\pi}e^{-i\omega\delta} \int d\omega' e^{i\omega'\delta} W(\omega - \omega')\mathcal{D}(\omega', \omega)\right]. \tag{5.68}$$

The latter can actually be regarded as another way of writing the equation of motion for G. This writing is very convenient in that it does not contain G^{-1}. Thus, the problem of having the inverse of G is now solved. Interestingly, this happened because we effectively removed the intermediate step of the calculation of Σ, that was problematic in the previous section.

Now one only needs to calculate $\mathcal{D}$ to have the solution for G. Of course, if this was done explicitly with the exponential expression one would retrieve the same expression for G. Here instead we use that solution to derive an expression for $\mathcal{D}$ (and therefore Γ) as a function of G. Using the expression for G in (5.22) and deriving with respect to φ one can show that, in the time domain,

$$\mathcal{D}(\tau, \tau') = \theta(-\tau)\theta(\tau')G(\tau - \tau'), \tag{5.69}$$

which is true for any non-interacting Green's function one decides to use as a starting point (i.e. with or without quasiparticle energy shift). This is a very interesting feature of the diagonal solution for G as it is a very compact expression for the vertex. Referring to the exponential representation for G, one

can see that $\delta G/\delta\varphi$ contains in this form an infinite series of satellites, i.e. the contribution "beyond GW" to the self-energy. The Fourier transform of $\mathcal{D}$ is then

$$\mathcal{D}(\omega,\omega') = \int \frac{d\omega_1}{2\pi} \frac{G(\omega_1)}{(\omega - \omega_1 - i\eta)(\omega' + \omega_1 + i\eta)}. \tag{5.70}$$

This expression can then be inserted in (5.64) and (5.66) to obtain an explicit form for Σ and Γ as a function of G and W. The vertex function reads then

$$\Gamma(\omega,\omega') = G^{-1}(\omega) \int \frac{d\omega_1}{2\pi} \frac{G(\omega_1)G^{-1}(-\omega')}{(\omega - \omega_1 - i\eta)(\omega_1 - \omega' + i\eta)} \tag{5.71}$$

and the full self-energy reads

$$\Sigma(\omega) = \int \frac{d\omega_1}{2\pi} \frac{G(\omega_1)}{(\omega + \omega_1 + i\eta)} \int \frac{d\omega'}{2\pi} \frac{e^{i\omega'\eta}W(\omega - \omega')}{(\omega' - \omega_1 - i\eta)} G^{-1}(\omega). \tag{5.72}$$

These expressions include again inverse Green's functions G^{-1}. On the other hand, they already contain the effect of $\mathcal{D}$ in the analytic structure. In other words one can say that the self-energy in (5.72) contains vertex correction (by construction). At this point, the simplest thing one could do is to use non-interacting Green's function instead of the full G and then work out the pole structure. This derivations strongly suggests to try the latter, as it is in principle quite straightforward. Moreover, this part highlights the link between the vertex and the two-particle correlation function L, of which the quantity $\mathcal{D}$ is a contracted version. This is possibly a better quantity to work with, if one is interested in dynamics, but it is arguably more complicated.

5.4   Summary

In the first part of this chapter I have discussed the solution of an approximate equation of motion that can be solved exactly. The solution of this equation is a Green's function containing dynamical effects beyond GW, that is therefore included in this treatment. I have shown how the Green's function obtained with this method connects to previously used models Hamiltonians, coupling electron with bosons, notably plasmons. I have shown how this approach can be improved and connected to GW in order to use the latter as an improved quasiparticle starting point on top of which one adds dynamical effects. The spectral function calculated using this G displays a quasiparticle peak at the GW quasiparticle energy, and a series of satellite peaks that behave depending on the structure of the screening W. In the simplest case of a plasmon-pole model, the satellites peaks are stemming at multiples of the plasmon frequency and decaying as a Poisson distribution to infinite order.

This approach can be in principle used to derive vertex corrections as it includes effects beyond GW; in the second part of the chapter I have focused the discussion on vertex corrections. I have shown how one can calculate the effective self-energy corresponding to a known interacting G. The calculation of the vertex and Σ through the inversion of the Dyson equation reveals itself as a not trivial task, due to the required inversion of the full Green's function.

The last part of the chapter clearly illustrates the difficulty of modeling the vertex Γ in order to treat dynamical effects. In fact, a calculation of the vertex using the exponential G through the inversion of the Dyson equation leads to a complicated expression including the inversion of an infinite summation, which is the consequence of the term containing G^{-1}. This fact suggests rather to concentrate on modeling $\mathcal{D} = \delta G / \delta \varphi$, where the various contributions of satellites are simply summed, and hence to search for a self-energy of the form $\Sigma = iW\mathcal{D}G^{-1}$ instead of the traditional $\Sigma = iGW\Gamma$.

In the remaining chapters of this manuscript I will show how the exponential representation for G can be applied to calculate the spectral function of real materials (notably silicon, graphite and graphene) and how it can yield great physical insight to the interpretation of experimental spectra.

6 | Valence-band satellites in semiconductors

In this chapter I will discuss the spectral properties of semiconductors in valence-band XPS, using bulk silicon as a paradigmatic example. I will focus on the study of intrinsic satellite structures in the photoemission spectrum, using newly measured spectra from the TEMPO beamline at the SOLEIL synchrotron facility. The unprecedented energy range and high resolution of these data allow one to make a close comparison with theory that brings up a number of interesting conclusions. Comparing with previous works in literature, I will analyze the performance of the GW approximation in the calculation of the spectral function and discuss the so-called *plasmaron* excitation, that has been now debated for more than four decades. I will show that this is a spurious excitation produced by the G_0W_0 approximation that can be considered a total breakdown of the approximation. The analysis of the data allows one to elucidate the failure of GW in describing the satellites. I will then study the performance of the exponential representation for G in the way it is derived in Chapter 5 and compare its performance with GW. The exponential representation for G produces a spectral function that has an excellent agreement with experiment. The new photoemission data yield a deeper understanding of intrinsic satellites from plasmon excitations and give an excellent benchmark to evaluate the performance of theory. An additional effort is necessary to describe correctly secondary effects such as the background of secondary electrons, matrix element effects and dependence on the photon energy. Moreover, the inclusion of a correction for extrinsic and interference effects, as proposed in [21], gives an added value to the final result. I will show how all these elements can be included in the calculation and how they yield a better description and interpretation of the experimental data.

6.1 Photoemission spectrum of bulk silicon

The valence-band photoemission spectrum of bulk silicon has been first measured by Ley *et al.* in 1972 [101]. While it is one of the most studied materials of the history of solid-state physics because of its massive implication in integrated devices technology, silicon still has something to reveal. In fact the incoherent part of the PES spectrum, i.e. where satellites are found, has

been studied only once for the valence states [26]. In fact satellites were at first considered mainly as an effect of extrinsic losses, i.e. due to scattering of the outgoing photoelectron. However several authors have pointed out that, while the extrinsic losses certainly have a contribution, a non-negligible part of the spectrum has an intrinsic origin and can be studied and discerned in photoemission theory by different means [21, 25, 27]. The intrinsic origin of photemission satellites has been also confirmed by Fuggle *et al.* using Auger spectra [102]. Recently, Offi *et al.* performed a comparative study on the origin of intrinsic satellites in core-level spectra of silicon, using reflection electron energy-loss measurements to evaluate the relative amount of extrinsic losses in their photoemission spectra [23]. One of the outcomes of their study is that there is a consistent and measurable amount of intrinsic satellites while the extrinsic contribution appears to increase with increasing photon energies.

I have obtained valence band photoemission data at high photon energy (XPS) that constitute a reliable and well-resolved benchmark, thanks to a collaboration with M.G. Silly and F. Sirotti from the TEMPO beamline at SOLEIL who measured a clean sample of bulk silicon with a photon energy of 800 eV [2, 3]. Details on the experimental setup at TEMPO will be given in the next chapter. The advantage of measuring at this photon energy is that surface and interference effects are reduced with respect to energies normally used for band-structure measurements (10-100 eV) and satellites should be enhanced [21]. This happens because for higher kinetic energies the inelastic mean-free path of photoelectrons increases (See Figure 6.1), thus allowing electrons from holes deeper in the bulk to be able to escape and be detected. Therefore increasing the photon energy one increases the bulk/surface ratio in the signal, reducing surface effects. The experimental data (dots), already shown in Figure 1.1, are reported here in Figure 6.2. One can distinguish the quasiparticle peaks between the Fermi level at zero and the bottom valence at

Figure 6.1: Calculated Mean free-path of electron in bulk silicon in the 5–10000 eV kinetic-energy range. (Solid line) inelastic mean free path (IMFP, λ_i); (Dotted line) elastic mean free path (EMFP, λ_e); dashed line, transport mean free path (TrMFP, λ_{tr}). From [23].

–15 eV, followed by two prominent satellite structures, each at a mutual distance of about 17 eV, as well as a more weakly visible third satellite between –52 and –60 eV. These structures are obviously related to the 17 eV silicon bulk plasmon [101, 103].

The band structure of silicon is possibly the most calculated band structure in ab-initio methods and it is used as the prototype for semiconductors in several solid-state books, e.g. [104]. However these calculation rarely go beyond the independent-particle picture. There is a number of *GW* quasiparticle cal-

culations [59] that can give a correct description of the quasiparticle part of the spectrum. However, to obtain a complete information on the photoemission spectrum, satellites included, one has to calculate the spectral function. The *GW* spectral function of bulk silicon has been already calculated by several authors [26, 51, 105]. In all but one case, there was not a direct comparison with experiment; the authors just reported the spectrum to overestimate the position of plasmon satellites, which was reported as a known problem of *GW*: Kheifets *et al.* compared theoretical calculations with experiment for the first time and they found a serious discrepancy between the two [26]. However they were focused more on the QP part of the spectrum and they did not have enough energy resolution in the satellite region to draw definite conclusions. In fact, as I will discuss in a few lines, there is a serious problem in the incoherent part of the *GW* spectral function that produces a completely wrong peak in the spectrum.
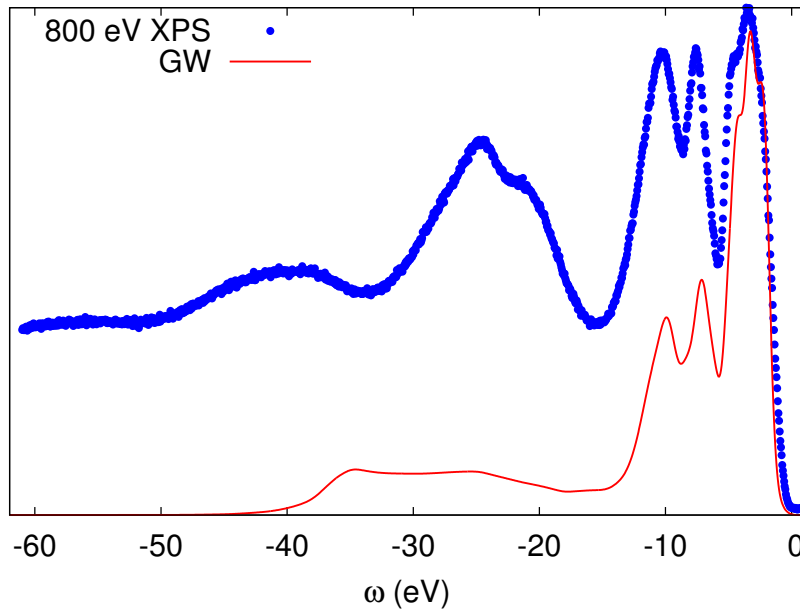
Figure 6.2: *GW* spectral function of bulk silicon (solid line) compared with XPS data at 800 eV photon energy. The Fermi energy is at 0 eV. The spectra are measured/calculated integrating over the full BZ. In the coherent part (0-15 eV) of the spectrum, the quasiparticle peaks of *GW* keep up with the experimental spectrum (neglecting the effect of the background). However the incoherent part — i.e. satellites — markedly differs: in *GW* there is a broad structure with a width of almost 30 eV, while the experiment displays a series of structures of about 10–15 eV FWHM, separated by ω_p=17 eV. While one-shot *GW* cannot give more than one satellite, this graph shows how the fictitious plasmaron peak dominates at −36 eV, destroying most of the (correct) plasmon peak at −25 eV.

6.2   The GW spectral function
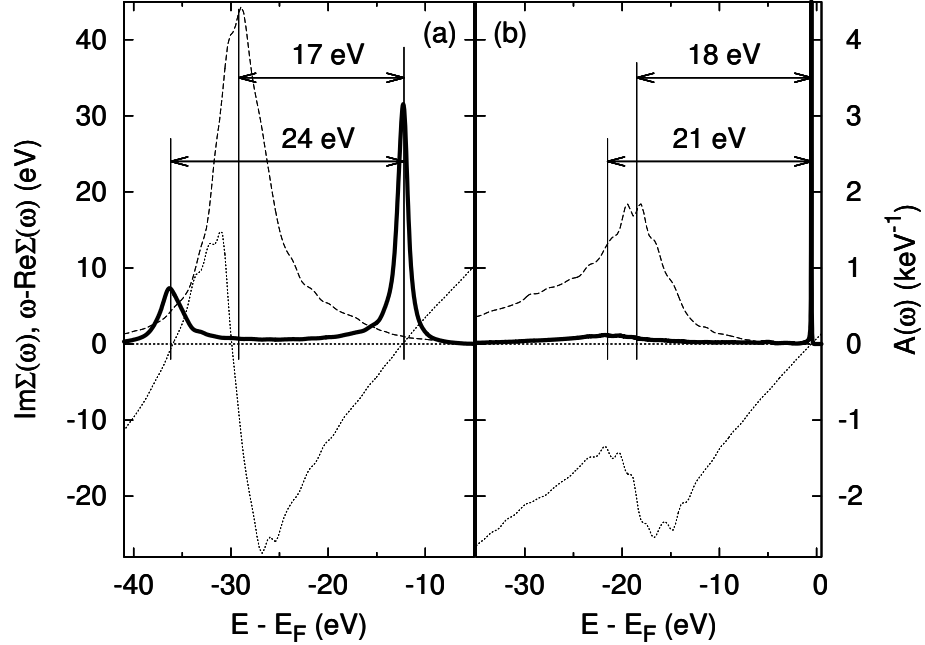

Figure 6.3: GW spectral function (solid line) of bulk silicon at the Γ point for (b) the top-valence band and (a) the bottom-valence band. The Fermi energy is at 0 eV. The real (dotted line) and imaginary (dashed line) parts of the corresponding self-energy are also shown. The arrows show, respectively, the position with respect to the QP peak of the maximum of the imaginary part and of the main satellite peak. The "ideal" picture is in panel (b), where the QP peak stems from a zero in the real-part term in the denominator of the spectral function; a plasmon satellite rises at a slightly overestimated energy (The experimental plasmon frequency being ≈ 17 eV) and it is the consequence of a structure in $\text{Im}\Sigma$, due to the main loss peak in $\text{Im}W$. In (a) the spectral function displays a main QP peak, more damped with respect to top-valence because of a larger value of $\text{Im}\Sigma(E^{QP})$, and a strong satellite peak at a much overestimated energy. This is in fact a *plasmaron* satellite, as it stems from a zero in $\omega - \epsilon_\text{H} - \text{Re}\Sigma(\omega)$.

While the capabilities of GW for the calculation of quasiparticle energies are well established, the ability to describe and predict incoherent spectral features like satellites has been studied for a few cases and the results vary from case to case. In general one knows — by the way one calculates the spectral function from a self-energy — how it should look with respect to the independent-particle case. The expression (3.60) for the spectral function as a function of the self-energy is repeated here for clarity:

$$A(\omega) = \frac{1}{\pi} \frac{|\text{Im}\Sigma(\omega)|}{[\omega - \epsilon_\text{H} - \text{Re}\Sigma(\omega)]^2 + \text{Im}\Sigma(\omega)^2}. \tag{6.1}$$

Analyzing the analytic structure, one can already predict what will be the gen-

eral behaviour of a curve obtained using this formula: the spectral function exibits a renormalized peak, centered on the real part of the quasiparticle energy and a width proportional to the imaginary part of $\Sigma(E_{QP})$; this is the coherent part and QP peaks rise at zeros in $\omega - \epsilon_H - \text{Re}\Sigma(\omega)$. The incoherent part should instead contain structures that are due to the imaginary part of the self-energy, therefore to the imaginary part of the screening W. When the term containin $\text{Re}\Sigma$ is comparable with $\text{Im}\Sigma$ and slowly varying, one can expect to observe peaks in the spectral function corresponding to structures in the imaginary part of Σ. I will now show how GW can deviate substantially from this picture and discuss the related implications.

In Figure 6.3 one can see the spectral function of silicon at the Γ point, along with real and imaginary parts of the self-energy, for (a) bottom- and (b) top-valence bands. This is a GW_0 calculation, i.e. it is the result of a self-consistent loop where the quasiparticle energies in the Green's function are updated while the screening W is kept fixed as calculated from step zero. This avoids any inconsistency in the energy scales of the input Green's functions with respect to the spectral function. The top-valence band — panel (b) — is a prototypical case that behaves as depicted at the beginning of the section: the QP peak stems from a zero in the real-part term in the denominator of the spectral function; a plasmon satellite rises at a slightly overestimated binding energy and it is the consequence of a structure in $\text{Im}\Sigma$, due to the main loss peak in $\text{Im}W$. The small shift is due to the fact that the real part is not constant in that range of energy. In fact, the experimental main peak of the loss spectrum of silicon is approximately 17 eV [101, 103]. In the bottom-valence case — panel (a) — the features are different: the spectral function displays a main QP peak, more damped with respect to top-valence because of a larger value of $\text{Im}\Sigma(E^{QP})$, which is somewhat expected, based on what is seen in the homogeneous electron gas and real systems [24, 25, 39]; differently with respect to top valence, here a sharp satellite peak appears at a much overestimated binding energy. This is not a plasmon satellite, as it stems from an additional zero in $\omega - \epsilon_H - \text{Re}\Sigma(\omega)$ — and not directly from a structure from the imaginary part — in much the same way as a quasiparticle peak. This structure has been observed in the GW spectral function of several models and real systems and discussed for the last four decades; it is called a *plasmaron*. There is a third zero in the real-part term — at about –30 eV — that could be assimilated to another plasmaron, but that does not give rise to any peak in the spectral function. This happens because the intensity of the imaginary part of the self-energy at that point is relatively high and it damps this other possible structure, which anyway would have a negligible lifetime. This zero is always present in the self-energy as soon as a plasmaron is there, because $\omega - \epsilon_H - \text{Re}\Sigma(\omega)$, after it has changed sign the first time to produce the plasmaron, it has to change sign again to be able to give rise to the QP peak, where it changes sign again. Since this singularity goes with the plasmaron, but its influence on the spectrum is none, I will just discuss the plasmaron, as it has been done in literature probably for the exact same reason. One can notice that between the plasmaron peak and the quasiparticle peak the spectral function is still non-zero. This can be regarded as the "'true" plasmon contribution to the satellite, as it is due

to the large peak in ImΣ and to ReΣ being comparably small. It is of course wiped out by the much stronger plasmaron. As noted by Fleszar and Hanke, it is striking how much the *GW* spectral function of silicon resembles to the one of the jellium: the two panels in Figure 6.3 could be assimilated, with the appropriate value of the Wigner radius, to the plots of $A(\omega)$ at (a) small and (b) large momentum k in the homogenous electron gas ([51] and references therein, [49]).

It is very important to note that the plasmaron is not a universal feature of *GW* and in several system it does not appear at all. Thus, there is no systematic way of knowing if a system will have this problem before actually calculating the self-energy. Nevertheless, *GW* satellites have been pointed out to be weak and to overestimate their distance with respect to the QP peaks. I will discuss in the next section whether these can be considered reasonable statements and how these findings connect to the plasmaron problem.

The one-shot *GW* spectral function of bulk silicon has been already calculated by several authors [26, 51, 105] and their findings confirm the existence of the plasmaron, but they do not always discuss it as such. The problem of the plasmaron has already been addressed — both for model and real systems — and several solutions have been proposed to eliminate it or, at least, improve the performance of the *GW* spectral function. In the next section I will overview the proposed solutions to the plasmaron problem and discuss how and when they can be appropriate or not.

6.3   The plasmaron: problems and solutions

Found for the first time by Hedin *et al.* in the *GW* spectrum of the homogeneous electron gas, the plasmaron was, in the span of five years, first brought up as a new many-body excitation and eventually ditched as a spurious product of the *GW* approximation [77, 106–108]. However, it has somewhat survived in a limbo for several decades and risen again in recent times. In the next section I try to trace an exhaustive chronological summary of its story, with all the literature involved. In fact it seems that several points made more than 40 years ago have been somewhat lost, therefore a recap of all the sources in a single place has become necessary. In this section I report and analyze the main points that determined the plasmaron to be recognized as a fake product of *GW*. Also, I discuss the different attempts of correcting the problem, notably with energy shifts or with the use of self-consistency.

After it was found in the homogeneous electron gas, the plasmaron was also found in the *GW* spectrum of core electrons [77, 106]. The spectra looked very much like the bottom valence of bulk silicon at the Γ point, and in fact — for the HEG — the plasmaron was found at momentum $k \approx 0$. The interpretation given by the authors was that this excitation was the result of the coupling between a hole and a bulk plasmon, that could bind under certain conditions. "Free" plasmon excitation could co-exist at different momenta and were quite well-separated, as they were located at the plasmon frequency ω_p, while the plasmaron was found at about 1.5–$2 \times \omega_p$. The homogeneous electron gas was the theoretical reference for metals and still today is considered the best model

for the so-called simple metals like Na and Al. For core levels, however, the reference model consisted of a model Hamiltonian where dispersionless electrons could couple to plasmons. This electron-boson (or *polaron*) model is considered the best model for core-level spectra including purely electronic excitations and has proven to be an almost exact representation of the physics of photoemission spectra in this case. It has proved its validity also for the description of electron-phonon coupling. D.C. Langreth, just a few months after the plasmaron was found in core-electron *GW* spectra, published the exact solution for the electron-boson model [75]. The difference with *GW* was striking: the exact solution displayed an infinite series of satellites at multiples of ω_p. A couple of years later, Blomberg and Bergersen published a study of the plasmaron, using a widely applicable model for the screening *W*, and proved that it was a spurious excitation created by the *GW* approximation that could be fixed using instead an expansion of the spectral function in terms of the Green's function, practically very close to the exponential representation for *G* derived in Chapter 5 [107, 108]. At that point it was clear that the plasmaron was not a physical feature of the photoemission spectrum of *GW*. However, there was a number of reasons because of which *GW* was still preferred over other approaches. On one hand, people were mostly interested in QP energies and the experimental information available on satellites was still very poor at the time; hence it remained merely a debate between theoreticians. Also, *GW* was really (and still is) the many-body tool with the best trade-off between accuracy and affordability and it is possibly the best tool to calculate QP energies. On the other hand, *GW* calculations on real materials would not have been done for another fifteen years after the discussion had taken place, as it was still too an expensive task for computers of that time; even then, another handful of years would have been necessary for someone to dare calculating the *GW* spectral function of a real material, as that was a much heavier task then just the calculation of QP energies. After that, people have found that the *GW* spectral function does not always display a plasmaron in the spectral function. There are several examples, especially in transition metals (e.g. Nickel [109]) and transition metal oxides (e.g. NiO, VO_2 [52]) that are free from the problem.[1] Also *sp* semiconductors can be without the plasmaron, as I will show in the next chapter with the example of graphite. There are however also simple metals that do suffer from the plasmaron problem, such as Na and Al [50, 110]. For these reasons, several authors focused on the spectral properties of *GW* and, knowing the built-in limitation of the approximation, tried to solve the problems and improve it. There have been two main solutions proposed to improve/correct the description of satellites in *GW*: the use of energy shifts and the use of self consistency.

Energy shift This issue has already been addressed in 3.3.7 and it has to do with a different alignment of the chemical potential that one can have in the

---

[1] These are more complex systems than *sp* semiconductors as here satellites can arise from other phenomena than plasmon excitations, namely hole-hole interaction as in the case of Nickel. This particular case, even in the absence of a plasmaron peak, hinders the ability of *GW* to fully describe the spectral properties [109].

non-interacting and the interacting Green's function. The problem is originated by the way GW is usually used to calculate the self-energy: a standard one-shot GW calculation would in general cause a shift in the Fermi energy, due to a shift of the topmost valence band.

This would result in using, in the calculation of the spectral function, a self-energy that is shifted by ΔE, with ΔE defined as the quasiparticle shift of the Fermi level. Hedin proposed to fix this problem imposing self-consistency at the Fermi energy, i.e. by effectively adding a ΔE shift in the self-energy used to calculate the spectral function [25, 38]. Another way of saying this is that the energy shift is already added to the energies of the non-interacting G. A GW_0 calculation is therefore immune from this problem. The general effect of the energy shift is that the QP peaks are enhanced (i.e. sharpened) while satellites are slightly damped. However, the amount of this effect depends strongly on the magnitude of the shift, which is, unfortunately, system-dependent. Some authors suggested that this energy shift could fix the plasmaron problem [105, 112]. While it is true that in silicon, looking at a single k point, one can see that the plasmaron tends to become weaker, my GW_0 calculations show how the problematic structure persists even with the shift applied. GW_0 calculations on the HEG have shown that the plasmaron peak appears to damp and to move a bit closer to the QP peak, but it does not disappear [46].[2] Now, the shift should be in general applied, as discussed by several authors, to avoid problems with too high values of ΔE that can destroy the spectrum [25, 112]. It is also true that, in principle, ΔE would be able to make the plasmaron disappear, as it acts as an effective downward shift of $\omega - \epsilon_H - \mathrm{Re}\Sigma(\omega)$. The
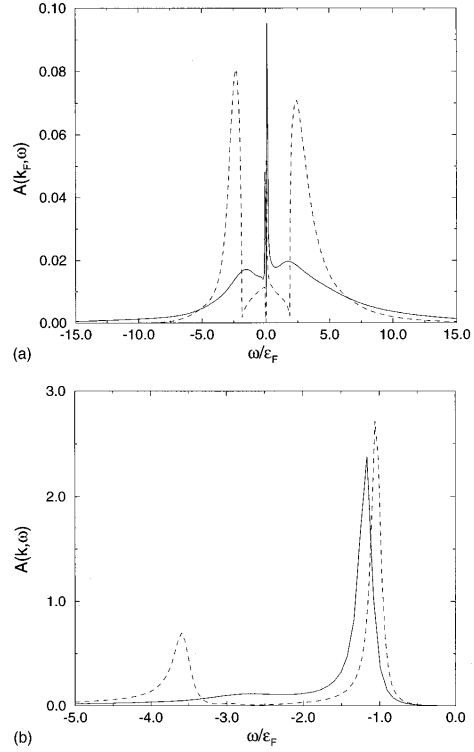

Figure 6.4: The spectral function $A(\mathbf{k}, \omega)$ from the full GW calculation in HEG (solid) is compared to the corresponding quantity from the partially self-consistent GW_0 calculation (dashed) [46]. In (a), the comparison is made at the Fermi surface, $|\mathbf{k}| = k_F$, and (b) shows the same comparison at the bottom of the band, $|\mathbf{k}| = 0$. In both cases the sharp overestimated satellite peaks become a broad plasmon satellite at the correct energy. Here $r_s = 4$, which is representative of bulk Na. From [111].

---

[2]In most publications e.g. on the HEG there is no mention of the plasmaron (even though it is there) and therefore the problem is not even discussed.

problem is that there is no guarantee that ΔE will be large enough to make it, as it varies from case to case. The claim by Pollehn *et al.* that the shift improves spectral features is certainly true for their special case of a Hubbard chain and in general for quasiparticle peaks, but it cannot be taken as a general way to improve satellite features (i.e. remove the plasmaron) [112]. On the other hand, the shift can indeed improve the shape of plasmon satellites, as in the case of VO_2. However, in that case there is no plasmaron to start with [52].

Self consistency The effects of self consistency on spectral features within the *GW* approximation have been discussed mainly for the model case of the homogeneous electron gas or for finite systems [113–115]. There exist no fully self-consistent *GW* calculations for a real solid, due to the numerical challenge that this would imply.[3] The self-consistency issue partly connects with the energy-shift issue, as including the shift in the calculation can be considered a poor man's way of applying self-consistent GW_0, although the latter is computationally more expensive. I have already discussed the effect of GW_0, where self-consistency lies only in the energies of the Green's function; I shall discuss here *GW*, where all the quantities are included in the loop and one actually solves the Dyson equation self-consistently. The only fully self-consistent *GW* result for extended systems was published for the HEG by Holm and von Barth [113], who had previously discussed also GW_0 [46]. Their results are summarized in Figure 6.4, where one can see the spectral function $A(\mathbf{k}, \omega)$ of GW_0 and *GW* compared. Holm and von Barth seem to dismiss the plasmaron issue as not relevant; in fact, while they acknowledge the work by Lundqvist on the HEG, they report $G_0 W_0$ as just overestimating the position of plasmon satellites and reckon that using the exponential representation for *G* (the cumulant expansion) is the way to go to fix the problem. In their full *GW* calculation, they observe that satellites are markedly damped with respect to GW_0, but also undergo a repositioning at the correct plasmon frequency. However, the authors consider that the weight of such satellites is too weak and that fully self-consistent *GW* actually *worsens* the spectral function! They therefore see this as a clear sign for the need of vertex corrections to *GW* that would "correct" the failure of fully self-consistent *GW*.

I argue here that, considering that (i) the plasmaron appears completely removed from the spectrum, (ii) the newly obtained satellites are at the correct position and (iii) they can thus be considered as "true" plasmon satellites, the fully self-consistent *GW* result is actually much better than any previous partial self-consistent attempt, at least considering just the incoherent part of the spectrum. The quasiparticle spectrum is anyway not very different from $G_0 W_0$ or GW_0. Holm and von Barth do not recognize this for the following reasons:

1. they consider as a reference for satellites the result by Holm and Aryasetiawan on the self-consistent cumulant expansion applied on the HEG, that gives much sharper satellite peaks than *GW*; however, that calculation is not self-consistent with respect to *W*, that is kept fixed at the RPA level. It is also not clear at what level plasmon lifetime effects are

---

[3]Approximated variant of fully self-consistent *GW* have been attempted, e.g. [116, 117]

included. If one takes e.g. the cumulant-expansion spectral function calculated for silicon at the Γ point in [26], the similarity with the full *GW* result of Holm and von Barth is striking as satellites are as broad as in the HEG case. The full frequency dependence of *W* is there taken into account. In fact, a small satellite weight should not *a priori* be a problem: extrinsic effects can improve substantially the intensity of satellites, that in the intrinsic case do not have to be very strong, as the results presented in this manuscript demonstrate.

2. They consider that the enlargement of the bandwith, seen in the full *GW* case, goes in the wrong direction with respect to partially self-consistent approaches. This conclusion is based on results extrapolated from bulk sodium, considered as the real-world equivalent to the electron gas. However, the electron gas remains a model, and the exact bandwith of a system is difficult to measure in photoemission, due to several effects such as the background of secondary electrons and satellite peaks. Thus, one can consider this justification for the failure of fully self-consistent *GW* doubtful, to say the least. Moreover, there is no exact solution for the quasiparticle spectrum of the homogeneous electron gas; this would be a necessary benchmark to draw definite conclusions about the performance of an approximation on the model.

3. They observe that self-consistency changes the properties of the screening *W*, which is no more a good response function, as it violates sum rules. This is a fair objection; at the same time it can be seen as an effect of the *GW* approximation, that could be corrected using vertex corrections. A direct link between this error and a "bad" spectral function is not obvious.

Fully self-consistent *GW* calculations remain today an almost unexplored path for real materials. For atoms and molecules, fully self-consistent GW produces accurate total energy differences, although *per se* the self-consistent total energies differ significantly from the exact values. Hence it can be said that self-consistent *GW* gives poor total energies for atoms and molecules. The ionization potentials obtained from self-consistent *GW* and calculated from the Extended Koopmans Theorem, are in very good agreement with experimental results. Moreover, the self-consistent ionization potentials are often better than the non-self-consistent G_0W_0 values [114]. Another general implementation is being developed, but it is not clear how satellites are described in finite systems [115]. There are no attempts yet for periodic systems. It is therefore quite hard to fully discuss the issue. Overall, the perspective offered by this paragraph suggests that the conclusions on the performance of self-consistent *GW* on HEG should be reconsidered for satellites. The results presented here and in the next chapter will bring up additional reasons to support this view.

Alternative solutions   The *GW* self-energy can be seen as the first-order term of an exact infinite expansion of Σ in terms of the screening *W*. While the calculation of additional terms of the self-energy have been already suggested, it

has almost never been explored, because of the much greater computational effort needed with respect to the first-order term [24, 38, 39]. Hedin showed that, expanding the self-energy to higher orders in W greatly corrects the plasmaron peak giving a spectral shape that approaches the exact one, with a satellite peak at $E_{\text{sat}} = \epsilon^{\text{QP}} - \omega_{\text{p}}$ [25, 118]. This test was performed on a model system; the actual feasibility of such endeavor for real systems is not clear as this approach has not been attempted yet. However, if the findings of Hedin were confirmed on real system, this would put a clear link between the first-order approximation of Σ and the presence of the plasmaron. Results by Ness *et al.* [119] on the HEG also suggest that higher-order terms in the self-energy can improve the shape of satellites in the spectral function.

6.4 The plasmaron: a historical view

In the late 1960s there has been a great improvement in the study of X-ray spectra of metals. A number of authors gave important contributions to the field and developed the theory, often surpassing what could be achieved in experiments by far. The first attempts were all based on model Hamiltonians or applied to model system such as the homogeneous electron gas, but the results of those years have important consequences still today. In many-body theory, people were focused on the calculation of the Green's function using e.g. the Dyson equation. In this case they were eventually looking at how to approximate the self-energy. A first-order perturbation expansion of the self-energy in the screened interaction was proposed by Lars Hedin [38]. That approximation has become widely known as the *GW* approximation. At that time people were mostly interested in quasiparticle properties, but models allowed authors to explore the features of the Green's function and of the spectral function $A(\omega)$, giving a deeper insight about the physics contained in the theoretical approaches.

6.4.1 The swedish electron gas

The performances of *GW* in the HEG were explored in 1967-1969 by Bengt I. Lundqvist, in a series of papers [47–49, 120] that was focused on the physics of the homogeneous electron gas, intended to model valence electrons in metals. There he discussed extensively the *GW* approximation and showed that the *GW* spectral function featured a sharp peak at the QP energy ϵ and a satellite structure, more damped, at energies lower than $\epsilon - \omega_{\text{p}}$, ω_{p} being the plasmon frequency of the system. This second structure had been announced — quite enthusiastically — in 1967 by Lars Hedin, Bengt I. Lundqvist and Stig Lundqvist (HLL hereafter) [106] and further discussed by Hedin for X-ray emission spectra [121] before the deeper analysis by B.I. Lundqvist in his HEG papers. They called it the *plasmaron* excitation, ascribing it to a bound state involving a quasiparticle and a plasmon and being logically located at a deeper energy than the bare plasmon frequency (which would imply a "free" plasmon is excited). A serious attempt to find the plasmaron was tried in 1968

by Cuthill *et al.* [122]. They measured the *L* edge of aluminum, but could not detect anything within their error bar.

B.I. Lundqvist continued to study the spectral properties of the *GW* approximation in another paper in 1969 [77] where he focused on the spectrum of core electrons using a model Hamiltonian. In this model the core electrons are coupled to a boson field representing plasmon excitations from valence electrons. He found that the results for core electrons did not differ much from what he had found before in the HEG for valence electrons and the *GW* spectral function was similar both in the quasiparticle and in the satellite region. The spectral function of the core electron displayed a plasmaron satellite, just the same way it was found in the electron gas. At that time there were no experimental data available that could disprove or confirm what HLL had found. HLL reviewed their results on the *GW* self-energy in 1970 [78]. By that time, they were less keen to stress the existence of the plasmaron, as there was no clue whether it was a physical feature of the spectrum or not, and they acknowledged the need for reliable experimental data. Also, the work done by D.C. Langreth to solve the polaron model [75] was calling for a more cautious view on the incoherent part of the spectral function. HLL acknowledged the work of Langreth and reckoned that the satellite shape of the *GW* spectral function was, however, a good estimate of the series of satellites found in the exact solution of the polaron model: the fact of having a single satellite peak was due to the first-order nature of *GW* — and to the way it was calculated, as a first-order perturbation — and thus considered as a built-in limitation of the approach.[4]

6.4.2   Exact solution vs *GW* for core electrons

D.C. Langreth, following the work of Nozières and De Dominicis in 1969 [76], studied the same electron-boson Hamiltonian used by B.I. Lundqvist to analyze the *GW* self-energy for the core-electron case. In 1970 Langreth calculated an exact solution for the Hamiltonian and showed that it yields substantially different results from *GW* in the satellite part [75]. The exact solution of the polaron Hamiltonian has an exponential form and the resulting spectral function contains a series of poles beside the quasiparticle peak. The series of satellites — each one appearing at exact multiples of ω_p — decays as a Poisson distribution. This model for core electron is faithful to the real situation and can be considered the best result available for the one-particle green's function including plasmons. In fact in literature it is often referred to as *the* exact solution for core electrons. A couple of years later, C. Blomberg and B. Bergersen [107] in one paper and again with F.W. Kus [108] in a second paper, discussed in great detail the plasmaron issue. They argued that the plasmaron is a spurious effect due to the *GW* approximation presenting a model with known exact results (similarly to what Langreth had found earlier). They showed that a direct expansion of the Green's function — including QP shifts — could solve the problem, removing the spurious excitation. In the end, they did not give a

---

[4]The results produced by HLL would be later become famous among colleagues as the "Swedish Electron Gas" also thanks to the book by Hedin and S. Lundqvist (Chapter VII) [39] that quickly became a reference in the field.

general mathematical proof of the unphysical character of the plasmaron, but they added a number of valid arguments — sensible also for a general case — supporting this idea. This, together with what Langreth had found and without any experimental evidence, was quite enough to be more than suspicious about the *plasmaron*.

6.4.3 Connection with experiment

It is important to understand that all these studies were purely theoretical and, for anything related to satellites, they were not backed by any experimental investigation. This was a natural consequence of early-stage experimental XPS techniques available and scarse interest in anything going beyond the QP part of the spectrum. There were issues with sample preparation (surface effects and contaminants) and effective resolution of the experimental setups that did not favor the study of satellites. In fact in many cases it would have been hard to detect satellite structures because of the low resolution available and the high levels of noise in the spectrometers. Satellite structures in photoelectron spectroscopy would be observed and studied in XPS spectra just a few years later (see e.g. [123, 124]). Notably, Baer and Busch observed in 1973 satellites replicas in core-level spectra of Al [123], citing the works of Lundqvist [77] and Langreth [75]. They reckoned that Langreth's exact solution to the electron-boson model would explain their result. A striking example of multiple plasmon satellites in core-level spectra of metals can be found in [125].

The problem of the description of satellites in core-electron spectra was later summarized in a review by F. Bechstedt [22, 79]. He reported the limitation of *GW* satellites and cited the exponential expression of Langreth as the solution to the problem.

6.4.4 The valence spectrum

While for core electrons the issue seemed to be eventually settled, for valence electrons the plasmaron problem of *GW* was never pointed out clearly; this happened partly because of the absence of *GW* calculation for real materials before the late 1980s and partly because of the low interest of the community — both theoretical and experimental — in photoemission satellites of valence electrons. So the plasmaron was thought more of an effective average of the correct solution than a total breakdown of *GW*, which is what it really is. Systematic experimental studies on series of valence-band satellites in metals were published in the late 1970s by Höchst and others [126, 127]. Even though initially they dismissed the satellite peaks as pure energy-loss peaks of the photoelectron, they later realised that the considerable weight of these structures could not be ascribed just to extrinsic losses. However, the intrinsic origin of satellites was never completely acknowledged by the experimental community. In 1980 Hedin proposed to use a modified polaron Hamiltonian and its exact exponential solution (very close to Langreth's) for valence-bands satellites [80]. It was not before the 1990s that *GW* calculations on real systems could be performed also including the calculation of the one-particle spectral func-

tion.[5] Hedin gave a further contribution in 1991, studying on a model system the effect of higher orders terms of the expansion in *W* of the self-energy — *GW* being the first-order term — and found that the satellite shape was closer to the exact solution than *GW* and could apparently make the plasmaron disappear [118]. The *GW* spectral function of silicon was analyzed in 1994 by Bechstedt and others [105]. They presented an extended study, also including the exponential expression for *G* through a so-called "satellite generator", of which *GW* would be the linearized version (see also [79]). This is similar to what was earlier proposed by Hedin [80] and Almbladh and Hedin [24]. Instead of using the exponential expression for *G* though, Bechstedt *et al.* pointed out that the inclusion of the QP shift in the non-interacting Green's function used to calculate the self-energy would allow them to avoid the plasmaron problem. While this is technically possible, it is not guaranteed that the QP shift removes the plasmaron in all cases, as the results of this thesis also demonstrate (see further discussion) [1]. In 1996, the exponential expression for *G* was used, using a *GW* starting point, to describe series of satellites in metals, giving a much better result than just *GW*; in fact, the latter was plagued by the plasmaron problem [50]. This way of deriving the exponential representation of *G* was called *ab-initio cumulant expansion* [81], in reference to an approach used in statistics with similar mathematical formulation. Strangely, the authors did not mention the plasmaron, not showing the details of the self-energy and dismissing *GW* as merely overestimating the plasmon satellite. However, the results by Cazzaniga [110] show how the *GW* spectral functions of Al and Na both display the characteristic plasmaron peak, just as HLL had found in the HEG in 1967 [47–49, 106]. Kheifets and others measured the spectral function of silicon in 2003 and compared it to *GW* and the cumulant expansion [26, 51]. Their data are not conclusive for the satellite part due to low energy resolution, but show clearly that the exponential solution for *G* is, for satellites, a great improvement with respect to *GW*. In fact the *GW* spectral function of silicon also suffers from the plasmaron. The spurious nature of the plasmaron in Si was confirmed by my work in 2011 and it is presented in this chapter [1]. New photomission data help to give a clearer picture of the physics of plasmon satellites in bulk silicon (see further discussion). At this point the plasmaron is officially a fake product of the *GW* approximation, due to the way the self-energy integrates the screened interaction *W*, i.e. simply to first order. This holds without a definite general mathematical proof, but with many examples in real systems and rigorous mathematical proofs in reliable model systems.

6.4.5   Rebirth in 2D systems

The plasmaron was "re-discovered" in 1992 by von Allmen [128]. He found that the *GW* spectral function of a 2D electron gas showed a satellite structure that was identical to the one found in the three-dimensional case by HLL. The author refers to HLL but he never uses the name "*GW*", speaking instead of *RPA* self-energy. As a consequence, the plasmaron has become since a possi-

---

[5]Until then *GW* calculations focused on *QP* energies as calculating the spectral function is a much heavier task [57].

ble many-body excitation in 2D systems and been the subject of a few articles. The possibility of it being a spurious peak produced by the *GW* approximation was not considered and apparently the long discussion that went on for the 3D case was not known in that scientific community. With all probability this happened because of the complete orthogonality between that community and the "traditional" (i.e. gravitating around Lars Hedin) *GW* community. Tediosi and others reported the detection of plasmarons in reflectivity measurements of Bismuth together with "normal" plasmon excitations [129]. No theoretical calculation supported these measurements. A plasmaron peak was found in the spectral function of doped graphene independently by two groups in 2008 [130, 131]. The authors studied a *GW* spectral function calculated for a 2D linear-dispersion model for doped graphene. This spectral function displays, not surprisingly, sharp plasmaron peaks close to the special point **K** of the Brillouin zone of graphene. An important paper came out in 2010, reporting of plasmaron satellites being measured in quasi-freestanding graphene [132]. The experiment was compared to the *GW* spectral function calculated for the 2D model of graphene, as in Polini *et al.* [130]. The main difference between the experiment and the model calculation is that in the experiment the QP peak seems to disappear for increasing momentum *k* and at that point the spectrum consists only of the plasmaron peak, while in the model spectral function the two structures exist always together. The paper has raised quite a debate as it would be the first observation of a plasmaron excitation in a real system confirmed by theory. Recent ab-initio results by Currey *et al.* have confirmed the presence of a plasmaron peak around the special point of graphene when one uses *GW* to calculate the spectral function [133]. These calculations also show that the plasmaron fades away as one goes away from the special point **K**. This is in clear contrast to what found by Bostwick *et al.* and promotes further debate. Also, the uncertainty on the experimental spectra does leave space for objections. Such spectra could be the result of an un-even graphene surface or local double-layer or stair effects. More simply put, the new structure could be an effect of a low-energy plasmon excitation present in the doped system, hence being a plasmon satellite. There is no reason to believe that in 2D systems the plasmaron would be a physical feature of the spectrum. This can be deduced by its mathematical nature as it was originally discussed by Blomberg and Bergersen in 1972 [107]; their arguments hold also in the two-dimensional case.

6.5 Exponential spectral function

I now present new results on the spectral function of silicon. I used the exponential representation for *G* as described in Chapter 5. I used (5.38) for each state in the BZ, using the self-energy to fit the parameters of the plasmon-pole model; I calculated the total spectral function $A(\omega)$ as a sum over occupied states in the BZ. A number of additional effects, such as the effect of photon cross section and the background of secondary electrons, have been included in the calculation to improve the interpretation of the spectra; they will be briefly discussed in the next paragraph. The results presented here on the photoemis-
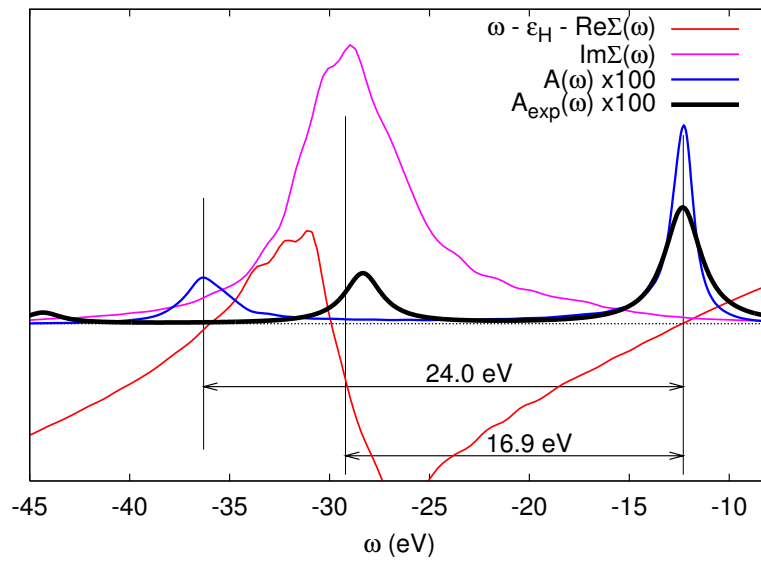
Figure 6.5: The intrinsic exponential spectral function of silicon (black line), calculated as in (5.38), is here compared with the GW spectral function (blue line) at the Γ point, bottom valence band. Real and imaginary part of the self-energy are reported here for clarity. The exponential solution for G displays a strong peak at the quasiparticle energy, slightly damped with respect to GW. The satellite shape of the spectral function is greatly improved with respect to GW: a peak of about the same intensity as the plasmaron peak appears at about 16.7 eV, which is exactly the plasmon frequency of silicon. A second weaker satellite appears at about −45 eV. The arrows indicate the distance of the center of mass of $\mathrm{Im}\Sigma$ and of the plasmaron peak with respect to the QP peak, respectively.

sion spectrum of bulk silicon have been published in [1, 134].

In Figure 6.5 the spectral functions calculated using the exponential representation for G and GW for silicon at the Γ point are compared. The exponential solution for G displays a strong peak at the quasiparticle energy, slightly damped with respect to GW. The satellite shape of the spectral function is greatly improved with respect to GW: a peak of about the same intensity as the plasmaron peak appears at about 16.7 eV from the QP energy, which is exactly the plasmon frequency of silicon. There are no lifetime effects due to plasmons, as this is a plasmon-pole model calculation.
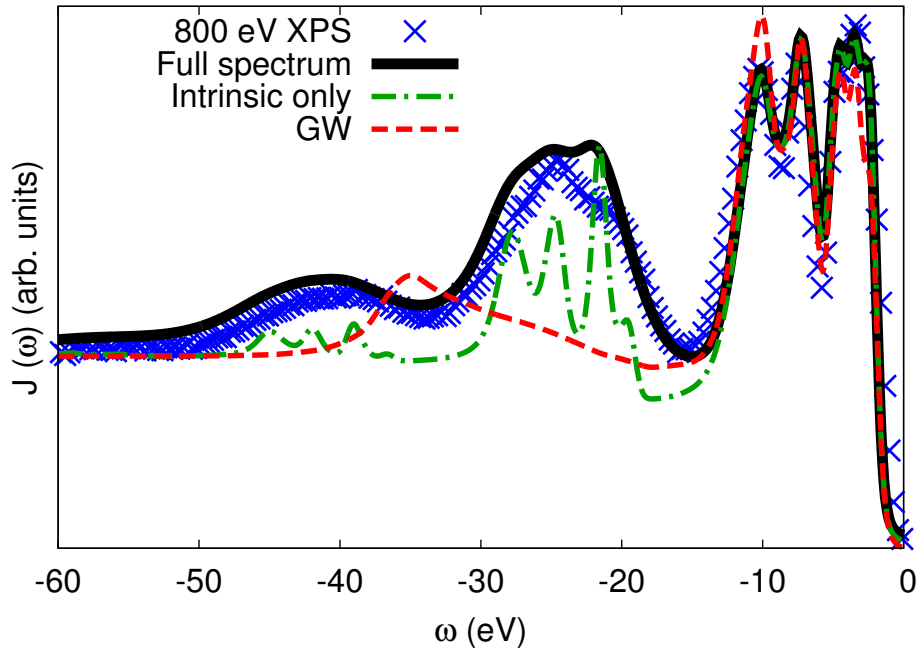

Figure 6.6: Experimental XPS spectrum of Si at 800 eV photon energy (blue crosses), compared to the theoretical intrinsic $A(\omega)$ calculated from G_0W_0 (red dashed), and from Eq. (5.38) (green dot-dashed). On top of the latter the black solid line also includes extrinsic and interference effects. All spectra contain photo-absorption cross sections, a calculated secondary electron background and 0.4 eV Gaussian broadening to account for finite k-point sampling and experimental resolution. The Fermi energy is set to 0 eV. This result has been published in [1].

The results for the total spectral function are summarized in Figure 6.6. The green dot-dashed line gives the result of the exponential expression for G together with the cross sections and the secondary electron background. The shapes of the QP peaks change little with respect to GW, but now the full series of satellites is present. The internal structure of the satellites which originate from the multiple valence bands, is also reproduced. This validates the decoupling approximation in the dense valence band region where, contrary to the case of an isolated core level, its success is *a priori* far from obvious. In fact, the major effect of recoil appears to be in the normalization of the quasiparti-

cle peaks, while satellites seem not to be very affected. Thus, the plasmaron problem appears to be completely solved by using the exponential representation of G. However, the intensity of the observed satellites is significantly underestimated. This discrepancy is similar to that found for the ab-initio cumulant expansion in simple metals, where extrinsic losses were suggested as a likely cause [50]. These might also be reduced by interference effects [21, 25]. To estimate the contribution of extrinsic losses and interference effects to the spectrum, I included a correction to the weights a in the spectral function, calculated in collaboration with J.J. Kas and J.J. Rehr. The total spectrum thus obtained (black line in Figure 6.6) is in unprecedented agreement with experiment. The change in the quasiparticle region is minimal, as the effect of the correction is only to reduce the overall intensity, transferring it to the incoherent part of the spectrum. The major change is in the satellite part: the intensity is increased and the lineshape is improved due to the inclusion of lifetimes. This final curve highlights the importance of extrinsic losses in the incoherent part of the photoemission spectrum, which are crucial as they give a substantial contribution to the intensity of plasmon satellites.

6.5.1   Correction for Extrinsic Losses and Interference Effects

Josh J. Kas and John J. Rehr, in the framework of a collaboration with our group, have calculated the extrinsic and interference contributions to the PES spectrum of bulk silicon based on the theoretical formalism of Hedin, Michiels, and Inglefield [21] and on my ab-initio results. The theory accounts for satellites in the PES spectrum in terms of a spectral function $A_{ik}(\omega)$ of exponential form. This allows one to connect this formalism to the exponential representation of the single-particle Green's function, to calculate corrections to the spectral function for extrinsic and interference effects.

In order to evaluate the relative weights of various contributions to the PES signal, one uses the Inglesfield fluctuation potential inside the solid (contributions outside being negligible).[6] One then calculates the weight of the extrinsic and interference $a^{extinf}(\nu_0)$ contributions to the PES due to plasmons of energy $\omega_p = 16.7$ eV, at a given photon energy $2\pi\nu_0$. These contributions are incorporated in the total spectral function correcting the intrinsic contribution of (5.38) with the addition of $a^{extinf}(\nu_0)$, i.e.

$$\bar{a}_i = a_i^{int} + a^{extinf}(\nu_0), \tag{6.2}$$

where i denotes the valence state, a_i^{int} is the intrinsic weight of the pole as it appears in (5.38). One can also calculate the width of the extrinsic+interference satellites and account for this by replacing the widths γ in the denominator of Eq. (5.38) with $\bar{\gamma}$:

$$\bar{\gamma} = \gamma + n\, w(\nu_0), \tag{6.3}$$

w being the width (directly proportional to the inverse lifetime) of the extrinsic plasmon at a given photon energy $2\pi\nu_0$ and n the number of plasmon excitations involved, i.e. the order of the expansion in Eq. (5.38). Values of $2\pi\nu_0$,

---

[6]Inglesfield fluctuation potentials are an alternative way to express the polarizable part of the screening W using density fluctuation potentials. See [21, 25] for a more detailed description.

a^{extinf} and w are listed in Table 6.1. The effect of the photon energy on photoemission spectra and their satellites are discussed in [134].

$2\pi\nu_0$(eV)	a^{extinf}	w
200	0.432	2.882
480	0.479	1.085
800	0.530	0.570
1200	0.568	0.341
2000	0.609	0.178
5000	0.669	0.066
10000	0.703	0.027

Table 6.1: Values of the correction term a^{extinf} including extrinsic losses and interference effects and relative width (inverse lifetime) w for a set of photon energies $2\pi\nu_0$. From [134].

6.5.2 Additional effects

I list here a number of processes that have an effect on the photoemission spectrum and cannot be systematically removed from the data. In fact, the only way to properly evaluate these effects is to calculate them using the electronic structure and the spectral function of the system, using the best estimate one can afford.

Lifetime of Intrinsic Plasmons

One must include a correction for the finite lifetime of intrinsic plasmons, which is infinite in (5.38) because of the plasmon-pole model used to calculate the intrinsic spectrum. Therefore, an additional width of 1.5 eV, taken from ab-initio calculations [135], is effectively added to the width of extrinsic plasmons w.

Photon Cross Sections

Matrix elements due to photon cross sections effects are calculated using theoretical values taken from tables in [83, 84]. For each element, the tables give the relative photon cross section of the atomic orbitals, calculated within the Hartree-Fock approximation. One then has to use the atomic data for bulk silicon; since it is a solid, the atomic character can be considered as mixed. The four valence bands of silicon contain two s electrons and two p electrons. The character of each band is calculated by projecting the wavefunctions onto spherical harmonics inside a sphere centered on the Si ion. The s and p character of each band sum up to one. One has then the following values:

Band	#1	#2	#3	#4
s-type	0.95	0.75	0.25	0.05
p-type	0.05	0.25	0.75	0.95

In this description, the relative weight of a photoemission peak will be the consequence of the s_k and/or p_k character of the corresponding state k. To include this effect in the spectral function, one can define an auxiliary $\tilde{A}$ so that

$$\tilde{A}(\omega) = \sum_k (s_k \sigma_s + p_k \sigma_p) A_k(\omega), \qquad (6.4)$$

where A_k is the spectral function of a single state k and σ_s and σ_p are the photon cross sections for s and p electrons, tabulated in [83, 84] and shown in Figure 6.7 up to 1500 eV. The inclusion of cross-section effects is very important to reproduce the relative weight of s and p peaks in the photoemission spectrum (which can differ by an order of magnitude) and the respective changes at different photon energies.
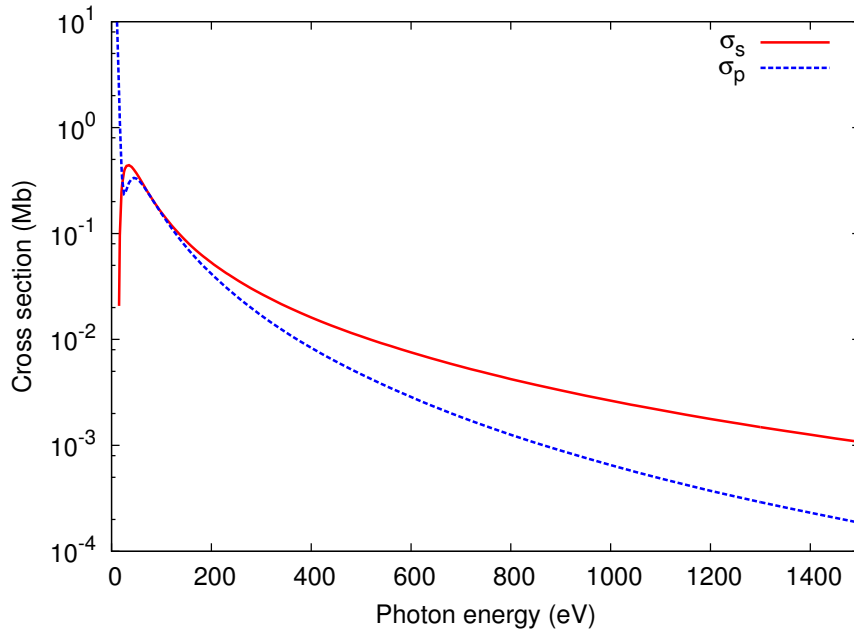

Figure 6.7: Photon cross sections, from [83]. Red solid line shows the values for the $3s$ electrons, while the blue dashed line shows the $3p$ electrons cross sections as a function of the photon energy.

Secondary Electrons

Photoelectrons can undergo a number of scattering processes beside the main plasmon losses — e.g. with lattice vibrations — before being detected. This produces a characteristic shape of the background that goes approximately as $\sqrt{\mu - \omega}$. The background of secondary electrons is calculated using the intrinsic spectral function $\tilde{A}(\omega)$, assuming that each peak in the intrinsic spectrum produces a constant flux of secondary electrons (i.e. a step function) at all binding energies greater than the quasiparticle energy ϵ. This means that one assumes that every hole excitation produces an equal number of random scattering processes. This way of calculating the background is due to D.C. Shirley

[101, 136]. The calculation of the background is achieved by the following integration of $\tilde{A}(\omega)$:

$$\mathcal{B}(\omega) = \int_\omega^\mu d\omega' \tilde{A}(\omega'), \tag{6.5}$$

where $\mathcal{B}$ is the background of secondary electrons and μ is the chemical potential. The final quantity that has to be compared with experimental data is given by the photocurrent $J(\omega)$ defined as:

$$J(\omega) = \alpha \tilde{A}(\omega) + \beta \mathcal{B}(\omega), \tag{6.6}$$

where α and β are two parameters that must be fixed to match the signal/background ratio in the experimental data. β is to be determined using the high binding-energy limit (where $\tilde{A}(\omega) \sim 0$) and then α is fixed so as to match the QP peak intensity. This formulation shows how the background cannot in principle be subtracted from the experiment without a prior knowledge of the pure signal underneath. However, many authors have used this technique to remove the background from experimental data, approximating $\tilde{A}$ in (6.5) with J. This allows one to close Equation (6.6), but it is not correct. It can however approximately work for the QP part of the spectrum — as long as one assumes no dependence of extrinsic losses on the binding energy — but it cannot work if one wants to analyze the incoherent part. Instead, the calculated background could be — legitimately — subtracted from the experimental curves using the correct formula, in case one wanted to evaluate certain quantities such as the intensity of satellites. This approach has been used in [134], where all the additional effects reported here are discussed so as to single out and analyze the incoherent part of the photoemission spectrum in bulk silicon.

6.6 Computational details

The Brillouin zone (BZ) was sampled using a $4 \times 4 \times 4$ Monkhorst-Pack grid centered at the Γ point, obtaining 256 points in the full BZ [137]. I have used Troullier-Martins norm-conserving pseudopotentials [138]. The plane-wave cutoff for the LDA ground-state calculation was fixed at 8 Ha. I used the `abinit` code for all ground-state and *GW* calculations [63], using the experimental values for lattice constants. The full frequency dependence of the self-energy for the 4 valence bands was calculated using a contour-deformation technique, applying partial self consistency on the quasiparticle energies in the Green's function (GW_0 calculations). W was calculated including 25 bands and using 169 plane waves for the wavefunctions (6 Ha cutoff). The dielectric matrix was calculated using 169 **G** vectors (6 Ha cutoff), 10 frequencies on the imaginary axis and 50 frequencies on the real axis, with a maximum value fixed at 2 Ha. The self-energy was calculated using 100 bands, 169 plane waves for the wavefunctions and 169 **G** vectors (6 Ha cutoff). It was calculated for 100 frequencies/Ha for a range of 90 eV below the Fermi energy.

6.7   Summary

In this chapter I have discussed the spectral properties of valence-band XPS spectra is silicon, used as a paradigmatic example for semiconductors. Comparing with previous works in literature, I have analyzed the performance of the *GW* approximation for the calculation of the spectral function and discussed the so-called *plasmaron* excitation, that has been now debated for more than four decades. This is a spurious excitation produced by the *GW* approximation that, when it appears, can be considered a total breakdown of the approximation. I have discussed the possible ways of correcting the plasmaron problem, using the available literature. I have traced a history of how the plasmaron was discovered and discussed more than forty years ago and of how it has been rediscovered in two-dimensional systems, more than twenty years later and again recently. I have shown how the exponential representation for *G* is an excellent way to overcome the plasmaron problem in *GW* and brings a much better description of the spectra, including full series of satellites. I have pointed out a number of simple but necessary corrections needed to have a sensible comparison with experiment. The use of new experimental data and additional inclusion of corrections for extrinsic losses and interference effects yield a striking agreement with experiment.

7 | Satellites in layered materials: theory and experiment

The exponential representation has given a great performance in the case of bulk silicon, as seen in the previous chapter, validating the decoupling approximation used to derive G in the case of a bulk system. In this chapter I will study bulk graphite as a prototypical example for layered materials, in order to evaluate the performance and adaptability of the method in a more complex (anisotropic) system as such. As for silicon, fresh photoemission data were required to explore the valence-band satellites, that were quite ignored in the past. I have personally taken care of the photoemission measurements at the TEMPO beamline in the SOLEIL synchrotron facility, in collaboration with the local group of experimentalists. Satellite structures in graphite are markedly different than in silicon. I will show what is the performance of the GW approximation in this case and discuss how the exponential G performs, including a complete treatment of the full frequency dependence of W. I take full account of symmetry effects due to the experimental geometry. The outcome of this work is going to be published in [139].

I will discuss a brief outlook on the study of graphene grown on top of bulk 4H-SiC and present preliminary results. Major challenges in this study are related to the ability to single out graphene from the substrate. The role of the inverse dielectric function appears crucial also in this case.

7.1 Previous studies

There is a significant number of studies on the photoemission spectrum of bulk graphite. Valence bands have been studied repeatedly, even though the spectra are mostly low-energy (Ultra-violet) ARPES. Available ab-initio many-body calculations are limited to quasiparticle energies and lifetimes [140], while there is only one calculation of a GW spectral function based on the LMTO formalism, that I shall discuss shortly. McFeely *et al.* have studied by means of XPS different allotropes of carbon, namely diamond, glassy carbon and graphite [141]. They study the valence-band spectrum, without including satellite structures. Interestingly, they also measure the $1s$ core-level spectra and analyze the

satellite structures down to ≈ -60 eV from the quasiparticle peak. They attribute a purely extrinsic character to these features and use them as a mean to evaluate the energy-loss spectra in the different carbon-based systems. These feature have surely an intrinsic contribution and the discussion of the authors is useful to understand better the results of this chapter. Vos *et al.* have studied the valence band of graphite by means of momentum spectroscopy, which gives a spectrum equivalent to direct photoemission [142]. Their measurements actually included satellite structures and they compared the data with results obtained by means of *GW* and ab-initio cumulant expansion. They claim not to have found any intrinsic contribution to satellites, however their data have a quite low energy resolution (about 2 eV) and they have undergone some heavy treatment (read: removal of the background) before being compared to theory. As I have already discussed in the previous chapter, removing the experimental background is correct only when one has the exact knowledge of the signal lying underneath, hence it is not in general correct and can be very wrong if one is to study satellite structures. The data by Vos *et al.* are therefore not reliable to give a solid conclusion on satellites. The original data are published in [143]. In this paper, the authors show the raw data and explain the background-removal procedure as a justified deconvolution with energy-loss data. The raw data of graphite show, in the range between 0 and 60 eV below the Fermi energy, prominent satellite structures, that are then removed with the aforementioned procedure. In the end, the low energy resolution of the experiment does not allow one to give any conclusion on the nature of satellites in graphite.

The lack of other experimental data have pushed me to try and obtain the photoemission data, applying for beamtime at the TEMPO beamline in the Soleil synchrotron facility. This way I have obtained high-resolution data for a wide range of energy. These data are essential to perform a reliable comparative study of graphite and verify the conclusions by Vos *et al.*.

7.2 Measurements at TEMPO

I could benefit from a week-long shift of measurements at TEMPO in July 2011, during which I had the opportunity to perform experimental measurements on graphite. While TEMPO is mainly focused on time-dependent photoemission measurements, it can cover a fairly wide range of photon energies with a high flux of photons, getting in its upper bound to the low end of hard *x* rays (about 1500 eV). It is therefore an optimal station where to study satellites, with a sufficiently high photon energy. At the same time, it is flexible enough to allow one for changes in photon energy, light polarization and geometry of the setup, that are useful to fully characterize the sample and to study satellites in different configurations. In Figure 7.1 I reported the photon flux characteristics as a function of the photon energy, for the two ondulators of TEMPO, HU44 and HU80. One can see here how 800 eV is an optimal value for the photon energy, because one gets the highest photon flux in the upper range of photon energies.
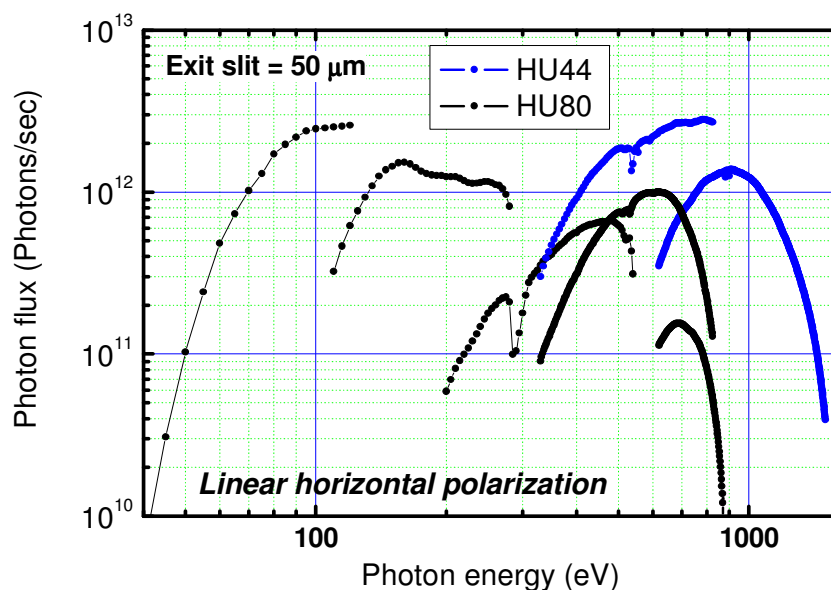
Figure 7.1: Photon flux characteristics as a function of the photon energy, for the two ondulators of TEMPO, HU44 and HU80. One can see here how at 800 eV there is a "sweet spot", in that one gets the highest photon flux at a comparably high photon energy. Courtesy of F. Sirotti.

7.2.1 The TEMPO beamline

TEMPO is a soft x-rays beamline attached onto an insertion device source of the Soleil synchrotron facility, adapted to the dynamic studies of the electronic and magnetic properties of materials. The project gathers various spectroscopic studies around its specificity, i.e. taking into account the temporal variable. This regards more specifically:

- the determination of the kinetics of chemical reactions at interface and surface by rapid photo-emission in the millisecond range. The high flux coupled to the high energy resolution of the electron energy analyser and of the beamline will allow the user to study the evolution of the chemical environment (surface coordination, chemical bonding with different elements) of selected chemical atoms at the surface using spectroscopic signatures in the electronic states. Physisorption kinetics, chemisorption or dissociation of molecules on a substrate, interface formation and inter-diffusion. The understanding of these processes is the key point to build new magnetic materials or to control chemical reactivity and catalytic properties.

- the dynamics of magnetisation reversal in nanostructures, using the temporal characteristics of Soleil at the scale of dozens of picoseconds , a problem of major significance for the magnetic storage of information at ultra-high density. These experiments will be performed using dif-

ferent techniques with different probing depths: X-ray magnetic circular dichroism, Magnetic dichroism in photoemission.

- carrying out pump-probe experiments with two photons (laser+synchrotron radiation) for the study of excited states using synchrotron impulses in the temporal range of a picosecond.

As one can see in Figure 7.2, the TEMPO beamline covers the photon energy range between 50 eV and 1500 eV. This energy range is particularly well suited for magnetic materials studies and for chemistry applications. On one hand, ultra-violet (valence-band) photoemission is feasible at $h\nu$=50 eV. On the other hand, the whole range of K edges (C, O, N, F $1s$) of organic molecules, the 4th period L ($2p$) edges of transition metals (with applications to metal-organic molecules and metal surfaces), and M edges of rare earths are covered [2, 13].

7.2.2   Experimental setup

The sample consists of a crystal of highly-oriented pyrolytic graphite (HOPG), that is one of the purest and most ordered versions of graphite, with a low percentage of imperfections. The advantage of graphite is that it is very poorly chemically reactive (i.e. it does not get contaminants on the surface very easily) and it can be therefore effectively cleaned in air by *cleavage*, i.e. mechanically removing a few layers on the top of the sample, usually using adhesive tape. This can be done thanks to its layered structure: the in-layer bonding forces are much stronger than the Van Der Waals forces between layers, that can be peeled away quite easily. In practice it is enough to peel away bits of layers a few times, until a new clean layer is completely uncovered. Then the sample must be readily put under vacuum to perform the measurements.

Angular-resolved valence photoemission (ARPES) measurements were performed at the UHV photoemission experimental station of the TEMPO beam line at the SOLEIL synchrotron radiation source. Linearly polarized photons from the Apple II type Insertion Device (HU44) were selected in energy using a high resolution plane grating monochromator with a resolving power $E/\Delta E$=5000. The end-station chamber (base pressure 10^{-10} mbar) is equipped with a modified SCIENTA-200 electron analyzer with a delay-line 2D detector which optimizes the detection linearity and signal/background ratio [2, 13]. The overall energy resolution was better than 200 meV. The photon beam impinges on the sample at an angle of 43°, and photoelectrons were detected around the sample surface normal with an angular acceptance of ±6°. At 800 eV kinetic energy the Brillouin zone is observed with an emission angle slightly smaller than 5°. The measured photoemission map is integrated over the spectral intensity originated approximately by one Brillouin zone. The Fermi level was obtained by measuring a clean Au(111) surface.

7.3   Experimental and theoretical spectrum

The experimental XPS data for graphite are summarized (red crosses) in Figure 7.3. The Fermi energy is at 0 eV and the measurements were performed at a
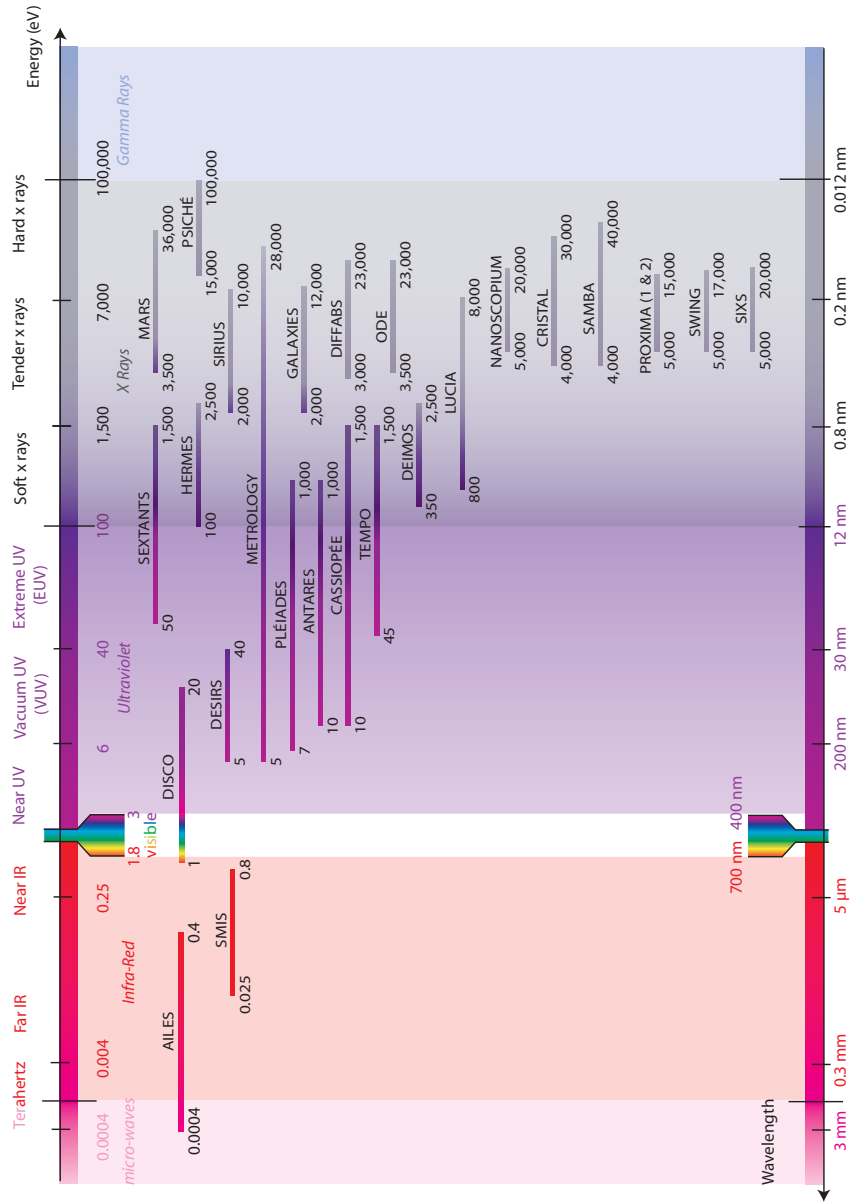
Figure 7.2: This scheme shows the photon energy range covered by the beamlines installed at the SOLEIL synchrotron facility [17]. The TEMPO beamline stands in the UV–Soft X-rays range.

photon energy of 800 eV over a range of 100 eV. There is a main structure be-
tween 0 and –30 eV that, comparing with previous literature, can be identified
as spectral weight due to the quasiparticle peaks of the valence bands [141].
There is then a visible second structure, between –30 and –65 eV. The distance
between QP peaks and this structure is around 30 eV. A third weak structure
is found between –65 and –100 eV. These two are, by definition, satellite peaks
and they appear to be part of a decaying series, just like it is observed in bulk
silicon. However, these features are broader and only two are clearly visible.
Theory will now help to analyze the origin of these structures and to elucidate
the differences between graphite and silicon.

A Kohn-Sham LDA calculation allows one to assign the main QP peak at
–20 eV to s-type bands and the smaller peak (about –10 eV) to p-type orbitals.
This is fully taken into account in the calculation of matrix elements, as de-
scribed in the previous chapter. The experimental spectrum can readily be
compared to the spectral function calculated in the GW_0 approximation (pur-
ple dot-dashed). This is a partially self-consistent calculation, where one up-
dates the energies in the Green's function and keeps fixed W at the LDA level.
Therefore there is no problem with the energy shift of the chemical potential.
One can see that the quasiparticle part of the spectrum is well reproduced.
The presence of a fairly smooth slope in the experimental spectrum instead of
a sharp p peak as in the theoretical curve is probably due to the presence of
different orientation domains in the HOPG sample, while the calculation sim-
ulates a perfect single crystal. This seems to be confirmed by other measure-
ments and calculations [141, 144, 145]. This discrepancy could also be an effect
of differences in the integration on the BZ between theory and experiment.

The incoherent part of the spectrum is less trivial to understand than the
case of silicon: in GW it shows a complex shape formed by two main broad
features. The first peak is at about –30 eV and could be identified with a
tail in the experimental spectrum at that energy. This tail is not described by
independent-particle calculations and has been dismissed as an "artificial tail-
ing" produced by experimental background [141]. The second structure visible
in GW is also very broad and corresponds approximately to the first large satel-
lite structure in experiment. The GW spectral function goes to zero at lower
energies. The weight of the large satellite is largely underestimated; while this
is not surprising — as GW has shown to underestimate plasmon satellites such
as these [52] — it is important to notice that here there are no plasmarons in the
spectral function. Also, GW is used only to calculate the intrinsic spectral func-
tion, whereas a full account of extrinsic losses could add the missing weight,
as seen in Chapter 6 for bulk silicon. As the spectral function is here free from
spurious peaks, GW should, in this case, give an approximate good description
of the first satellite.

As in the case of silicon, one can apply (5.38) to calculate the spectral func-
tion using the exponential representation of G and a plasmon-pole model for
W, starting from a GW calculation. This spectral function is plotted in Figure
7.3 (blue dotted) and it gives additional understanding of the spectrum. The
quasiparticle peaks are almost identical to GW. The first visible difference is in
the shoulder at –30 eV. The plasmon-pole G does not show any spectral weight

here and it goes rapidly to 0, just before the onset of the first satellite peak. The first satellite peak appears in good agreement with the first structure in experiment, considered that no plasmon lifetime effects are included in this calculation. There is a second smaller peak in the spectral function that could correspond to the second broad feature in experiment. The curve has overall good agreement in that it reproduces the main series of satellites and goes beyond *GW*, but it remains otherwise an incomplete description of the satellite spectrum. Moreover, in the region close to the quasiparticle peaks, *GW* appears to give a better description of the spectrum, even though it is unable to reproduce satellite series. The analysis of these curves already gives an idea of the complex structure of satellites in graphite. To completely elucidate the role of *W* in this, it is necessary to include the full frequency dependence of *W* in the spectral function of the exponential *G*.
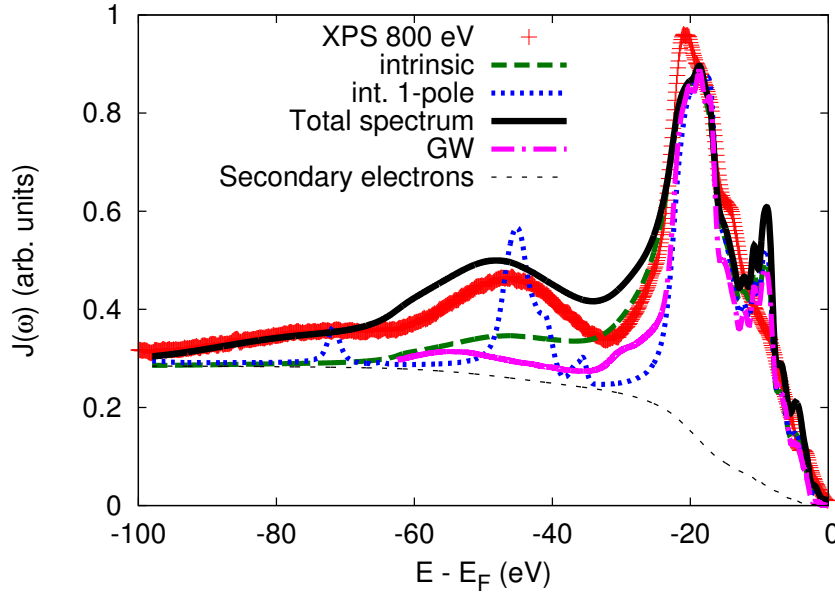

Figure 7.3: XPS spectrum of HOPG graphite at 800 eV photon energy. The data collected at normal emission (red crosses) are compared to the spectral function $A(\omega)$ calculated using several approximations: GW_0 (purple dot-dashed), plasmon-pole model for W as in (5.38) (blue dotted) and generalized model as in (5.44) (green dashed). On top of the latter the black solid line also includes extrinsic and interference effects. The calculated background of secondary electrons (black thin dashed) is also shown. All curves are scaled to match the intensity of the s QP peak at -20 eV. All spectra contain photoabsorption cross sections, a calculated secondary electron background and 0.4 eV Gaussian broadening to account for finite k-point sampling and experimental resolution. This result will be published in [139].

7.4   A full frequency-dependent W

I have shown, in the previous chapter, how the structure of photoemission satellites in silicon is due to the main plasmon loss at 16.7 eV, that can be measured in EELS experiments. It is now important to remember that, as already discussed in Chapter 5, $\mathrm{Im}[\Sigma^{GW}] \propto \mathrm{Im}[W]$, which is proportional to $\mathrm{Im}[\varepsilon^{-1}]$. The structure of $W = \varepsilon^{-1}v$ enters in the exponential expression for G and determines how satellites appear in the spectral function. However, the precise behaviour of satellites as a function of the screening is far from obvious. In the case of silicon, the EELS spectrum has one main sharp peak at 16.7 eV [23] and this justifies the use of a plasmon-pole model for W. This is also the reason why plasmon satellites are so strong in silicon. In graphite though, the inverse dielectric function has a more complex shape, due to the anisotropic geometry of the system [146–148]. In Figure 7.4 one can see the imaginary part of the inverse dielectric function $\varepsilon^{-1}(\mathbf{q}, \omega)$ of graphite, calculated at $|\mathbf{q}| = 0$ with the *dp* code.[1] The spectrum is in agreement with measurements and previous calculations [147, 149]. The main peak is centered around 28 eV and it is due to long-range bulk contributions; it is called $\sigma + \pi$ plasmon, as it is originated by the collective excitation of the valence bands.[2] The peculiarity of the EELS spectrum of graphite lies in the smaller sharp peak at about 7 eV. This peak is mostly due to in-layer transitions involving the π bands; it is therefore called a π plasmon. It becomes clear now that a single plasmon-pole model is systematically going to miss the complex structure of the screening in graphite.

While the numerical implementation of GW_0 — used here for all systems under study — takes full account of the energy dependence of W, one has to go beyond the simple plasmon-pole model to include the full W in the exponential representation.[3] This can be done as described in 5.2.4, where one generalizes the treatment to a W that is written on a basis of N_p poles. For a sufficiently high number of poles, the approach is exact. At the same time, it allows one to keep an analytic treatment, avoiding to switch to a numerical implementation of the problem. The many-pole model used here for W is very general and it is equivalent to the one used by J.J. Kas *et al.* for the inverse dielectric function [100].

Using the full frequency dependence of W one can calculate the exponential G in the same way it is done for the plasmon-pole model. The corresponding spectral function is shown in Figure 7.3 (green dashed). The quasiparticle peaks show a little difference with respect to the other approaches. Instead, the satellite peaks show now remarkable differences with respect to the plasmon-pole calculation: the tail at –30 eV is present and follows closely the slope of the experimental data; between –30 and –65 eV the spectral function displays a broad structure that closely matches in width the first satellite peak in ex-

---

[1] http://www.dp-code.org

[2] In a tight-binding model, the valence bands of graphite can be divided in σ bands, formed by the hybridized sp^2 electrons, and π bands, formed by the p_z electrons. See e.g. [150]

[3] The ABINIT code implements a contour deformation technique for the calculation of the full frequency-dependence of the GW self-energy on the real axis. This includes the calculation of W on a range of frequencies without a plasmon-pole model [57, 63].
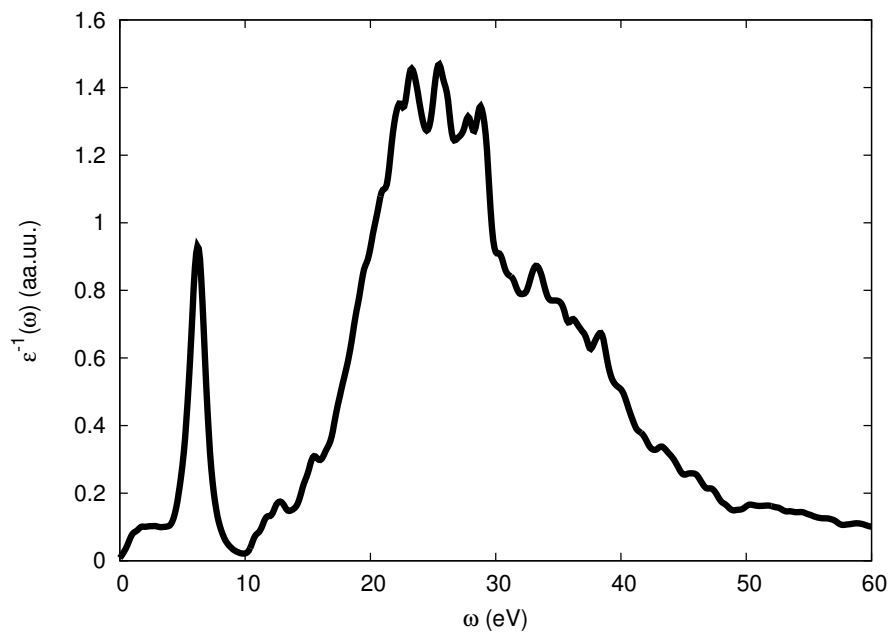
Figure 7.4: Inverse dielectric function of bulk graphite at $|\mathbf{q}| = 0$. The main $\sigma + \pi$ plasmon is centered around 28 eV. The smaller π plasmon is located at about 7 eV. A Gaussian broadening of 0.2 eV has been added to compensate finite k-point sampling. Courtesy of C. Giorgetti.

periment, even though heavily underestimating it; there is then little remaining spectral weight below –65 eV. The difference with the single plasmon-pole, apart from the absence of lifetimes, is clearly in the low-energy tail at –30 eV. In fact this tail can be ascribed to the π plasmon at 7 eV in the energy-loss spectrum of graphite. Instead, the broad feature around –50 eV can be assigned to the main $\pi + \sigma$ plasmon around 28 eV, which in fact is about the distance between the satellite and the main quasiparticle peak. An attempt with a simple two-pole model for W (not shown) shows that the main effect of the additional pole is the appearance of spectral weight under the tail at the bottom of the quasiparticle peaks. However, the inclusion of the full frequency-dependence is necessary to obtain the correct slope.

This result is in very good agreement with experiment, considered that there are no corrections for extrinsic losses and interference effects applied. If one compares this result with the intrinsic spectral function of silicon — considering the added full account of intrinsic plasmon lifetimes — the relative weight of the intrinsic satellites with respect to experiment is of the same order of magnitude. In fact, the coefficients a_j are of the order of $0.3/N_p$, as in the case of silicon. One can now re-discuss the conclusions by Vos *et al.* [142]: it is clear now that with the low energy-resolution they had in the experimental data, it was virtually impossible to affirm the existence of intrinsic satellite structures; moreover, the technique used to remove the background from the raw data hinders any further investigation [143]. Using the exponential representation of G with the generalized treatment of W, one can conclude that intrinsic satellites are indeed present, even though the low intensity makes them hard to be detected.

The performance of the (energy-only) GW_0 calculation can now be better understood: while it can only hope to describe the first order of satellites, it contains the full dynamic structure of W; therefore, it can in principle seize the two-plasmon structure of W in graphite. In practice, considering now what one observes in the exponential spectral function, GW behaves decently: if one considers the "first satellite" as the tail (for the π plasmon) plus the first distinct satellite (for the $\pi + \sigma$), one can see that the GW spectral function in Figure 7.3 displays a structure for each one of this features of the experimental spectrum. As GW does not incorporate the effect of extrinsic losses or interference effects, it is reasonable that satellites are underestimated. To summarize, the description of GW_0 satellites in the case of graphite appears to be correct, notably much better than in bulk silicon, where plasmon satellites are completely destroyed by a spurious plasmaron peak.

The advantage of using the exponential representation for the one-particle Green's function is that the spectral function can be connected to the formalism by Hedin *et al.* to include corrections for extrinsic losses and interference effects [21]. These have been calculated and provided by J.J. Kas, using my ab-initio input, and consist of complex a_j^{extinf} that is added to the a_j contained in (5.44), providing for intensity and lifetime from extrinsic losses and a correction for interference effects. The final spectrum (See Figure 7.3) is in very good agreement with experiment: the quasiparticle peaks have the same good agreement as the intrinsic spectrum; great improvement is obtained in the incoherent part of the

spectrum: the missing weight of the satellite at –50 eV is restored and now also the second satellite structure at -75 eV is visible. It is important to note that these corrections effectively produce only an increased intensity of the intrinsic satellites, which must be composed of the correct structures beforehand. In this sense, the excellent agreement of the total spectrum with experiment validates the performance of the decoupling approximation for the calculation of the one-particle Green's functions and of the intrinsic spectral function.

7.5 An outlook to graphene

In a theoretical calculation, graphite can be stretched in the *z* directions, i.e. the direction normal to the hexagonal layers. When the distance between layers reaches infinity, one has obtained *graphene*. Graphene is an extremely promising two-dimensional system, that has gathered the attention of the scientific community as a material with possible applications in a myriad of fields, from microelectronics to photovoltaics or gas sensing, just to name a few (See e.g. [151, 152]).

While the special properties of graphene are mostly connected with the highly-symmetric points $\mathbf{K}$ and $\mathbf{K}'$ in the Brillouin zone, I will here focus on the differences and similarities between graphite and graphene in the total spectral function $A(\omega)$ or, more in general, in the photoemission spectrum integrated over the full BZ.

In the perspective of the discussion on plasmarons in graphene it will be interesting to see if there are any in this case. The main differences between this study and [130, 131] are (i) the ab-initio approach (as opposed to parametrized model calculations) and (ii) the fact that here graphene is not doped (as opposed to *n*-doped graphene).

7.5.1 Exponential spectral function

As a part of an ongoing project, I have calculated the exponential spectral function for graphene. It is reported in Figure 7.5. In this figure, the intrinsic spectral functions of graphite and graphene, calculated using (5.44), are compared. The curves include cross section effects (at 800 eV), to keep the correct ratio between π and σ orbitals, and a 0.1 Gaussian broadening, to compensate for finite *k*-point sampling of the BZ. The main differences of graphene with respect to graphite are the following:

- the quasiparticle bandwidth appears to be slightly reduced (the main peak appears to be shifted by 1-2 eV), while the proportion between π and σ band does not appreciably change;

- the structure of satellites changes dramatically: there is a long tail between –30 and –50 eV, but the main satellite peak at –50 eV has disappeared.

There are no plasmaron peaks found in the GW_0 spectral function (not shown), but the *k*-point sampling did not include explicitly the special points $\mathbf{K}$ and $\mathbf{K}'$,
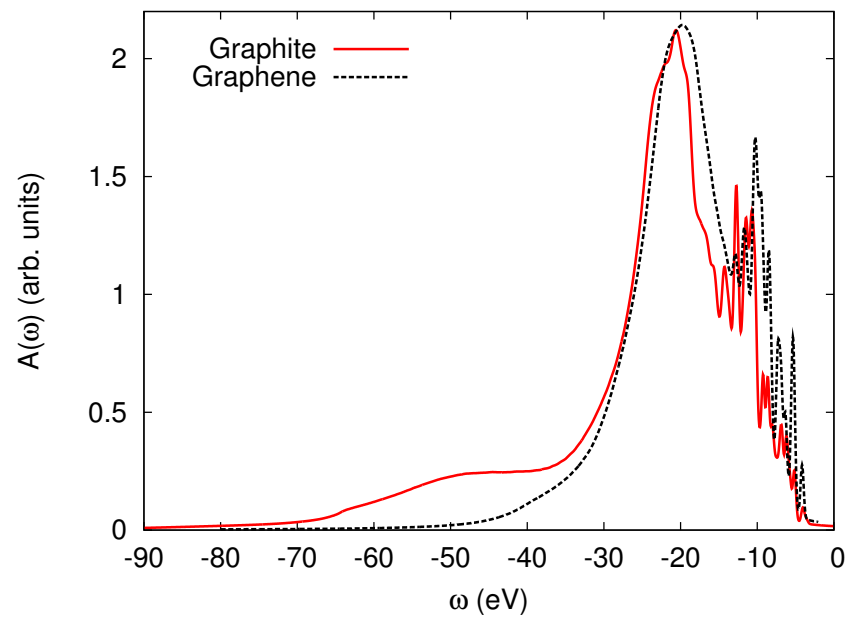
Figure 7.5: Comparison of Graphite (solid red) and Graphene (dashed black) spectral functions using the decoupling approximation (*aka* Cumulant Expansion) for the Green's function. There is almost no difference in the quasiparticle part, while the satellite part is remarkably different. The satellite shoulder at -30 eV does not change going from graphite to graphene, while most of the satellite weight below -40 eV disappears.

where they might possibly be found. Unpublished results confirm the presence of plasmaron peaks in the *GW* spectral function at the special points of doped graphene [133], confirming what has been found in model calculations [130, 131]: low-energy plasmarons appear (around 0.3 eV from the quasiparticle peak) that however should not change the shape of the total spectral function. Moreover, ours is a calculation for undoped graphene and there are no reports of plasmaron peaks in undoped graphene. The great difference in the region of intrinsic satellites between graphite and graphene is to be ascribed to the differences between the screening of the two systems, as I will show in the following. The analysis of the loss function will give a clear interpretation of these difference.

In fact, as noted by several authors [146, 147, 153], there is a dramatic change in the energy-loss spectra when one goes from graphene to graphite and inter-layer interactions are restored. Experimentally, this can be achieved by measuring single and multi-layer graphene foils. In fact, for more than some tens of layers, it appears not to be any difference with bulk graphite [153]. The experimental results have confirmed the theoretical calculations by Marinopoulos *et al.* [146, 147]. As shown in Figure 7.6, the energy-loss spectrum of single-layer graphene displays a π plasmon around 5 eV. There is then a small peak at 15 eV: this is what remains of the $\pi + \sigma$ plasmon of graphite. One can see that, increasing the number of layers, there are two main effects on the spectrum:

- the π plasmon is slightly shifted by about 2 eV and tends to become identical to the π peak in graphite at 7 eV;

- the $\pi + \sigma$ plasmon shifts toward larger energies (around 25 eV) and gains significant intensity.

One can see that, at ten graphene layers or more, the spectrum has become very close to the calculated energy-loss spectrum of graphite (Figure 7.4). One can now understand what changes the shape of the incoherent part of the spectral function of graphene: the extremely low intensity (and red shift) of the $\pi + \sigma$ plasmon leave in the spectral function only a long fading tail.

7.5.2 Experimental spectra

I have performed additional measurements at TEMPO in 2012 which have allowed me to study the photoemission spectrum of graphene. Graphene sheets were grown on a SiC bulk substrate with a 4H hexagonal structure — similarly to the technique shown in [154] — and studied by means of XPS with a similar setup to the one used for graphite. These data will hopefully confirm what is found in the theoretical spectrum and shed further light on the physics of graphene. The analysis of data is still ongoing, and the main challenge will be to be able to separate the signal coming from the substrate from the signal coming from the graphene at the top, hoping that the influence of the interface buffer layer will be negligible or at least controllable. This will be possible only in conjunction with the theoretical calculations on the substrate and on graphene.
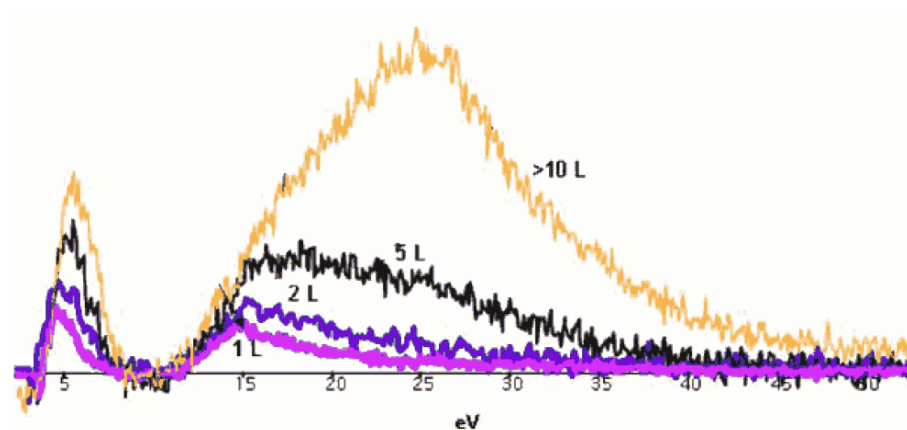
Figure 7.6: Electron energy-loss spectrum of single- and multi-layer graphene. The greatest change in the transition from single- to multi-layer graphene can be seen in the $\pi + \sigma$ plasmon, that goes from an energy of 14 eV to around 25 eV, gaining intensity by at least an order of magnitude. From [153].
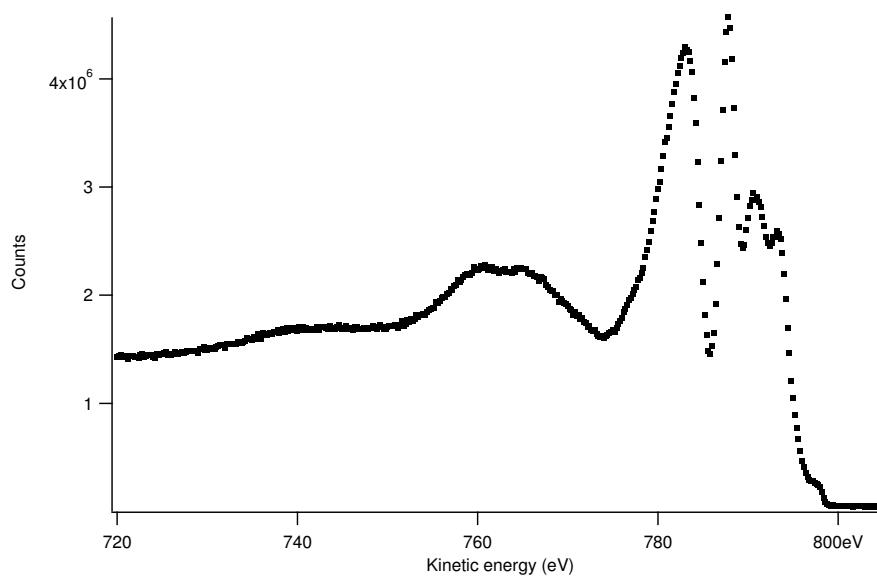

Figure 7.7: Raw XPS spectrum of bulk SiC-4H with single-layer graphene grown on top. The photoelectrons are detected at normal emission and the signal is integrated over an angle of about 6°. The Fermi energy is at 800 eV. With this configuration and at this photon energy, the spectrum is virtually indistinguishable from bulk SiC.

I present in Figure 7.7 preliminary raw data taken at TEMPO in February 2012. The spectrum is taken at normal emission and the signal is integrated over an angle of about $6°$. With this configuration one is probing several layers below the surface, that give the greatest contribution to the signal, totally overwhelming the signal from the surface. In fact, this spectrum could well be considered as if it was obtained with simple bulk SiC. To obtain information on the surface, one has to probe the minimum possible depth on the sample. This can be achieved by detecting the electrons at a very low angle α (5-10 degrees) above the surface: being determined by their kinetic energy, the inelastic mean free path of the electrons — proportional to the probing depth as $\sin \alpha$ — will allow them to escape in that direction only for small depths. This has been done in conjunction with measurements of the carbon $1s$ core-level spectra, the position of which is very sensitive to the chemical environment and can be used to understand if one is probing bulk, interface or surface [155]. The analysis of these spectra (not shown) is still ongoing and will be crucial to understand the full picture in conjunction with the theoretical results.

SiC-4H energy-loss spectrum

4H is only one of the four polytypes of SiC. Quasiparticle band structure have already been studied for all polytypes [156, 157]. My preliminary calculations for the energy-loss spectrum (See Figure 7.8) agree with previous theoretical results [158]. The main plasmon peak is located at about 23 eV. With this knowledge, one can now see that the satellites in Figure 7.7 are with all probability due to the excitation of plasmons in bulk SiC, as they are separated by a 23 eV distance.

Further analysis of experimental data is ongoing along with theoretical calculations to obtain the spectral functions of graphene and of bulk SiC. Eventually this collective effort will elucidate the physics of satellites in graphene and hopefully tell a bit more about the role of the interface. The long-range nature of plasmon excitations already suggests that the correct description of the full system will be crucial for a complete understanding.

7.6 Computational details

The Brillouin zone (BZ) of graphite was sampled using a $9 \times 9 \times 2$ Monkhorst-Pack grid, obtaining 162 points in the full BZ [137]. I have used Troullier-Martins norm-conserving pseudopotentials [138]. The plane-wave cutoff for the LDA ground-state calculation was fixed at 30 Ha. I used the `abinit` code for all ground-state and *GW* calculations [63], using the experimental values for lattice constants. The full frequency dependence of the self-energy for the 8 valence bands was calculated using a contour-deformation technique, applying partial self consistency on the quasiparticle energies in the Green's function (GW_0 calculations). *W* was calculated including 160 bands and using 997 plane waves for the wavefunctions. The dielectric matrix was calculated using 287 **G** vectors, 4 frequencies on the imaginary axis and 60 frequencies on the real axis, with a maximum value fixed at 2 Ha. The self-energy was calculated us-
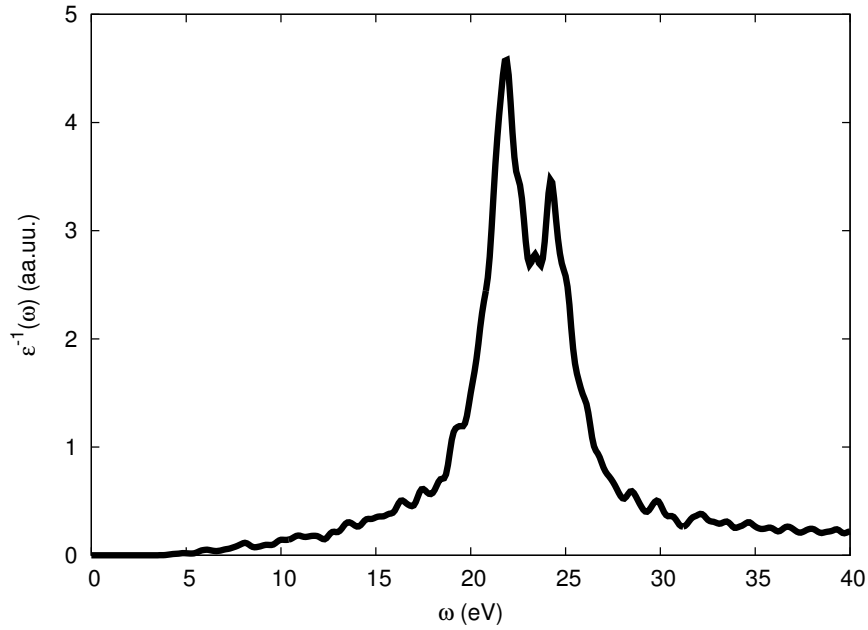
Figure 7.8: Energy-loss spectrum $-\mathrm{Im}\varepsilon^{-1}(\mathbf{q},\omega)$ of bulk 4H-SiC at $|\mathbf{q}| = 0$. The main plasmon peak is around 23 eV. A Gaussian broadening of 0.2 eV has been added to compensate finite k-point sampling.

ing 250 bands, 1385 plane waves for the wavefunctions, 287 $\mathbf{G}$ vectors for the dielectric matrix and 585 plane waves for the exchange term. The self-energy of graphite was calculated for 50 frequencies/Ha for a range of 65 eV below the Fermi energy.

The Brillouin zone (BZ) of graphene was sampled using a $10 \times 10 \times 1$ Monkhorst-Pack grid, obtaining 100 points in the full BZ [137]. I have used Troullier-Martins norm-conserving pseudopotentials [138]. The plane-wave cutoff for the LDA ground-state calculation was fixed at 31 Ha. I used the `abinit` code for all ground-state and *GW* calculations [63], using the experimental values for lattice constants. The distance between the graphene planes in the supercell lattice is equivalent to 6 times the inter-plane distance in graphite, in order to avoid interaction between the graphene planes. The full frequency dependence of the self-energy for the 8 valence bands was calculated using a contour-deformation technique, applying partial self consistency on the quasiparticle energies in the Green's function (GW_0 calculations). W was calculated including 150 bands and using 715 plane waves for the wavefunctions. The dielectric matrix was calculated using 169 $\mathbf{G}$ vectors, 5 frequencies on the imaginary axis and 200 frequencies on the real axis, with a maximum value fixed at 2 Ha. The self-energy was calculated using 200 bands, 715 plane waves for the wavefunctions, 169 $\mathbf{G}$ vectors for the dielectric matrix and 715 plane waves for the exchange term. The self-energy of graphene was calculated for 67 frequencies/Ha for a range of 55 eV below the Fermi energy.

7.7   Summary

The exponential representation of *G* can give an excellent description and understanding of the satellite structures in the photoemission spectrum of graphite. This is possible thanks to a complete treatment of the full frequency dependence of *W* and accounting for symmetry effects due to the experimental geometry (as described in Chapter 6). The use of new experimental data has made possible to observe that the shape of satellites in graphite is strictly connected to the electron energy-loss spectrum. I appears that the tail next to the quasi-particle peaks is a satellite feature and it is due to the π plasmon at 7 eV. The main (two) visible satellite peaks are instead due to the 28 eV $\pi + \sigma$ plasmon peak. The complex structure of ε^{-1} causes a general broadening of satellites, that are less sharp than in silicon. Thus the intrinsic origin of satellites is clarified. However, to obtain the correct intensity, one has to include corrections for extrinsic losses and interference effects. These produce a spectrum in excellent agreement with experiment.

The results obtained in the study of graphite are very promising for the study of graphene. Preliminary results indicate, in agreement with literature, that satellites in graphene are stricly connected to the change in the inverse dielectric function with respect to graphene. Theory allows us to trace the transition from graphite to graphene and, in conjunction with new experimental data, will shed new light on the physics of graphene.

8 | Conclusion

"Fu vera gloria? Ai posteri
l'ardua sentenza"

— Alessandro Manzoni,
Il cinque maggio (1832), vv 31-32

I have discussed and clarified in this manuscript the connection between photoelectron spectroscopy (PES) and electron energy-loss spectroscopy (EELS) through the inverse dielectric function, and the role of plasmon losses in the photoemission spectrum. Notably, I have focused my attention on correlation effects in PES. While this can be a very large domain, I have restricted my search to the smaller subset of satellite excitations. In fact satellites can be considered as a signature of correlation. They cannot be described by single-particle approaches and therefore need more sophisticated techniques to be understood. They appear in theoretical approaches that are able to describe, to some extent, the collective behavior of electrons and for this reason satellites are rightfully considered as effects of pure many-body excitations.

I have presented the photocurrent as the most correct quantity to compare with photoemission experiments and discussed its connection with the one-particle spectral function $A(\omega)$, which is a crucial quantity to calculate in theory. In Green's function theory, it is straightforward to calculate the spectral function, once the single-particle Green's function G is known. For this reason, several theoretical methods focus on the calculation of the latter, which also gives access to several key observables beside the spectral function. The GW method is a very successful approximation for the self-energy, that gives access to the Green's function through the Dyson equation. The success of GW is mainly due to its use for the calculation of quasiparticle energies. Its performance for the actual calculation of the full energy dependence of the spectral function is largely unexplored and still under debate, and it is one of the main topics of this thesis.

Throughout this manuscript, I have discussed the limits of GW for the description of the spectral function, focusing in particular on the description of satellites. I have then developed and discussed a number of methods to go beyond the GW approximation; these methods can be gathered in two main families:

- Vertex corrections: these are improvements made to the self-energy in the framework of Hedin's equations;

- Approximations for G: in this case one focuses on the Green's function directly, avoiding to use a self-energy.

To be precise, all discussed results are calculated in the GW_0 approximation, which understands partial self-consistency in the Green's function G; the screening W_0 is instead kept at the RPA level and not updated.

General knowledge about GW is that the energies of plasmon satellites are overestimated — i.e. they are too far from the QP peaks — and they tend to be quite weak with respect to experiment. I have discussed this quite vague statement and given several examples that allow one to assess more precisely the performance of GW for the calculation of spectral properties, notably of satellites.

One cheap way of applying vertex corrections is to derive approximate vertices using TDDFT exchange-correlation kernels. This results in an effective GW calculation where one uses an improved screened interaction W, calculated with a test-particle (TP) or test-electron (TE) inverse dielectric function $\varepsilon^{-1}(\mathbf{q}, \omega)$. This is equivalent to applying vertex corrections only in the polarization part (W) or both in that and in the self-energy, respectively. I have explored this path in Chapter 4, using exact relations in the homogeneous electron gas to study the q-dependence of several TDDFT kernels. Bulk silicon was used as a test system. While the LDA shows a pathologic behavior for large values of $\mathbf{q}$, that has also been found in older works, the general finding is that only small values of $\mathbf{q}$ in $\varepsilon^{-1}(\mathbf{q}, \omega)$ contribute to quasiparticle corrections in the self-energy. It appears that the greatest effects on the relative shift of quasiparticle energies — and therefore on the band gap — happens when a W^{TP} is used. When both vertices are applied, there is a compensation that brings the value of the band gap back, quite close to the GW result. The effect of these vertex corrections on the spectral function of silicon are minimal: there is a slight renormalization of the quasiparticle peaks, accompanied by a very small shift of the satellite part that can be appreciated only looking at single states in the Brillouin zone. The effect on the structure of the total spectral function, integrated over the full BZ, is negligible. This result does not exclude the theoretical possibility to find effective vertex corrections, but shows the difficulty of finding one using the connection with TDDFT.

A more complicated tool than TDDFT is Green's function theory. While authors have often opted for the use of a self-energy Σ to simplify the way to the single-particle Green's function, as in GW, it is in principle possible to derive a G without recurring to Σ. I have shown in Chapter 5 how to obtain an expression for the Green's function that includes dynamical effects beyond GW from the exact solution of an approximate equation of motion for G. This Green's function and its spectral function have an exponential form and are able to describe quasiparticle excitations and infinite series of satellites. I have shown how this approach can be effectively connected to GW to exploit the good description of QP energies in the latter. This expression for G effectively includes vertex corrections beyond GW. It appears at first quite difficult to

derive, from this result, a vertex correction that can be used to improve *GW*, as it involves the inversion of an infinite summation; this somewhat suggests that the direct approach to *G* and a calculation of an improved self-energy are two exclusive paths. Nevertheless, the knowledge of the explicit dependence of *G* on the external perturbation φ can be used to derive a class of vertex corrections, but the validity of such has yet to be proved and tested.

The exponential expression for *G* is tested in Chapter 6 for the calculation of the spectral function of silicon against *GW*, where silicon is a representative example of semiconductors. New high-quality photoemission data show that the spectrum of silicon exhibits a decaying series of satellites beside the QP peaks. The main effect in the shape of satellites appears to come from the main plasmon peak of silicon at about 17 eV. In this chapter I extensively discuss the shortcomings of *GW* in the description of satellites: this approximation exhibits in silicon a spurious peak, that has been debated for quite some time, the *plasmaron*. The plasmaron has been observed in the *GW* spectral function of the HEG and of other systems and presented at first as a bound state of quasiparticles and plasmons. Later, it was pointed out that it is with all probability an artificial product of *GW* and in fact it was never found in experiment. I extensively discuss the related literature: the big picture is quite eloquent and suggests how the recent excitement about plasmaron excitations in doped quasi-freestanding graphene is quite questionable and needs further investigation: the plasmaron cannot be considered just as a poor description of plasmon satellites; one can infer its qualitative difference with plasmon satellites by analysis of the spectral function and comparison with experiment.

Several options to improve the *GW* spectral function and free it from the plasmaron are analyzed and discussed. While self consistency appears to be a possible way to correct the problem, there is not a failsafe prescription for this. The results of this thesis promote further debate on the role of self consistency in the *GW* approximation. The exponential spectral function has a very good agreement with experiment and is free from the plasmaron problem, that ruins the *GW* satellites. I discuss a number of effects that have to be included in the spectral function to correctly compare theory and experiment, such as dipole matrix elements and secondary electron background. This result for the intrinsic spectral function shows that satellites appear to be weaker than in experiment. Including a correction for extrinsic losses and interference effects as suggested by Hedin *et al.* [21], the theoretical spectrum is in almost perfect agreement with experiment. This results highlights the importance of going beyond the sudden approximation when comparing quantitatively theory and experiment in photoemission.

To further assess the quality of the method, I have measured new photoemission data for bulk graphite, to measure the performance of the approach on a more complex material as such. I have performed the measurements at the TEMPO x-ray beamline in the Soleil synchrotron facility in France. The description of this system has needed an improved description of *W*, with a generalized model, to seize the complex structure of the energy-loss spectrum of this layered material. The satellite photoemission spectrum of graphite is more complex than in silicon and I find that this is directly connected with

the double structure of the EELS spectrum of graphite. Apart from a decaying series of visible peaks, due to the $\pi + \sigma$ plasmon at about 28 eV, there is a significant tail beside the quasiparticle peaks, that is due to the low energy π plasmon, at about 8 eV. The exponential spectral function is in good agreement with experiment, but also in this case corrections for extrinsic losses and interference effects are crucial to obtain excellent agreement. The comparison with the *GW* result is in this case revealing: in graphite the GW_0 spectral function appears free from the plasmaron problem and actually gives a correct description of the overall shape of satellites. This is to be ascribed to the shape of the loss function, that ultimately enters in the self-energy: a sharp peak in the loss function will cause a sudden variation in the real part of the self-energy that will probably produce a plasmaron, as it happens in silicon; a more complex loss function — hence broader on average — will cause smoother variations of the self-energy and will be less likely to produce a plasmaron. This qualitative explanation still calls for a rigorous formal proof.

An additional challenge for the theory is presented at the end of Chapter 7, as I have performed additional measurements at TEMPO on quasi-freestanding graphene. The ongoing project will help to improve the implementation of the exponential expression for *G* and will hopefully give further insight about the physics of graphene. For now, results show that differences between graphite and graphene are minimal in the QP region. Satellites should display significantly different behavior because of the markedly different energy-loss spectrum of the two systems.

To summarize, the exponential expression has proven to be a great example of an approximation for *G* that is derived using systematic and controlled approximations on the exact equation of motion for *G*. The great success of it comes from the automatic inclusion of dynamic vertex corrections that give rise to series of satellites in the photoemission spectrum. I have shown how to obtain the same result using vertex corrections to *GW* is a virtually impossible task. Moreover, the exponential expression for *G* allows one to assess the description of satellites in *GW*: while the exponential *G* can remove the plasmaron problem, it shows that *GW* is able to give a correct description when the plasmaron is absent, a fact that is confirmed by other authors.

Overall, this work shows how a great improvement in theory has to go hand-in-hand with the knowledge of experimental techniques. The brute comparison of the spectral function with a photoemission spectrum is never a good idea, especially if one is not aware of the experimental conditions. It can be a futile exercise trying to blindly improve the theory: one has before to take into full account all the effects that concur to what is eventually detected in an experimental measurement. Only then a reasonable assessment of the approximations used can be done. The account of additional effects that modify what is contained in the spectral function is key to a complete understanding of photoemission spectra. This, once again, demonstrates that the collaboration between theoreticians and experimentalists is crucial to obtain real insight about a problem in solid-state physics.

A | Exact relations for xc kernels in TDDFT

In this appendix I explore the relations between TP and TE dielectric function, with the final hope to sort out systematic behaviors, at least in the case of selected approximations. When possible, a general f_{xc} is treated.

A.1 Connection between test-particle and test-electron dielectric function

Within the HEG-α kernel

The inverse dielectric function ε^{-1} can be written for the two cases:

$$\varepsilon_{TP}^{-1} = 1 + v\chi \tag{A.1}$$

$$\varepsilon_{TE}^{-1} = 1 + (v + f_{xc})\chi. \tag{A.2}$$

Being still quite general, I will point out that if $f_{xc} = \alpha/q^2 = (\alpha/4\pi)v$ it follows that $\varepsilon_{TE}^{-1} = 1 + (1 + \frac{\alpha}{4\pi})v\chi$. In this particular case ($\alpha = -8\pi/3$, exact HEG limit for $q \to \infty$) one has

$$\varepsilon_{TE}^{-1} = 1 + (1/3)v\chi. \tag{A.3}$$

It follows that:

$$\text{Im}[\varepsilon_{TE}^{-1}] = \frac{1}{3}\,\text{Im}[\varepsilon_{TP}^{-1}] \tag{A.4}$$

$$\text{Re}[\varepsilon_{TP}^{-1}] = 3\,\text{Re}[\varepsilon_{TE}^{-1}] - 2. \tag{A.5}$$

NB: $\text{Im}[\varepsilon^{-1}] = $ *loss function*. These equations allow one to establish several expressions that relate ε_M^{TP} e ε_M^{TE}. Using eq. (A.4) and (A.5) and substituting in the definition $\varepsilon_2 = \text{Im}[1/\varepsilon^{-1}]$ one gets

$$\varepsilon_2^{TP} = -\frac{\text{Im}[\varepsilon_{TP}^{-1}]}{\text{Re}[\varepsilon_{TP}^{-1}]^2 + \text{Im}[\varepsilon_{TP}^{-1}]^2} \tag{A.6}$$

$$= -\frac{3\ \text{Im}[\varepsilon_{TE}^{-1}]}{\{1 + 3\ \text{Re}[\varepsilon_{TE}^{-1} - 1]\}^2 + 9\ \text{Im}[\varepsilon_{TE}^{-1}]^2} \tag{A.7}$$

$$= -\frac{1}{3}\frac{\text{Im}[\varepsilon_{TE}^{-1}]}{\{\text{Re}[\varepsilon_{TE}^{-1}] - \frac{2}{3}\}^2 + \text{Im}[\varepsilon_{TE}^{-1}]^2} \tag{A.8}$$

and for the real part:

$$\varepsilon_1^{TP} = \frac{\text{Re}[\varepsilon_{TP}^{-1}]}{\text{Re}[\varepsilon_{TP}^{-1}]^2 + \text{Im}[\varepsilon_{TP}^{-1}]^2} \tag{A.9}$$

$$= \frac{3\,\text{Re}[\varepsilon_{TE}^{-1}] - 2}{\{1 + 3\,\text{Re}[\varepsilon_{TE}^{-1} - 1]\}^2 + 9\,\text{Im}[\varepsilon_{TE}^{-1}]^2} \tag{A.10}$$

$$= \frac{1}{9} \frac{3\,\text{Re}[\varepsilon_{TE}^{-1}] - 2}{\{\,\text{Re}[\varepsilon_{TE}^{-1}] - \frac{2}{3}\}^2 + \text{Im}[\varepsilon_{TE}^{-1}]^2} \tag{A.11}$$

Connection between RPA and the HEG-α kernel

TE-RPA connection   For this case, one just needs to recall that

$$\varepsilon^{RPA} = 1 - v\chi^0 \tag{A.12}$$

$$\varepsilon_{TE} = 1 - (v + f_{xc})\chi^0 \tag{A.13}$$

then one should evaluate $\text{Im}[\varepsilon]$, *aka* ε_2, knowing that at $q \to \infty$ in the HEG $f_{xc} = -8\pi/(3q^2) = -2v/3$:

$$\varepsilon_2^{RPA} = -\,\text{Im}[v\chi^0] \tag{A.14}$$

$$\varepsilon_2^{HEG-TE} = -\,\text{Im}[(v + f_{xc})\chi^0] = -\,\text{Im}[\frac{v}{3}\chi^0] \tag{A.15}$$

$$= -\frac{1}{3}\,\text{Im}[v\chi^0] = \frac{1}{3}\varepsilon_2^{RPA} \tag{A.16}$$

that is

$$\varepsilon_2^{HEG-TE} = \frac{1}{3}\varepsilon_2^{RPA}. \tag{A.17}$$

This result can be generalised to an f_{xc} of the form α/q^2. Following the same steps as above, one can find

$$\varepsilon_2^{\alpha-TE} = \left(1 + \frac{\alpha}{4\pi}\right)\varepsilon_2^{RPA}. \tag{A.18}$$

Concerning the real part ε_1, some expressions can be derived in an equivalent way:

$$\varepsilon_1^{HEG-TE} = 1 + \frac{1}{3}\left(\varepsilon_1^{RPA} - 1\right). \tag{A.19}$$

$$\varepsilon_1^{\alpha-TE} = 1 + \left(1 + \frac{\alpha}{4\pi}\right)\left(\varepsilon_1^{RPA} - 1\right). \tag{A.20}$$

It is possible to play around ε^{-1} as well. In fact:

$$\varepsilon_{RPA}^{-1} = 1 + v\chi = 1 + v\left[1 - \chi^0\right]^{-1} \tag{A.21}$$

$$\varepsilon_{TE}^{-1} = 1 + (v + f_{xc})\chi \tag{A.22}$$

TP-RPA connection To analyse the behaviour of ε_{HEG-TP} with respect to ε_{RPA}, one can work around eq. (A.8):

$$\varepsilon_2^{HEG-TP} = -\frac{1}{3} \frac{\text{Im}[\varepsilon_{TE}^{-1}]}{\{\text{Re}[\varepsilon_{TE}^{-1}] - \frac{2}{3}\}^2 + \text{Im}[\varepsilon_{TE}^{-1}]^2} \tag{A.23}$$

and first focus on $\text{Im}[\varepsilon_{TE}^{-1}]$ and $\text{Re}[\varepsilon_{TE}^{-1}]$. Using previously derived expressions (A.17) and (A.19) one gets:

$$\text{Im}[\varepsilon_{TE}^{-1}] = -\frac{\varepsilon_2^{TE}}{\left(\varepsilon_1^{TE}\right)^2 + \left(\varepsilon_2^{TE}\right)^2} \tag{A.24}$$

$$= -\frac{\frac{1}{3}\varepsilon_2^{RPA}}{\left[1 + \frac{1}{3}(\varepsilon_1^{RPA} - 1)\right]^2 + \left(\frac{1}{3}\varepsilon_2^{RPA}\right)^2} \tag{A.25}$$

$$= -3\frac{\varepsilon_2^{RPA}}{\left(\varepsilon_1^{RPA} + 2\right)^2 + \left(\varepsilon_2^{RPA}\right)^2} \tag{A.26}$$

and for the real part:

$$\text{Re}[\varepsilon_{TE}^{-1}] = \frac{\varepsilon_1^{TE}}{\left(\varepsilon_1^{TE}\right)^2 + \left(\varepsilon_2^{TE}\right)^2} \tag{A.27}$$

$$= \frac{1 + \frac{1}{3}(\varepsilon_1^{RPA} - 1)}{\left(\varepsilon_1^{TE}\right)^2 + \left(\varepsilon_2^{TE}\right)^2}. \tag{A.28}$$

One notices also that $(\varepsilon_1^{TE})^2 + (\varepsilon_2^{TE})^2 = |\varepsilon^{TE}|^2$. Hence ε_2 becomes:

$$\varepsilon_2^{HEG-TP} = \frac{\frac{1}{3}\varepsilon_2^{RPA}/|\varepsilon^{TE}|^2}{3\left[\varepsilon_1^{TE}/|\varepsilon^{TE}|^2 - \frac{2}{3}\right]^2 + 3\left[\frac{1}{3}\varepsilon_2^{RPA}/|\varepsilon^{TE}|^2\right]^2} \tag{A.29}$$

$$= \frac{1}{9} \frac{\varepsilon_2^{RPA}/|\varepsilon^{TE}|^2}{\left[(\varepsilon_1^{TE} - \frac{2}{3}|\varepsilon^{TE}|^2)/|\varepsilon^{TE}|^2\right]^2 + \left[\frac{1}{3}\varepsilon_2^{RPA}/|\varepsilon^{TE}|^2\right]^2} \tag{A.30}$$

$$= \frac{\varepsilon_2^{RPA}|\varepsilon^{TE}|^2}{\left[3\varepsilon_1^{TE} - 2|\varepsilon^{TE}|^2\right]^2 + \left[\varepsilon_2^{RPA}/3\right]^2} \tag{A.31}$$

A.1.1   Remarks on q-dependent behaviour of ALDA-TP/TE with respect to RPA

Let us start with a brief recap on RPA:

$$\chi_{RPA} = \left[1 - \chi^0 v\right]^{-1} \chi^0 \tag{A.32}$$

$$\varepsilon_{RPA} = 1 - v\chi^0 \tag{A.33}$$

$$\varepsilon_{RPA}^{-1} = 1 + v\chi = 1 + v\left[1 - \chi^0 v\right]^{-1}\chi^0 \tag{A.34}$$

and then on ALDA:

$$\chi_{ALDA} = \left[1 - \chi^0(v + f_{xc})\right]^{-1}\chi^0 \tag{A.35}$$

$$\begin{aligned}\varepsilon_{ALDA}^{TP} &= 1 - v\tilde{\chi} \\ &= 1 - v\left[1 - \chi^0 f_{xc}^{ALDA}\right]^{-1}\chi^0\end{aligned} \tag{A.36}$$

$$\varepsilon_{TP}^{-1} = 1 + v\chi \tag{A.37}$$

$$\varepsilon_{ALDA}^{TE} = 1 - (v + f_{xc}^{ALDA})\chi^0 \tag{A.38}$$

$$\begin{aligned}\left[\varepsilon_{ALDA}^{TE}\right]^{-1} &= 1 + (v + f_{xc})\chi_{ALDA} \\ &= 1 + (v + f_{xc})\left[1 - \chi^0(v + f_{xc})\right]^{-1}\chi^0 \\ &= 1 + \left[(v + f_{xc})^{-1} - \chi^0\right]^{-1}\chi^0 \\ &= 1 + v\left[(v + f_{xc})^{-1}v - \chi^0 v\right]^{-1}\chi^0 \\ &= 1 + v\left[(1 + v^{-1}f_{xc})^{-1} - \chi^0 v\right]^{-1}\chi^0\end{aligned} \tag{A.39}$$

NB: $\tilde{\chi} = \chi^0 + \chi^0 f_{xc}\tilde{\chi}$.

Two trends can be described comparing eq. (A.33) with eq. (A.36) and eq. (A.34) with eq. (A.39). In fact, is it apparent that

$$\text{if}\quad \chi^0 f_{xc} \ll 1 \quad\text{then}\quad \varepsilon_{TP} \to \varepsilon_{RPA}. \tag{A.40}$$

and that

$$\text{if}\quad v^{-1} f_{xc} \ll 1 \quad\text{then}\quad \varepsilon_{TE}^{-1} \to \varepsilon_{RPA}^{-1}. \tag{A.41}$$

Hence, there are two different situations where ALDA can recover RPA, whether in Test-Particle or in Test-Electron. One should now point out several things:

- for $q \to 0$, $v \sim 1/q^2$ and $\chi^0 \sim q^2$. This means that for $q \sim 0$ both conditions are satisfied;

- a zeroth-order estimation of how ε_{TP} and ε_{TE}^{-1} behave with respect to their RPA counterparts can be given from calculations on silicon;

- knowing that $\varepsilon_{RPA} = 1 - v\chi^0$ one can have a rough estimation of the $v\chi^0$ term in the case of silicon. Looking at the RPA spectra for small values of q, one could tell that $v\chi^0 \sim 6$;

- it is known that, for $q \to \infty$, $\varepsilon_M \to 1$, which means that $v\chi^0 \to 0$. In general $\chi^0 \to 0$ as $q \to \infty$, hence condition (A.40) holds also in this latter case.

The inverse dielectric unction

Remaining in the ALDA framework, there is something to say about ε^{-1}, i.e. the inverse dielectric function. This is the function that enters in the energy-loss spectrum, by the formula

$$EELS = -\operatorname{Im}\left\{\frac{1}{\varepsilon_M}\right\} = -\operatorname{Im}\left\{\varepsilon_{00}^{-1}\right\}. \tag{A.42}$$

Just to point out its relevance, ε^{-1} enters also in Hedin's equations for the calculation of the self-energy. Now, keeping in mind Eq. (A.35) and (A.37) one can write

$$\varepsilon_{TP}^{-1} = 1 + v\left[1 - \chi^0(v + f_{xc})\right]^{-1}\chi^0 \tag{A.43}$$

and equivalently

$$\varepsilon_{TE}^{-1} = 1 + (v + f_{xc})\left[1 - \chi^0(v + f_{xc})\right]^{-1}\chi^0 \tag{A.44}$$

$$= 1 + v\left[1 - \chi^0(v + f_{xc})\right]^{-1}\chi^0 + f_{xc}\left[1 - \chi^0(v + f_{xc})\right]^{-1}\chi^0 \tag{A.45}$$

$$= \varepsilon_{TP}^{-1} + \left[f_{xc}^{-1} - \chi^0(v + f_{xc})f_{xc}^{-1}\right]^{-1}\chi^0 \tag{A.46}$$

$$= \varepsilon_{TP}^{-1} + \left[\left(f_{xc}\chi^0\right)^{-1} - vf_{xc}^{-1} - 1\right]^{-1} \tag{A.47}$$

$$= \varepsilon_{TP}^{-1} + \left[\left(f_{xc}\chi^0\right)^{-1} - \frac{4\pi f_{xc}^{-1}}{q^2} - 1\right]^{-1}. \tag{A.48}$$

Hence one can write

$$\varepsilon_{TE}^{-1} - \varepsilon_{TP}^{-1} = \left[\left(f_{xc}\chi^0\right)^{-1} - \frac{4\pi f_{xc}^{-1}}{q^2} - 1\right]^{-1}. \tag{A.49}$$

This is a very general formula which holds for any TDDFT kernel, in fact no approximations have been made on the kernel till now. At this point however, it is possible to analyze the asymptotic limits within a chosen approximation. Let us first take the ALDA. One can write (still with no particular approximation)

$$\varepsilon_{TE}^{-1} - \varepsilon_{TP}^{-1} = \frac{1}{\dfrac{1}{f_{xc}\chi^0} - \dfrac{4\pi}{f_{xc}q^2} - 1} \tag{A.50}$$

Now, for ALDA, it follows that (f_{xc} is treated as a constant as it is not q-dependent)

$$\text{if} \quad q \to 0 \quad \text{then} \quad \varepsilon_{TE}^{-1} - \varepsilon_{TP}^{-1} \sim \frac{1}{\dfrac{c}{f_{xc}q^2} - \dfrac{4\pi}{f_{xc}q^2} - 1} \to 0 \qquad \text{(A.51)}$$

$$\text{if} \quad q \to \infty \quad \text{then} \quad \varepsilon_{TE}^{-1} - \varepsilon_{TP}^{-1} \sim \frac{1}{\dfrac{1}{f_{xc}\chi^0} - 1} \to 0, \qquad \text{(A.52)}$$

where $\chi^0 \to c/q^2$ for $q \to 0$. Hence, TE-ALDA should recover TP-ALDA both at small and large q. It is worth to point out that in the case of increasing wavevector, ε_{TE}^{ALDA} has already proven to be pathologic and hence meaningless. Hence in this case the TE-ALDA dielectric function should not even be taken into account.

B | Spectral resolutions

This is a general description of some properties of time-ordered response functions. Examples of this are the one-particle Green's function or notably the plasmon-pole models used for the derivation of G in Chapter 5. See also Appendix C in [39] from where this part is taken. For a given time-ordered function $R(r, r'; \tau)$ one can write:

$$R(r, r'; \tau) = -i \sum_s \left[\rho_s(r) \rho_s^*(r') e^{-i\epsilon_s \tau} \theta(\tau) + \rho_s(r') \rho_s^*(r) e^{i\epsilon_s \tau} \theta(-\tau) \right] \quad \text{(B.1)}$$

where ρ_s are in general oscillator strengths and ϵ_s the poles of the response function. This, in the case of a plasmon-pole-model screening, becomes

$$\mathcal{W}(t_1 - t_2) = -i\lambda \left\{ e^{i\omega_p(t_1 - t_2)} \theta(t_2 - t_1) + e^{-i\omega_p(t_1 - t_2)} \theta(t_1 - t_2) \right\} \quad \text{(B.2)}$$

with $\omega_p > 0$. So its Fourier transfom is

$$
\begin{aligned}
\mathcal{W}(\omega) &= -i \frac{\lambda}{2\pi} \int_{-\infty}^{\infty} d\tau e^{i\omega\tau} \left[e^{i\omega_p \tau} \theta(-\tau) + e^{-i\omega_p \tau} \theta(\tau) \right] \\
&\stackrel{\eta \to 0^+}{=} -i \frac{\lambda}{2\pi} \int_{-\infty}^{\infty} d\tau e^{i\omega\tau} \left[e^{i\omega_p \tau} \left(-\frac{1}{2\pi i} \int_{-\infty}^{\infty} d\omega' \frac{e^{i\omega'\tau}}{\omega' + i\eta} \right) \right. \\
&\qquad\qquad\qquad\qquad\qquad \left. + e^{-i\omega_p \tau} \left(-\frac{1}{2\pi i} \int_{-\infty}^{\infty} d\omega'' \frac{e^{-i\omega''\tau}}{\omega'' + i\eta} \right) \right] \\
&= \frac{\lambda}{2\pi} \int_{-\infty}^{\infty} d\omega' \left\{ \frac{1}{\omega' + i\eta} \int_{-\infty}^{\infty} d\tau \left[e^{i(\omega + \omega_p + \omega')\tau} + e^{i(\omega - \omega_p - \omega')\tau} \right] \right\} \quad \text{(B.3)} \\
&= \frac{\lambda}{2\pi} \int_{-\infty}^{\infty} d\omega' \left\{ \frac{2\pi}{\omega' + i\eta} \left[\delta(\omega + \omega_p + \omega') + \delta(\omega - \omega_p - \omega') \right] \right\} \\
&= \lambda \left(\frac{1}{\omega - \omega_p + i\eta} - \frac{1}{\omega + \omega_p - i\eta} \right) \\
&= \lambda \left[\mathcal{P} \left(\frac{1}{\omega - \omega_p} - \frac{1}{\omega + \omega_p} \right) \right] - i\pi\lambda \left[\delta(\omega - \omega_p) + \delta(\omega + \omega_p) \right]
\end{aligned}
$$

where we have used the integral representation of the Heaviside step function:

$$
\begin{aligned}
\theta(\tau) &= -\frac{1}{2\pi i} \lim_{\eta \to 0^+} \int_{-\infty}^{\infty} d\omega \frac{e^{-i\omega\tau}}{\omega + i\eta} = \frac{1}{2\pi i} \lim_{\eta \to 0^+} \int_{-\infty}^{\infty} d\omega \frac{e^{i\omega\tau}}{\omega - i\eta} \\
\theta(-\tau) &= -\frac{1}{2\pi i} \lim_{\eta \to 0^+} \int_{-\infty}^{\infty} d\omega \frac{e^{i\omega\tau}}{\omega + i\eta} = \frac{1}{2\pi i} \lim_{\eta \to 0^+} \int_{-\infty}^{\infty} d\omega \frac{e^{-i\omega\tau}}{\omega - i\eta}.
\end{aligned}
\quad \text{(B.4)}
$$

Now one must remember that

$$\lim_{\eta \to 0^+} \frac{1}{x + i\eta} = \mathcal{P}\frac{1}{x} - i\pi\delta(x) \tag{B.5}$$

$$\lim_{\eta \to 0^+} \frac{1}{x - i\eta} = \mathcal{P}\frac{1}{x} + i\pi\delta(x) \tag{B.6}$$

hence the imaginary part of $\mathcal{W}(\omega)$ is

$$\text{Im}\mathcal{W}(\omega) = -\pi\lambda \left[\delta(\omega + \omega_p) + \delta(\omega - \omega_p)\right]. \tag{B.7}$$

C | Published articles from this thesis

I list here the papers directly derived from the work described in this thesis that have already been published. The papers are attached in the following pages and are:

- Matteo Guzzo, Giovanna Lani, Francesco Sottile, Pina Romaniello, Matteo Gatti, Joshua J. Kas, John J. Rehr, Mathieu G. Silly, Fausto Sirotti, and Lucia Reining. Valence electron photoemission spectrum of semiconductors: Ab Initio description of multiple satellites. Phys. Rev. Lett., 107:166401, Oct 2011 [1].

- Matteo Guzzo, Giovanna Lani, Francesco Sottile, Pina Romaniello, Matteo Gatti, Joshua J. Kas, John J. Rehr, Mathieu G. Silly, Fausto Sirotti, and Lucia Reining. Valence-band satellites in photoemission spectroscopy. 2011 Scientific Highlights of Soleil synchrotron facility, 2012, `http://www.highlights-synchrotron-soleil.fr/Highlights-2011-Booklet/#/20/`.

- M. Guzzo, J. J. Kas, F. Sottile, J. J. Rehr, M. G. Silly, F. Sirotti, and L. Reining. Plasmon satellites in valence-band photoemission spectroscopy. European Physical Journal B, 85(9):324, 2012 [134].

147

Valence Electron Photoemission Spectrum of Semiconductors: *Ab Initio* Description of Multiple Satellites

Matteo Guzzo,[1,2,*] Giovanna Lani,[1,2] Francesco Sottile,[1,2] Pina Romaniello,[3,2] Matteo Gatti,[4,2] Joshua J. Kas,[5] John J. Rehr,[5,2] Mathieu G. Silly,[6] Fausto Sirotti,[6] and Lucia Reining[1,2,†]

[1]*Laboratoire des Solides Irradiés, École Polytechnique, CNRS, CEA-DSM, F-91128 Palaiseau, France*
[2]*European Theoretical Spectroscopy Facility (ETSF)*
[3]*Laboratoire de Physique Théorique, CNRS, Université Paul Sabatier, F-31062 Toulouse, France*
[4]*Departamento Física de Materiales, CSIC-UPV/EHU-MPC and DIPC, Universidad del País Vasco, E-20018 San Sebastián, Spain*
[5]*Department of Physics, University of Washington, Seattle, Washington 98195, USA*
[6]*Synchrotron-SOLEIL, BP 48, Saint-Aubin, F91192 Gif sur Yvette CEDEX, France*
(Received 1 July 2011; published 12 October 2011)

The experimental valence band photoemission spectrum of semiconductors exhibits multiple satellites that cannot be described by the *GW* approximation for the self-energy in the framework of many-body perturbation theory. Taking silicon as a prototypical example, we compare experimental high energy photoemission spectra with *GW* calculations and analyze the origin of the *GW* failure. We then propose an approximation to the functional differential equation that determines the exact one-body Green's function, whose solution has an exponential form. This yields a calculated spectrum, including cross sections, secondary electrons, and an estimate for extrinsic and interference effects, in excellent agreement with experiment. Our result can be recast as a dynamical vertex correction beyond *GW*, giving hints for further developments.

Photoemission is a prominent tool to access information about electronic structure and excitations in materials. Modern synchrotron sources can provide detailed insight, thanks to their high intensity and broad photon energy range. But the interpretation of the experimental data is far from obvious, and theory is an essential complementary tool. However, *ab initio* calculations typically focus on bulk band structure [1,2]; thus surface effects are ignored, and satellites are not included. The latter are a pure many-body effect due to coupling to excitations of the material. Such many-body effects are contained in approaches developed for correlated materials [3,4]; however, these are usually based on models with short-range interactions, whereas satellites such as plasmons involve long-range effects. Plasmon satellites have been extensively studied in core-level experiments [5]. There they can be described by a theoretical model where a single dispersionless fermion couples to bosons. The resulting exact Green's function has an exponential form given by the so-called cumulant expansion (CE). A Taylor expansion of the exponential leads to a well-defined quasiparticle (QP) peak followed by a decaying series of plasmon satellites at energy differences given by the plasmon energy, consistent with experimental observations [6–10]. In the valence region, plasmon satellites are much less studied, though *ab initio* approaches can provide a good starting point. At high photoelectron energies the photoemission spectrum is approximately proportional to the intrinsic spectral function $A(\omega) = -(1/\pi)\mathrm{Im}\mathcal{G}(\omega)$, where $\mathcal{G}$ is the one-particle Green's function. The latter is typically calculated using the widely used *GW* approximation (GWA) [7,11,12]. In principle, the GWA contains correlation effects beyond the quasiparticle approximation. However, these additional features are rarely calculated due to computational complexity and, more importantly, the serious discrepancies between GWA and experiment (see, e.g., [13–16]). The CE has also been used for homogeneous electron gas [17] and simple metals [14,15], yielding an improved description of satellites over *GW*. Silicon [16] and graphite [18] were also studied, but no plasmon satellite series were observed. However, these results are not conclusive due to difficulties of interpreting the experimental data. This leaves a series of important questions: (i) Do materials generally exhibit intrinsic satellites in the valence band region following a cumulant like distribution, or are the extrinsic plasmon peaks, due to losses incurred by the escaping photoelectron, dominant? (ii) If such series are seen, how bad are *ab initio GW* calculations? what is the reason for their failure? and (iii) how can they be improved? Answering these questions would be a crucial step towards a better understanding of correlation effects in electronic excitations and a predictive *ab initio* approach to photoemission.

In this Letter we focus on plasmon satellites using silicon as a prototypical example. We have obtained valence band photoemission data at high photon energy (XPS) that constitute a reliable and well resolved benchmark. Analysis of the data allows us to elucidate the failure of *GW* in describing the satellites. Then, starting from the fundamental equations of many-body perturbation theory (MBPT), we show how the failure can be overcome by

using a decoupling approximation that leads to an exponential representation of the one-particle Green's function. Together with an estimate for extrinsic and interference effects, we obtain results for the quasiparticle peaks and satellites in excellent agreement with experiment. Our theoretical results can be expressed in terms of a dynamical vertex correction, a powerful basis for further modeling.

Angular resolved valence photoemission (ARPES) measurements were performed at the UHV photoemission experimental station of the TEMPO beam line [19] at the SOLEIL synchrotron radiation source. Linearly polarized photons from the Apple II type Insertion Device (HU44) were selected in energy using a high resolution plane grating monochromator with a resolving power $E/\Delta E = 5000$. The end-station chamber (base pressure 10^{-10} mbar) is equipped with a modified SCIENTA-200 electron analyzer with a delay-line 2D detector which optimizes the detection linearity and signal/background ratio [20]. The overall energy resolution was better than 200 meV. The photon beam impinges on the sample at an angle of $43°$, and photoelectrons were detected around the sample surface normal with an angular acceptance of $\pm 6°$. An n-type ($N_D \simeq 2 \times 10^{-18} P$ atoms/cm^3) Si(001) wafer was cleaned from the native oxide by flash annealing at $1100 °C$ after prolonged degassing at $600 °C$ in ultrahigh vacuum. The silicon surface was annealed at $300 °C$ to prevent surface etching, and hydrogenated in a partial pressure of activated hydrogen about 2×10^{-8} mbar for 20 min. The ARPES was measured along the Σ direction. At 800 eV kinetic energy the Si Brillouin zone is observed with an emission angle slightly smaller than $5°$. The measured photoemission map was integrated over the spectral intensity originated by two Brillouin zones. The Fermi level was obtained by measuring a clean Au(111) surface. The experimental data (crosses) are summarized in Fig. 1. One can distinguish the quasiparticle peaks between the Fermi level at zero and the bottom valence at -12 eV, followed by two prominent satellite structures, each at a mutual distance of about 17 eV, as well as a more weakly visible third satellite between -52 and -60 eV. These structures are obviously related to the 17 eV silicon bulk plasmon [21,22].

The exact one-electron Green's function $\mathcal{G}$ is described by an equation of motion with the form of a functional differential equation [23],

$$\mathcal{G} = \mathcal{G}_0 + \mathcal{G}_0 V_H \mathcal{G} + \mathcal{G}_0 \varphi \mathcal{G} + i \mathcal{G}_0 v_c \frac{\delta \mathcal{G}}{\delta \varphi}. \quad (1)$$

Here $\mathcal{G}_0$ is the noninteracting Green's function, φ is a fictitious external perturbation that is set to zero at the end of the derivation, v_c is the bare Coulomb interaction, and all quantities are understood to be matrices in space, spin, and time. The Hartree potential V_H gives rise to screening to all orders. Linearizing V_H with respect to φ yields [24]
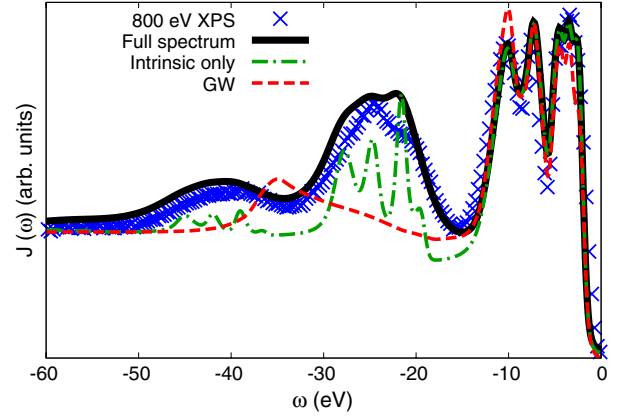

FIG. 1 (color online). Experimental XPS spectrum of Si at 800 eV photon energy (blue crosses), compared to the theoretical intrinsic $A(\omega)$ calculated from $G_0 W_0$ (red dashed line), and from Eq. (4) (green dot-dashed line). On top of the latter the black solid line also includes extrinsic and interference effects. All spectra contain photoabsorption cross sections, a calculated secondary electron background and 0.4 eV Gaussian broadening to account for finite k-point sampling and experimental resolution. The Fermi energy is set to 0 eV.

$$\mathcal{G}(t_1 t_2) = \mathcal{G}_H^0(t_1 t_2) + \mathcal{G}_H^0(t_1 t_3)\bar{\varphi}(t_3)\mathcal{G}(t_3 t_2)$$
$$+ i \mathcal{G}_H^0(t_1 t_3)\mathcal{W}(t_3 t_4)\frac{\delta \mathcal{G}(t_3 t_2)}{\delta \bar{\varphi}(t_4)}, \quad (2)$$

where $\bar{\varphi}$ is equal to φ screened by the inverse dielectric function, $\mathcal{W}$ is the screened Coulomb interaction, and $\mathcal{G}_H^0$ is the Green's function containing the Hartree potential at vanishing $\bar{\varphi}$; only time arguments are displayed explicitly and repeated indices are integrated. This linearization preserves the main effects of $\mathcal{W}$ and hence of plasmons. With the additional approximation $\frac{\delta \mathcal{G}(t_3 t_2)}{\delta \bar{\varphi}(t_4)} \simeq \mathcal{G}(t_3 t_4)\mathcal{G}(t_4 t_2)$ one obtains the Dyson equation $\mathcal{G} = \mathcal{G}_H^0 + \mathcal{G}_H^0 \Sigma \mathcal{G}$ in the GWA for the self-energy Σ. However this approximation can be problematic. For the following analysis we use the standard $G_0 W_0$ approach, where $\mathcal{G}_0$ is taken from a local-density approximation calculation and $\mathcal{W}_0$ is the screened interaction in the random phase approximation. Figure 2 shows the $G_0 W_0$ spectral function $A(\omega) = \frac{1}{\pi}|\text{Im}\Sigma(\omega)|/\{[\omega - \varepsilon_H - \text{Re}\Sigma(\omega)]^2 + [\text{Im}\Sigma(\omega)]^2\}$ of Si [25] at the Γ point, for the top valence (solid line) and bottom valence (dashed), respectively. The top valence shows a sharp quasiparticle peak followed by a broad, weak satellite structure at about -21 eV. This peak stems from the prominent peak in ImΣ (full circles) at about -18 eV, itself due to the plasmon peak in Im$\mathcal{W}$. It is a typical plasmon satellite, though (cf. [7]), the QP-satellite spacing is slightly overestimated because the term $\omega - \varepsilon_H - \text{Re}\Sigma$ (full squares) in the denominator of the expression for $A(\omega)$ is not constant. However the GWA has a more severe problem: for the bottom valence, the satellite structure at about -36 eV is much too far from the QP
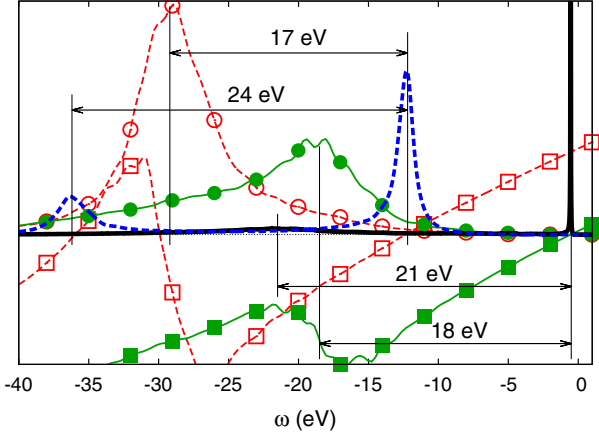
FIG. 2 (color online). G_0W_0 spectral function of bulk silicon for the top and bottom valence bands at the Γ point (black solid and blue dashed lines, respectively). The corresponding imaginary parts of the self-energy (red empty circles and dashed line, and green full circles and solid-line) and $\omega - \varepsilon_H - \mathrm{Re}\Sigma$ (red empty squares and dashed line, and green full squares and solid line) are also shown. The Fermi energy is set to 0 eV.

peak at about -12 eV, and much too sharp. This satellite does not correspond to a plasmon peak in ImΣ (empty circles), but to a zero in $\omega - \varepsilon_H - \mathrm{Re}\Sigma$ (empty squares) in the denominator of $A(\omega)$, as for a QP peak. It has been interpreted in the HEG as a *plasmaron*, a coupled hole-plasmon mode [26], but as noted below it is an artifact of the GWA [27,28]. Figure 1 compares the total *GW* spectral function (dashed red line) summed over all valence bands and k points, with our XPS data. The effects of cross sections are included by projecting on angular momenta in atomic spheres using the atomic data of Ref. [29]. The secondary electrons' background at energy ω was determined by integrating the calculated intrinsic spectral intensity between ω and the Fermi level, similar to [22]. A constant scaling factor was set such that the measured photoemission intensity at the highest binding energy (60 eV), where primary electrons intensity is absent, is reproduced. As expected, the dominant QP spectrum is well described by *GW*, but the satellite is dominated by the plasmaron around -36 eV, in complete disagreement with experiment. The experimental plasmon satellite at about -25 eV appears only as a weak shoulder in the GWA. Thus the plasmaron peak is responsible for the GWA failure [27,28] in silicon.

Vertex corrections are required to go beyond the GW self-energy. However, adiabatic vertex corrections (see, e.g., [30]) only lead to renormalization of energies and do not create new structures. Thus alternatively, we concentrate here on dynamical effects, and we choose to approximate directly Eq. (2), without passing through a self-energy.

We decouple Eq. (2) approximately by supposing that G and G_H are diagonal in the same single particle basis.

Equation (2) is then applicable separately for every single matrix element of G and each state couples independently to the neutral excitations of the system through W [31]. The latter can now be understood as the screened intra-orbital Coulomb matrix element for the chosen state. Such a decoupling approximation can be optimized [27,28] by adding and subtracting a self-energy correction, hence by using a QP Green's function G_Δ obtained from a good QP self-energy instead of G_H. Since the GWA is currently the state-of-the art for QP properties, we suppose that for every decoupled state k, $G_\Delta^k(\tau) = i\theta(-\tau)e^{-i\varepsilon_k\tau}$ is determined from $\Sigma^{GW}(\varepsilon_k)$, where $\varepsilon_k = \varepsilon_k^0 + \Sigma^{GW}(\varepsilon_k)$ is the (complex) *GW* quasiparticle energy and $\tau = t_1 - t_2$. Now Eq. (2) can be solved exactly for each state. Briefly the main steps are: (i) solve the noninteracting ($W = 0$) version of (2), which leads to an explicit solution G_Δ^φ; (ii) iterate the result $G = G_\Delta^\varphi - G_\Delta^\varphi \Delta G + iG_\Delta^\varphi W \frac{\delta G}{\delta\bar\varphi}$ starting from $G^{(0)} = G_\Delta^\varphi$. Here Δ compensates for the self-energy insertion used for the optimized decoupling; (iii) use the exact relation $\frac{\delta G_\Delta^\varphi(t_3 t_2)}{\delta\bar\varphi(t_4)} = G_\Delta^\varphi(t_3 t_4)G_\Delta^\varphi(t_4 t_2) = iG_\Delta^\varphi(t_3 t_2)\theta(t_2 - t_4)\theta(t_4 - t_1)$ to derive

$$G(t_1 t_2) = G_\Delta(\tau)e^{i\Delta\tau}e^{i\int_{t_1}^{t_2} dt'[\bar\varphi(t') - \int_{t'}^{t_2} dt'' W(t't'')]}. \quad (3)$$

The equilibrium solution is obtained setting $\bar\varphi = 0$.

In silicon, where the peaks in the loss function are well defined, it is justified to use a single plasmon pole model $W(\tau) = -i\lambda_k\{e^{-i\tilde\omega_k\tau}\theta(\tau) + e^{i\tilde\omega_k\tau}\theta(-\tau)\}$ with plasmon energy $\tilde\omega_k$ and intrinsic strengths λ_k for each matrix element of W. Besides $\bar\varphi$, the total exponent becomes then $a_k[e^{i\tilde\omega_k\tau} - 1]$ with $a_k = \lambda_k/\tilde\omega_k^2$ obtained from the corresponding *GW* results. We find that a_k varies around 0.3. Taylor expansion of the exponential leads then to the spectral function

$$A_k(\omega) = \frac{e^{-a_k}}{\pi}\sum_{n=0}^\infty \frac{a_k^n}{n!}\frac{\Gamma_k}{(\omega - \epsilon_k + n\tilde\omega_k)^2 + \Gamma_k^2}, \quad (4)$$

where $\epsilon_k = \mathrm{Re}[\varepsilon_k]$ and $\Gamma_k = \mathrm{Im}[\varepsilon_k]$. Equation (4) is similar to the plasmon pole version of the CE (cf. Ref. [13]). However here the exponential solution arises from a straightforward approximation to the fundamental differential equation (1): the linearization of the Hartree potential reveals the boson of the model (i.e., the plasmon *via* peaks in W), and the diagonal approximation of G gives rise to each isolated fermion. Our results are summarized in Fig. 1. The dot-dashed line gives the result of this procedure together with the cross sections and the secondary electron background. The shapes of the QP peaks change little with respect to *GW*, but now the full series of satellites is present. The internal structure of the satellites which originate from the multiple valence bands, is also reproduced. This validates the decoupling approximation in the dense valence band region where, contrary to the case of an isolated core level, its success is *a priori* far from

obvious. However, the intensity of the observed satellites is significantly underestimated. This discrepancy is similar to that found for the CE in simple metals, where extrinsic losses were suggested as a likely cause [14]. These might also be reduced by interference effects [32]. To check this possibility we estimated the contributions from both effects to the satellite strengths a_k using Eq. (32) and (36) of Ref. [33]. This approach uses a plasmon pole model, Inglesfield fluctuation potentials, and an average over hole position that takes account of the photoelectron mean free path λ [33]. We observe that the averaged total satellite line shape in this model is similar to that for the intrinsic part, with a width $\gamma \approx 2$ eV due to plasmon dispersion. Thus we can approximate the extrinsic and interference effects by renormalizing the intrinsic satellite intensity, i.e., by the replacement $\bar{a}_k = a_k + a^{\mathrm{ext}} + a^{\mathrm{inf}}$ in Eq. (4). These quantities are evaluated with $\omega_p = 16.7$ eV and $\lambda = 17.5$ Å at 800 eV for Si, yielding $a^{\mathrm{ext}} = 0.63$ and $a^{\mathrm{inf}} = -0.11$. This also modifies the strength $Z_k = e^{-\bar{a}_k}$ of the QP peaks, but preserves overall normalization. The broadening of the satellites must also be increased, $\Gamma \rightarrow \Gamma + n\gamma$. The total spectrum thus obtained (black line) is in unprecedented agreement with experiment. We stress that this result contains no fit parameters besides the two scaling factors (for spectrum and background) due to the arbitrary units of the experiment.

The success of our present approach stresses the need to go beyond the GWA. The exponential representation of G implicitly corresponds to a vertex correction $\tilde{\Gamma} = -\frac{\delta G^{-1}}{\delta\bar{\varphi}}$ to the self-energy. Since our derivation yields G as a function of the screened potential $\bar{\varphi}$ (3), this functional derivative can be performed explicitly, using $-\frac{\delta G^{-1}}{\delta\bar{\varphi}} = G^{-1}\frac{\delta G}{\delta\bar{\varphi}}G^{-1}$. From Eq. (3), a straightforward derivative of G contains a series of satellite contributions. The two inverse Green's functions lead to a significant complication, because they contain the inverse of this series. This clearly illustrates the difficulty of modeling $\tilde{\Gamma}$ in order to treat dynamical effects. It suggests rather to concentrate on modeling $\frac{\delta G}{\delta\bar{\varphi}}$, where the various contributions are simply summed, and hence to search for a self-energy of the form $\Sigma = -iW\frac{\delta G}{\delta\bar{\varphi}}G^{-1}$ instead of $\Sigma = iGW\tilde{\Gamma}$. In conclusion, on the basis of our experimental XPS data we have analyzed the failure of GW to reproduce plasmon satellites and linked this failure to the appearance of an artificial plasmaron peak. On the other hand, GW results are fair when the imaginary part of Σ, hence the intensity of the corresponding plasmon, is small enough so that no sharp plasmaron is created. Thus surprisingly, one might expect GW to work better in describing satellites stemming from local plasmon or interband excitations close to the Fermi level in "strongly correlated" materials than for the strong plasmon structures in conventional semiconductors. Starting from the fundamental equations of MBPT we have derived an exponential solution to the one-particle Green's function,

analogous to that from the CE, that overcomes the drawbacks of the GWA. Comparison to new photoemission data shows that this yields a very good description of the spectral function of bulk silicon, including the satellites series. By calculating the secondary electron background, cross section corrections as well as a correction for extrinsic and interference effects, we achieve an agreement between theory and experiment that can be considered as a benchmark. Our derivation also suggests how the results can be improved in cases where the presently used approximations are inadequate. Finally, by accessing an expression for the vertex function, our approach yields precious hints for directions to take in modeling dynamical effects beyond the GWA.

---

*matteo.guzzo@polytechnique.edu
†lucia.reining@polytechnique.fr

[1] F. Aryasetiawan and O. Gunnarsson, Rep. Prog. Phys. **61**, 237 (1998).

[2] W. G. Aulbur, L. Jonsson, and J. W. Wilkins, Solid State Phys. **54**, 1 (2000).

[3] A. Georges, G. Kotliar, W. Krauth, and M. J. Rozenberg, Rev. Mod. Phys. **68**, 13 (1996).

[4] G. Kotliar et al., Rev. Mod. Phys. **78**, 865 (2006).

[5] F. Offi et al., Phys. Rev. B **76**, 085422 (2007).

[6] L. Hedin, Phys. Scr. **21**, 477 (1980).

[7] L. Hedin, J. Phys. Condens. Matter **11**, R489 (1999).

[8] P. Nozières and C. De Dominicis, Phys. Rev. **178**, 1097 (1969).

[9] D. Langreth, Phys. Rev. B **1**, 471 (1970).

[10] F. Bechstedt, Principles of Surface Physics (Springer, New York, 2003), Chap. 5, pp. 199–201.

[11] L. Hedin, Phys. Rev. **139**, A796 (1965).

[12] L. Hedin and S. Lundqvist, Solid State Physics (Academic Press, New York, 1969), Vol. 23.

[13] F. Aryasetiawan, Phys. Rev. B **46**, 13 051 (1992).

[14] F. Aryasetiawan, L. Hedin, and K. Karlsson, Phys. Rev. Lett. **77**, 2268 (1996).

[15] M. Vos et al., Phys. Rev. B **66**, 155414 (2002).

[16] A. S. Kheifets et al., Phys. Rev. B **68**, 233205 (2003).

[17] B. Holm and F. Aryasetiawan, Phys. Rev. B **56**, 12 825 (1997).

[18] M. Vos, A. S. Kheifets, E. Weigold, and F. Aryasetiawan, Phys. Rev. B **63**, 033108 (2001).

[19] F. Polack et al., AIP Conf. Proc. **1234**, 185 (2010).

[20] N. Bergeard et al., J. Synchrotron Radiat. **18**, 245 (2011).

[21] J. Stiebling, Z. Phys. B **31**, 355 (1978).

[22] L. Ley, S. Kowalczyk, R. Pollak, and D. A. Shirley, Phys. Rev. Lett. **29**, 1088 (1972).

[23] L. P. Kadanoff and G. Baym, Quantum Statistical Mechanics (W. A. Benjamin Inc., New York, 1964).

[24] G. Lani, P. Romaniello, and L. Reining, arXiv:1103.1630.
[25] A. Fleszar and W. Hanke, Phys. Rev. B **56**, 10 228 (1997).
[26] B. Lundqvist, Z. Phys. B **6**, 193 (1967); Phys. Kondens. Mater. **7**, 117 (1968).
[27] C. Blomberg and B. Bergersen, Can. J. Phys. **50**, 2286 (1972).
[28] B. Bergersen, F. Kus, and C. Blomberg, Can. J. Phys. **51**, 102 (1973).
[29] J. Yeh and I. Lindau, At. Data Nucl. Data Tables **32**, 1 (1985).

[30] R. Del Sole, L. Reining, and R. W. Godby, Phys. Rev. B **49**, 8024 (1994).
[31] In a similar spirit the equation of motion for the Green's function is decoupled in: C.-O. Almbladh and L. Hedin, *Handbook on Synchrotron Radiation* (North-Holland, Amsterdam, 1983), Chap. 8.
[32] F. Bechstedt, K. Tenelsen, B. Adolph, and R. DelSole, Phys. Rev. Lett. **78**, 1528 (1997).
[33] L. Hedin, J. Michiels, and J. Inglesfield, Phys. Rev. B **58**, 15 565 (1998).

Valence-band satellites in photoemission spectroscopy

TEMPO beamline
Valence electron photoemission spectrum of
semiconductors : ab initio description of multiple satellites

M. Guzzo*, G. Lani, F. Sottile, P. Romaniello, M. Gatti, J. J. Kas, J. J. Rehr, M. G. Silly, F. Sirotti and L. Reining

Physical Review Letters 107 (2011), 166401

* Laboratoire des Solides Irradiés, École Polytechnique, CNRS, CEA-DSM, 91128 Palaiseau, France; European Theoretical Spectroscopy Facility (ETSF). matteo.guzzo@polytechnique.edu

The experimental valence band photoemission spectrum of semiconductors is typically used to extract information about the band structure of materials. Satellites are much less explored, both experimentally and theoretically. The state-of-the-art approach to calculate bandstructures, the GW approximation, often fails to describe these many-body effects. Taking silicon as a prototypical example, we compare experimental high energy photoemission spectra with GW calculations and analyze the origin of the GW failure. We then show how to go beyond GW in a systematic way. Our calculated spectrum, including cross sections, secondary electrons, and an estimate for extrinsic and interference effects, is in unprecedented agreement with experiment down to 60 eV from the Fermi energy.

Photoemission is a prominent tool to access information about electronic structure and excitations in materials. Thanks to their high intensity and broad photon energy range, modern synchrotron sources can provide detailed insight. The interpretation of the experimental data is far from obvious, and theory is an essential complementary tool. However, ab initio calculations typically focus on bulk band structure; thus surface effects are ignored, and satellites are not included. The latter are a pure many-body effect due to coupling of primary photoexcitation to neutral excitations of the material, such as plasmons.

Plasmon satellites have been extensively studied in core-level photoemission experiments [1]. There they can be described by a model where a single dispersionless fermion couples to bosons [2], which yields a description consistent with experimental observations. In the valence region, plasmon satellites are much less studied theoretically, even though *ab initio* approaches can provide a good starting point. At high photoelectron energies the photoemission spectrum is approximately proportional to the intrinsic spectral function $A(\omega)=1/\pi|\mathrm{Im}G(\omega)|$, where G is the one-particle Green's function. The latter is typically calculated using the widely used GW approximation (GWA) [2]. In principle, the GWA contains correlations effects beyond the quasiparticle approximation. However, these additional features are rarely calculated due to computational complexity and, more importantly, serious discrepancies between GWA and experiment.

We have proposed an approximate differential equation for the one-particle Green's function with an exponential solution that contains multiple plasmon excitations through the dynamical screening of the material. Extrinsic effects due to the losses of the outgoing electron through bulk and surface [3], as well as interference effects [2,3], can be straightforwardly included in this formulation, on top of the intrinsic satellites created by the photoemission hole and contained in $A(\omega)$.

The performance of the approach could be assessed thanks to benchmark measurements performed on the UHV photoemission experimental station of the TEMPO beamline. The experimental spectrum was obtained by integrating over almost ten degrees angular resolved photoemission of a Si(001) surface. At 800 eV photon energy along the Σ direction this is equivalent to the emission of two Brillouin zones. To prevent surface oxidation, the surface was hydrogenated in a partial pressure of activated hydrogen under a pressure of 10^{-8} mbar.

The calculated intrinsic spectral function of our approach reproduces the observed series of multiple satellites with correct positions; extrinsic and interference effects are crucial to describe the weight of the satellites with respect to the quasiparticle peaks.
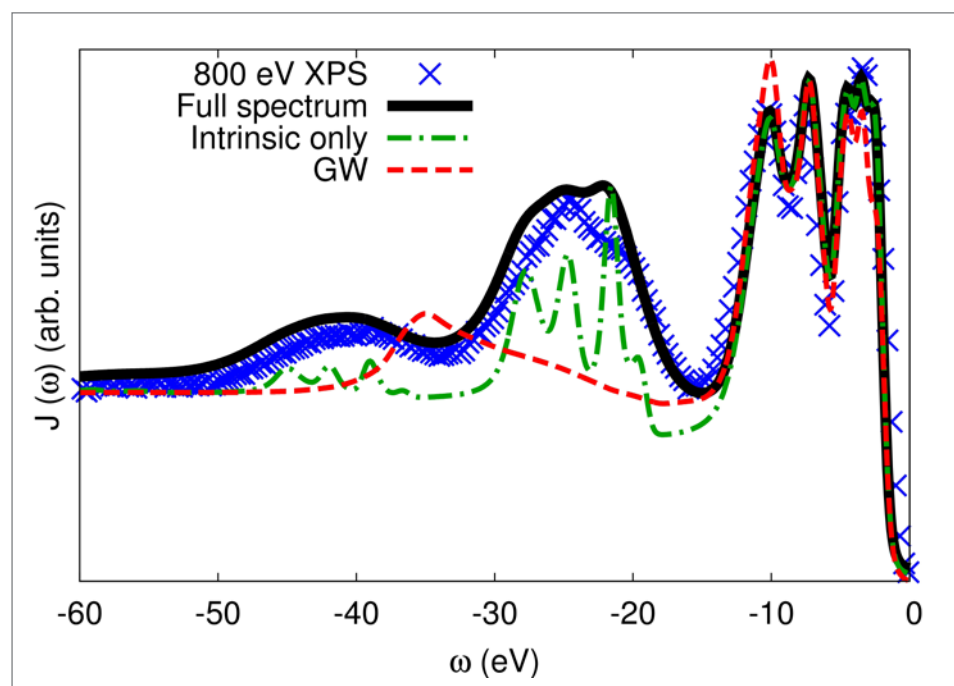

Figure 1: Experimental XPS spectrum of Si at 800 eV photon energy (blue crosses), compared to the theoretical intrinsic A(ω) calculated from GW (red dashed), and from the exponential solution for G (green dot-dashed). On top of the latter the black solid line also includes extrinsic and interference effects. All spectra contain photoabsorption cross sections, a calculated secondary electron background and 0.4 eV Gaussian broadening to account for finite k-point sampling and experimental resolution. The Fermi energy is set to 0 eV.

References:

[1] see e.g. F. Bechstedt, "Principles of surface physics," (Springer, 2003) Chap. 5; F. Offi et al. Phys. Rev. B 2007 76, 085422
[2] L. Hedin, J. Phys.: Cond. Mat. 1999 11, R489
[3] L. Hedin et al. Phys. Rev. B 1998 58, 15565

Regular Article

Plasmon satellites in valence-band photoemission spectroscopy

Ab initio study of the photon-energy dependence in semiconductors

M. Guzzo[1,a,b], J.J. Kas[2], F. Sottile[1,b], M.G. Silly[3], F. Sirotti[3], J.J. Rehr[2], and L. Reining[1,b]

[1] Laboratoire des Solides Irradiés, École Polytechnique, CNRS, CEA-DSM, 91128 Palaiseau, France
[2] Department of Physics, University of Washington, Seattle, 98195 WA, USA
[3] Synchrotron-SOLEIL, BP 48, Saint-Aubin, 91192 Gif sur Yvette Cedex, France

Abstract. We present experimental data and theoretical results for valence-band satellites in semiconductors, using the prototypical example of bulk silicon. In a previous publication we introduced a new approach that allows us to describe satellites in valence photoemission spectroscopy, in good agreement with experiment. Here we give more details; we show how the the spectra change with photon energy, and how the theory explains this behaviour. We also describe how we include several effects which are important to obtain a correct comparison between theory and experiment, such as secondary electrons and photon cross sections. In particular the inclusion of extrinsic losses and their dependence on the photon energy are key to the description of the energy dependence of spectra.

1 Introduction

Photoemission spectroscopy (PES) is an established tool for the analysis of the electronic structure of solids and molecules. Its increasing capability in energy-resolution and flexibility has made more urgent the need for advanced theoretical approaches able to cope with the huge range of systems being measured and with the high precision needed to match the experiment [1]. One powerful and commonly used framework is based on the one-particle Green's function $G(\mathbf{x}, \mathbf{x}', t, t')$ [2], which describes the propagation of one particle in the system. A popular approximation for the propagator is the GW approximation [3], which has proven to be successful in a variety of systems calculations of photoemission band gaps [4,5]. The quantity to be compared with experiment is the one-particle spectral function $A(\omega)$ which is proportional to the imaginary part of G. The main features of the spectral function $A(\omega)$ are quasiparticle (QP) peaks with finite lifetime. In addition, the spectral function shows incoherent satellite structures. In sp semiconductors these satellites are mainly due to the excitation of plasmons (both surface and bulk). Satellites in photoemission spectroscopy have been extensively studied for core-level spectra [6–8], while for valence-band spectroscopy there has been much less effort [9–11]. Still, valence-band satellites have been measured in a number of systems and are at the center of the debate around some highly interesting systems like tran-

sition metal oxides. In a previous work [12] we introduced a new method to describe satellites with an improved description of the intrinsic spectral function, including effects beyond the latter. In particular our method includes the dependence of the spectrum on photon energy. In this paper we present details of the method. We also show how the photoemission spectrum of silicon depends on the photon energy and we give a prediction for the trend at very high photon energies.

1.1 The sudden approximation and the three-step model

When making comparisons between theory and experiment, it is worth noting that there is not a complete coincidence between the spectral function $A(\omega)$ and the PES spectrum. This is because $A(\omega)$ only describes the propagation of the hole created by the incoming photon, while completely neglecting the losses of the photoelectron before it leaves the system. The use of $A(\omega)$, within these limits, to describe PES is known as the *sudden approximation*. While this approximation simplifies the description of PES, it is safe to say that it is never actually true. In fact it turns out that the losses of the outgoing photoelectrons are roughly the same at all photon energies. This is the result of two competing processes [6]:

(i) the reduction of the inelastic scattering cross section of electrons as their kinetic energy increases. As the photon energy increases, the average kinetic energy

[a] e-mail: matteo.guzzo@polytechnique.edu
[b] European Theoretical Spectroscopy Facility (ETSF), http://www.etsf.eu

of the electrons in the solid will increase. With it, the average loss probability per electron will decrease;

(ii) the increase of the mean free path of electrons as their kinetic energy increases. A larger mean free path will correspond to a greater maximum depth of a hole for which the corresponding photoelectron is fast enough to reach the surface and be detected. This implies that, on average, electrons will have to travel through a thicker layer of atoms before escaping the material. This way, the energy-loss probability will increase.

These two phenomena make the losses of the photoelectrons non-negligible at any photon energy. The good news is that the effect of these losses on the QP part of the spectrum is often only an overall renormalization of the peaks, which explains the success of the sudden approximation for the description of QP band structures. However, an appropriate calculation and interpretation of satellite structures in photoemission spectra requires one to go beyond the sudden approximation. A more complete, yet simplistic way of modeling the photoemission process is to divide it in three independent sequential steps:

1. optical excitation of the electron in the bulk;
2. travel of the excited electron to the surface;
3. escape of the photoelectron into vacuum.

This is known as the *three-step* model, as first proposed by Berglund and Spicer [13]. The total photoemission intensity is then given by the product of the probabilities of the three different processes. The first step is described by the one-particle spectral function $A(\omega)$. Losses coming from $A(\omega)$ are called *intrinsic* [6]. Step two is described by the electron energy-loss spectrum of the system and, along with step three, is considered part of the *extrinsic* losses. At this point, to get the total intensity, it would be sufficient to convolute $A(\omega)$ with the energy-loss spectrum. This case is referred to as the *sudden limit* [6]. However, this condition is met only at very high photon energies that are rarely accessed in usual PES conditions. In fact, there is quantum-mechanical interference between intrinsic and extrinsic losses, which is due to the interaction between the outgoing photoelectron and the hole it has left behind. The changes occurring in the photoemission spectrum following this kind of process, are referred to as *interference effects*. To describe this kind of processes one should in principle make use of a two-particle propagator [14], but it is possible to treat this effect in an approximate way retaining at the same time a good deal of physical insight. Within this picture, we use an optimized three-step model that attempts to overcome the shortcomings of its original formulation.

2 Theoretical framework

Our method is based on the exact equation of motion of the fully-interacting 1-particle electronic Green's function $G_\sigma(\mathbf{x}, \mathbf{x}', t, t')$. The equation reads [15]

$$G = G_0 + G_0 V_H G + G_0 \varphi G + i G_0 v_c \frac{\delta G}{\delta \varphi}, \quad (1)$$

where G_0 is the non-interacting Green's function, φ is a fictitious external perturbation that is set to zero at the end of the derivation, v_c is the bare Coulomb interaction, and all quantities are understood to be matrices in space, spin, and time. The Hartree potential V_H gives rise to screening to all orders. Spin only gives rise to a factor of 2, since we are interested here in non-magnetic systems where G is spin-diagonal.

2.1 Decoupling approximation for the Green's function

Linearizing V_H with respect to φ and assuming G and G^H diagonal on the same discrete basis yields a scalar equation for each matrix element $\mathcal{G} = G_{ii}$ which corresponds to a single state of the system [12,16]:

$$\mathcal{G}(t_1 t_2) = \mathcal{G}_H^0(t_1 t_2) + \mathcal{G}_H^0(t_1 t_3)\bar{\varphi}(t_3)\mathcal{G}(t_3 t_2)$$
$$+ i\mathcal{G}_H^0(t_1 t_3)\mathcal{W}(t_3 t_4)\frac{\delta \mathcal{G}(t_3 t_2)}{\delta \bar{\varphi}(t_4)}, \quad (2)$$

where $\mathcal{G}_H^0$ is the Hartree Green's function in the limit of vanishing external potential; $\bar{\varphi} = \varepsilon^{-1}\varphi$ is the screened external perturbation potential;

$$\mathcal{W}(t_3 t_4) = \int dr dr' |\phi(r)|^2 |\phi(r')|^2 W(rr' t_3 t_4) \quad (3)$$

is a diagonal matrix element of the screened Coulomb interaction W; ϕ is the single-particle wavefunction of the corresponding state; and ε^{-1} is the inverse microscopic dielectric function. It is worth noting that in equation (2) the approximation $\delta G/\delta\bar{\varphi} = GG$ – which corresponds to the Random-Phase Approximation (RPA) for the response to the screened external potential $\bar{\varphi}$ – gives back the GW approximation [3], which is hence included in the current approximation. The solution of equation (2) at vanishing φ, for a single occupied state, is

$$\mathcal{G}(t_1 t_2) = \mathcal{G}_H^0(t_1 t_2) \exp\left[-i\int_{t_1}^{t_2} dt' \int_{t'}^{t_2} dt'' \mathcal{W}(t' t'')\right]. \quad (4)$$

We assume that $\mathcal{W}$ can be represented by a sum of N_p poles $\tilde{\omega}_j$ with strength λ_j, which is exact for infinite N_p:

$$\mathcal{W}(\tau) = \sum_j^{N_p} \lambda_j \left[e^{i\tilde{\omega}_j \tau}\theta(-\tau) + e^{-i\tilde{\omega}_j \tau}\theta(\tau)\right], \quad (5)$$

where $\tau = t - t'$. Using equation (5), the double integration of $\mathcal{W}$ in equation (4) is then analytically feasible. Once this is carried out, the matrix elements of the Green's function read

$$\mathcal{G}(\tau) = i\theta(-\tau)e^{-i(\epsilon + i\Gamma)\tau} \exp\left[\sum_j^{N_p} a_j(1 - e^{i\tilde{\omega}_j \tau})\right], \quad (6)$$

with $a_j = \lambda_j/\tilde{\omega}_j^2$. In equation (6), the first exponent $\epsilon + i\Gamma$ is the *complex* QP energy within the GW approximation. The GW correction to the Hartree energy naturally

emerges from the integral of $\mathcal{W}$ in equation (4), provided that the same level of approximation is used for $\mathcal{W}$ in the GW self energy. The second exponential term provides for renormalization and formation of satellites at all orders. After having expanded and Fourier-transformed the latter, $A(\omega) = 1/\pi |\text{Im}\mathcal{G}(\omega)|$ becomes

$$
A(\omega) = \frac{\Gamma}{\pi} e^{-\sum_j^{N_p} a_j} \left[\frac{1}{(\omega - \epsilon)^2 + \Gamma^2} \right.
$$
$$
+ \sum_j^{N_p} \frac{a_j}{(\omega - \epsilon + \tilde{\omega}_j)^2 + \Gamma^2}
$$
$$
+ \frac{1}{2} \sum_{jk}^{N_p} \frac{a_j a_k}{(\omega - \epsilon + \tilde{\omega}_j + \tilde{\omega}_k)^2 + \Gamma^2}
$$
$$
\left. + \frac{1}{6} \sum_{jkl}^{N_p} \frac{a_j a_k a_l}{(\omega - \epsilon + \tilde{\omega}_j + \tilde{\omega}_k + \tilde{\omega}_l)^2 + \Gamma^2} + \cdots \right].
$$
$$(7)$$

Equation (7) shows how the spectral function can be expanded as a sum of poles, which are regrouped here in different terms following the corresponding order. The zeroth order (first term) is the QP peak, centered at the QP energy ϵ. The following terms are centered at $\omega - n\tilde{\omega}_j$ (at order n, giving rise to the n-th satellite replica for that frequency) with a weight decreasing exponentially with n. In general, the weights a_j are of the order of $0.1/N_p$.

The electron energy-loss function of bulk silicon has a well-defined single-peaked shape, centered at 16.7 eV. This fact justifies the use of a single plasmon-pole model which is equivalent, in the above formulation, to the case $N_p = 1$.

2.2 Calculation of extrinsic losses and interference effects

In order to take the extrinsic and interference terms into account, we use the theoretical formalism of Hedin, Michiels, and Inglefield [6], which includes all three effects, i.e., intrinsic, extrinsic, and interference. In addition, the theory is based on a semi-infinite model of the system, and thus the satellite spectrum depends on the average distance traveled by the photo-electron through the surface. However, these calculations use a rather crude approximation for the valence electrons, treating them as localized states. The strategy is thus to use this complete model to calculate the extrinsic and interference terms only, replacing the intrinsic contribution with the more rigorous calculations detailed in the previous section. One might worry that the intrinsic spectrum would then not include effects due to the semi-infinite model. However, we find that the intrinsic spectrum is quite insensitive to distance from the surface. The theory accounts for the satellites in the PES spectrum in terms of a spectral function $A(\omega)$ of exponential form consistent with equation (7), which allows us to combine the two approaches. In this approach

the photocurrent is given by

$$
\langle J_k(\omega) \rangle = \sum_i |M_{ik_0}|^2 \int_0^\infty e^{-a} \int_{-\infty}^\infty e^{i(\omega_0 - \epsilon_k + \epsilon_i)t} \tag{8}
$$

$$
\times \exp \left[\int \gamma_{ik}(\omega)(e^{-i\omega t} - 1) \, d\omega \right] dt \, dz_c, \tag{9}
$$

where

$$
a \approx \int d\omega \, \gamma_{ik}(\omega) = 2z_c \text{Im}\tilde{k} + a_{int}^i. \tag{10}
$$

Here ω_0 is the photon-frequency, $k_0 = \sqrt{2(\omega_0 + \epsilon_i)}$ is the photo-electron momentum at threshold, and we have made the approximation that the matrix elements $M_{ik} = \langle i|d|k \rangle$ are roughly constant over the range of photo-electron energies of interest, i.e., from a few multiples of the plasmon energy below the photon energy to threshold where $\epsilon_k = \omega$. The function $\gamma_{ik}(\omega)$ characterizes the losses due to the excitation of single plasmons of energy $\omega_{\mathbf{q}}$ and can be split into intrinsic, extrinsic and interference contributions,

$$
\gamma_{ik}(\omega) = \sum_{\mathbf{q}} |g_{\mathbf{q}}|^2 \delta(\omega - \omega_q) = \gamma_i^{int} + \gamma_k^{ext} + \gamma_{ik}^{inf}. \tag{11}
$$

We calculate the extrinsic and interference terms by assuming that the intrinsic amplitude is independent of the initial (valence) state, which gives the amplitudes,

$$
|g_{\mathbf{q}}| = \left| \frac{V^{\mathbf{q}}(z_c)}{\omega} + \frac{i}{\kappa} \int_{-\infty}^{z_c} e^{i(\tilde{k}-\kappa)(z-z_c)} V^{\mathbf{q}}(z) dz \right| \tag{12}
$$

where the solid occupies the space $z > 0$. The first term gives the intrinsic amplitude, while the second term gives the extrinsic, and the cross terms give the interference, i.e.,

$$
|g_q|^2 = |g_q^{\text{int}}|^2 + |g_q^{\text{ext}}|^2 + 2\text{Re}[g_q^{\text{int}} g_q^{\text{ext}}]. \tag{13}
$$

The complex wave numbers κ and $\tilde{k}$ are given by

$$
\kappa = \sqrt{2(\omega_0 + \phi + \epsilon_F + i\Gamma(\omega + \epsilon_k)) - |\mathbf{Q} + \mathbf{K}|^2}, \tag{14}
$$
$$
\tilde{k} = \sqrt{k^2 + 2(\phi + \epsilon_F + i\Gamma(\epsilon_k))}, \tag{15}
$$

and correspond to a time-inverted LEED state,

$$
|\tilde{k}\rangle = e^{i\mathbf{K}\cdot\mathbf{R}} \left[\theta(z)e^{-i\tilde{k}^* z} + \theta(-z)e^{-ikz} \right]. \tag{16}
$$

Here ϵ_F is the Fermi energy and ϕ is the work function. Further, bold capitals denote components of the vector perpendicular to the z direction (parallel to the surface). With the above definitions, $\epsilon_k = k^2$, and ω is measured relative to the valence binding energy so that the first detectable photo-electron comes at $\omega = \epsilon_k = 0$.

In order to evaluate the relative weights of various contributions to the PES signal, we use the Inglesfield fluctuation potential inside the solid (contributions outside being negligible) [6]. We then calculate the weight of the extrinsic and interference $a^{extinf}(\omega_0) = a^{ext}(\omega_0) + a^{inf}(\omega_0)$

Table 1. Values of the correction term a^{extinf} including extrinsic losses and interference effects and relative width (inverse lifetime) η for a set of photon energies ω_0.

ω_0 (eV)	a^{extinf}	η
200	0.432	2.882
480	0.479	1.085
800	0.530	0.570
1200	0.568	0.341
2000	0.609	0.178
5000	0.669	0.066
10000	0.703	0.027

contributions to the PES due to plasmons of energy $\omega_p = 16.7$ eV, at a given photon energy ω_0, i.e.,

$$a^{\mathrm{extinf}}(\omega_0) = \int dk \gamma_k^{\mathrm{ext}}(\omega_0) + \gamma_k^{\mathrm{inf}}(\omega_0). \qquad (17)$$

We incorporate these contributions in our total spectral function correcting the intrinsic contribution of Section 2.1 with the addition of $a^{extinf}(\omega_0)$ i.e.,

$$\bar{a}_i = a_i^{int} + a^{extinf}(\omega_0), \qquad (18)$$

where i denotes the valence state, a_i^{int} is the intrinsic weight of the pole as it appears in equation (7) for the case $N_p = 1$. We can also calculate the width of the extrinsic + interference satellites and account for this by replacing the widths Γ in equation (7), i.e.

$$\Gamma \rightarrow \Gamma + n\,\eta(\omega_0), \qquad (19)$$

η being the width (related to the dispersion of the plasmon) of the extrinsic plasmon peak at a given photon energy ω_0 and n the number of plasmon excitations involved, i.e. the order of the expansion in equation (7). Values of ω_0, a^{extinf} and η are listed in Table 1.

2.3 Additional effects

2.3.1 Lifetime of intrinsic plasmons

We must include a correction for the finite lifetime of intrinsic plasmons, which is infinite in (7) because of the plasmon-pole model we are using for the intrinsic part. Therefore, an additional width of 1.5 eV [17] is added to the inverse lifetime of extrinsic plasmons η.

2.3.2 Photon cross sections

Photon cross sections are taken from references [18,19]. For each element, the tables give the relative photon cross section of the atomic orbitals, calculated within the Hartree-Fock approximation. We have to use the atomic data for bulk silicon; since we are in a solid, the atomic character is mixed. The four valence bands of silicon contain two s electrons and two p electrons. The character of each band is calculated by projecting the wavefunctions
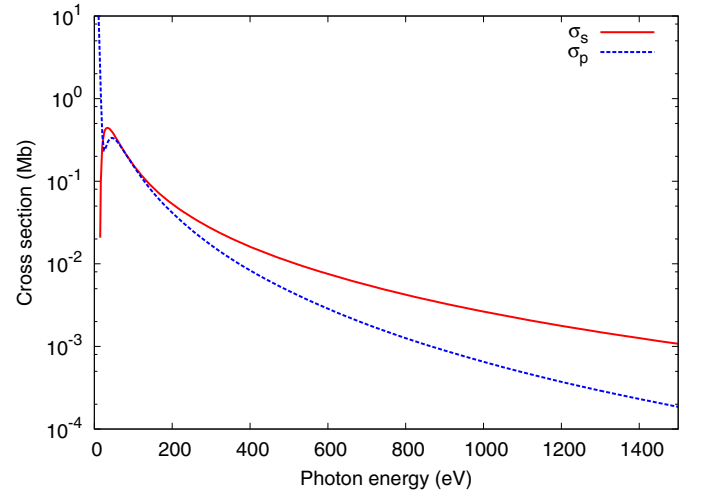

Fig. 1. (Color online) Photon cross sections, from reference [18]. Red solid line shows the values for the $3s$ electrons, while the blue dashed line shows the $3p$ electrons cross sections.

onto spherical harmonics inside a sphere centered on the Si ion. The s and p character of each band sum up to one. We have then the following values:

Band	#1	#2	#3	#4
s-type	0.95	0.75	0.25	0.05
p-type	0.05	0.25	0.75	0.95

In this picture, the relative weight of a photoemission peak will be the consequence of the s_k and/or p_k character of the corresponding state k. To include this effect in the spectral function, we can define an effective $\tilde{A}$ so that

$$\tilde{A}(\omega) = \sum_k (s_k \sigma_s + p_k \sigma_p) A_k(\omega), \qquad (20)$$

where A_k is the (intrinsic or corrected) spectral function of a single state k and σ_s and σ_p are the photon cross sections for s and p electrons, tabulated in references [18,19] and shown in Figure 1 up to 1500 eV. The inclusion of cross-section effects is very important to reproduce the relative weight of s and p peaks in the photoemission spectrum (which can differ by an order of magnitude) and the respective changes at different photon energies.

2.3.3 Secondary electrons

The background of secondary electrons is calculated using the effective intrinsic spectral function $\tilde{A}(\omega)$, assuming that each peak in the intrinsic spectrum produces a constant flux of secondary electrons (i.e. a step function) at all binding energies greater than the quasiparticle energy ϵ. This is commonly known as a *Shirley* background [20]. The calculation of the background is achieved by the following integration of $\tilde{A}(\omega)$:

$$\mathcal{B}(\omega) = \int_\omega^\mu d\omega' \tilde{A}(\omega'), \qquad (21)$$

where $\mathcal{B}$ is the background of secondary electrons. The final quantity that has to be compared with experimental data is given by the photocurrent $J(\omega)$ defined as:

$$J(\omega) = \alpha\tilde{A}(\omega) + \beta\mathcal{B}(\omega), \qquad (22)$$

where α and β are two parameters that must be fixed to match the signal/background ratio in the experimental data. β is to be determined using the high binding-energy limit (where $\tilde{A}(\omega) \sim 0$) and then we fix α so as to match the QP peak intensity. The calculated background could also be subtracted from the experimental curves, in case one wishes e.g. to evaluate the intensity of satellites (see below).

3 Experimental setup

Valence PES measurements were performed at the UHV photoemission experimental station of the TEMPO beamline [21] at the SOLEIL synchrotron radiation source. Linearly polarized photons from the Apple II type Insertion Device (HU44) were selected in energy using a high resolution plane grating monochromator with a resolving power $E/\Delta E = 5000$. The end-station chamber (base pressure 10^{-10} mbar) is equipped with a modified SCIENTA-200 electron analyzer with a delay-line 2D detector which optimizes the detection linearity and signal/background ratio [22]. The overall energy resolution was better than 200 meV. The photon beam impinges on the sample at an angle of $43°$, and photoelectrons were detected around the sample surface normal with an angular acceptance of $\pm 6°$. A doped n^+-type Si(001) wafer ($N_D \simeq 2 \times 10^{-18}P$ atoms/cm^3) was cleaned from the native oxide by flash annealing at 1100 °C after prolonged degassing at 600 °C in ultra-high vacuum. The silicon surface annealed at 300 °C to prevent surface etching was then hydrogenated in a partial pressure of activated hydrogen about 2×10^{-8} mbar for 20 min. At 800 eV kinetic energy the Si Brillouin zone (BZ) is observed with an emission angle slightly smaller than $5°$. The Fermi level was obtained by measuring a clean Au(111) surface. The measured photoemission map at 800 eV was integrated over the spectral intensity originated by two BZ. For lower photon energies it was not possible to have a complete integration of the BZ. Considering the ratio between satellites and QP peaks – which is a key quantity for our analysis – independent of the integration on the BZ (as our theory assumes), justifies the use of photon energies lower than 800 eV for comparison with theory.

4 Results

We have measured PES data for several photon energies between 200 and 800 eV. Using our procedure we have calculated the photoemission spectra for a range of photon energies between 200 eV and 10 keV. A standard GW calculation was performed using the ABINIT code [23]. The GW calculation was used to evaluate the
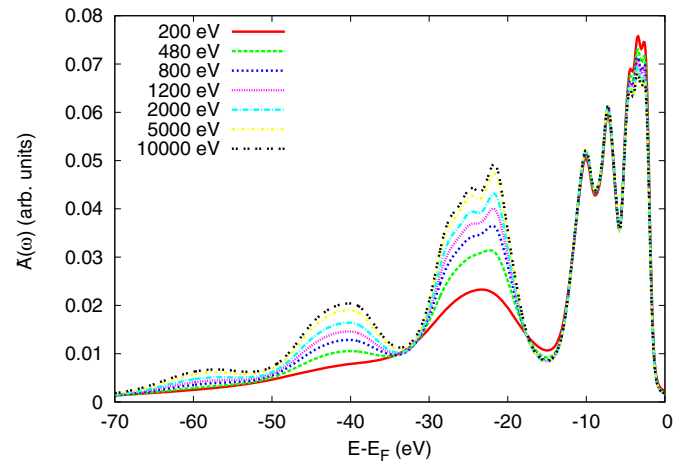

Fig. 2. (Color online) Calculated spectrum $\tilde{A}(\omega)$ for several photon energies between 200 eV and 10 keV. The spectra include the effect of cross sections and extrinsic losses. The curve intensities are aligned to match in the QP region, between -15 and 0 eV, to highlight the relative change of the satellite spectral weight, i.e. below -15 eV. The Fermi energy is at 0 eV.

parameters of equation (7), under the assumption that $\mathrm{Im}W \sim 1/\pi\,\mathrm{Im}\Sigma$ [24], hence using an RPA screening. We calculated the correction paramenters for extrinsic losses and interference effects as described earlier in Section 2.2, and eventually included cross-section effects as in equation (20). The graph in Figure 2 shows the calculated photoemission spectra $\tilde{A}(\omega)$ for a number of selected photon energies, from 200 eV to 10 keV. In this figure the intensity of the curves has been scaled so that the spectra match in the QP region. Varying the photon energy, there is a small change in the QP part of the spectrum – between -15 and 0 eV from the Fermi energy – due to cross-section effects[1]. The most apparent change is in the satellite part, i.e. below -15 eV, where three satellites are visible. Our calculations show that with increasing photon energy the satellites have a tendency to show more structures. More importantly, the relative weight of satellites increases as the photon energy increases. This trend is the same as the one found in the experimental data, as reported in Figure 3. In this figure we also include data from reference [25]. We assume a complete integration of the BZ. The ratio between the weight of the first satellite – taken between -33 and -15 eV – and the QP peaks has been calculated, both in the theoretical and experimental case, evaluating the integral under the curves. The calculated background has been removed from the experimental curves before the evaluation of the integrals. The set of experimental values is small with respect to what would be needed to perform an exhaustive comparison with theory. For smaller photon energies (between 200 and 400 eV), the ratios are systematically overestimated. Partial integration of the BZ, caused by the low photon energy used, is probably the cause of the overestimation

---

[1] Additional variations related to different integrations of the BZ (found in experiment) are here neglected.
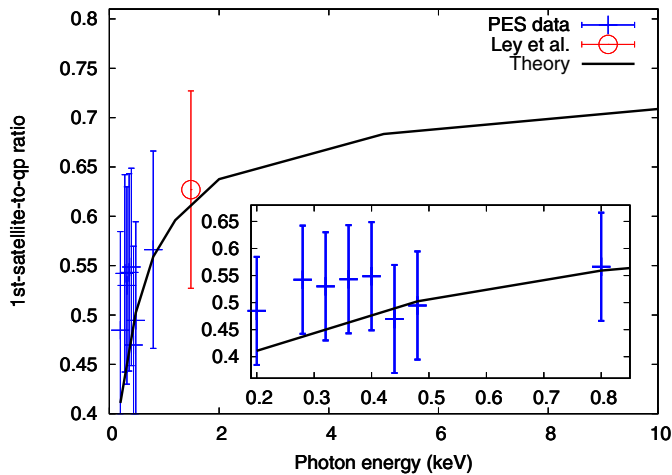
Fig. 3. (Color online) Intensity ratio between the first satellite and the QP part of the spectrum as a function of the photon energy. Our experimental data (blue crosses) are compared to theoretical calculation (black solid line). An additional point (red circle) taken from [25] has also been included for comparison. The inset shows a detail of the same plot.

of the satellite/QP ratio in these cases. In fact, the lower the photon energy, the smaller the portion of BZ measured for the same emission angle [1]. In our theory, we assume that QP states do not mix and each QP state has its own plasmons. This is a good approximation if done to evaluate a total spectrum, which is the result of a sum over all the states, i.e. over the whole BZ. Moreover our background is calculated assuming a uniform integral over the full BZ. Taken into account this and the inherent difficulty to precisely determine the points that define the QP region and the first satellite, our experimental points have an absolute error of ± 0.1.

Theory allowed us to calculate spectra at high values of photon energies that we could not reach in experiment. Figure 3 shows how the satellite/QP ratio increases significantly from 0 up to $1-2$ keV and how above $5-10$ keV there is a sort of saturation effect. However, the satellite shape continues to sharpen (show more structure) as the photon energy increases. The origin of this sharpening is to be found in the width of extrinsic plasmon peak (see Tab. 1), which decreases as the photon energy increases and changes more than the intensity of plasmons, hence being the crucial quantity in the equation that determines most changes in the shape of satellites, as it appears from our analysis. The behavior of the satellite/QP ratio is more complicated due to the inelastic mean free path (IMFP) of the photoelectron, which increases with energy. This increase in IMFP gives rise to two competing effects: (i) the increased IMFP allows electrons from deeper in the material to escape, which increases the strenth of the extrinsic plasmon peak; (ii) the IMFP is (inversely) a measure of the probability of scattering plasmons, thus a larger IMFP means that the contribution to the plasmon peak from each hole is lowered.

5 Conclusion

In conclusion we have shown how to describe ab initio satellites in valence-band photoemission spectroscopy. Our method is able to describe multiple excitation of plasmons including lifetimes. This gives an accurate description of the intrinsic part of the spectrum. A number of effects that are not removable from experiment have to be added to the theoretical calculations to obtain an appropriate comparison with experimental data. The photon-energy dependence of satellites was studied including, in the spectral function $A(\omega)$, correcting terms for the intensity and width of extrinsic plasmon peaks, also taking into account interference effects. We compared the theoretical results with our experimental photoemission data, taken at several photon energies, between 200 and 800 eV. Using our theoretical approach, we could give a prediction on a larger range of energies. We evaluated the ratio between the weight of the first satellite and of the QP peaks. Satellites grow bigger with respect to QP peaks as the photon energy increases, until the sudden limit is reached, above $5-10$ keV. The measured data are in agreement with the theoretical curve. The main physical process behind the increase of satellite weight appears to be the variation of the IMFP of photoelectrons. The evaluation of extrinsic and interference effects could be done in a relatively straightforward way thanks to the formulation we introduced for the Green's function and the spectral function. The same would not have been possible if one stayed within the GW approximation, where spurious plasmaron excitations spoil the satellite spectra [12] and multiple satellites are absent.

References

1. A. Damascelli, Z. Hussain, Z.-X. Shen, Rev. Mod. Phys. **75**, 473 (2003)
2. A.L. Fetter, J.D. Walecka, *Quantum theory of Many-Particle Systems* (MacGraw-Hill, New York, 1971)
3. L. Hedin, Phys. Rev. **139**, A796 (1965)
4. W. Aulbur, L. Jonsson, J. Wilkins, Solid State Phys. **54**, 1 (2000)
5. F. Aryasetiawan, O. Gunnarsson, Rep. Prog. Phys. **61**, 237 (1998)
6. L. Hedin, J. Michiels, J. Inglesfield, Phys. Rev. B **58**, 15565 (1998)
7. F. Bechstedt, *Principles of Surface Physics* (Springer, 2003), Chap. 5, pp. 199–201
8. F. Offi et al., Phys. Rev. B **76**, 085422 (2007)
9. L. Hedin, J. Phys.: Condens. Matter **11**, R489 (1999)
10. C.-O. Almbladh, L. Hedin, *Handbook on Synchrotron Radiation* (North-Holland, Amsterdam, 1983), Chap. 8
11. A.S. Kheifets et al., Phys. Rev. B **68**, 233205 (2003)

12. M. Guzzo, G. Lani, F. Sottile, P. Romaniello, M. Gatti, J.J. Kas, J.J. Rehr, M.G. Silly, F. Sirotti, L. Reining, Phys. Rev. Lett. **107**, 166401 (2011)
13. C.N. Berglund, W.E. Spicer, Phys. Rev. **136**, A1030 (1964)
14. F. Bechstedt, K. Tenelsen, B. Adolph, R. DelSole, Phys. Rev. Lett. **78**, 1528 (1997)
15. L.P. Kadanoff, G. Baym, *Quantum Statistical Mechanics* (W.A. Benjamin Inc., New York 1964)
16. G. Lani, P. Romaniello, L. Reining, New J. Phys. **14**, 013056 (2012)
17. B. Arnaud, S. Lebègue, M. Alouani, Phys. Rev. B **71**, 035308 (2005)
18. J. Yeh, I. Lindau, At. Data Nucl. Data Tables **32**, 1 (1985)
19. J.H. Scofield, *Theoretical photoionization cross sections from 1 to 1500 kev*, Tech. Rep. UCRL-51326, Lawrence Livermore National Laboratory, 1973
20. D.A. Shirley, Phys. Rev. B **5**, 4709 (1972)
21. F. Polack et al., AIP Conf. Proc. **1234**, 185 (2011)
22. N. Bergeard et al., J. Synch. Rad. **18**, 245 (2011)
23. X. Gonze, G.-M. Rignanese, M. Verstraete, J.-M. Beuken, Y. Pouillon, R. Caracas, F. Jollet, M. Torrent, G. Zerah, M. Mikami, P. Ghosez, M. Veithen, J.-Y. Raty, V. Olevano, F. Bruneval, L. Reining, R. Godby, G. Onida, D. Hamann, D. Allan, Z. Kristallogr. **220**, 558 (2005)
24. F. Aryasetiawan, L. Hedin, K. Karlsson, Phys. Rev. Lett. **77**, 2268 (1996)
25. L. Ley, S. Kowalczyk, R. Pollak, D.A. Shirley, Phys. Rev. Lett. **29**, 1088 (1972)

D | List of publications

- Matteo Guzzo, Giovanna Lani, Francesco Sottile, Pina Romaniello, Matteo Gatti, Joshua J. Kas, John J. Rehr, Mathieu G. Silly, Fausto Sirotti, and Lucia Reining. Valence electron photoemission spectrum of semiconductors: Ab Initio description of multiple satellites. Phys. Rev. Lett., 107:166401, Oct 2011 [1].

- Matteo Guzzo, Giovanna Lani, Francesco Sottile, Pina Romaniello, Matteo Gatti, Joshua J. Kas, John J. Rehr, Mathieu G. Silly, Fausto Sirotti, and Lucia Reining. Valence-band satellites in photoemission spectroscopy. Scientific Highlights of Soleil synchrotron facility 2011, http://www.highlights-synchrotron-soleil.fr/Highlights-2011-Booklet/#/20/.

- M. Guzzo, J. J. Kas, F. Sottile, J. J. Rehr, M. G. Silly, F. Sirotti, and L. Reining. Plasmon satellites in valence-band photoemission spectroscopy. European Physical Journal B, 85(9):324, 2012 [134].

- N. Bergeard, M. G. Silly, D. Krizmancic, C. Chauvet, M. Guzzo, J. P. Ricaud, M. Izquierdo, L. Stebel, P. Pittana, R. Sergo, G. Cautero, G. Dufour, F. Rochet, and F. Sirotti, *Time-resolved photoelectron spectroscopy using synchrotron radiation time structure*, Journal of Synchrotron Radiation **18**, 245-250 (2011) [3].

- Giacomo Miceli, Matteo Guzzo, Clotilde Cucinotta, and Marco Bernasconi, *First Principles Study of Hydrogen Desorption from The NaAlH$_4$ Surface Doped by Ti Clusters*, The Journal of Physical Chemistry C, 116(6):4311–4315, February 2012 [159].

- Matteo Guzzo, Lorenzo Sponza, Christine Giorgetti, Francesco Sottile, Joshua J. Kas, John J. Rehr, Debora Pierucci, Mathieu G. Silly, Fausto Sirotti, and Lucia Reining, *Ab initio description of multiple satellites in layered materials: graphite and graphene*, in preparation

- Matteo Guzzo, Matteo Gatti, and Lucia Reining, *Electronic spectral properties of NiO: Quasiparticles and satellites*, in preparation

- Matteo Guzzo, Lorenzo Sponza, Christine Giorgetti, Francesco Sottile, Abdelkarim Ouerghi, Claire Mathieu, Debora Pierucci, Mathieu G. Silly, Fausto Sirotti, and Lucia Reining. *Ab initio valence-band satellites in single and multi-layer graphene: energy and thickness dependence*, in preparation

- Matteo Gatti and Matteo Guzzo, *Dynamical screening in correlated metals: spectral properties of SrVO$_3$ in GW and beyond*, in preparation

- Jianqiang Zhou, Claudia Rödl, Matteo Guzzo, and Lucia Reining, *Structure and pathologies of satellites in the spectral function of the two-site Hubbard model within many-body approximations*, in preparation

Acknowledgements

A thesis is the result of very many events and very many interactions that can hardly be summarised in a few pages and would easily make a book by themselves. The list of people who gave small but sometimes very important contributions to my work would be quite long, and I would also probably forget many names. This is why I am going to name a few important people, hoping for forgiveness if I will leave someone out.

This thesis exists solely thanks to a couple of giants on whose shoulders I could sit. My supervisors Lucia and Francesco were some incredibly helpful people and I am grateful to have been able to work my way through Green's functions and numerical physics in their company. Beside their top-level expertise, I will always take as an example their great friendliness and respect towards anybody else. I could not make it through the trickeries of experimental physics without the good advice of Fausto. He and all the team at TEMPO made possible my journey through days and nights of experimental measurements and were a very pleasant company, which is all but the least. Thanks also to the omni-present Matteo G_1: he was always there to help and give good advice whenever I needed, on and off work. My American colleagues, John and Josh, added great value to my work and were always of very good company. Thanks to John for pushing towards the satellite direction and to Josh for his dedication and for interesting discussions together.

Thanks to all the people in my group at the building 411. The atmosphere there has always been the best possible and everyone has always supported me in every possible way. This is especially true for all the people who left the group before myself and who welcomed me when I first arrived. I will always be proud of having been part of this little community. I have in particular to thank France, who gave me a lot of help and good advice, always beyond what was strictly needed.

I have to thank all the people part of the ETSF, the European Theoretical Spectroscopy Facility: thanks to this community I could learn a lot and meet very friendly people. In particular some people were so kind to give me some valuable help in a very uninterested way. I would like to thank in particular Martin Stankowski, Tonatiuh Rangel Gordillo and David Kammerlander. These and many other people made my journey not only possible, they made it especially enjoyable! I can say I was lucky enough to make a lot of good encounters and very few bad ones, if any.

During my stay in France I met a countless number of people and had really

165

Bibliography

[1] Matteo Guzzo, Giovanna Lani, Francesco Sottile, Pina Romaniello, Matteo Gatti, Joshua J. Kas, John J. Rehr, Mathieu G. Silly, Fausto Sirotti, and Lucia Reining. Valence electron photoemission spectrum of semiconductors: *Ab Initio* description of multiple satellites. *Phys. Rev. Lett.*, 107:166401, Oct 2011.

[2] F. Polack, M. Silly, C. Chauvet, B. Lagarde, N. Bergeard, M. Izquierdo, O. Chubar, D. Krizmancic, M. Ribbens, J.-P. Duval, C. Basset, S. Kubsky, and F. Sirotti. Tempo: a new insertion device beamline at soleil for time resolved photoelectron spectroscopy experiments on solids and interfaces. *AIP Conference Proceedings*, 1234(1):185–188, 2010.

[3] N. Bergeard, M.G. Silly, D. Krizmancic, C. Chauvet, M. Guzzo, J.P. Ricaud, M. Izquierdo, L. Stebel, P. Pittana, R. Sergo, G. Cautero, G. Dufour, F. Rochet, and F. Sirotti. Time-resolved photoelectron spectroscopy using synchrotron radiation time structure. *J. Synch. Rad.*, 18(Part 2):245–250, 2011.

[4] V. P. Zhukov, E. V. Chulkov, and P. M. Echenique. Lifetimes of excited electrons in fe and ni: First-principles GW and the T-matrix theory. *Phys. Rev. Lett.*, 93:096401, Aug 2004.

[5] F. Manghi, C. Calandra, and Stefano Ossicini. Quasiparticle band structure of nio: The mott-hubbard picture regained. *Phys. Rev. Lett.*, 73(23):3129, 1994.

[6] Andrea Damascelli, Zahid Hussain, and Zhi-Xun Shen. Angle-resolved photoemission studies of the cuprate superconductors. *Rev. Mod. Phys.*, 75(2):473–541, Apr 2003.

[7] This file is licensed under the Creative Commons Attribution-Share Alike 3.0 Unported license. http://commons.wikimedia.org/wiki/File:Scheme_TEM_en.svg.

[8] Shigemi Kohiki, Masao Arai, Hideki Yoshikawa, Sei Fukushima, Masaoki Oku, and Yoshio Waseda. Energy-loss structure in core-level photoemission satellites of $SrTiO_3$, $SrTiO_3$: La, and $SrTiO_3$: Nb. *Phys. Rev. B*, 62:7964–7969, Sep 2000.

[9] Ray Egerton. *Physical Principles of Electron Microscopy*. Springer US, 2005.

[10] Ralf Hambach. *Theory and* ab-initio *calculations of collective excitations in nanostructures : towards spatially-resolved EELS*. PhD thesis, École Polytechnique, Palaiseau (France), 2010.

[11] H. Hertz. Über einen Einfluss des ultravioletten Lichtes auf die electrische Entladung. *Annalen der Physik*, 267(8):983–1000, 1887.

[12] A. Einstein. Über einen die Erzeugung und Verwandlung des Lichtes betreffenden heuristischen Gesichtspunkt. *Annalen der Physik*, 322(6):132–148, 1905.

[13] Nicolas Bergeard. *Matériaux pour l'étude de la dynamique de l'aimantation*. PhD thesis, Université Paris-Sud 11, November 2010.

[14] A. Fujimori, I. Hase, H. Namatame, Y. Fujishima, Y. Tokura, H. Eisaki, S. Uchida, K. Takegahara, and F. M. F. de Groot. Evolution of the spectral function in mott-hubbard systems with d^1 configuration. *Phys. Rev. Lett.*, 69(12):1796–1799, Sep 1992.

[15] Friedrich Reinert and Stefan Hüfner. Photoemission spectroscopy—from early days to recent applications. *New Journal of Physics*, 7(1):97, 2005.

[16] E.-E. Koch, G. V. Marr, G. S. Brown, D. E. Moncton, S. Ebashi, M. Koch, and E. Rubenstein., editors. *Handbook on Synchrotron Radiation*. Elsevier Science, Amsterdam, 1991.

[17] Soleil synchrotron radiation facility. http://www.synchrotron-soleil.fr/.

[18] G. Beamson, D. Briggs, S.F. Davies, I. W. Fletcher, D. T. Clark, J. Howard, U. Gelius, B. Wannberg, and P. Balzer. *Surf. Interface Anal.*, 15:541, 1990.

[19] N. Martensson, P. Baltzer, P.A. Brühwiler, J.-O. Forsell, A. Nilsson, A. Stenborg, and B. Wannberg. A very high resolution electron spectrometer. *Journal of Electron Spectroscopy and Related Phenomena*, 70(2):117 – 128, 1994.

[20] László Kövér. X-ray photoelectron spectroscopy using hard x-rays. *Journal of Electron Spectroscopy and Related Phenomena*, 178–179(0):241 – 257, 2010. Trends in X-ray Photoelectron Spectroscopy of solids (theory, techniques and applications).

[21] Lars Hedin, John Michiels, and John Inglesfield. Transition from the adiabatic to the sudden limit in core-electron photoemission. *Phys. Rev. B*, 58(23):15565–15582, Dec 1998.

[22] F Bechstedt. *Principles of Surface Physics*, chapter 5, pages 199–201. Springer, 2003.

[23] F. Offi, W. S. M. Werner, M. Sacchi, P. Torelli, M. Cautero, G. Cautero, A. Fondacaro, S. Huotari, G. Monaco, G. Paolicelli, W. Smekal, G. Stefani, and G. Panaccione. Comparison of hard and soft x-ray photoelectron spectra of silicon. *Phys. Rev. B*, 76:085422, Aug 2007.

[24] C.-O. Almbladh and L. Hedin. *Handbook on Synchrotron Radiation*. North-Holland, Amsterdam, 1983.

[25] Lars Hedin. On correlation effects in electron spectroscopies and the *GW* approximation. *J. Phys.: Condens. Matter*, 11:R489–R528, 1999.

[26] A. S. Kheifets, V. A. Sashin, M. Vos, E. Weigold, and F. Aryasetiawan. Spectral properties of quasiparticles in silicon: a test of many-body theory. *Phys. Rev. B*, 68:233205, Dec 2003.

[27] C. N. Berglund and W. E. Spicer. Photoemission studies of copper and silver: Theory. *Phys. Rev.*, 136:A1030–A1044, Nov 1964.

[28] F. Bechstedt, K. Tenelsen, B. Adolph, and R. Del Sole. Compensation of dynamical quasiparticle and vertex corrections in optical spectra. *Phys. Rev. Lett.*, 78(8):1528–1531, Feb 1997.

[29] G. D. Mahan. Theory of photoemission in simple metals. *Phys. Rev. B*, 2:4334–4350, Dec 1970.

[30] M. Born and R. Oppenheimer. *Ann. Phys.*, 84:457, 1927.

[31] T.A. Koopmans. *Physica*, 1:104, 1933.

[32] P. Hohenberg and W. Kohn. Inhomogeneous electron gas. *Phys. Rev.*, 136(3B):B864 – B871, Nov 1964.

[33] M. Marsman, A. Gruneis, J. Paier, and G. Kresse. Second-order m[o-slash]ller–plesset perturbation theory applied to extended systems. i. within the projector-augmented-wave formalism using a plane wave basis set. *The Journal of Chemical Physics*, 130(18):184103, 2009.

[34] W. Kohn and L. J. Sham. Self-consistent equations including exchange and correlation effects. *Phys. Rev.*, 140(4A):A1133–A1138, Nov 1965.

[35] Erich Runge and E. K. U. Gross. Density-functional theory for time-dependent systems. *Phys. Rev. Lett.*, 52(12):997, Mar 1984.

[36] Silvana Botti, Arno Schindlmayr, Rodolfo Del Sole, and Lucia Reining. Time-dependent density-functional theory for extended systems. *Rep. Progr. Phys.*, 70(3):357–407, 2007.

[37] Robert van Leeuwen. Causality and symmetry in time-dependent density-functional theory. *Phys. Rev. Lett.*, 80(6):1280–1283, Feb 1998.

[38] Lars Hedin. New method for calculating the one-particle green's function with application to the electron-gas problem. *Phys. Rev.*, 139(3A):A796–A823, Aug 1965.

[39] L. Hedin and S. Lundqvist. *Solid State Physics*, volume 23. Academic Press, New York, 1969.

[40] A. L. Fetter and J. D. Walecka. *Quantum theory of Many-Particle Systems*. MacGraw-Hill, New York, 1971.

[41] Gerald D. Mahan. *Many-particle physics*. Plenum Press, New York, 1981.

[42] Eleftherios N. Economou. *Green's Functions in Quantum Physics*. Springer Series in Solid-State Sciences. Springer, 2010.

[43] V. M. Galitskii and A. B. Migdal. *Sov. Phys. - JETP*, 7:96, 1958.

[44] H. Lehmann. *Nuovo Cimento*, 11:342, 1954.

[45] H.A. Kramers. La diffusion de la lumiere par les atomes. *Atti Cong. Intern. Fisica, (Transactions of Volta Centenary Congress) Como*, 2:545–557, 1927.

[46] Ulf von Barth and Bengt Holm. Self-consistent GW_0 results for the electron gas: Fixed screened potential W_0 within the random-phase approximation. *Phys. Rev. B*, 54(12):8411–8419, Sep 1996.

[47] B.I. Lundqvist. Single-particle spectrum of the degenerate electron gas i. the structure of the spectral weight function. *Phys. Kondens. Materie*, 6:193–205, 1967.

[48] B.I. Lundqvist. Single-particle spectrum of the degenerate electron gas ii. numerical results for electron coupled to plasmons. *Phys. Kondens. Materie*, 6:206–217, 1967.

[49] B.I. Lundqvist. Single-particle spectrum of the degenerate electron gas iii. numerical results in random phase approximation. *Phys. Kondens. Materie*, 7(2):117–123, 1968.

[50] F. Aryasetiawan, L. Hedin, and K. Karlsson. Multiple plasmon satellites in Na and Al spectral functions from ab initio cumulant expansion. *Phys. Rev. Lett.*, 77(11):2268–2271, 1996.

[51] A Fleszar and W Hanke. Spectral properties of quasiparticles in a semiconductor. *Phys. Rev. B*, 56(16):10228–10232, 1997.

[52] Matteo Gatti and Lucia Reining. Private communication. On VO_2, 2012.

[53] J. Schwinger. *Proc. Nat. Accad. Sci.*, 37:452, 1951.

[54] F. Aryasetiawan and O. Gunnarsson. The GW method. *Rep. Prog. Phys.*, 61(3):237–312, 1998.

[55] Fabien Bruneval, Nathalie Vast, Lucia Reining, M. Izquierdo, F. Sirotti, and N. Barrett. Exchange and correlation effects in electronic excitations of cu[sub 2]o. *Phys. Rev. Lett.*, 97(26):267601, 2006.

[56] C. Rödl, F. Fuchs, J. Furthmüller, and F. Bechstedt. Quasiparticle band structures of the antiferromagnetic transition-metal oxides mno, feo, coo, and nio. *Phys. Rev. B*, 79:235114, Jun 2009.

[57] Fabien Bruneval. *Exchange and Correlation in the Electronic Structure of Solids, from Silicon to Couprous Oxide: GW Approximation and beyond*. PhD thesis, École Polytechnique, Palaiseau (France), 2005.

[58] Matteo Gatti. *Correlation effects in valence-electron spectroscopy of transition-metal oxides : many-body perturbation theory and alternative approaches*. PhD thesis, École Polytechnique, Palaiseau (France), 2007.

[59] Mark S. Hybertsen and Steven G. Louie. Electron correlation in semiconductors and insulators: Band gaps and quasiparticle energies. *Phys. Rev. B*, 34(8):5390–5413, Oct 1986.

[60] R. W. Godby and R. J. Needs. Metal-insulator transition in Kohn-Sham theory and quasiparticle theory. *Phys. Rev. Lett.*, 62(10):1169–1172, Mar 1989.

[61] Wolfgang von der Linden and Peter Horsch. Precise quasiparticle energies and hartree-fock bands of semiconductors and insulators. *Phys. Rev. B*, 37(14):8351–8362, May 1988.

[62] G. E. Engel and Behnam Farid. Generalized plasmon-pole model and plasmon band structures of crystals. *Phys. Rev. B*, 47:15931–15934, Jun 1993.

[63] X. Gonze, G.-M. Rignanese, M. Verstraete, J.-M. Beuken, Y. Pouillon, R. Caracas, F. Jollet, M. Torrent, G. Zerah, M. Mikami, Ph. Ghosez, M. Veithen, J.-Y. Raty, V. Olevano, F. Bruneval, L. Reining, R. Godby, G. Onida, D.R. Hamann, and D.C. Allan. *Zeit. Kristallogr.*, 220:558–562, 2005.

[64] W.G. Aulbur, L. Jönsson, and J.W. Wilkins. Quasiparticle calculations in solids. *Solid State Physics*, 54:1–218, 2000.

[65] R. Del Sole, Lucia Reining, and R. W. Godby. *GWΓ* approximation for electron self-energies in semiconductors and insulators. *Physical Review B*, 49:8024–8028, Mar 1994.

[66] Andrea Marini and Angel Rubio. Electron linewidths of wide-gap insulators: Excitonic effects in LiF. *Phys. Rev. B*, 70:081103, Aug 2004.

[67] P. Romaniello, S. Guyot, and L. Reining. The self-energy beyond *GW*: Local and nonlocal vertex corrections. *The Journal of Chemical Physics*, 131(15):154111, 2009.

[68] G. Strinati, H. J. Mattausch, and W. Hanke. Dynamical aspects of correlation corrections in a covalent crystal. *Phys. Rev. B*, 25(4):2867–2888, Feb 1982.

[69] Mark S. Hybertsen and Steven G. Louie. First-principles theory of quasiparticles: Calculation of band gaps in semiconductors and insulators. *Phys. Rev. Lett.*, 55(13):1418–1421, Sep 1985.

[70] Francesco Sottile, Valerio Olevano, and Lucia Reining. Parameter-free calculation of response functions in time-dependent density-functional theory. *Phys. Rev. Lett.*, 91(5):056402, Jul 2003.

[71] Gordon Baym and Leo P. Kadanoff. Conservation laws and correlation functions. *Phys. Rev.*, 124(2):287–299, Oct 1961.

[72] L. P. Kadanoff and G. Baym. *Quantum Statistical Mechanics*. W.A. Benjamin Inc., New York, 1964.

[73] Giovanna Lani. *Towards a Novel Approach for the Calculation of Many-Body Green's Functions*. PhD thesis, École Polytechnique, Palaiseau (France), 2011.

[74] Giovanna Lani, Pina Romaniello, and Lucia Reining. Approximations for many-body green's functions: insights from the fundamental equations. *New Journal of Physics*, 14(1):013056, 2012.

[75] David C. Langreth. Singularities in the x-ray spectra of metals. *Phys. Rev. B*, 1(2):471–477, Jan 1970.

[76] P. Nozières and C.T. De Dominicis. Singularities in x-ray absorption and emission of metals .3. one-body theory exact solution. *Phys. Rev.*, 178(3):1097–&, 1969.

[77] B. I. Lundqvist. Characteristic structure in core electron spectra of metals due to the electron-plasmon coupling. *Zeitschrift für Physik B Condensed Matter*, 9:236–248, 1969.

[78] L. Hedin, B.I. Lundqvist, and S. Lundqvist. Beyond one-electron approximation - density of states for interacting electrons. *JOURNAL OF RESEARCH OF THE NATIONAL BUREAU OF STANDARDS SECTION A-PHYSICS AND CHEMISTRY*, A 74(3):417, 1970.

[79] F. Bechstedt. Electronic relaxation effects in core level spectra of solids. *physica status solidi (b)*, 112(1):9–49, 1982.

[80] L Hedin. Effects of recoil on shake-up spectra in metals. *Phys. Scripta*, 21(3-4):477–480, 1980.

[81] O. Gunnarsson, V. Meden, and K. Schönhammer. Corrections to migdal's theorem for spectral functions: A cumulant treatment of the time-dependent green's function. *Phys. Rev. B*, 50:10462–10473, Oct 1994.

[82] M.G. Kendall and A. Stuart. *The Advanced Theory of Statistics, Volume 1*. Griffin, London, 3rd edition edition, 1969.

[83] J.J. Yeh and I. Lindau. Atomic subshell photoionization cross-sections and asymmetry parameters - 1 less-than-or-equal-to z less-than-or-equal-to 103. *Atom. Data Nucl. Data Tables*, 32(1):1–155, 1985.

[84] James H. Scofield. Theoretical photoionization cross sections from 1 to 1500 kev. Technical Report UCRL-51326, Lawrence Livermore National Laboratory, 1973.

[85] Silvana Botti, Francesco Sottile, Nathalie Vast, Valerio Olevano, Lucia Reining, Hans-Christian Weissker, Angel Rubio, Giovanni Onida, Rodolfo Del Sole, and R. W. Godby. Long-range contribution to the exchange-correlation kernel of time-dependent density functional theory. *Phys. Rev. B*, 69:155112, Apr 2004.

[86] Francesco Sottile, Margherita Marsili, Valerio Olevano, and Lucia Reining. Efficient *ab initio* calculations of bound and continuum excitons in the absorption spectra of semiconductors and insulators. *Phys. Rev. B*, 76:161103, Oct 2007.

[87] Giovanni Onida, Lucia Reining, and Angel Rubio. Electronic excitations: density-functional versus many-body green's-function approaches. *Rev. Mod. Phys.*, 74(2):601–659, Jun 2002.

[88] Saverio Moroni, David M. Ceperley, and Gaetano Senatore. Static response and local field factor of the electron gas. *Phys. Rev. Lett.*, 75:689–692, Jul 1995.

[89] E. K. U. Gross and Walter Kohn. Local density-functional theory of frequency-dependent linear response. *Phys. Rev. Lett.*, 55(26):2850–2852, Dec 1985.

[90] Randolph Q. Hood, M. Y. Chou, A. J. Williamson, G. Rajagopal, R. J. Needs, and W. M. C. Foulkes. Quantum monte carlo investigation of exchange and correlation in silicon. *Phys. Rev. Lett.*, 78(17):3350–3353, Apr 1997.

[91] Massimiliano Corradini, Rodolfo Del Sole, Giovanni Onida, and Maurizia Palummo. Analytical expressions for the local-field factor $g(q)$ and the exchange-correlation kernel $K_{xc}(r)$ of the homogeneous electron gas. *Phys. Rev. B*, 57:14569–14571, Jun 1998.

[92] Marco Cazzaniga, Hans-Christian Weissker, Simo Huotari, Tuomas Pylkkänen, Paolo Salvestrini, Giulio Monaco, Giovanni Onida, and Lucia Reining. Dynamical response function in sodium and aluminum from time-dependent density-functional theory. *Phys. Rev. B*, 84:075109, Aug 2011.

[93] Andrew J. Morris, Martin Stankovski, Kris T. Delaney, Patrick Rinke, P. García-González, and R. W.gu Godby. Vertex corrections in localized and extended systems. *Phys. Rev. B*, 76:155106, Oct 2007.

[94] Martin Stankovski. *Local and Non-local Vertex Corrections Beyond The GW Approximation*. PhD thesis, University of York, York (UK), 2008.

[95] J. Hubbard. *Proc. Roy. Soc. A*, 243:336, 1957.

[96] A. J. Layzer. Properties of the one-particle green's function for nonuniform many-fermion systems. *Phys. Rev.*, 129:897–907, Jan 1963.

[97] Rodolfo Del Sole, Giovanni Adragna, Valerio Olevano, and Lucia Reining. Long-range behavior and frequency dependence of exchange-correlation kernels in solids. *Phys. Rev. B*, 67:045207, Jan 2003.

[98] M. Stankovski, G. Antonius, D. Waroquiers, A. Miglio, H. Dixit, K. Sankaran, M. Giantomassi, X. Gonze, M. Côté, and G.-M. Rignanese. G^0W^0 band gap of zno: Effects of plasmon-pole models. *Phys. Rev. B*, 84:241201, Dec 2011.

[99] Miguel A. L. Marques, Julien Vidal, Micael J. T. Oliveira, Lucia Reining, and Silvana Botti. Density-based mixing parameter for hybrid functionals. *Phys. Rev. B*, 83:035119, Jan 2011.

[100] J. J. Kas, A. P. Sorini, M. P. Prange, L. W. Cambell, J. A. Soininen, and J. J. Rehr. Many-pole model of inelastic losses in x-ray absorption spectra. *Phys. Rev. B*, 76:195116, Nov 2007.

[101] L. Ley, S. Kowalczyk, R. Pollak, and D. A. Shirley. X-ray photoemission spectra of crystalline and amorphous si and ge valence bands. *Phys. Rev. Lett.*, 29:1088–1092, Oct 1972.

[102] John C. Fuggle, Rainer Lässer, Olle Gunnarsson, and Kurt Schönhammer. Plasmon gains as a monitor of incomplete relaxation, interference effects, and the transition from sudden to adiabatic limits in electron spectroscopies. *Phys. Rev. Lett.*, 44:1090–1093, Apr 1980.

[103] J Stiebling. Optical-properties of mono-crystalline silicon by electron-energy loss measurements. *Zeitschrift für Physik B-Condensed Matter*, 31(4):355–357, 1978.

[104] Neil W. Ashcroft and N. David Mermin. *Solid state physics*. Holt, Rinehart and Winston, New York, 1976.

[105] F. Bechstedt, M. Fiedler, C. Kress, and R. Del Sole. Dynamical screening and quasiparticle spectral functions for nonmetals. *Phys. Rev. B*, 49:7357–7362, Mar 1994.

[106] L. Hedin, B.I. Lundqvist, and S. Lundqvist. New structure in the single-particle spectrum of an electron gas. *Solid State Communications*, 5(4):237 – 239, 1967.

[107] Clas Blomberg and Birger Bergersen. Spurious structure from approximations to the dyson equation. *Canadian Journal of Physics*, 50(19):2286–2293, 1972.

[108] B. Bergersen, F. W. Kus, and C. Blomberg. Single particle green's function in the electron–plasmon approximation. *Canadian Journal of Physics*, 51(1):102–110, 1973.

[109] F. Aryasetiawan. Self-energy of ferromagnetic nickel in the *GW* approximation. *Phys. Rev. B*, 46(20):13051–13064, 1992.

[110] Marco Cazzaniga. *GW* and beyond approaches to quasiparticle properties in metals. *Phys. Rev. B*, 86:035120, Jul 2012.

[111] B Holm and F Aryasetiawan. Self-consistent cumulant expansion for the electron gas. *Phys. Rev. B*, 56(20):12825–12831, 1997.

[112] Thomas J. Pollehn, Arno Schindlmayr, and R.W. Godby. Assessment of the *GW* approximation using hubbard chains. *J. Phys.: Condens. Matter*, 10(6):1273–1283, 1998.

[113] B. Holm and U. von Barth. Fully self-consistent *GW* self-energy of the electron gas. *Phys. Rev. B*, 57(4):2108–2117, Jan 1998.

[114] A. Stan, N. E. Dahlen, and R. van Leeuwen. *Europhys. Lett.*, 76(2):298 – 304, 2006.

[115] F. Caruso, P. Rinke, X. Ren, M. Scheffler, and A. Rubio. Unified description of ground and excited states of finite systems: The self-consistent *GW* approach. *Phys. Rev. B*, 86:081102, Aug 2012.

[116] Eric L. Shirley. Self-consistent *GW* and higher-order calculations of electron states in metals. *Phys. Rev. B*, 54(11):7758–7764, Sep 1996.

[117] Wolf-Dieter Schöne and Adolfo G. Eguiluz. Self-consistent calculations of quasiparticle states in metals and semiconductors. *Phys. Rev. Lett.*, 81(8):1662–1665, Aug 1998.

[118] Lars Hedin. Properties of electron self-energies and their role in electron spectroscopies. *Nuclear Instruments and Methods in Physics Research Section A: Accelerators, Spectrometers, Detectors and Associated Equipment*, 308(1–2):169 – 177, 1991.

[119] H. Ness, L. K. Dash, M. Stankovski, and R. W. Godby. *GW* approximations and vertex corrections on the keldysh time-loop contour: Application for model systems at equilibrium. *Phys. Rev. B*, 84:195114, Nov 2011.

[120] B. Lundqvist and V. Samathiyakanit. Single-particle spectrum of the degenerate electron gas iv. ground state energy. *Zeitschrift für Physik B Condensed Matter*, 9:231–235, 1969. 10.1007/BF02422566.

[121] L. Hedin. Many-body effects in soft x-ray emission in metals. *Solid State Communications*, 5(6):451 – 454, 1967.

[122] J. R. Cuthill, R. C. Dobbyn, A. J. McAlister, and M. L. Williams. Search for plasmaron structure in the soft x-ray $L_{2,3}$ emission spectrum of al. *Phys. Rev.*, 174:515–517, Oct 1968.

[123] Y. Baer and G. Busch. X-ray photoemission from aluminum. *Phys. Rev. Lett.*, 30:280–282, Feb 1973.

[124] B. Wallbank, C.E. Johnson, and I.G. Main. Multi-electron satellites in core electron photoemission from 3d0 ions in solids. *JOURNAL OF PHYSICS C-SOLID STATE PHYSICS*, 6(24):L493–L495, 1973.

[125] W. J. Pardee, G. D. Mahan, D. E. Eastman, R. A. Pollak, L. Ley, F. R. McFeely, S. P. Kowalczyk, and D. A. Shirley. Analysis of surface- and bulk-plasmon contributions to x-ray photoemission spectra. *Phys. Rev. B*, 11:3614–3616, May 1975.

[126] H Höchst, P Steiner, and S Hüfner. X-ray photoemission investigation of the density of states of simple metals. *Journal of Physics F: Metal Physics*, 7(11):L309, 1977.

[127] H. Höchst, P. Steiner, and S. Hüfner. Xps investigation of simple metals. *Zeitschrift für Physik B Condensed Matter*, 30:145–154, 1978. 10.1007/BF01320979.

[128] Paul von Allmen. Plasmaron excitation and band renormalization in a two-dimensional electron gas. *Phys. Rev. B*, 46:13345–13350, Nov 1992.

[129] Riccardo Tediosi, N. P. Armitage, E. Giannini, and D. van der Marel. Charge carrier interaction with a purely electronic collective mode: Plasmarons and the infrared response of elemental bismuth. *Phys. Rev. Lett.*, 99:016406, Jul 2007.

[130] Marco Polini, Reza Asgari, Giovanni Borghi, Yafis Barlas, T. Pereg-Barnea, and A. H. MacDonald. Plasmons and the spectral function of graphene. *Phys. Rev. B*, 77:081411, Feb 2008.

[131] E. H. Hwang and S. Das Sarma. Quasiparticle spectral function in doped graphene: Electron-electron interaction effects in arpes. *Phys. Rev. B*, 77:081412, Feb 2008.

[132] Aaron Bostwick, Florian Speck, Thomas Seyller, Karsten Horn, Marco Polini, Reza Asgari, Allan H. MacDonald, and Eli Rotenberg. Observation of plasmarons in quasi-freestanding doped graphene. *Science*, 328(5981):999–1002, 2010.

[133] Derek Vigil Currey, Johannes Lischner, and Steven G. Louie. Satellite structures in spectral functions of silicon and graphene from ab initio *GW* and cumulant expansion calculations. Unpublished, 2012.

[134] Matteo Guzzo, J.J. Kas, F. Sottile, M.G. Silly, F. Sirotti, J.J. Rehr, and L. Reining. Plasmon satellites in valence-band photoemission spectroscopy. *Eur. Phys. J. B*, 85(9):324, 2012.

[135] B. Arnaud, S. Lebègue, and M. Alouani. Excitonic and quasiparticle lifetime effects on silicon electron energy loss spectra from first principles. *Phys. Rev. B*, 71:035308, Jan 2005.

[136] D. A. Shirley. High-resolution x-ray photoemission spectrum of the valence bands of gold. *Phys. Rev. B*, 5(12):4709–4714, 1972.

[137] Hendrik J. Monkhorst and James D. Pack. Special points for brillouin-zone integrations. *Phys. Rev. B*, 13(12):5188–5192, Jun 1976.

[138] N. Troullier and José Luriaas Martins. Efficient pseudopotentials for plane-wave calculations. *Phys. Rev. B*, 43(3):1993–2006, Jan 1991.

[139] Matteo Guzzo, Lucia Reining, et al. Valence-band satellites in the photoemission spectrum of layered materials. *In preparation*, 2013.

[140] Catalin D. Spataru, Miguel A. Cazalilla, Angel Rubio, Lorin X. Benedict, Pedro M. Echenique, and Steven G. Louie. Anomalous quasiparticle lifetime in graphite: Band structure effects. *Phys. Rev. Lett.*, 87:246405, Nov 2001.

[141] F. R. McFeely, S. P. Kowalczyk, L. Ley, R. G. Cavell, R. A. Pollak, and D. A. Shirley. X-ray photoemission studies of diamond, graphite, and glassy carbon valence bands. *Phys. Rev. B*, 9:5268–5278, Jun 1974.

[142] M. Vos, A.S. Kheifets, E. Weigold, and F. Aryasetiawan. Electron correlation effects in the spectral momentum density of graphite. *Phys. Rev. B*, 63(3):033108, 2001.

[143] T. Sattler, Th. Tschentscher, J. R. Schneider, M. Vos, A. S. Kheifets, D. R. Lun, E. Weigold, G. Dollinger, H. Bross, and F. Bell. Anisotropy of the electron momentum density of graphite studied by $(\gamma, e\gamma)$ and $(e, 2e)$ spectroscopy. *Phys. Rev. B*, 63:155204, Mar 2001.

[144] A. R. Law, J. J. Barry, and H. P. Hughes. Angle-resolved photoemission and secondary electron emission from single-crystal graphite. *Phys. Rev. B*, 28:5332–5335, Nov 1983.

[145] R. Ahuja, S. Auluck, J. Trygg, J. M. Wills, O. Eriksson, and B. Johansson. Electronic structure of graphite: Effect of hydrostatic pressure. *Phys. Rev. B*, 51:4813–4819, Feb 1995.

[146] A. G. Marinopoulos, Lucia Reining, Valerio Olevano, Angel Rubio, T. Pichler, X. Liu, M. Knupfer, and J. Fink. Anisotropy and interplane interactions in the dielectric response of graphite. *Phys. Rev. Lett.*, 89(7):076402, Jul 2002.

[147] A. G. Marinopoulos, Lucia Reining, Angel Rubio, and Valerio Olevano. *Ab initio* study of the optical absorption and wave-vector-dependent dielectric response of graphite. *Phys. Rev. B*, 69:245419, Jun 2004.

[148] R. Hambach, C. Giorgetti, N. Hiraoka, Y. Q. Cai, F. Sottile, A. G. Marinopoulos, F. Bechstedt, and Lucia Reining. Anomalous angular dependence of the dynamic structure factor near bragg reflections: Graphite. *Phys. Rev. Lett.*, 101:266406, Dec 2008.

[149] K. Zeppenfeld. Anisotropic plasmon behaviour in graphite. *Physics Letters A*, 25(4):335 – 336, 1967.

[150] G. S. Painter and D. E. Ellis. Electronic band structure and optical properties of graphite from a variational approach. *Phys. Rev. B*, 1:4747–4752, Jun 1970.

[151] A. K. Geim and K. S. Novoselov. The rise of graphene. *Nature Materials*, 6(3):183–191, March 2007.

[152] Daniel R. Dreyer, Rodney S. Ruoff, and Christopher W. Bielawski. From conception to realization: An historial account of graphene and some perspectives for its future. *Angewandte Chemie International Edition*, 49(49):9336–9344, 2010.

[153] T. Eberlein, U. Bangert, R. R. Nair, R. Jones, M. Gass, A. L. Bleloch, K. S. Novoselov, A. Geim, and P. R. Briddon. Plasmon spectroscopy of freestanding graphene films. *Phys. Rev. B*, 77:233406, Jun 2008.

[154] A. Ouerghi, M. Ridene, A. Balan, R. Belkhou, A. Barbier, N. Gogneau, M. Portail, A. Michon, S. Latil, P. Jegou, and A. Shukla. Sharp interface in epitaxial graphene layers on 3*c*-sic(100)/si(100) wafers. *Phys. Rev. B*, 83:205429, May 2011.

[155] T. Langer, H. Pfnur, H. W. Schumacher, and C. Tegenkamp. Graphitization process of sic(0001) studied by electron energy loss spectroscopy. *Applied Physics Letters*, 94(11):112106, 2009.

[156] Bernd Wenzien, Peter Käckell, Friedhelm Bechstedt, and Giancarlo Cappellini. Quasiparticle band structure of silicon carbide polytypes. *Phys. Rev. B*, 52:10897–10905, Oct 1995.

[157] R. T. M. Ummels, P. A. Bobbert, and W. van Haeringen. First-order corrections to random-phase approximation *GW* calculations in silicon and diamond. *Phys. Rev. B*, 57(19):11962–11973, May 1998.

[158] B. Adolph, K. Tenelsen, V. I. Gavrilenko, and F. Bechstedt. Optical and loss spectra of sic polytypes from ab initio calculations. *Phys. Rev. B*, 55:1422–1429, Jan 1997.

[159] Giacomo Miceli, Matteo Guzzo, Clotilde Cucinotta, and Marco Bernasconi. First principles study of hydrogen desorption from the $NaAlH_4$ surface doped by ti clusters. *J. Phys. Chem. C*, 116(6):4311–4315, February 2012.